Frequency chirping of energetic particle driven modes in tokamaks; self-consistent modelling and simulation

Hooman Hezaveh Hesar Maskan

A thesis submitted for the degree of
Doctor of Philosophy of
The Australian National University

August, 2021

This doctorate thesis is dedicated to

My parents (Amir and Monir), grandma (Maman Faati), brother (Hoomaan)

and

my grandpa (Baba Jalil) and aunt (Zari) who passed away back in Persia while I was doing my PhD in Australia.

These lovely family members have taught me to believe in myself and have reminded me of this life changing quote

" to get what you want, you just need to get past your fear! "

Declaration

This thesis is an account of research undertaken between September 2017 and June 2018 at Research School of Physics and Engineering and between June 2018 and April 2021 at the Mathematical Sciences Institute, the Australian National University, Canberra ACT 2601, Australia. Except where referenced in the customary manner, the material presented in this thesis is, to the best of my knowledge, original and has not been submitted in whole or part for a degree in any university.

The supervisory panel of this thesis includes

- Prof. Matthew J. Hole (ANU, Panel chair),
- Em. Prof. Robert L. Dewar (ANU, co-supervisor),
- Dr. Zhisong Qu (ANU, co-supervisor).

This research has been accomplished in collaboration with Prof. Boris Breizman of University of Austin, Texas, USA and Prof. Yasushi Todo of National Institute for Fusion Sciences (NIFS), Gifu, Japan.

Hooman Hezaveh Hesar Maskan
August, 2021

Publications

This thesis is a thesis by compilation. Its main body consists of four of my publications (published and unpublished) as follows.

- Chapter 2: H. Hezaveh, Z.S. Qu, B. Layden and M.J. Hole (2017). *Impact of energetic particle orbits on long range frequency chirping of BGK modes*, **Nucl. Fusion**, 57, 126010.

  90% my work, 90% my writing

- Chapter 3: H. Hezaveh, Z. S. Qu, B. N. Breizman and M.J. Hole (2020). *Long range frequency chirping of Alfvén eigenmodes*, **Nucl. Fusion**, 60, 056014.

  90% my work, 90% my writing

- Chapter 4: H. Hezaveh, Z. S. Qu, M.J. Hole and R. L. Dewar (2021). *Theoretical description of chirping waves using phase-space waterbags*, **Plasma Phys. Control. Fusion**, 63, 065008.

  90% my work, 90% my writing

- Chapter 5: H. Hezaveh, Y. Todo, Z. S. Qu, B. N. Breizman and M.J. Hole (2022). *Simulation of convective transport in phase-space during the frequency chirping of a TAE using the MEGA code*, **Nucl. Fusion**

  90% my work, 90% my writing

I have contributed to other publications relevant to the topic but not included in the main body:

- A Johnston, M.J. Hole, Z.S. Qu and H Hezaveh (2018). *The effect of pressure anisotropy on ballooning modes in tokamak plasmas*, **Plasma Phys. Control. Fusion**, 60, 065006.

  15% my work

- M.J. Hole, Z.S. Qu, B Layden, C A Michael, M H Woo, J G Bak, J Kim, H. Hezaveh and the KSTAR team (2019). *Bursting toroidal Alfvén eigenmodes in KSTAR plasmas*, **Plasma Phys. Control. Fusion**, 61, 025016.

  10% my work

- A. Kumar, Z. Qu, C. Nührenberg, J. Doak, R. L Dewar, M. J. Hole, S. R. Hudson, J. Loizu and H. Hezaveh *Ideal MHD instabilities of Multi-Region relaxed MHD*, **Submitted to Plasma Phys. Control. Fusion**.

  5% my work

Acknowledgements

Firstly, I would like to give my heartfelt gratitude and appreciation to my supervisor Prof. Matthew Hole and sincerely thank him for his great support and huge amount of time and energy he has spent on my education and PhD research. Matthew is a world-class scientist in burning plasma physics and his support, guidance, help and comments have truly had a magnificent impact on the improvement of my academic life. Since the first day I arrived at the ANU in 2015, I have learned so many things in plasma physics and have achieved valuable experiences even beyond the framework of a PhD research. Without Matthew and his diligent supervision, these achievements would have been impossible. He considered me as a friend by supporting me and talking to me not only about research and academia but also when I had difficult times in my life. On the other hand, he sometimes treated me as his colleague, which gave me a sense of confidence and the fact that I can be trusted in this highly topical field of research -magnetic confinement fusion. He supported me to attend various conferences and meetings and travel twice to National Institute for Fusion Sciences (NIFS), Japan for collaboration on a simulation code and Festival de theorie, France as a research fellow. Matthew is still supporting me to develop my future career and I am honestly indebted to him for his fantastic supervision and support.

Em. Prof. Robert Dewar, we call him "Bob", is among highly top plasma physicists across the globe. I have had the pleasure of working with Bob as my co-supervisor and highly appreciate his support towards my education. The depth of Bobs knowledge means even a short conversation with him can ignite various highly topical fields of research.

Dr Zhisong Qu, my co-supervisor, was a PhD student when I arrived at the ANU and now he is a postdoctoral fellow in our group. Zhisong is brilliant! He has a very high knowledge in both plasma physics and computer coding. Every time I had a discussion with him, I learned new things from him! He has been a great friend and co-supervisor. We have got into deep scientific discussions many times and he has always been patient to listen to me and convince me about a plasma physics problem. Again, I would like to acknowledge Zhisong's efforts and time on my education.

During my PhD, I have had the honor of collaborating with Prof. Boris Breizman, a world-class scientist, of university of Texas at Austin, USA. Boris has played a significant role in progressing the knowledge of energetic particle physics in magnetic toroidal confinement. The well-known Berk-Breizman (BB) model and its corresponding findings are just one example of his valuable efforts in this respect. I was very excited when I first met him at the Marseille airport. Boris has very high standards in research and his comments have taught me a lot and gone a long way towards my education. I would like to also acknowledge his time spent on academic discussions with me on Skype.

The simulation part of my PhD research has been done in collaboration with Prof. Yasushi Todo of National Institute for Fusion Science (NIFS) where I have accomplished two internships in 2018 and 2019. As the head of the Theory and Simulation group at NIFS, he was my supervisor during these interships. It has been a pleasure for me working with Todo-sensei, another world-class scientist in fields of energetic particles. Todo-sensei has enormous knowledge and experience in hybrid simulation of burning plasmas and has

helped me a lot in learning the details of his famous code, MEGA. He has been very responsive to my emails and I highly appreciate it. With great enthusiasm, I would like to thank Todo-sensei and all the members of NIFS for their kind and disciplined hospitality during my stay at NIFS.

I would like to also thank Dr. Brett Layden, a former postdoctoral fellow in our group, with whom I have had fruitful discussions about different plasma physics problems. Brett has always been generous with his time, listening to my questions and answering them in detail by illustration in his notebook.

There have been great academic staff and colleagues from both the Mathematical Sciences Institute (MSI) and the Research School of Physics and Engineering (RSPE) at the Australian National University who I genuinely enjoyed working with during my PhD. This includes Prof. Lilia Ferrario, Prof. Stephen Roberts, Prof. Markus Hegland and Dr. Kenneth Duru. I have also received great administrative support from MSI staff including Mandy Gordon, Cecilia Zhang, Brittany Joyce, Therese McMahon, Macarena Rojas and Andrew Chew. I would like to send my sincere appreciation and gratitude to the students of our group in both MSI and RSPE including Dr. Adelle Wright, Dr. George Bowden, Dr. Craig Bowie, Dr. Qixiang, Sandra Jeyakumar, Dean Muir, Arunav Kumar, Joshua Doak, Stuart Benjamin and Ashley Barnes. It has been a valuable experience to work with each of you. Also, I would like to express my special thanks to Prof. Mohsen Rahmani, who is now the leader of Advanced Optics and Photonics Lab at Nottingham Trent University, for being a compassionate mentor and sharing his useful experiences with me at the early days of my PhD.

Last but not least, I would like to express my immeasurable thanks to my parents and my brother. I would not be where I am today without the immense sacrifices and support from my parents. I highly appreciate the love and kindness they have always given me.

I acknowledge and highly appreciate the funding support from the Australian Research Council through Grant No. DP140100790 for my PhD scholarship and academic travels. I also acknowledge National Computational Infrastructure (NCI), The Australian National University for kindly supporting us with the necessary resources which made the computationally expensive simulations possible. I also appreciate MSI for travel funding. In addition, this work received travel funds from National Institutes of Natural Sciences (NINS)/National Institute for Fusion Sciences (NIFS)-Strategic International Research Interaction Acceleration Initiative, Japan which enabled me to do two internships at NIFS, Japan in 2018 and 2019. Also, Festival de Theorie 2019 partly funded my travel to Festival de Theorie as a research fellow which I acknowledge and appreciate. I would like to thank the Australian Nuclear Science and Technology Organisation (ANSTO), The Australian Institute of Nuclear Science and Engineering (AINSE) Ltd for providing travel funds. I would like to acknowledge the Scholarship AINSE/ANSTO/French Embassy (SAAFE) awarded by AINSE Ltd in 2019 to do collaborative research at the ITER organization. Unfortunately, due to COVID-19 related travel restrictions, I am yet to complete the SAAFE scholarship but look forward to doing it in the future.

Abstract

Frequency chirping waves have been observed in various experiments with tokamak plasmas and there is evidence which shows frequency chirping can occur over long ranges, up to the initial frequency itself. Theoretical toy models and simulations reveal that the nonlinear saturation of an initially unstable plasma wave driven by energetic particles may lead to the emergence of chirping waves. This process is associated with formation and evolution of coherent structures which carry the particles in phase space. In tokamak plasmas, this motion can lead to ejection of the particles from the hot core of the plasma and degrade the machine performance. Therefore, it is essential to develop theory and simulation models to better understand and control chirping waves, as energetic particle driven instabilities, in future fusion plasmas e.g. ITER.

Fast particles of tokamak plasmas can destabilize weakly damped Alfvén eigenmodes during their slowing down process. This can cause the wave amplitude to grow and saturate due to non-linear particle trapping, which may lead to redistribution of particles and a diffusive transport in tokamak plasmas. Depending on physical parameters of the plasma wave, hard non-linear evolution of energetic particle driven instabilities can exhibit different phenomena. Previous numerical simulations reveal that Alfvén eigenmodes emerge inside the gaps of the shear Alfvén continuum and evolve into chirping signals if the mode is subject to intrinsic damping into the cold plasma. In 1997, Berk-Breizman and co-workers [H. Berk et al, Physics Letters A 234 3 213–218] observed chirping signals in simulation studies of an electrostatic plasma wave in inverse Landau damping problem. These signals were interpreted as Bernstein-Greene-Kruskal waves with sweeping frequencies. These chirping waves are associated with formation and evolution of coherent structures (islands) in phase space of energetic particles. Such structures, the so-called "holes" and "clumps", have been found to move adiabatically which implies the trapped particles inside these structure can be carried in phase space as the frequency of the wave chirps; so called convective transport. Various models and codes have been developed to study the chirping phenomenon but restricted to short ranges of frequency chirping since a fixed spatial dependency of the plasma wave is assumed. During long ranges of frequency chirping, however, the spatial profile of the wave can change considerably and hence theoretical/simulation models, capable of updating the wave structure as a result of frequency shifts, are required to study long range frequency chirping of Alfvénic perturbations in tokamaks. In 2010, Boris Breizman [B. N. Breizman, Nuclear Fusion, 50 8 084014] developed a 1D electrostatic non-perturbative model which enables an adiabatic study of chirping waves as a 1D paradigm of electromagnetic chirping signals in resonance with fast particle dynamics in realistic geometries.

In order to build more realistic theoretical models necessary to better understand the chirping waves observed in plasma experiments, nonperturbative theory needs to be extended to electromagnetic plasma waves and also fast particle orbital dynamics should be captured. In this work, a model is developed to investigate the effect of fast particle orbital dynamics in tokamaks in a 1D description. This new trapped/passing orbital model demonstrates how fast particle orbits can impact the hard non-linear behaviour

of the chirping waves. The evolution of the wave spatial profile as well as the rate of frequency chirping as a function of the fast particles orbits are studied.

As the next step, the theory of adiabatic frequency chirping is developed for Alfvénic -type perturbations in realistic configurations. The impact of long range frequency deviations on the radial mode structure of a global Alfvén eigenmode is studied and the chirping rate analysed. In this model, the radial profile of the Alfvén wave is described using the method of finite elements. The expression for the non-linear mode structure is constructed by varying the total Lagrangian of the system with respect to the weight of each finite element. To analyze the phase-space, exact constants of motion during the long range frequency chirping are introduced.

In this work, the theory of chirping waves is extended further by investigating the impact of particle trapping in phase-space for a growing wave potential in the orbital model introduced above. In this respect, a phase space waterbag model is developed by using Lagrangian contours to discretize the phase-space island in adiabatic invariants. In addition, a study of the influence of higher particle resonances on the behaviour of chirping waves is also performed.

The above theoretical frameworks implement an adiabatic approach for long range frequency chirping and a convective transport mechanism is implemented to analyse the phase space of energetic particles. To justify and evaluate this approach, self-consistent simulations are performed using the hybrid model of the MEGA code. A novel phase-space analysis tool is built which enables a reduction of EPs dynamics to an essentially 1D picture. This is based on a new conservation law for particle dynamics which remains valid even when the frequency of the perturbation changes. Therefore, it is possible to observe the hard-nonlinear evolution of holes and clumps on appropriate sub-slices of EPs phase-space. For a toroidicity-induced Alfvén eigenmode, the mechanism of the associated frequency chirping phenomenon has been clarified. The observations of the wave behaviour and the corresponding phase space dynamics are consistent with the adiabatic theory.

Contents

Chapter 1

Introduction

Fusion is the nuclear reaction in which two light atoms combine to form other atoms and particles, called fusion products, and to release energy by mass conversion. Fusion reactions between tritium and deuterium have high cross sections for their occurrence and also high energy yields- 17.58 Mev for the D-T reaction given by

$$\mathrm{D} + \mathrm{T} \rightarrow \mathrm{n}\ (14.07\ \mathrm{Mev}) + {}^{4}\mathrm{He}\ (3.52\ \mathrm{Mev}). \tag{1.1}$$

A possible way of achieving nuclear fusion, as a clean and peaceful source of energy, is the thermonuclear fusion using very high temperatures in a plasma, the 4th state of matter. A precise definition of a plasma, as given in [1], reads: a plasma is a quasi-neutral gas of charged and neutral particles which exhibits collective behaviour. For fusion reactions to happen in a plasma, the average kinetic energy of charged particles should bring them close enough so that the nuclear attraction force overcomes the electric repulsion. This hot plasma needs to be confined which is a challenging step towards designing a nuclear fusion power plant on the earth. In the Sun and the stars, which are heated by thermonuclear fusion, the plasma is confined by gravitational fields. On our planet, there are two main approaches for confining the plasma, namely the magnetic confinement and the inertial confinement.

A tokamak is a device which aims to confine the plasma using helical shape magnetic fields and to date is the most promising candidate of the main core in a fusion power plant. The magnetised plasma inside the tokamak is firstly heated up through current induction called ohmic heating. Subsequently, external sources of heating are implemented such as radio frequency (RF) heating or neutral beam injection (NBI). External heating and the fusion products (α-particles) are the two ways through which energetic particles (EPs) can exist inside the tokamak bulk plasma. These particles gradually slow down and lose energy through collisions with the bulk plasma particles. In some modelling works, the plasma particles are divided into two parts: bulk plasma particles and energetic particles. This classification is based on the theoretical frameworks implemented to model each group of particles. Generally speaking, a plasma can be considered as an N-body dynamical system and the trajectory of each individual charged particle in the presence of electric and magnetic fields (single particle orbit theory) can be studied to determine the plasma behaviour. However, depending on the specific plasma process and phenomenon of interest and whether a microscopic or macroscopic description is required, different theories or a combination of them can be used to model the plasma. Here, we introduce two approaches: kinetic and fluid theories.

1.1 Kinetic description of plasma particles

Single particle orbit theory is valid only in the limit of very low interactions between plasma particles. This requires very low densities which is not usually the case. Therefore, a more appropriate approach is required. Statistical mechanics provides a model to describe the collective behaviour of plasma charged particles. With the advantage of investigating microscopic fluctuations and including the collective effects of the plasma, the kinetic theory excels at plasma modelling but in the expense of being more complicated.

The number of particles having a specific energy and position in space in a plasma can be given by a distribution function $f_\alpha(\mathbf{r}, \mathbf{v}, t)$ of the plasma particles, where α denotes various plasma species. The detailed evolution of such a distribution, which expresses the microscopic information of the plasma as a whole, in a 6D phase-space $(\mathbf{r}, \mathbf{v})$ and time (t) is known as kinetic theory. The evolution of the density of each 6-dimensional phase-space volume is given by

$$\frac{\mathrm{d}f_\alpha(\mathbf{r}, \mathbf{v}, t)}{\mathrm{d}t} \equiv \frac{\partial f_\alpha}{\partial t} + \frac{\partial f_\alpha}{\partial \mathbf{r}} \cdot \frac{d\mathbf{r}}{dt} + \frac{\partial f_\alpha}{\partial \mathbf{v}} \cdot \frac{d\mathbf{v}}{dt}, \tag{1.2}$$

where long range electromagnetic interactions between particles are taken into account. By taking into account the short-range binary collisions between particles, the Boltzman equation is found

$$\frac{\partial f_\alpha}{\partial t} + \frac{\partial f_\alpha}{\partial \mathbf{r}} \cdot \frac{d\mathbf{r}}{dt} + \frac{\partial f_\alpha}{\partial \mathbf{v}} \cdot \frac{d\mathbf{v}}{dt} \equiv \left(\frac{\partial f_\alpha}{\partial t}\right)_{\text{collisions}} \tag{1.3}$$

If the binary collisions between particles are not taken into account then the phase-space density will be preserved along each particle trajectory in phase-space. This gives the Liouville theorem, $\frac{\mathrm{d}f}{\mathrm{d}t} = 0$, that leads to the Vlasov equation [2]

$$\frac{\partial f_\alpha}{\partial t} + \mathbf{v} \cdot \frac{\partial f_\alpha}{\partial \mathbf{r}} + \frac{q_\alpha}{m_\alpha} (\mathbf{E} + \mathbf{v} \times \mathbf{B}) \cdot \frac{\partial f_\alpha}{\partial \mathbf{v}} = 0, \tag{1.4}$$

where $\boldsymbol{E}$ and $\boldsymbol{B}$ represent the total electric and magnetic field, respectively. So far, we have introduced the PDE governing the evolution of the distribution function and this system needs to be closed by the set of Maxwell's equations that determine the electric $\boldsymbol{E}$ and the magnetic field $\boldsymbol{B}$:

$$\nabla \times \mathbf{E} = -\frac{\partial \mathbf{B}}{\partial t}, \tag{1.5a}$$

$$\nabla \times \mathbf{B} = \mu_0 \mathbf{j} + \frac{1}{c^2} \frac{\partial \mathbf{E}}{\partial t}, \tag{1.5b}$$

$$\nabla \cdot \mathbf{E} = \frac{\tau}{\epsilon_0}, \tag{1.5c}$$

$$\nabla \cdot \mathbf{B} = 0, \tag{1.5d}$$

where μ_0 is the magnetic permeability in vacuum, ϵ_0 is the vacuum permittivity, $\mathbf{j}$ is the current density, τ is the charge density. The link between the kinetic equation and the Maxwell's equation is created through the charge and current density source terms given by

$$\tau = \sum_\alpha q_\alpha n_\alpha, \tag{1.6a}$$

$$\mathbf{j} = \sum_\alpha q_\alpha n_\alpha \mathbf{u}_\alpha, \tag{1.6b}$$

where n_α and $\mathbf{u}_\alpha$ are particle density and average velocity, respectively, obtained by taking the zeroth and first moment of the distribution function as

$$n_\alpha(\mathbf{r},t) \equiv \int f_\alpha(\mathbf{r},\mathbf{v},t)d^3v, \tag{1.7a}$$

$$\mathbf{u}_\alpha(\mathbf{r},t) \equiv \frac{1}{n_\alpha(\mathbf{r},t)}\int \mathbf{v} f_\alpha(\mathbf{r},\mathbf{v},t)d^3v. \tag{1.7b}$$

1.2 Fluid theory of plasma

The idea of the fluid theory is to find macroscopic equations by taking the moments of the Boltzman equation in a limited numbers. For taking each moment, we multiply the Boltzman equation (1.3) by powers of $\mathbf{v}$ and then average/integrate over velocity space. This expansion needs to be truncated after a few terms to be practical. One can then use the transport theory to justify the truncation after the 2^{nd} power of v i.e. after $\int d^3v v^2 \cdots$. The scalar zeroth moment of Eq.(1.3), which is integrating over the velocity space, gives the continuity equation. The vector first moment of Eq.(1.3), which is multiplying by $m_\alpha \mathbf{v}$ and integrating over the velocity space, results in the momentum equation. Subsequently, the scalar second moment of Eq.(1.3) yields the energy equation. In general, the k^{th} moment equation contains a term which is a $(k+1)^{\text{th}}$ moment. To achieve a sensible result, we have to truncate this hierarchy and stop this sequence using certain assumptions and turn these equations into a closed set. Following Ref. [3], we describe these assumptions as a three step procedure:

- Splitting the particle velocity into an averaged and random part denoted by $\mathbf{u}_\alpha$ and $\tilde{\mathbf{v}}_\alpha$, respectively:

  $$\tilde{\mathbf{v}}_\alpha \equiv \mathbf{v} - \mathbf{u}_\alpha. \tag{1.8}$$

  This enables the definition of thermal quantities, namely temperature, stress tensor, heat flow, momentum transfer and heat transfer in the momentum equations explained above. A Maxwellian distribution reads

  $$f_\alpha^{\text{eq}}(\mathbf{r},\mathbf{v},t) = n_\alpha \left(\frac{m_\alpha}{2\pi K T_\alpha}\right)^{3/2} \exp\left(-\frac{m_\alpha \tilde{\mathbf{v}}_\alpha^2}{2KT_\alpha}\right), \tag{1.9}$$

  where m_α is the particle mass and K is the Boltzman constant. The above function is an example of a distribution that is consistent with these definitions and for which the LHS of the Boltzman equation vanishes when the distribution of ions and electrons have equal average velocities and temperatures i.e. $\mathbf{u}_e = \mathbf{u}_i$ and $T_e = T_i$, so that the RHS collision term should also vanish.

- Then the set of continuity, momentum and energy equations discussed above will be given by

  $$\frac{\partial n_\alpha}{\partial t} + \nabla\cdot(n_\alpha \mathbf{u}_\alpha) = 0, \tag{1.10a}$$

  $$n_\alpha m_\alpha \left(\frac{\partial \mathbf{u}_\alpha}{\partial t} + \mathbf{u}_\alpha\cdot\nabla\mathbf{u}_\alpha\right) + \nabla\cdot\mathbf{P}_\alpha - n_\alpha q_\alpha(\mathbf{E} + \mathbf{u}_\alpha\times\mathbf{B}) = \mathbf{R}_\alpha, \tag{1.10b}$$

  $$\frac{3}{2} n_\alpha K\left(\frac{\partial T_\alpha}{\partial t} + \mathbf{u}_\alpha\cdot\nabla T_\alpha\right) + \mathbf{P}_\alpha : \nabla\mathbf{u}_\alpha + \nabla\cdot\mathbf{h}_\alpha = Q_\alpha, \tag{1.10c}$$

where $\mathbf{h}_\alpha$ is the heat flow, $\mathbf{R}_\alpha$ is the mean momentum transfer and Q_α is the heat transferred to the system due to collisions between unlike particles associated with resistivity η. By splitting the divergence of the stress tensor into an isotropic part and an anisotropic part, we have

$$\nabla \cdot \mathbf{P} = \nabla p_\alpha + \nabla \cdot \boldsymbol{\pi}_\alpha, \tag{1.11}$$

where the first term on the RHS involves the scalar pressure p_α while the other term involves the off-diagonal pressure tensor ($\boldsymbol{\pi}_\alpha$).

- The above set of moment equations can be closed by using the transport coefficients found by transport theory, which studies deviations from local thermodynamic equilibrium. Therefore we write the form of the transport coefficients as

$$\boldsymbol{\pi}_\alpha \sim \mu_\alpha \nabla \mathbf{u}_\alpha, \tag{1.12a}$$
$$\mathbf{h}_\alpha \sim -k_\alpha \nabla (K T_\alpha), \tag{1.12b}$$
$$\mathbf{R}_\alpha \approx -q_\alpha n_\alpha \eta \mathbf{j}, \qquad \sum Q_\alpha \approx \eta |\mathbf{j}|^2, \tag{1.12c}$$

where μ_α and k_α denote viscosity and thermal conductivity coefficients, respectively. Then, the set of momentum Equations (1.10a) to (1.10c) with the Maxwell's equations transform into the closed set of two-fluid and single-fluid plasma models. It is noteworthy that most of the transport is neglected by the fact that its been assumed to operate on much longer time scales than those for macroscopic dynamics. For such a fluid description, the electrons and ions must also undergo frequent collisions to create the separate electron and ion fluids. According to the transport theory, the criterion for the time scale τ_h on which the hydrodynamic description is valid, reads

$$\tau_h \gg \tau_i [\gg \tau_e], \tag{1.13}$$

where τ_e and τ_i correspond to the collisional relaxation times of electrons and ions, respectively.

1.3 Magnetohydrodynamic model - Ideal MHD

The fluid equations given in the previous subsection still contain the small length and time scales of the plasma dynamics. In the magnetohydrodynamics description of the plasma, we consider length and time scales on which the plasma can be described as a single conducting fluid as a whole. For this purpose, we consider length and time scales much larger than the ion cyclotron radii and the inverse of the ion cyclotron frequency, respectively. Under these conditions, we can neglect most of the dissipative terms ($\boldsymbol{\pi}_{\mathrm{e,i}} \to 0, \mathbf{h}_{\mathrm{e,i}} \to 0$) while some of them are still kept. By setting $q_e = -e$ and $q_i = Ze$ for electrons and ions, respectively, one can find a set of resistive two-fluid equations, given by

$$\frac{\partial n_\alpha}{\partial t} + \nabla \cdot (n_\alpha \mathbf{U}_\alpha) = 0, \tag{1.14a}$$
$$n_\alpha m_\alpha \left(\frac{\partial \mathbf{u}_\alpha}{\partial t} + \mathbf{u}_\alpha \cdot \nabla \mathbf{u}_\alpha \right) + \nabla p_\alpha - n_\alpha q_\alpha (\mathbf{E} + \mathbf{u}_\alpha \times \mathbf{B}) = \mathbf{R}_\alpha. \tag{1.14b}$$
$$\frac{\partial p_\alpha}{\partial t} + \mathbf{u}_\alpha \cdot \nabla p_\alpha + \gamma p_\alpha \nabla \cdot \mathbf{u}_\alpha = (\gamma - 1) Q_\alpha, \tag{1.14c}$$

where γ is the ratio of specific heats. These equations are completed by Maxwell's equations. By defining macroscopic one-fluid variables, as linear combinations of the two-fluid variables, a set of one-fluid equations is obtained. Next, one can implement the quasi charge-neutrality approximation, $|n_e - Zn_i| \ll n_e$, which is very well satisfied at the macroscopic level. In addition, more assumptions are still required to remove the small length and time scale dynamics of the two-fluid equation, namely

$$|\mathbf{u}_i - \mathbf{u}_e| \ll v, \tag{1.15a}$$
$$v \ll c. \tag{1.15b}$$

The former implies that the electron skin depth should be small and the latter imposes non-relativistic speeds. Finally we can write the combination of the one-fluid equations and the Maxwell's equations to give the resistive MHD equations

$$\frac{\partial \rho}{\partial t} + \nabla \cdot (\rho \mathbf{v}) = 0, \tag{1.16a}$$
$$\rho(\frac{\partial \mathbf{v}}{\partial t} + \mathbf{v} \cdot \nabla \mathbf{v}) + \nabla p - \mathbf{j} \times \mathbf{B} = 0, \tag{1.16b}$$
$$\frac{\partial p}{\partial t} + \mathbf{v} \cdot \nabla p + \gamma p \nabla \cdot \mathbf{v} = (\gamma - 1)\eta |\mathbf{j}|^2, \tag{1.16c}$$
$$\frac{\partial \mathbf{B}}{\partial t} + \nabla \times \mathbf{E} = 0, \tag{1.16d}$$
$$\mathbf{j} = \mu_0^{-1} \nabla \times \mathbf{B}, \tag{1.16e}$$
$$\mathbf{E}' \equiv \mathbf{E} + \mathbf{v} \times \mathbf{B} = \eta \mathbf{j}, \tag{1.16f}$$
$$\nabla \cdot \mathbf{B} = 0. \tag{1.16g}$$

The expression (1.16f) represents the generalised Ohm's law for moving conducting media. For a perfectly conducting plasma,

$$\mathbf{E}' \equiv \mathbf{E} + \mathbf{v} \times \mathbf{B} = 0, \tag{1.17}$$

almost everywhere across the plasma. This is valid for many laboratory and astrophysical plasmas. By neglecting the resistivity, one can find the ideal MHD equations as

$$\frac{\partial \rho}{\partial t} + \nabla \cdot (\rho \mathbf{v}) = 0, \tag{1.18a}$$
$$\rho \left(\frac{\partial \mathbf{v}}{\partial t} + \mathbf{v} \cdot \nabla \mathbf{v} \right) + \nabla p - \mu_0^{-1} (\nabla \times \mathbf{B}) \times \mathbf{B} = 0 \tag{1.18b}$$
$$\frac{\partial p}{\partial t} + \mathbf{v} \cdot \nabla p + \gamma p \nabla \cdot \mathbf{v} = 0 \tag{1.18c}$$
$$\frac{\partial \mathbf{B}}{\partial t} - \nabla \times (\mathbf{v} \times \mathbf{B}) = 0, \quad \nabla \cdot \mathbf{B} = 0. \tag{1.18d}$$

1.4 Plasma electron oscillations and kinetic damping

For an electrically neutral plasma consisting of ions and electrons in the equilibrium state, a small perturbation or displacement applied to the electron population with respect to ions will be followed by the action of the Coulomb force which will pull the electrons back as a restoring force. If the charge imbalance is imposed on a macroscopic scale, it will be neutralized extremely fast to preserve charge neutrality of the plasma. On finer time

and scale length, the applied perturbation appear in the form of rapid oscillations of the electron density known as plasma electron oscillations. The frequency of these oscillations (plasma frequency) is usually very high and hence not captured in the large time scales considered in the MHD approximation. Hence, we implement the fluid model of subsection 1.2 to study these oscillations. For a cold plasma without a background magnetic field, all the thermal effects can be neglected. Using Eqs. (1.10a) and (1.10b), we find

$$\frac{\partial n_\alpha}{\partial t} + \nabla \cdot (n_\alpha \mathbf{u}_\alpha) = 0, \tag{1.19a}$$

$$m_\alpha \left(\frac{\partial \mathbf{u}_\alpha}{\partial t} + \mathbf{u}_\alpha \cdot \nabla \mathbf{u}_\alpha \right) = q_\alpha \mathbf{E}. \tag{1.19b}$$

The above system describing the electrostatic oscillations needs to be closed by the Poisson equation,

$$\nabla \cdot \mathbf{E} = \frac{e}{\epsilon_0}(Z n_i - n_e). \tag{1.20}$$

For electron plasma oscillations, the ions can be considered as immobile due to their much heavier mass and hence $\mathbf{u}_i = 0$. Therefore, we only study the one-fluid set of equations for electrons. The physical quantities can be describe as a sum of their corresponding constant background values plus the small perturbations, i.e.

$$\begin{aligned} n_e &\approx n_0 + n_1(\mathbf{r}, t), \\ \mathbf{u}_e &\approx \mathbf{u}_1(\mathbf{r}, t). \end{aligned} \tag{1.21}$$

Substituting these expressions in Eqs. (1.19a), (1.19b) and (1.22), followed by a linearization gives a 2$^{\text{nd}}$ order ODE for electron density perturbation as

$$\frac{\partial^2 n_1}{\partial t^2} = -\frac{n_0 e^2}{\epsilon_0 m_e} n_1. \tag{1.22}$$

which represents oscillations with a frequency of $\omega_{\text{pe}} \equiv \sqrt{\frac{n_0 e^2}{\epsilon_0 m_e}}$.

At this stage, we aim to study an important kinetic phenomenon called Landau damping. For a 1D plasma, this occurs in the velocity space, and in a Maxwellian distribution, leads to a decay in the amplitude for the plasma oscillations. For this purpose, we consider the same plasma and perturbations as the previous case but implement a Vlasov-Poisson system to describe the electron dynamics. This gives

$$\begin{aligned} \frac{\partial f_1}{\partial t} + v\frac{\partial f_1}{\partial x} &= \frac{e}{m_e}\frac{\partial f_0}{\partial v} E_1, \\ \frac{\partial E_1}{\partial x} &= -\frac{e}{\epsilon_0}\int_{-\infty}^{\infty} f_1 dv. \end{aligned} \tag{1.23}$$

Substituting the plane wave solutions and linearization gives the following dispersion relation

$$1 = \frac{\omega_{\text{pe}}^2}{k^2 n_0}\int_{-\infty}^{\infty} \frac{1}{v - \omega/k}\frac{\partial f_0}{\partial v} dv. \tag{1.24}$$

A Maxwellian distribution function can be considered to describe f_0 and perform the integration over the velocity space in Eq. (1.24). However, if the frequency is real, then particles with velocities $v = \frac{\omega}{k}$ will resonate with the wave and a singularity occurs. For real ω, Vlasov [4,5] estimated the principle value of the integral for long wavelengths which

gives

$$\omega^2 \approx \omega_{\mathrm{pe}}^2 + \frac{3}{2}k^2 v_{\mathrm{th}}^2, \tag{1.25}$$

where v_{th} is the thermal velocity of the electrons used in the Maxwellian distribution. By neglecting the thermal effects as before, the above expression agrees with the expression obtained for ω_{pe} using fluid approximation. However, in the method of Vlasov, the singularity of (1.24) has not been carefully analyzed and a more accurate analysis is required. By treating the time dependence through the Laplace transform, Landau [6] shows that there exists an imaginary part of the waves frequency, "Landau damping", and the correct dispersion relation for all values of ω reads

$$1 = \frac{\omega_{\mathrm{pe}}^2}{k^2 n_0}[\mathcal{P}\int_{\infty}^{\infty} \frac{1}{v - \omega/k}\frac{\partial f_0}{\partial v}dv + i\pi\frac{\partial f_0}{\partial v}|_{\omega/k}]. \tag{1.26}$$

The imaginary component of the RHS of (1.26) depends on the gradient of the equilibrium distribution function at the phase velocity of the wave. Consequently, the perturbations can damp or grow in time depending on the sign of the gradient. For an inverted population of plasma particles in velocity space, the plasma wave can be excited and grow in time i.e. inverse Landau damping. In a 1D picture, injection of fast particles into the bulk plasma for heating purposes can be modelled by adding a bump on the tail of the Maxwellian distribution of the bulk plasma. This model is known as the bump-on-tail model. Plasma waves with phase velocities lying on the increasing side of the bump will gain energy from the resonant particles and grow in time. These are known as energetic particle driven modes. This simple example explains the mechanism of one class of instability associated with energetic particles in tokamaks. These fast particles exist in tokamak plasmas either through acceleration by radio-frequency heating and neutral beam injection or as fusion-born α-particles. They gradually lose their energy by interacting with the bulk plasma particles. During this slowing-down phase, the energetic particles can resonant with weakly damped plasma waves, such as Alfvén waves, and transfer net energy to the waves. At large amplitude, such waves can expel fast ions from the hot core of the plasma, leading to a loss of confinement. Understanding and controlling these instability driven phenomena requires detailed modelling and numerical simulations of the excited plasma wave behaviour. In terms of temporal evolution of the wave amplitude, the physics studies can be split into a linear and a non-linear phase. This thesis mainly focuses on the hard non-linear regime of wave evolution. In the next subsection, Alfvén waves are introduced.

1.5 Alfven waves in tokamaks

The bulk plasma in tokamaks is a magnetised plasma which can support a zoo of waves. In general, these waves can be classified as either electromagnetic or electrostatic. Further classification can be applied depending on the plasma species associated with the oscillation and also the direction of wave propagation (wave number k) with regards to the background magnetic field (B_0). For a homogeneous plasma with a constant background magnetic field in the z-direction, one can apply a perturbative approach to the ideal MHD

equations, and linearize to find

$$\frac{\partial \rho_1}{\partial t} = \rho_0 \nabla \cdot \mathbf{v}_1, \tag{1.27a}$$

$$\rho_0 \frac{\partial \mathbf{v}_1}{\partial t} = -\nabla p_1 + \mu_0^{-1} (\nabla \times \mathbf{B}_1) \times \mathbf{B}_0, \tag{1.27b}$$

$$\frac{\partial p_1}{\partial t} = -\gamma p_0 \nabla \cdot \mathbf{v}_1, \tag{1.27c}$$

$$\frac{\partial \mathbf{B}_1}{\partial t} = \nabla \times (\mathbf{v}_1 \times \mathbf{B}_0). \tag{1.27d}$$

For a very low pressure plasma $p_0 \approx 0$ and taking plane wave solutions, Eqs. (1.27b) and (1.27d) give an algebraic eigenvalue equation as

$$-\rho_0 \omega^2 \hat{\mathbf{v}} = -\mu_0^{-1} B_0^2 \mathbf{e}_z \times (\mathbf{k} \times (\mathbf{k} \times (\mathbf{e}_z \times \hat{\mathbf{v}}))) \,. \tag{1.28}$$

The cross product on the RHS implies that $v_\parallel = 0$ or $\mathbf{v}_1 \cdot \mathbf{B}_0 = 0$. By fixing the direction of the wave vector $\mathbf{k}$ to be in $x-z$ plane and focusing on the flow velocities perpendicular to both $\mathbf{k}$ and $\mathbf{B}_0$, we find $\mathbf{k} \cdot \mathbf{v}_1 = 0$. Hence, the dispersion relation reads

$$(\omega^2 - k_\parallel^2 v_A^2) \hat{v}_y = 0, \tag{1.29}$$

which gives two Alfvén waves ($\omega = \pm \omega_A$) that run along the magnetic field to the right ($+$) and left ($-$) with $\omega_A \equiv k_\parallel v_A = \mathbf{k} \cdot \mathbf{B} / \sqrt{\mu_0 \rho_0}$ being the Alfvén frequency. These types of traveling oscillations are known as shear/torsional Alfvén Waves (SAWs) which exist due to the tension of the field lines, which provides the restoring force, and the inertia of the ion mass density.

In a uniform plasma, the above dispersion relation implies that the phase velocity and group velocity are equal and hence low frequency shear Alfvén waves are dispersionless. In toroidal configuration, the helical magnetic field rotates in both toroidal and poloidal directions with magnetic field helicity $q = \frac{1}{2\pi} \int \frac{1}{R} \frac{B_\phi}{B_\mathrm{p}} ds = \frac{B \cdot \nabla \phi}{B \cdot \nabla \theta}$. In this case, we have $k_\parallel = \frac{m - nq}{Rq}$, where m and n are corresponding wave mode numbers in poloidal and toroidal directions, respectively. Since the safety factor usually changes with radius, the dispersion relation, Eq. (1.29), is also a function of the radius. This means that the waves experiences a different velocity at different radius and hence rapidly disperses. The plasma waves that satisfy this dispersion relation are part of the shear Alfvén continuum and are highly damped, known as continuum damping. However, factors such as configuration of the device, the cross sectional shape of the plasma and the axial current can result in the existence of modes that are subject to weak continuum damping [7–10]. A generic example of such gap modes is toroidicity-induced Alfvén eigenmodes (TAEs) which exist due to toroidal coupling of two neighbouring poloidal harmonics in a torus. Figure 1.1b shows the dispersion relation in a cylinder (dashed) and in a tokamak (solid) configuration. Unlike continuum modes that are not easily excited by EPs, gap modes can gain energy through their interaction with slowing-down EPs and grow in time [11–15]. In what follows, various models (1D paradigms) to understand and study this phenomenon are discussed. As mentioned, the interaction of AEs with EPs can result in an instability inside the plasma which may lead to undesirable ejection of energetic particles from the hot core towards the walls of a toroidal device. This loss deteriorates plasma heating and degrades the confinement in a power plant.

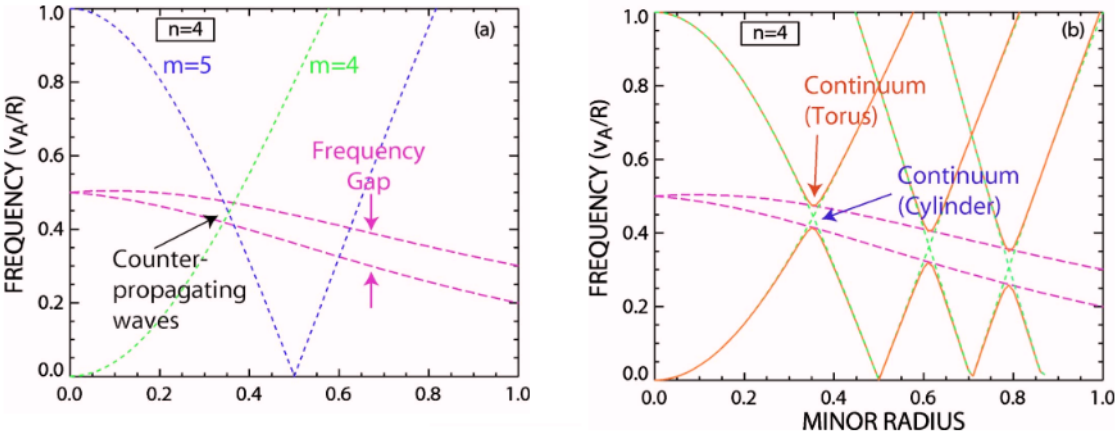

Figure 1.1: Panel (a) shows the dispersion relation of two waves with toroidal mode number n=4 and poloidal harmonics of m=4 and m=5 in a plasma with a q profile that increases monotonically with radius. Frequencies are plotted as positive for both signs of $k_{\|}$. The two waves are counterpropagating in the frequency gap. Panel (b) shows the dispersion relation with (solid) and without (dashed) toroidal coupling of the waves. The $m = 6$ and $m = 7$ waves are also shown and intersect at larger radii. Figure 3 of Ref. [11]

.

1.6 Wave-particle interaction- Berk-Breizman (BB) model

The particles in resonance with a plasma wave can transfer net energy with the wave if the velocity of their motion has a non-zero dot product into the electric field of the wave. For a distribution of particles, a proportion of the resonant EPs lose energy by transferring it to the wave while other resonant EPs gain energy from the wave. For a sufficiently small wave amplitude without nonlinear effects, if the number of particles that transfer energy to the wave is higher, this results in a net energy transfer and hence the wave amplitude grows, known as the linear growth phase. The rate at which the amplitude grows at this stage is called the linear growth rate denoted by γ_l. The plasma wave loses energy through dissipation into the bulk plasma. The rate of this intrinsic damping from the background plasma is denoted by (γ_d) and for $\gamma = \gamma_l - \gamma_d > 0$ instability occurs. As the wave amplitude increases, the resonant particles become trapped inside the wave potential and bounce with a frequency proportional to the wave amplitude and the particle does not transfer net energy to the wave on average over a bounce period. This is known as non-linear particle trapping.

1.6.1 Berk-Breizman (BB) model - saturation levels

Particle trapping in inverse Landau damping was first studied by O'Neil [16] and Mazitov [17]. An adiabatic study of particle trapping was also presented in [18]. In the collisionless limit, the distribution function flattens under the impact of particle trapping around the resonance [19,20] and for the 1D bump-on-tail instability problem with $\gamma_d = 0$, the maximum value of a trapped particle frequency is $\omega_{b,\max}$=3.2γ_l [21,22]. But collisions can create a finite slope in the distribution function which will lead to wave damping [23]. The reader is referred to Ref. [24] for an interesting discussion about this value and its connection to other phsycial phenomena.

In a series of works [25–27], Berk and Breizman (BB) developed theoretical models

to calculate the saturation level of a discrete mode excited by the distribution function generated by a beam injected at high-energy. In Ref. [25], an electrostatic plasma wave is investigated for the bump-on-tail instability problem. High energy beam particles, injected uniformly in space, form a weakly destabilising distribution to a discrete plasma wave by classical transport mechanisms namely drag, pitch-angle scattering and charge exchange losses. Two cases are considered: One has particle annihilation at a rate denoted by ν_α as the only transport process and the other includes both drag and annihilation. The saturation level of the plasma mode is predicted by calculating the power transfer between a finite amplitude wave and beam particles. The wave energy equation,

$$\frac{\partial \mathrm{WE}}{\partial t} + P_h + P_d = 0 \tag{1.30}$$

is considered to investigate the growth of the field amplitude, where WE is the wave energy, P_h is the power transferred to the resonant particles and P_d is the power dissipated into the background plasma. In the first case, the power transfer between particles and waves is reduced by a factor of $\nu_{\mathrm{eff}}/\omega_b$, where ν_{eff} is the rate at which particles leave the resonance region. The resonant particles are formed from direct injection of neutral particle source into the resonance region. The only process that terminates the wave-particle interaction of a resonant particle is annihilation of that particle by charge exchange. For sufficiently large wave amplitudes, $\omega_b > \nu_\alpha$, the ratio of nonlinear power transfer of the beam particles to the wave (P_{NL}) to the linear power transfer (P_L) is

$$P_{\mathrm{NL}}/P_L \equiv \nu_\alpha/\omega_b. \tag{1.31}$$

Therefore, according to the prediction of linear theory, the relative power transfer of particles to the wave decreases with increasing field amplitudes. If the wave continues to damp linearly into the bulk plasma, with $P_d/P_L < 1$, then the amplitude for saturation happens at

$$\omega_b/\nu_\alpha \equiv P_L/P_d. \tag{1.32}$$

In the second case where drag is included, particles that are not trapped by the wave can not enter the trapping region as they slow down. Therefore, unless the injected velocity of the source is in the trapping region, which is not the case in this work, the source of the particles can not feed the region where particles are trapped. This means that in the nonlinear problem with annihilation, the distribution function in the trapping region is zero and a discontinuity is formed in the distribution function between passing and trapped particles. In this case, [25] gives a nonlinear calculation of the power transfer as

$$P_{\mathrm{NL}}/P_L \equiv k^2\alpha^2/\nu_\alpha\omega_b^3, \tag{1.33}$$

where k is the wave number. The above equation for the case with drag is only valid for

$$\omega_b > (k\alpha)^{1/2}, \tag{1.34}$$

with α being the drag coefficient. For large enough field amplitudes, $P_{\mathrm{NL}} < P_L$, and saturation is predicted when

$$P_{\mathrm{NL}}/P_L \equiv k^2\alpha^2/\nu_\alpha\omega_b^3. \tag{1.35}$$

In Ref. [26], Berk and Breizman have shown how a nonlinear drift wave exhibits a similar discontinuity in phase-space and the generalisation of the formalism of Ref [25] to

solve the drift wave problem in a sheared magnetic field. Finally, Ref. [27] represents a formalism to describe the saturation of Alfvén waves excited by density gradient free energy drive from alpha particles created in an ignition system. The BB [25–27] model predicts a steady-state nonlinear wave when classical transport of alpha particles are included. This solution is derived using a balance between the nonlinear alpha particle instability drive and the plasma dissipation. Ref. [28] shows that the type of solution discussed in BB model needs the damping rate (γ_d) to be sufficiently weak. Otherwise, stronger damping rates result in unstable nonlinear solutions and the system does not maintain a steady-state solution and pulsations are observed.

To study the problem of inverse Landau damping, Berk, Breizman and Pekker developed a reduced non-linear simulation model [29]. Unlike the weakly nonlinear model, the simulation model is not limited to small amplitudes of the electrostatic wave. The amplitude and the phase of the wave can change but the angular dependency of the plane wave is assumed to be fixed during EPs non-linear dynamics. The differential equations for the time evolution of plasma wave are found by varying the total Lagrangian of the system with respect to its dynamical variables. Subsequently, one needs to integrate the equation of conservation of momentum and Amperes law over time to find the electron fluid velocity and the electric field, respectively. The linearized single fluid model for electrons results in the following differential equation for the evolution of the fluid velocity including the impact of energetic energetic electrons current

$$mn_0 \frac{\partial^2 u(x,t)}{\partial t^2} = -\frac{n_0^2 e^2}{\epsilon_0} u(x,t) + \frac{e n_0}{\epsilon_0} J_{\mathrm{EP}} u(x,t), \tag{1.36}$$

If explicit integrators e.g. Runge-Kutta method are implemented, then the time step needs to be on the order of the plasma oscillation. However, this requirement has been eliminated in the reduced model by assuming growth rates much smaller than the wave frequency ($\gamma_l \ll \omega_{\mathrm{pe}}$) and substituting linear solutions for the electrostatic wave i.e. electron fluid velocity and the electric field. Consequently, the time scale on which the model requires to be analysed is on the order of γ_l^{-1}. The fast particle current can be derived by taking the first moment of their distribution function. The evolution of the fast particles distribution is described by the Vlasov equation which can be solved either in a grid based method (an Eulerian approach) or following particle trajectories in phase-space (a Lagrangian approach). The simulation model shows that depending on the parameter range under study, a steady state saturation or quasi periodic nonlinear bursts of the wave energy can be observed. The simulation model confirms that in the bump-on-tail instability model with $\gamma_d = 0$ and in the absence of sources and sinks, the saturation level gives a bounce frequency of $\omega_b \approx 3.2\gamma_l$ which is when the saturation mechanism is nonlinear particle trapping and phase-mixing. In addition, these simulations showed that the ratio of $\omega_b/(\gamma_l - \gamma_d)$ varies from 3.2 to 2.9 as γ_d/γ_l changes from 0 to 0.6. The threshold for the resonance overlap condition and particle global diffusion in the phase space are also quantified. The simulation model was extended in Ref. [30] to describe the excitation of TAEs in a toroidal plasma. A transition from a single mode saturation to mode overlap and global quasi-linear diffusion has been observed. This results in a considerable increase in the wave energy due to mode overlap.

Berk, Breizman (BB) and co-workers developed a weakly ($\gamma_d/\gamma_l \equiv 1$) nonlinear theory to study the evolution of marginally unstable energetic particle driven modes [31]. The model studies 1D electrostatic perturbations but since wave-particle interaction is essentially a one-dimensional phenomenon, it can also be applied to AEs in toroidal con-

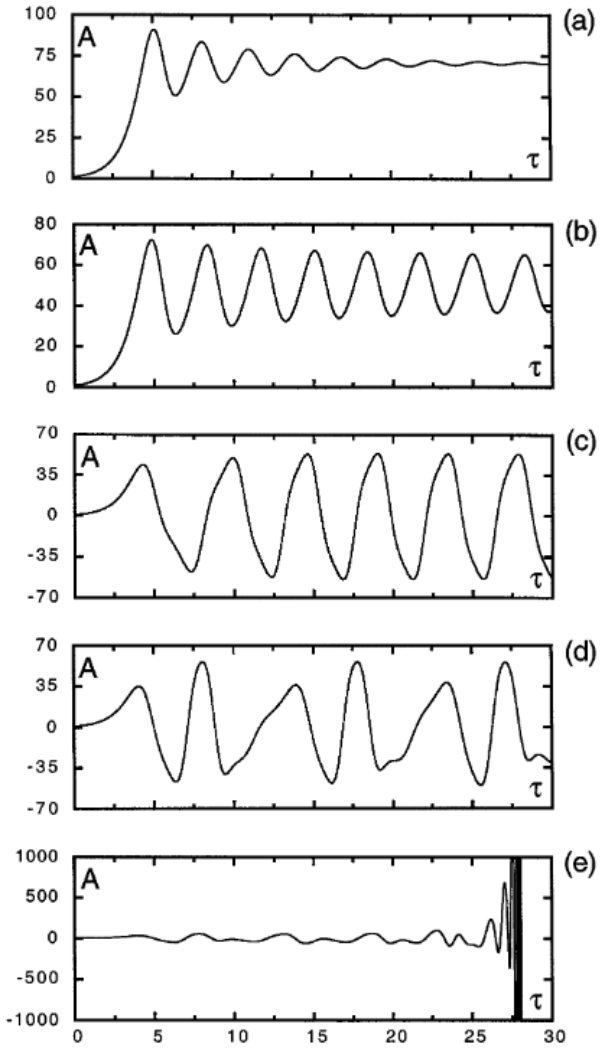

Figure 1.2: Time evolution of the wave amplitude in the weakly non-linear BB model for $\hat{\nu}_{\rm cr} \equiv 4.38$, $A(0) = 1$ and (a) $\hat{\nu} = 5.0$, (b) $\hat{\nu} = 4.3$, (c) $\hat{\nu} = 3.0$, (d) $\hat{\nu} = 2.5$, (e) $\hat{\nu} = 2.4$. Figure 2 of Ref. [31]

figurations [32]. In this theory, a single isolated eigenmode with the wavenumber k and the frequency $\omega_{\rm pe}$ is considered. The linear distribution function of EPs in velocity space has positive gradients around $v = \omega/k$. The sink (EPs collision) was modelled by Krook type collisions with the frequency ν. In this work, a critical value of the collision frequency is found, $\nu_{\rm crt}$, above which the amplitude reaches steady saturation with an amplitude of $A_0 = 2\sqrt{2}\hat{\nu}^2$, where $\hat{\nu} = \frac{\nu}{\gamma_l - \gamma_d}$. This gives

$$\omega_b^2 = 2\sqrt{2}\nu^2 (\frac{\gamma_l - \gamma_d}{\gamma_l})^{1/2}, \tag{1.37}$$

where γ_d is the intrinsic damping of the plasma wave. If the Krook collision frequency decreases below the critical value, the following behaviours can be observed in the wave amplitude: periodic limit cycle, chaotic regime and explosive growth. These behaviours of the wave amplitude are depicted in figure 1.2 for different values of $\hat{\nu}$. The last case is beyond the applicability of the model since in this model its been assumed $\omega_b \ll \gamma_l, \gamma_d$:

the wave amplitude is so small that the expansion in the wave amplitude converges within the third order. Breizman et al studied the impact of pitch-angle scattering on the weakly non-linear model [32] and Lilley et al [33] added drag in velocity space to the weakly non-linear model.

1.6.2 Berk-Breizman model – frequency chirping

In the explosive growth regime mentioned above in the instability threshold model, the unstable mode grows explosively to a level that remains finite. When ω_b reaches the value of γ_l, the frequency of the mode shifts with the amount of shifts comparable to γ_l. At this stage, the explosive growth stops and the mode amplitude saturates. The saturated wave lasts much longer than the background dissipative damping time and the mode frequency keeps shifting i.e. the spectrum of the output signal contains an up-chirping branch with an increasing frequency in time as well as a down-chirping branch. These observations were reported by Berk-Breizman and co-workers for simulations using the bump-on-tail model with small intrinsic damping rates into the bulk plasma (Refs. [34–36]). In this 1D electrostatic model, the linear growth rate of the plane wave is assumed to be much lower than the wave frequency and the wave is excited near the instability threshold. The model requires a cold bulk i.e. the plasma is not modified by the thermal effect, and a weak beam with low beam density such that the real part of the dispersion relationship is not modified by the fast particles. On top of that, it also assumes the damping rate to be external, and does not depend on frequency or wave number. It requires the fast ion collision rate to be much lower than the damping rate, such that the damping mechanism is dominated by prescribed external damping not by fast ion collisions. The frequency spectrum of an excited plasma wave studied in [34] is shown in figure 1.3. At the saturation level, a frequency shift ($\delta\omega \equiv \omega - \omega_0$) much larger than γ_l is observed. Upwards and downward

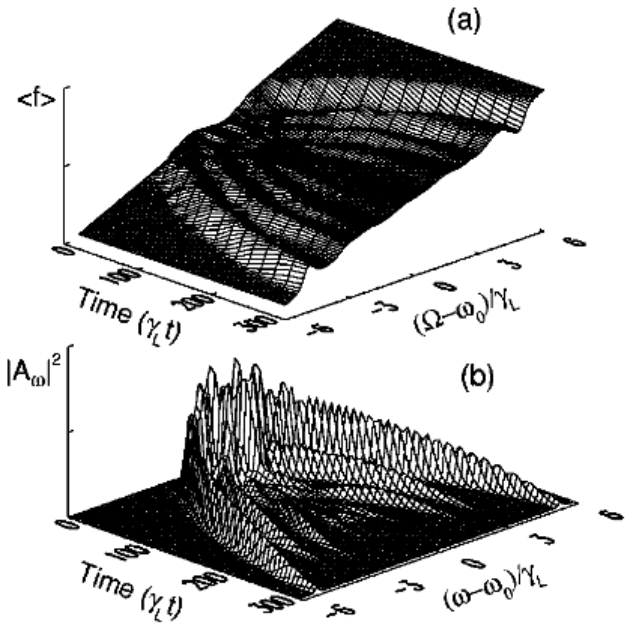

Figure 1.3: Hole-clump structures with time-dependent frequencies. (a) The spatially averaged particle distribution as a function of time and the distance from the linear resonance. (b) The frequency spectrogram of the plasma wave. Figure 3 of Ref. [34]

branches of frequency sweeping are observed. The frequency chirping is associated with the spontaneous formation of phase-space structures. Each chirping wave, described as a Bernstein-Greene-Kruskal (BGK)-type wave with a chirping behaviour in its frequency, is attributed to the formation and evolution of coherent structures namely holes and clumps, in the phase-space of fast particles. It was found that, once formed, these structures evolve adiabatically. Therefore, the Hamiltonian of the fast particles evolves slowly/adiabatically which conserves adiabatic invariants. This implies that the phase-space density inside holes/clumps is preserved.

Pinches et al [37] developed the HAGIS code which models the nonlinear self-consistent interaction between spectrum of linear eigenfunctions and fast particle distribution function. Further simulation studies on frequency chirping during the non-linear evolution have been done by Lesur et al [38, 39] and Vann et al [40]. Lesur et al have shown that the formation of holes and clumps is not a near threshold phenomenon in Ref. [38] with Krook collisions and in Ref. [39] with drag and diffusion. In both cases, significant holes and clumps are demonstrated even for γ_d one order of magnitude smaller than γ_l. In Ref. [41], Lesur has interpreted the physical mechanism of holes and clumps formation as a result of sharp edges of the plateau which can excite waves called secondary eigenmodes. This mechanism was further developed in Ref. [42]. Further simulation studies have been performed to nonlinear evolution of bump-on-tail instability. Lilley et al [43] developed the bump-on-tail (BOT) code , as a Vlasov solver, which enables a study of EPs collisions namely Krook, drag and diffusion. Lilley et al [44] have also shown that the formation of phase-space coherent structures (holes and clumps) in kinetically driven dissipative systems is not a near threshold phenomenon. It has been shown that holes and clumps can form in both close and far from instability threshold. The physical mechanism is related to sideband oscillations, resulting from incomplete phase-mixing, at the sharp edges of the plateau formed in the distribution function after phase-mixing. These waves, from which holes and clumps develop, are interpreted as negative energy waves that grow in the presence of damping in the bulk plasma and evolve into chirping modes. Figure 1.4 shows the evolution of the phase-space for an excited electron plasma wave far from instability threshold ($\gamma_D/\gamma_l = 0.1$) using the BOT code. It can be observed in panel c that after phase-mixing and flattening of the distribution function, hole-clump pairs have been formed and detached from the flattened region. Another important observation is

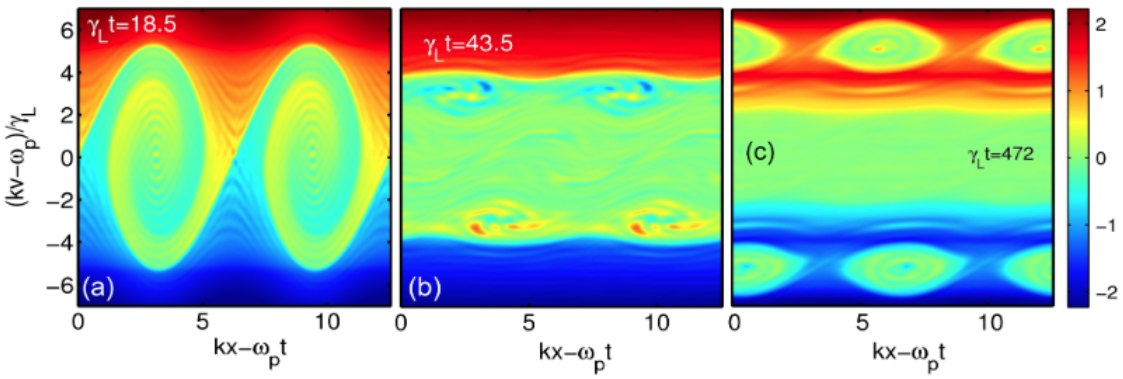

Figure 1.4: Phase space of the energetic electrons using the BOT code: (a) the initial nonlinear phase-mixing (b) formaiton of a plateau with sidebands close to the edge and (c) coherent phase space structures (holes and clumps) detached from the initial resonance region. Figure 2 of Ref. [44]

that the phase-space density remains the same inside the phase space structures and the energetic electrons are being carried by these structures in phase space i.e. a convective transport, also called a bucket transport in the literature since the wave potential acts like a bucket and moves the fast particles in phase-space. The motion of holes and clumps in phase space is synchronized to the wave frequency change which is successfully described by adiabatic theory [45]. Close to marginal instability, the convective transport of holes and clumps tends to be more significant than quasilinear diffusion.

The aforementioned models to study frequency chirping, assume a fixed spatial dependency for the plasma wave. However, as the frequency of a chirping wave changes, its spatial profile will be modified and for long deviations of frequency it may experience considerable modifications with respect to its initial profile. This implies that the validity of the above models is restricted to short ranges of frequency sweeping where the spatial dependency of the wave is not modified considerably from the initial linear eigenvector. In the next part, we demonstrate experimental examples of long range frequency chirping which indicate the need to develop models to study long range chirping events.

1.7 Motivation – experimental observations of long range chirping

As mentioned above, frequency chirping can lead to convective transport in phase space of energetic particles. In realistic geometries, this convective transport occurs in generalised phase-space of energetic particles which results in a change in the particles flux surface number [47] i.e. an inward or outward drift of the particles in the radial direction. In long range frequency chirping, this may lead to the ejection of the particles from the hot core of the plasma and degrade the confinement in a fusion reactor. Therefore, it is necessary to understand and control these instabilities in future tokamaks e.g. ITER. This forms the main motivation of this PhD research.

To justify the need of theoretical and simulation studies for long range frequency chirping, examples of experiments exhibiting long range frequency chirping behaviour are discussed. Ref. [46] reports on experiments with super-Alfvénic NBI on the spherical tokamak START (Culham Science Centre, UK). In NBI heated START discharges, low

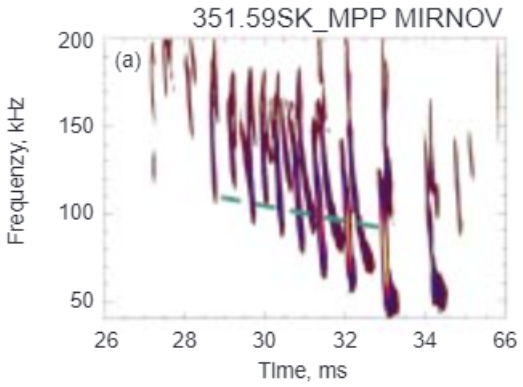

Figure 1.5: The Fourier transformed data from the Mirnov coil showing the frequency sweeping Alfvén perturbations: NBI heated START discharge 35159. NBI starts at 23 ms. Figure 3 of Ref. [46]

values of aspect ratio enables high values of plasma β, which is the ratio of the plasma pressure to the magnetic pressure, with toroidal magnetic fields as low as $B_T \approx 0.15$ T and plasma densities as high as $n_e = 6 \times 10^{19}$ m^{-3}. This implies that Alfvén instabilities can be an important issue in NBI heated plasmas in START because the Alfvén velocity, introduced after Eq. (1.29), is small and NBI produced ions with even $E_{\rm beam} \approx 30$ keV can satisfy the resonance condition during their slowing down process. In these discharges, "chirping" modes become the dominant type of Alfvén instability. Some specifications of the experiments include: line averaged electron density varying in the range $\bar{n}_e = (1-6)\times 10^{19}$ m^{-3}, toroidal magnetic field at the magnetic axis in the range $B_T = 0.2$–0.4 T, plasma current in the range $I_p = 140$–260 kA, major radius $R_0 = 0.3 - 0.37$ m and minor radius $a = 0.23 - 0.3$ m. Figure 1.5 demonstrates the frequency content of the magnetic perturbation detected by the Mirnov coils for discharge No. 35159. In this discharge, a hydrogen beam, injected tangentially to the magnetic axis, with maximum energy $E_{\rm beam} \approx 30$ keV and power $P_{\rm NBI} \approx 0.8$ MW heats the deuterium plasma. NBI heating starts at 23 ms and it is shown that the frequency sweeping Alfvén waves exist in this discharge from $t \approx 29$ ms. This activity was during the flat-top stage of the plasma current evolution. The chirping modes were sweeping on a time scale much less than 1 ms. The whole chirping mode was within 0.3 ms. This time scale is about 30 times shorter than the current evolution time scale. The repetitive bursts started with a frequency in the range $125 - 200$ kHz, close to the TAEs, and chirped down as low as 40 kHz in a very short time, $t \sim 2 \times 10^{-4}$ s .

The NSTX is a low aspect ratio toroidal device. A sequence of high frequency bursts has been observed during early period of NSTX plasma. The range of operational parameters used for these experiments are 0.7 to 1.2 MA of toroidal plasma current, 3.0 to 4.5 kG toroidal field, central electron density of $1.5 - 8 \times 10^{19}$ m^{-3}, central electron temperature of up to ≈ 1 keV. The plasmas were heated with 1.5 to 6 MW of deuterium NBI power at a full energy as high as 90 kV. The frequency content of Mirnov coil data is depicted in figure 1.6 which shows a sequence of bursting global Alfvén eigenmodes (GAEs) in figure 1.6a. The data corresponds to the early phases of NBI heating during current ramp-up. The chirping waves can be seen between 300 and 700 kHz. Figure 1.6b demonstrates a single burst in which the wave chirps both upward and downward in frequency over a range of about 150 kHz or $\delta f/f_0 \approx 30\%$.

Further experimental observations of frequency chirping can be found in Refs. [49–52]. In the next subsection, we discuss a nonperturbative model which describes chirping waves as BGK-type waves with evolving frequencies. The model shows how long range frequency sweeping results in deviations of the angular dependency of a 1D electrostatic plasma wave from its initial linear sinusoidal shape. Accordingly, in order to understand and study experimental data, shown above, with long deviations of the frequency which can be as high as the initial eigenfrequency itself, theoretical models needs to be developed in which the structure of the wave is updated self-consistently as the frequency chirps.

1.8 An adiabatic nonperturbative model for long range chirping

Long range deviations of frequency can change the spatial dependency of the plasma wave. Boris Breizman [53] developed an adiabatic model to describe the nonlinear evolution of a single branch (upward-downward) of electrostatic chirping waves as BGK-type

waves with chirping frequencies. The model assumes that the phase-space structure have already formed and evolve adiabatically. Figure 1.7 shows the evolution of a phase-space clump during the downward chirping in the bump-on-tail model. The initial separatrix centered at normalised momentum $p/m\dot{s}_0 = 1$ corresponds to the saturated wave amplitude prior to chirping. A downward shift in the wave frequency results in a downward motion of the separatrix in phase-space. In this case, as the frequency chirps downward, the amplitude of the chirping wave decreases and hence the separatrix shrinks. The separatrix centered around $p/m\dot{s}_0 = 0.5$ is an illustration of a shrunk separatrix. This model is only applicable to cases where the potential of the chirping wave, and hence the separatrix of the phase-space structure shrinks. This implies that particle trapping in phase-space, which occurs for a deepening potential, is avoided in this model.

The Poisson equation is used to derive an expression for the wave potential energy (U) as a function of the wave phase velocity ($\dot{s}$). The RHS of the Poisson equation is fed with the perturbed density of the cold electrons and energetic electrons. The bulk plasma is assumed to respond linearly and hence the perturbed density of cold electrons is found by linearizing the set of fluid equations for a uniform plasma. The perturbed density of energetic electrons, which involves the non-linear term in the equation, needs to be found by solving the nonlinear kinetic equation. On the other hand, the adiabatic evolution of the coherent phase-space structures permits bounce averaging the kinetic equation to find the perturbed density as a result of their motion (frequency sweeping). Hence the

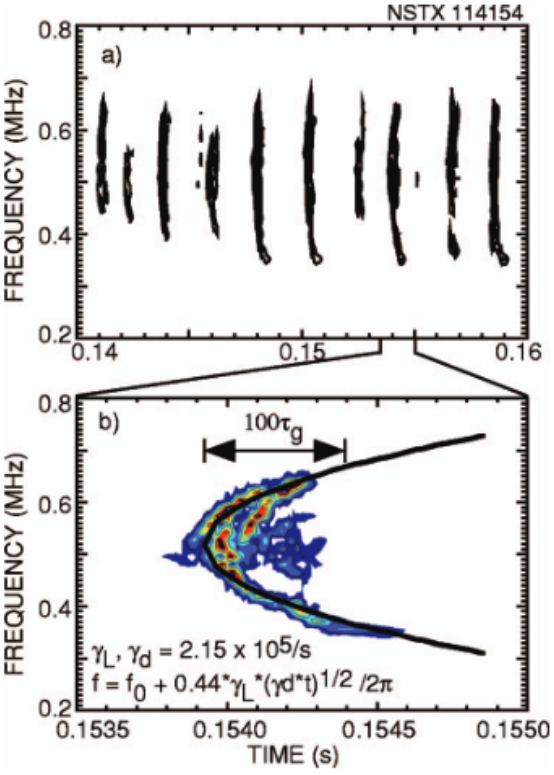

Figure 1.6: Frequency spectrogram of bursting GAE modes during early NBI heating. (a) the sequence of GAE bursts (b) a single burst. Figure 12 of Ref. [48]

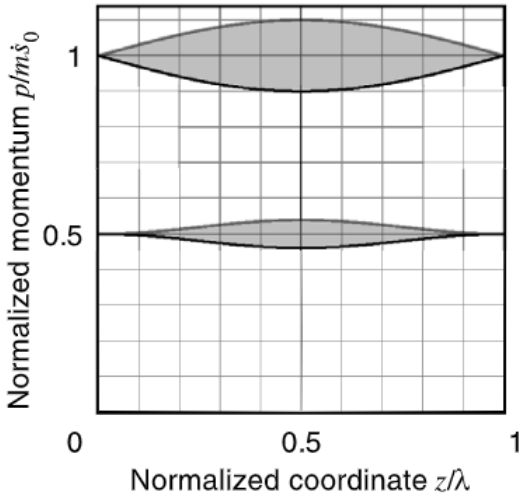

Figure 1.7: A shrinking phase-space clump during downward chirping of the BGK wave frequency. Figure 2 of Ref. [53]

following expression is found for the potential energy of the wave

$$U = \frac{m\dot{s}^2}{2}\frac{8\dot{s}[f_0(\dot{s}_0) - f_0(\dot{s})]}{3n_0\cos\alpha}^2 \left[\frac{1+2\cos^2\alpha}{2} - \frac{3\sin 2\alpha}{4\alpha} - [\cos\alpha - \cos(\alpha\frac{2z}{\lambda} - \alpha)]^2\right], \quad (1.38)$$

where f_0 is the equilibrium distribution function of fast electrons, $\alpha = \omega_{\rm pe}\lambda/4\dot{s}$ with λ being the wavelength. Figure 1.8 demonstrates U for different $\dot{s}$. The curves (b) and (c), which show the deviations from the linear sinusoidal profile, correspond to 20% and 50% of frequency shift, respectively. It can be observed that the plane wave has experienced notable change even for a 20% of frequency sweep.

As mentioned above, chirping waves emerge in the presence of small damping into the bulk plasma. This model implements an energy balance principle approach to find the

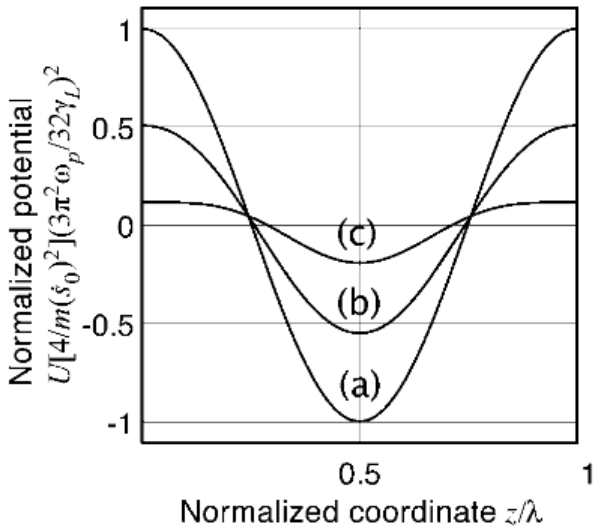

Figure 1.8: Spatial dependency of the wave potential energy:(a) the linear wave, (b)$\dot{s} = 0.8\dot{s}_0$ and (c)$\dot{s} = 0.5\dot{s}_0$. Figure 3 of Ref. [53]

rate at which the frequency sweeps i.e. the energy released by the phase-space structure is equal to the amount of energy deposited into the bulk plasma. In other words, holes and clumps move in a wave to extract energy from the distribution function of EPs and deposit it into the bulk plasma. Accordingly, the following differential equation can be derived to track the slowing-down rate of the phase space clump

$$\begin{aligned}\frac{\mathrm{d}\dot{s}}{\mathrm{d}t} &= -\frac{\nu\dot{s}}{3|\cos\alpha|}\frac{\alpha}{\sin\alpha-\alpha\cos\alpha}\left|\frac{4\dot{s}[f_0(\dot{s}_0)-f_0(\dot{s})]^2}{3n_0\cos\alpha}\right|^2 \\ &\times\left[\tfrac{1}{2}+\tfrac{11\sin 4\alpha}{24\alpha}+8\cos^2\alpha-(\tfrac{3\sin 2\alpha}{2\alpha})^2-\tfrac{2\sin 2\alpha}{3\alpha}\right].\end{aligned} \tag{1.39}$$

For early stages of wave evolution, the above differential equation reproduces the square root scaling of frequency chirping reported in [35] which was discussed above. However, for later evolution, it deviates from the square root dependency. In addition, Nyqvist et al investigated the impact of fast electrons collisions of Krook and drag types [54] followed by a study of the impact of diffusion and particle trapping in phase-space [55] on this model.

1.9 Aims and outline of the thesis

The research undertaken in this PhD dissertation aims to extend the existing knowledge of long range frequency chirping in tokamaks by developing theoretical models as well as performing self-consistent simulations. The theoretical framework of Ref. [53] serves as a 1D electrostatic paradigm of BGK-type chirping waves in realistic geometries. However, more comprehensive efforts are required to model and study Alfvénic chirping signals observed in realistic experiments as examples shown in subsection 1.7. Therefore, it is essential to extend the model of Ref. [53] to include electromagnetic perturbations and also more realistic particle dynamics. This theoretical extension is covered in chapters 2,3 and 4. In addition, numerical simulations of long range frequency chirping of AEs in tokamak plasmas using the MEGA code are given in chapter 5. This work is in collaboration with Prof. Yasushi Todo of the National Institute for Fusion Science, Japan and Prof. Boris Breizman of the University of Texas, Austin, USA.

Fast particle dynamics determines both the existence and the evolution of BGK-type chirping waves. In the model of Boris [53], fast electrons move freely and their motion is not bounded to certain orbit trajectories. In terms of guiding centre dynamics, this only captures highly passing particles. In tokamaks, however, particles follow certain orbits types depending on their energy and pitch angle namely, trapped and passing. In order to develop a more realistic model with respect to particle dynamics and investigate the impact of orbital dynamics on the long range frequency chirping signals, we have developed a trapped-passing locus model [56] which includes energetic particle orbits in the adiabatic model of [53]. This captures the essential features of guiding centre motion in tokamaks and its been performed by a 1D magnetic mirror system in which energetic particles are magnetically trapped and follow certain types of orbits. Then, a numerical scheme is required to solve the nonlinear wave equation which allows us to investigate the evolution of the nonlinear mode which does not remain sinusoidal. By balancing the energy extracted from the distribution function with the energy deposited into the bulk, we can find the rate of frequency chirping. The details of the orbital model can be found in chapter 2.

Chapter 3 represents a theoretical framework which has been developed to extend

the adiabatic model to long range frequency chirping of Alfvén eigenmodes in realistic geometries [47]. A Lagrangian formalism is considered in which the radial envelope of the Alfvén eigenmode is represented using finite elements. Varying the total Lagrangian of the system which respect to the weight of each element gives the nonlinear equation for the evolution of the radial profile. Two separate codes need to be developed. One solves the generalised eigenvalue problem to find the linear MHD eigenvectors and the other is used to solve for the chirping rate and the nonlinear radial structure of the mode. These models will help better understand the long range frequency chirping events observed in experiments. In addition, exact constants of motion are constructed for particle dynamics perturbed by electromagnetic waves in tokamak geometries. This allows for a reduction of the dynamics to 1D, as wave-particle interaction is essentially a 1D problem. These exact constants of motion are very important when studying the evolution of holes and clumps structures during the frequency chirping. These constants of motion are referred to in chapter 5 where a novel phase-space analysis method is developed to study the phase-space of energetic particles using simulation data.

In chapter 4, the model of chapter 2 is extended. The 1D orbital model represented in chapter 2 is restricted to cases where the separatrix of the phase-space island shrinks since particle trapping in phase-space is avoided. In order to study the impact of phase space particle trapping on the hard non-linear evolution of chirping waves, a new model [57] is developed which enables capturing this effect using phase space waterbags. In this case, the phase space island is discretized by Lagrangian contours. In addition, we have studied the impact of higher particle resonances on the evolution of chirping waves in chapter 4.

Chapter 5 involves numerical self-consistent simulations of Alfvénic long range frequency chirping in realistic geometries. The theoretical frameworks introduced above are based on the convective transport of EPs in phase space and assume an adiabatic description for the evolution of holes and clumps. Self-consistent simulations in realistic configurations can shed light on emergence of convective transport associated with long range frequency chirping in which the spatial profile of the wave changes. For this purpose, the MEGA code [58] has been used to perform computationally expensive nonlinear simulations on National Computational Infrastructure (NCI) at the Australian National University (ANU). This code, as an initial value solver, uses a hybrid model to describe the wave evolution. The cold plasma is described by MHD equations that are discretized using the method of finite difference where the field are solved in an Eulerian approach. The population of EPs are modelled kinetically in a Lagrangian picture and the effect of EPs are projected on the grid points using a particle-in-cell approach. In addition, a novel phase space analysis is required to analyze the numerical data. This task is accomplished by utilising the exact constants of motion during frequency chirping introduced in chapter 3. The simulation work is detailed in chapter 5 with the most important result depicted in figure 5.9 which demonstrates convective transport of the EPs during large range frequency chirping of an initially unstable TAE [59]. Chapter 6 contains concluding remarks and future works.

Chapter 2

Impact of energetic particle orbits on long range frequency chirping of BGK modes

Abstract

Long range frequency chirping of Bernstein-Greene-Kruskal modes, whose existence is determined by the fast particles, is investigated in cases where these particles do not move freely and their motion is bounded to restricted orbits. A nonuniform equilibrium magnetic field is included into the bump-on-tail instability problem of a plasma wave. The parallel field gradients account for the existence of different orbit topologies of energetic particles. With respect to fast particles dynamics, the extended model captures the range of particles motion (trapped/passing) with energy and thus represents a more realistic 1D picture of the long range sweeping events observed for weakly damped modes, e.g. global Alfven eigenmodes, in tokamaks. The Poisson equation is solved numerically along with bounce averaging the Vlasov equation in the adiabatic regime. We demonstrate that the shape and the saturation amplitude of the nonlinear mode structure depends not only on the amount of deviation from the initial eigenfrequency but also on the initial energy of the resonant electrons in the equilibrium magnetic field. Similarly, the results reveal that the resonant electrons following different equilibrium orbits in the nonuniform field lead to different rates of frequency evolution. As compared to the previous model [Breizman B.N. 2010 Nucl. Fusion 50 084014], it is shown that the frequency sweeps with lower rates. The additional physics included in the model enables a more complete 1D description of the range of phenomena observed in experiments.

2.1 Introduction

Fast particles are abundantly present in burning plasmas. They exist either through external heating or eventually by fusion-born alpha particles. Energetic particle driven modes (EPMs) [60] can occur as a result of fast particles interaction with weakly damped plasma modes, e.g. Alfven eigenmodes (AEs) [11]. The resulted excited modes can cause the undesirable ejection of energetic particles from the hot core towards the walls of a toroidal machine [12, 61, 62]. This loss deteriorates plasma heating and degrades the

confinement in a power plant. Accordingly, understanding the behavior of these modes is momentous in burning plasmas of future fusion reactors.

Experimental results, in the case of neutral beam injection, demonstrate that EPMs, as a result of AEs excitation, exhibit a "hard" nonlinear regime [63–67] with rapid frequency sweeping. Small deviations from the initial eigenfrequency for the case of a near-threshold instability $|\gamma_l - \gamma_d| \ll \gamma_d \leq \gamma_l$, where γ_l is the kinetic drive and γ_d is the damping rate due to dissipation in the background plasma, were first studied using a 1D bump-on-tail (BOT) model by Berk-Breizman (BB) and co-workers [35]. This model shows the nonlinear process of holes and clumps formation in the fast particle distribution function. A pair of Bernstein-–Greene—Kruskal (BGK) [68] nonlinear modes chirping up and down in frequency is supported by these nonlinear phase-space structures and the frequency shifts are associated with the motion of these coherent structures due to energy dissipation in the bulk plasma. The much longer evolution time scale of these nonlinear structures in comparison with their development time scale in the explosive formation stage is one of the key results in [35] to be taken into consideration. It should be mentioned that holes and clumps form not only in case of a weakly unstable mode but also with any amount of background dissipation [44]. The Berk-Breizman scenario has been proved to be successful in explaining the frequency chirping events observed in experiments with AEs [69, 70]. Moreover, the effect of different types of relaxation processes on the nonlinear evolution has been investigated in [33] and [43], with the BOT code introduced in the latter. All the mentioned models are based on the assumption that the range of frequency chirping is short and the mode structure is fixed.

However, experimental evidence exists for mode activities in which the frequency shifts are as large as the initial eigenfrequency itself [48,71,72]. As the mode amplitude saturates due to flattening of the distribution function of the energetic particles, the physical picture of each evolving phase-space structure is a BGK mode whose frequency changes in time and its structure is notably affected by the frequency shift. Recently, a nonperturbative model based on the adiabatic description of the fast particles contribution has been developed by Breizman [53] using a 1D BOT instability to interpret the long range chirping for an isolated nonlinear resonance. This approach is premised on the assumption that the width of the separatrix supported by the BGK mode is small compared with the characteristic width of the unperturbed distribution function. The Breizman model remains valid as long as the separatrix of the energetic particles inside the clump shrinks for a downward shift in the frequency. As an extension, the adiabatic description of treating an expanding separatrix which traps the ambient particles is presented in [55] by Nyqvist and Breizman.

In magnetized plasmas, e.g. magnetic confinement devices, the particles gyrate about the magnetic field lines and follow certain trajectories depending on their energy and the magnetic field inhomogeneity. Therefore, the impact of particle orbits on the long range frequency sweeping events, should also be investigated in order to better understand and control these instability-driven phenomena. A physical system where the energetic particles are not moving freely and their equilibrium motion is bounded to certain orbits, enables such an investigation through a 1D picture. This physical model is the subject of this paper. We add a fixed nonuniform equilibrium magnetic field to the BOT problem presented in [53], thus creating an energy-dependence of the particle oscillation frequency through the mirror effect of the parallel field gradients. In this new model, the equilibrium field is pointed mainly in the z-direction and has $B_\theta = 0$. For a 1D representation, we consider only the axis (r=0) of this magnetic mirror system and represent the magnetic

field by

$$B = B_c - B_0 \cos(k_{\text{eq}} z), \tag{2.1}$$

where k_{eq} is the spatial frequency of the magnetic field. We assume that the energetic particle confinement is due to the confinement of a single magnetic moment (μ) and treat the chirping of an unstable mode which has a low eigenfrequency compared to the ion cyclotron frequency and its wavelength is large compared to the electron Larmor radius of the resonant electrons. Therefore, the constants B_0 and B_c are determined by

$$B_c - B_0 \gg \left[\frac{m_i \omega_{\text{pe}}}{e Z_i}, \frac{m_e v_\perp}{e \lambda_p} \right], \tag{2.2}$$

where m_i and m_e are the ion and electron mass, respectively, ω_{pe} is the electron plasma frequency, Z_i is the number of ion charges, e is the elementary charge, $v_\perp$ is the velocity of fast particle perpendicular to the magnetic field and λ_p is the wavelength of the perturbed mode. In this new model, the unperturbed guiding center motion of the fast particles in the equilibrium field is governed by the following orbit-averaged Littlejohns Hamiltonian [73]:

$$H_0 = \frac{p_z^2}{2m_e} - \mu B_0 \cos(k_{\text{eq}} z) + \mu B_c, \tag{2.3}$$

where p_z is the energetic particles momentum in the z-direction and it is assumed $A_z = 0$ with A the vector potential. The energetic particles interacting with the perturbed field are considered as trapped or passing in this magnetic mirror system, depending on their pitch angle. Figure 2.1, whose construction is detailed at the end of subsection 2.2.1, demonstrates the behavior of the equilibrium oscillation frequency of the fast electrons versus their energy. For each frequency of trapped particles motion in the equilibrium magnetic field, there exists a group of passing particles having the same frequency of the equilibrium motion. Hence, the mode can be simultaneously in resonance with both the trapped and passing electrons in this equilibrium field. This trapped and passing locus model resembles the trapped particles following the banana orbits and the passing particles in the magnetic field lines of a tokamak (Cf. Section 3.6). In addition to enabling the impact of particle orbits on the long range chirping of BGK modes, the contribution from different resonances can also be investigated through the energy dependence.

The nonlinear wave equation is expanded using Fourier decomposition which allows us to find an explicit expression for the Hamiltonian of the fast particles motion in terms of the action-angle variables of the unperturbed motion. This expansion, together with treating the kinetic equation adiabatically, allows us to implement a numerical treatment to investigate the impact of particle orbits on the structure and the sweeping rate of the nonlinear wave.

In Section 2.2, the basic system of equations adopted for the analysis and the dynamic equations of the unperturbed motion are presented, followed by the derivation of the linear growth rate, the equation for the BGK mode structure and the chirping rate. The numerical scheme used for solving the equations is assigned to Section 2.3. Section 4.5 presents the results in the regions where the adiabatic invariant of the trapped particles in the BGK mode decreases (the separatrix shrinks) during chirping and the effect of the electrons equilibrium orbit on the nonlinear evolution of the mode. Finally, Section 3.6 contains concluding remarks.

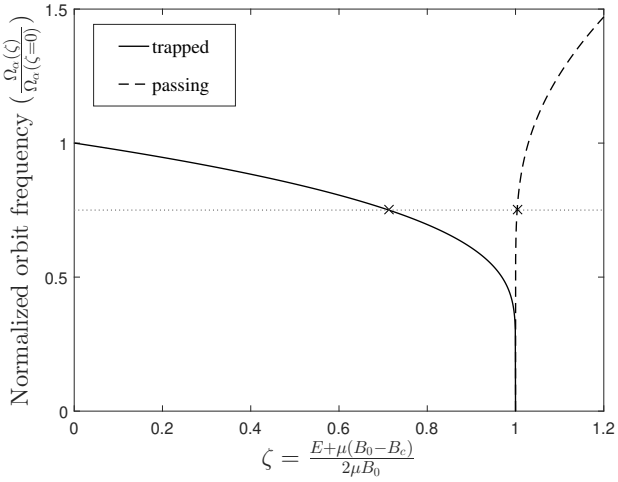

Figure 2.1: Normalized equilibrium frequency of the fast particles in the nonuniform magnetic field vs. energy parameter. The dotted line shows a sample eigenfrequency simultaneously in resonance with particles of two different orbit types

2.2 The model

In this extended 1D BOT model, we study a purely electrostatic mode in a plasma consisting of static background ions, cold electrons responding linearly to the mode and fast electrons which are trapped and co/counter-passing in the nonuniform magnetic field and are in resonance with the electrostatic mode. We focus on propagation and dynamics parallel to the equilibrium magnetic field where the cold plasma has an isotropic distribution and its density will be uniform along the magnetic field. The distribution function of each group of the fast electrons, which is treated through the Vlasov equation, is assumed to be a linearly increasing function of the fast electrons energy providing the instability drive. The damping mechanism is modelled by a Krook collision model, which induces frequency chirping behavior when affecting the resonant energetic electrons as an energy sink. The system of equations considered to investigate both the linear evolution of the mode and the structure of the BGK mode during frequency chirping consists of Poisson, Vlasov, equation of motion and continuity equation, given by

$$\frac{\epsilon_0}{e}\frac{\partial^2 U}{\partial z^2} = -e\left[\sum_\alpha \int \tilde{f}_\alpha dv + \delta n_c\right], \tag{2.4a}$$

$$\frac{\partial f_\alpha}{\partial t} + \{f_\alpha, H_\alpha\} = 0, \tag{2.4b}$$

$$\frac{\partial V_c}{\partial t} = -\frac{1}{m_e}\frac{\partial U}{\partial z} - \nu V_c, \tag{2.4c}$$

$$\frac{\partial \delta n_c}{\partial t} = -n_c\frac{\partial V_c}{\partial z}, \tag{2.4d}$$

with α a label that denotes the orbit type of the fast electrons motion in the magnetic field: ($\alpha = \mathbf{T}$) and ($\alpha = \mathbf{P}$) for the trapped and passing electrons in this field, respectively. The Poisson bracket is denoted by $\{\}$ in equation (2.4b). The total distribution function of energetic electrons is $f_\alpha = F_{\mathrm{eq},\alpha} + \tilde{f}_\alpha$, with $F_{\mathrm{eq},\alpha}$ and $\tilde{f}_\alpha$ being the initial and the perturbed parts, respectively. The energy of the electrostatic mode is given by U, ϵ_0 is the permittivity of free space, $\nu = 2\gamma_d$ is the Krook collision frequency of the cold electrons, V_c

is the flow velocity of the cold electrons and n_c and δn_c are the unperturbed and perturbed density of the cold electrons, respectively.

2.2.1 Fast particles orbits and dynamics

For the completely integrable system consisting of trapped and co/counter-passing particles whose motion is governed by the Hamiltonian presented in equation (2.3), it is possible to transform canonically from the variables (z, p_z) to action–angle variables (θ, J_α), written as

$$J_{\alpha=\mathbf{T}} = \frac{1}{2\pi}\oint p_z dz = \frac{2}{\pi}\int_0^{z_{\max}} \sqrt{2m_e\left[E - \mu B_c + \mu B_0 \cos\left(k_{\mathrm{eq}} z\right)\right]} dz$$
$$= \frac{8\sqrt{m_e \mu B_0}}{k_{\mathrm{eq}}\pi}\left[\left(\zeta - 1\right)\mathbb{K}\left(\zeta\right) + \mathbb{E}\left(\zeta\right)\right] \tag{2.5a}$$
$$J_{\alpha=\mathbf{P}} = \frac{1}{2\pi}\int_0^{\lambda} p_z dz = \frac{4\sqrt{\mu B_0}}{k_{\mathrm{eq}}\pi}\mathbb{E}\left(\zeta^{-1}\right), \tag{2.5b}$$

where J_α is the action for the unperturbed motion of the fast particles, $z_{\max}$ is determined by $p_z = 0$ using equation (2.3), λ is the wavelength of the equilibrium field, E is the unperturbed energy denoting the orbits, ζ is the energy parameter given by

$$\zeta = \frac{E + \mu\left(B_0 - B_c\right)}{2\mu B_0} \tag{2.6}$$

and $\mathbb{K}(\zeta)$ and $\mathbb{E}(\zeta)$ are the complete elliptic integral of the first and second kind, respectively, given by

$$\mathbb{K}\left(\zeta\right) = \int_0^{\frac{\pi}{2}} \frac{d\varrho}{\sqrt{1 - \zeta\sin^2\varrho}}, \tag{2.7a}$$
$$\mathbb{E}\left(\zeta\right) = \int_0^{\frac{\pi}{2}} \sqrt{1 - \zeta\sin^2\varrho}\, d\varrho. \tag{2.7b}$$

Using the canonical equations of motion, the frequency of the motion reads

$$\Omega_{\alpha=\mathbf{T}} = \frac{\partial H_{0,\alpha=\mathbf{T}}}{\partial J_{\alpha=\mathbf{T}}} = \frac{k_{eq}\pi\mu B_0}{2\mathbb{K}\left(\zeta\right)\sqrt{m_e\mu B_0}}, \tag{2.8a}$$
$$\Omega_{\alpha=\mathbf{P}} = \frac{k_{eq}\pi\mu B_0\sqrt{\zeta}}{\mathbb{K}\left(\zeta^{-1}\right)\sqrt{m_e\mu B_0}}. \tag{2.8b}$$

The behavior of these frequencies (shown in figure 2.1) is similar to the bounce and transit frequency of the guiding center motion in tokamaks [74].

2.2.2 The linear growth rate

In this subsection, we investigate the linear interaction between the plasma mode and the fast particles that are trapped and co/counter-passing in the equilibrium magnetic field. For a traveling wave solution, the general form of the physical quantities can be represented as $U = \sum_{n=1}^{\infty}\frac{e\phi_n}{2}\exp\left[in(k_p z - \omega t)\right] + c.c = \sum_{n=1}^{\infty}\frac{e\phi_n}{2}\sum_{p=-\infty}^{\infty}V_{\alpha,n,p}(J_\alpha)\exp\left[i(p\theta - n\omega t)\right] + c.c$ and $\tilde{f}_\alpha = \sum_{n=1}^{\infty}\sum_{p=-\infty}^{\infty}\hat{f}_{\alpha,n,p}(J_\alpha)\exp[i(p\theta - n\omega t)] + c.c$, where $\omega = \omega_r + i\gamma_l$

is the complex frequency, k_p the wave-number of the plasma mode, $V_{\alpha,n,p}(J_\alpha)$ the orbit averaged mode amplitude which specifies the coupling strength and plays the same role as the so-called matrix element in [30, 32], given by

$$\begin{aligned} V_{\alpha,n,p} &= \frac{1}{2\pi}\int_{-\pi}^{\pi} \exp(ink_p z)\exp(-ip\theta)d\theta \\ &= \frac{1}{2\pi}\int_{-\pi}^{\pi} \cos(nk_p z - p\theta)d\theta, \end{aligned} \tag{2.9}$$

where $z(J,\theta)$ is presented in 2.6.1 and we have used the property that z is an odd function of θ (see figure 2.5). In the previous BOT models for long range chirping [53–55], $V_{\alpha,n,p}$ is unity for the dominant resonance and is zero otherwise. In contrast, the presented approach enables investigation of different types of resonances in wave-particle interaction through a 1D model. It is noteworthy that the value of $k_p/k_{\text{eq}} = m$, where m is an integer, can be associated with the mode numbers in realistic geometries.

The total Hamiltonian describing the fast particle motion can be written in the form, $H_\alpha = H_{0,\alpha} + U$. This Hamiltonian along with the linearization of equation (2.4b), is used to derive the linearized Vlasov equation in the form given by

$$\frac{\partial \tilde{f}_\alpha}{\partial t} + \frac{\partial \tilde{f}_\alpha}{\partial \theta}\frac{\partial H_{0,\alpha}}{\partial J_\alpha} = \frac{\partial F_{\text{eq},\alpha}(J_\alpha)}{\partial J_\alpha}\frac{\partial U}{\partial \theta}. \tag{2.10}$$

Neglecting the higher harmonics ($n \geq 2$) in the linear approximation,

$$\hat{f}_{\alpha,n=1,p} = \frac{pe\phi_{n=1}V_{\alpha,n=1,p}(J_\alpha)\frac{\partial F_{\text{eq}}(J_\alpha)}{\partial J_\alpha}}{2(p\Omega_\alpha - \omega)}. \tag{2.11}$$

It can be infered from expression (4.10) that the resonance condition is

$$\omega_r = p\Omega_\alpha. \tag{2.12}$$

The sign of Ω_α is affected by the definition of the angle and considering $\Omega_\alpha > 0$, the resonance condition will be satisfied only for $p > 0$. This means the lower summation index for p in U and $\tilde{f}_\alpha$ should be set to one and the negative values of p correspond to non-resonant particles.

The perturbed density of the cold electrons can be derived from the linear fluid equations, (4.8a) and (4.8b). To first order in perturbations, we have

$$V_c = \frac{k_p U}{\omega m_e}, \tag{2.13a}$$

$$\delta n_c = \frac{k_p^2 n_c U}{m_e \omega^2}. \tag{2.13b}$$

Now we substitute the relevant terms into (2.4a) to find the dispersion relation of the mode given by

$$\frac{\epsilon_0 k_p m_e}{e^2}\left(1 - \frac{\omega_{\text{pe}}^2}{\omega^2}\right) = \sum_\alpha \int \sum_p \frac{p\left(\frac{\partial F_{\text{eq},\alpha}}{\partial J_\alpha}\right)}{p\Omega_\alpha - \omega} V_{\alpha,n=1,p}^2 dJ_\alpha, \tag{2.14}$$

where $\omega_{\rm pe} = \sqrt{\frac{n_c e^2}{m_e \epsilon_0}}$ is the electron plasma frequency. Neglecting the small contribution of the principal value which does not modify the real part of the frequency significantly, allows us to set $\omega_r = \omega_{\rm pe}$. Assuming $\gamma_l \ll \omega_{\rm pe}$ (the wave evolves slowly compared with $\omega_{\rm pe}^{-1}$), equation (2.14) can be solved for ω. Consequently, the linear growth rate is found to be

$$\gamma_l = \frac{\omega_{\rm pe}\pi e^2}{2\epsilon_0 k_p m_e} \sum_\alpha \sum_p \left[\frac{\partial F_{{\rm eq},\alpha}}{\partial \zeta_\alpha} V^2_{\alpha,n=1,p} \left| \frac{{\rm d}\Omega_\alpha}{{\rm d}\zeta_\alpha} \right|^{-1}_{\Omega_\alpha(J_\alpha)=\frac{\omega_{\rm pe}}{p}} \right], \tag{2.15}$$

which involves summing the contribution from all the resonances denoted by p. Equation (4.12) is a function of the energy parameter (ζ). This indicates the dependency of the linear growth rate on particle orbits (see figure 2.3). It should be noted that the contribution from the counter-passing electrons in the equilibrium field is much less than the co-passing ones. This can be shown by changing z to $-z$ in equation (2.9) and evaluating the corresponding values of the coupling strength for counter-passing electrons numerically.

2.2.3 Nonlinear BGK modes

Nonlinear frequency chirping can occur in unstable systems both near or far from marginal stability, in the absence of collisions. For a near-threshold instability, the presence of dissipation leads to the formation of an unstable plateau in the distribution function of the energetic electrons which supports sideband oscillations that finally evolve into chirping modes [35, 44]. In this case, the chirping mode emerges nearly immediately near the marginal stability. However, for the case of a far from threshold instability, the system is so unstable that many modes are likely to be excited. If modes are comparable in frequency with overlapping eigenfunctions, this may lead to mode overlap. Simple chirping can however naturally occur in experiment when the system first goes unstable where there is only a discrete number of unstable modes that can arise from a near continuum of damped modes. Accordingly, we consider the case of a near-threshold instability. The condition $\frac{{\rm d}\omega}{{\rm d}t} < \omega_b^2$, with $\omega\,(t)$ the frequency of the BGK mode and ω_b the bounce frequency of trapped electrons in this mode, ensures the existence of a trapping structure with a hole/clump in the phase-space of energetic particles. After development, the time scale of the motion of already established holes and clumps is much longer than the time scale of the energetic particles motion trapped in the BGK mode, i.e. ω_b^{-1} [34, 35]. In the present model, we focus on the adiabatic description of nonlinear BGK modes and construct our formalism based on the limit $\left[\frac{{\rm d}\omega_b}{{\rm d}t}, \frac{{\rm d}\omega}{{\rm d}t}\right] \ll \omega_b^2 \sim \gamma_l^2 \sim \gamma_d^2$, where the kinetic equation can be bounce-averaged to find the perturbed distribution function of the fast electrons. The adiabatic limit should, in general, be checked if it remains valid as the frequency deviates from the initial eigenfrequency [34, 75, 76].

Adopting a Fourier expansion for the periodic structure, the electrostatic energy of the nonlinear BGK mode can be written in the form

$$U[z,t] = \sum_n A_n(t) \cos\left[n\left(k_p z - \phi\,(t)\right)\right], \tag{2.16}$$

where the Fourier coefficients $A_n(t)$ evolve on a slow time scale but the periodic behavior of the BGK mode represents rapid oscillations with a time scale on the order of the inverse initial plasma frequency. The motion of the fast electrons can be investigated using the

following Hamiltonian

$$\begin{aligned} H_\alpha \quad &= H_{0,\alpha}\left(J_\alpha\right) + \tfrac{1}{2}\textstyle\sum_n \sum_p A_n\left(t\right) \\ &\times V_{\alpha,n,p} \exp\left[i\left(p\theta - n\phi\left(t\right)\right)\right] + c.c, \end{aligned} \tag{2.17}$$

written in terms of the action–angle variables of the unperturbed motion. A simple canonical transformation can be used to cancel the fast time scale included in $\phi\left(t\right)$. We consider $\tilde{\theta}_l = l\theta - \phi\left(t\right)$ and $\tilde{J}_\alpha = \frac{J_\alpha}{l}$ and the type 2 generating function for this canonical transformation is $\Phi\left[\theta, \tilde{J}_\alpha, t\right] = l\theta\tilde{J}_\alpha - \phi\left(t\right)\tilde{J}_\alpha$, where $l = \frac{p}{n}$ denotes the type of the resonance. Considering the first resonance as having the dominant contribution to the interaction, the model can be evaluated by setting $l = 1$. In section 4.5, it is discussed that the contribution from the first resonance is dominant in this model. However, other types of resonances can be treated likewise. The new Hamiltonian is

$$K_\alpha(\tilde{\theta}, \tilde{J}, t) = H_{0,\alpha}\left(\tilde{J}_\alpha\right) - \frac{\mathrm{d}\phi\left(t\right)}{\mathrm{d}t}\tilde{J}_\alpha + \frac{1}{2}\sum_n A_n\left(t\right) V_{\alpha,n,n} \exp\left(in\tilde{\theta}\right) + c.c. \tag{2.18}$$

The small separatrix width assumption allows us to neglect the higher order terms in the Taylor expansion of the unperturbed Hamiltonian near the resonant orbit. In addition, we also approximate $V_{\alpha,n,n}\left(\tilde{J}\right)$ with the first term of its Taylor expansion about the value of action variable at resonance, denoted by $J_{\mathrm{res},\alpha}$. Using $\left.\frac{\partial H_{0,\alpha}}{\partial \tilde{J}_\alpha}\right|_{\tilde{J}_\alpha = J_{\mathrm{res},\alpha}(t)} = \Omega_\alpha = \frac{\mathrm{d}\phi(t)}{\mathrm{d}t} = \omega\left(t\right)$, the new Hamiltonian becomes

$$K_\alpha = \frac{1}{2}\left.\frac{\partial^2 H_{0,\alpha}}{\partial \tilde{J}_\alpha^2}\right|_{\tilde{J}_\alpha = J_{\mathrm{res},\alpha}(t)} \left(\tilde{J}_\alpha - J_{\mathrm{res},\alpha}\left(t\right)\right)^2 + \frac{1}{2}\sum_n A_n\left(t\right) V_{\alpha,n,n} \exp\left(in\tilde{\theta}\right) + c.c. \tag{2.19}$$

Substituting K_α with the extremum value of the BGK mode electrostatic energy in equation (4.15), gives the dynamics of the fast electrons on the separatrix supported by the nonlinear mode. This condition is used to identify the boundary of the trapped and passing electrons in the BGK mode, i.e. the separatrix. A simple manipulation of equation (4.15) gives

$$\tilde{J}_{\alpha,\pm} - J_{\mathrm{res},\alpha}\left(t\right) = \pm\left[\left(U_{\mathrm{ext},\alpha} - \frac{1}{2}\sum_n A_n\left(t\right) V_{\alpha,n,n}\left(J_{\mathrm{res},\alpha}\right) \exp\left(in\tilde{\theta}\right) + c.c\right)\frac{2}{\Delta_\alpha}\right]^{\frac{1}{2}}, \tag{2.20}$$

where $U_{\alpha,\mathrm{ext}}$ is the extremum value of the BGK mode energy.
The value of $\left.\frac{\partial^2 H_{0,\alpha}}{\partial \tilde{J}_\alpha^2}\right|_{\tilde{J}_\alpha = J_{\mathrm{res},\alpha}(t)} = \left.\frac{\partial \Omega_\alpha}{\partial \tilde{J}_\alpha}\right|_{\tilde{J}_\alpha = J_{\mathrm{res},\alpha}(t)}$ (denoted by Δ_α) can be negative or positive for the trapped or passing electrons in the equilibrium field, respectively. Mathematically, this affects $U_{\mathrm{ext},\alpha}$ in order to have a positive value under the square root in equation (2.20) and from the physical point of view, it shows that the passing electrons in the magnetic field are trapped in the energy well of the BGK mode, while the trapped electrons in this field are trapped in the energy hill of the BGK mode. This implies

$$U_{\mathrm{ext},\alpha} = \begin{cases} U_{\min}, & \alpha = \mathbf{T} \\ U_{\max}, & \alpha = \mathbf{P} \end{cases}. \tag{2.21}$$

Phase-space trajectories of constant energy for the motion of energetic particles in the

BGK mode are plotted in figure 2.2. It is shown that the separatrix supported by the nonlinear mode corresponding to the electrons trapped in the equilibrium magnetic field (figure 2.2(b)) has a phase shift of π with respect to the separatrix related to the passing group (figure 2.2(a)).

As the separatrix moves adiabatically, the phase-space area enclosed by the trajectories of the deeply trapped particles in the nonlinear wave, i.e. the shaded areas in figure 2.2, is conserved. Without trapping or detrapping over this region, the aforementioned conservation ensures that the value of the distribution function is conserved. The separatrix moves the trapped electrons in the BGK mode while the passing electrons are affected through the direction of their motion [53]. The adiabatic invariant of the motion of these electrons in the BGK mode reads (see 2.6.2 for more details)

$$I_\alpha = 2\int_0^{2\pi}\left[\left(K_\alpha - \frac{1}{2}\sum_n A_n(t)V_{\alpha,n,n}\exp\left(ip\tilde{\theta}\right) + c.c\right)\frac{2}{\Delta_\alpha}\right]^{\frac{1}{2}} d\tilde{\theta}. \tag{2.22}$$

Substituting expression (4.13) into equation (2.4a) gives

$$-\sum_n A_n(t)n^2k_p^2\cos\left[n\left(kz-\phi\left(t\right)\right)\right] = -\frac{e^2}{\epsilon_0}\left[\frac{1}{m_e}\sum_\alpha\int_{-\infty}^{\infty}\tilde{f}_\alpha(z,p_z)dp_z + \delta n_c\right], \tag{2.23}$$

where δn_c can be derived under the linear response assumption of the bulk electrons. Sim-

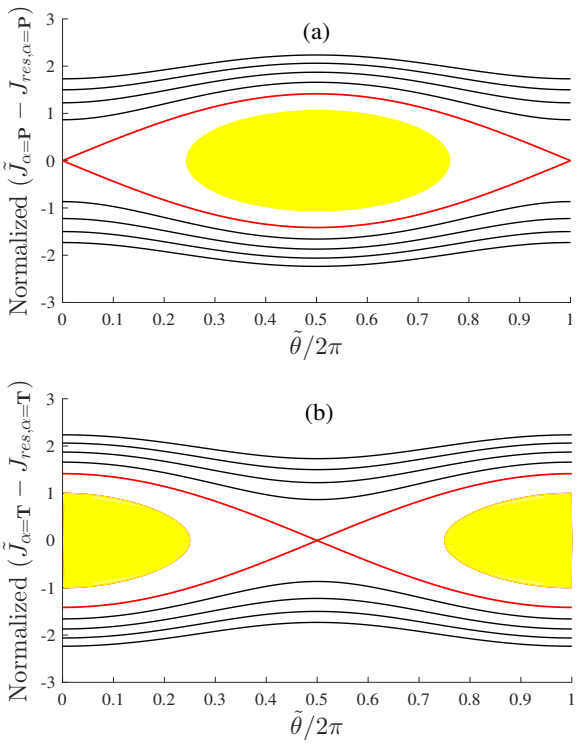

Figure 2.2: The panels (a) and (b) describe energy contours in phase space of the electrons which are passing and trapped in the equilibrium field, respectively. The black lines specify the trajectories of the passing electrons and the shaded area is a sample of the adiabatic invariant of the trapped electrons in the nonlinear BGK mode. The red line is the separatrix.

ilar to subsection 2.2.2, we multiply equation (2.23) by $\cos\left[n\left(k_p z-\phi(t)\right)\right]$ and integrate over one wavelength. We also write all the physical quantities in the fast particle term in terms of the new action–angle variables $(\tilde{\theta},\tilde{J})$. After substituting the Fourier expansion of $\cos\left[n\left(kz(\tilde{\theta},\tilde{J})-\phi(t)\right)\right]$ and neglecting the highly oscillating terms one finds

$$A_n\left(t\right)=\frac{1}{2\pi k_p n_c}\left[\frac{\omega^2}{n^2\hat{\omega}^2-1}\right]\sum_{\alpha}\int_0^{2\pi}d\tilde{\theta}\int_0^{\infty}\left[\tilde{f}_{\alpha}(\tilde{\theta},\tilde{J})V_{\alpha,n,n}\exp\left(in\tilde{\theta}\right)+c.c\right]|\mathbf{J}|d\tilde{J}, \tag{2.24}$$

where the Jacobian of the canonical transformation $(z,p_z)\leftrightarrow(\tilde{\theta},\tilde{J})$ is unity and $\hat{\omega}=\frac{\omega}{\omega_{\mathrm{pe}}}$ is the normalized frequency with respect to the initial electron plasma frequency. In this model, the phase-space density of the fast electrons (the distribution function) is assumed to be the same inside the narrow shrinking separatrix supported by the BGK mode, the so-called top-hat model. The perturbed part of the fast electrons distribution function dominated by the trapped electrons inside the separatrix [53] is calculated using the bounce averaging method described in 2.6.2,

$$\tilde{f}_{\alpha}=\begin{cases}0, & \text{passing in BGK}\\ F_{\mathrm{eq},\alpha}\left(J_{\mathrm{res}}\left(t=0\right)\right)-F_{\mathrm{eq},\alpha}\left(J_{\mathrm{res}}\left(t\right)\right). & \text{trapped in BGK}\end{cases}$$

Using the above expression, equation (4.26) transforms into

$$A_n\left(t\right)=\frac{\omega^2}{2\pi k n_c\left(n^2\hat{\omega}^2-1\right)}\sum_{\alpha}\left[F_{\mathrm{eq},\alpha}\left(t=0\right)\right.$$
$$\left.-F_{\mathrm{eq},\alpha}\left(t\right)\right]\int_0^{2\pi}d\tilde{\theta}\left[V_{\alpha,n,n}\exp\left(in\tilde{\theta}\right)+c.c\right]\Delta\tilde{J}_{\alpha,max}\left(\tilde{\theta}\right), \tag{2.25}$$

where $\Delta\tilde{J}_{\alpha,\max}\left(\tilde{\theta}\right)$ is the width of the separatrix. Using equation (2.20), we have

$$A_n\left(t\right)=\tfrac{\omega^2}{\pi k n_c(n^2\hat{\omega}^2-1)}\textstyle\sum_{\alpha}\left[F_{\mathrm{eq},\alpha}\left(t=0\right)-F_{\mathrm{eq},\alpha}\left(t\right)\right]$$
$$\times\textstyle\int_0^{2\pi}\left[\left(U_{\alpha,\mathrm{ext}}-\frac{1}{2}\sum_n A_n\left(t\right)V_{\alpha,n,n}\exp\left(in\tilde{\theta}\right)+c.c\right)\frac{2}{\Delta_{\alpha}}\right]^{\frac{1}{2}}$$
$$\times\left[V_{\alpha,n,n}\exp\left(in\tilde{\theta}\right)+c.c\right]d\tilde{\theta}. \tag{2.26}$$

The above equation can be solved numerically to derive the Fourier coefficients with which we can construct the structure of the plane wave. The numerical method used is presented in section 2.3.

The trapped electrons in the BGK mode travel in phase-space together with the nonlinear mode. Depending on whether the clumps are trapped or passing in the equilibrium field, their energy increases or decreases respectively with decreasing frequency of the mode and vice versa for the holes. Hence, formation of a hole in the distribution function of trapped particles in the equilibrium field accompanies a clump in the distribution of passing ones and vice versa. The change in the perturbed potential energy of the trapped electrons in the BGK mode is relatively small compared to the change in their equilibrium energy when the change in $J_{\mathrm{res},\alpha}(t)$ is greater than the change in the separatrix width (see 2.6.3 for more details). More energy is released by the fast particles via the motion of the phase-space structures than in the process of their formation and the released energy during chirping should compensate the dissipated energy in the bulk. The total amount

of power released corresponding to the change of the structure energy is given by

$$P_r = -\sum_{\alpha} N_\alpha \frac{\mathrm{d}E_\alpha}{\mathrm{d}t}, \tag{2.27}$$

where N_α is the total number of each group of electrons in the hole/clump, $\frac{\mathrm{d}E_\alpha}{\mathrm{d}t} = \Omega_\alpha \left(\frac{\mathrm{d}\Omega_\alpha}{\mathrm{d}J_\alpha}\right)^{-1} \frac{\mathrm{d}\omega(t)}{\mathrm{d}t}$ is the rate of change of the energy of each particle and the resonance condition allows setting $\Omega_\alpha = \omega\,(t)$. Regarding to the definition of the adiabatic invariant of the trapped particles, N_α can be calculated as

$$N_\alpha = \frac{2}{m_e}\left[F_{\mathrm{eq},\alpha}\,(t=0) - F_{\mathrm{eq},\alpha}\,(t)\right] \int_0^{2\pi} \left[\left(U_{\alpha,\mathrm{ext}} - \frac{1}{2}\sum_n A_n\,(t)\, V_{\alpha,n,n} \times \exp\left(in\tilde{\theta}\right) + c.c\right) \frac{2}{\Delta_\alpha}\right]^{\frac{1}{2}} d\tilde{\theta}. \tag{2.28}$$

The work done by the collision force can be used to calculate the dissipated power (P_d) in the bulk via collisions. Using the equation of motion (4.8a) and considering the collisional term, we have

$$P_d = \frac{2\pi\nu k_p}{\omega^2 m_e}\langle U^2\rangle, \tag{2.29}$$

where $\langle\rangle$ denotes averaging over one wavelength and $\langle U^2\rangle = \frac{1}{2}\sum_n A_n^2\,(t)$. The released power during the motion of the holes/clumps is equal to the power dissipated in the bulk through collisions. This power balance can be used to calculate the rate at which sweeping occurs, which results in

$$\frac{\mathrm{d}\omega\,(t)}{\mathrm{d}t} = -\left[\frac{\nu n_c \pi k_p}{\omega^3 m_e}\sum_n A_n^2\,(t)\right] \frac{1}{\sum_\alpha N_\alpha \left(\frac{\mathrm{d}\Omega_\alpha}{\mathrm{d}J_\alpha}\right)^{-1}}. \tag{2.30}$$

2.3 Numerical Scheme

In this section, we first derive the equation of the mode structure at early stage of chirping, say t_0, considering only the contribution from the trapped electrons in the equilibrium magnetic field. It is worth noting that here the contribution of passing electrons in the magnetic field to the equations of early stage is arbitrarily neglected just for the purpose of normalization. A simple evaluation of equation (2.26) at initial phase of sweeping when $F_{\mathrm{eq},\alpha}\,(t=0) - F_{\mathrm{eq},\alpha}\,(t) = 0$ and $\hat{\omega} = 1$, demonstrates that only the first Fourier coefficient is non-zero (a sinusoidal mode structure) and is presented by

$$A_{1,0} = -\left[\frac{8\omega_{\mathrm{pe}}^2 \frac{\partial F_{\mathrm{eq},\mathbf{T}}}{\partial \zeta_{\mathbf{T}}} \left.\frac{\partial \zeta_{\mathbf{T}}}{\partial \hat{\omega}}\right|_{\hat{\omega}=1}}{3\pi k_p n_c \sqrt{|\Delta_{\mathbf{T},0}|}}\right] V_{\mathbf{T},1,1,0}\sqrt{A_{1,0} V_{\mathbf{T},1,1,0}}. \tag{2.31}$$

Here, we have used the subscript 0 to denote evaluation at $t = t_0$. The term $A_{1,0}$ can be expressed in terms of the linear growth rate to have

$$A_{1,0} = \frac{16^2\gamma_l^2}{9|\Delta_{\mathbf{T},0}|V_{\mathbf{T},1,1,0}\pi^4}. \tag{2.32}$$

We also let $\hat{A}_n(t) = A_n(t)/A_{1,0}$, $\hat{V}_{\alpha,n,n}(t) = V_{\alpha,n,n}(t)/V_{\mathbf{T},1,1,0}$, $\hat{\Gamma}_\alpha = \Delta_\alpha/|\Delta_{\mathbf{T},0}|$, $\hat{U}_{\alpha,\text{ext}} = U_{\alpha,\text{ext}}/A_{1,0}V_{\mathbf{T},1,1,0}$ and $F_{\text{eq},\alpha}(t) = c_\alpha\zeta_\alpha(t)$.

Normalizing equation (2.26) with respect to $A_{1,0}$ results in

$$\begin{aligned}\hat{A}_n \quad (t) = &\left[\frac{-3\hat{\omega}^2}{8c_{\mathbf{T}}\frac{\partial\zeta_{\mathbf{T}}}{\partial\hat{\omega}}\Big|_{\hat{\omega}=1}(n^2\hat{\omega}^2-1)}\right]\sum_\alpha c_\alpha\left[\zeta_{\alpha,0}-\zeta_\alpha\right]\\ &\times\int_0^{2\pi}\left[\left(\hat{U}_{\alpha,\text{ext}}-\tfrac{1}{2}\sum_n\hat{A}_n(t)\,\hat{V}_{\alpha,n,n}\exp\left(in\tilde{\theta}\right)\right.\right.\\ &\left.\left.+c.c\right)\tfrac{2}{\hat{\Gamma}_\alpha}\right]^{\frac{1}{2}}\left[\hat{V}_{\alpha,n,n}(t)\exp\left(in\tilde{\theta}\right)+c.c\right]d\tilde{\theta},\end{aligned}\tag{2.33}$$

which can be solved iteratively to derive the Fourier coefficients. In order to avoid the singularity in the numerical approach, a special treatment is applied to the first coefficient when the values of ω are close to ω_{pe}. In this case, $\zeta_\alpha(t)$ can be linear-approximated around the initial plasma frequency to cancel the effect of the pole in the denominator of equation (2.33).

Likewise, differential equation (4.21) can be investigated for the early phase of the structures motion in phase-space considering only the effect of trapped particles in the magnetic field. Substituting expression (2.28) into differential equation (4.21) and using equations (4.12) and (2.32), one finds

$$\frac{\mathrm{d}}{\mathrm{d}t}\frac{(\omega-\omega_{\text{pe}})^2}{\omega_{\text{pe}}^2}=\frac{\nu}{3}\left(\frac{16\gamma_l}{3\pi^2\omega_{\text{pe}}}\right)^2.\tag{2.34}$$

We define the dimensionless time $\tau = \frac{\nu}{3}\left(\frac{16\gamma_l}{3\pi^2\omega_{\text{pe}}}\right)^2 t$ and multiply differential equation (4.21) by $\frac{3}{\nu\left(\frac{16\gamma_l}{3\pi^2\omega_{\text{pe}}}\right)^2}$ to have

$$\begin{aligned}\frac{\mathrm{d}\hat{\omega}}{\mathrm{d}\tau}=-\left[\frac{4}{\hat{\omega}^3}\right]&\frac{c_{\mathbf{T}}\left|\left(\frac{\mathrm{d}\hat{\omega}}{\mathrm{d}\zeta}\right)^{-1}_{\mathbf{T},0}\right|_{\zeta=\zeta_{\text{resonance}}}\sum_n\hat{A}_n^2}{\sum_\alpha\text{sgn}_\alpha c_\alpha\left[\zeta_{\alpha,0}-\zeta_\alpha\right]}\left\{\int_0^{2\pi}\left[\left(\hat{U}_{\alpha,\text{ext}}-\sum_n\frac{\hat{A}_n}{2}\hat{V}_{\alpha,n,n}\right.\right.\right.\\ &\left.\left.\left.\times\exp\left(in\tilde{\theta}\right)+c.c\right)\frac{2}{\hat{\Gamma}_\alpha^3}\right]^{\frac{1}{2}}d\tilde{\theta}\right\}^{-1},\end{aligned}\tag{2.35}$$

where sgn_α is -1 and 1 for $\alpha = \mathbf{T}$ and $\mathbf{P}$, respectively. The above equation can be solved by a fourth-order Runge-Kutta method along with the iterative method used for solving the Fourier coefficients on the RHS.

If the electrons have small enough pitch angles (deeply passing electrons with $\zeta \gg 1$), their motion will not be affected by the equilibrium magnetic field and they move freely. In other words, $\theta = k_{\text{eq}}z$ (see figure 2.5(b) for $\zeta = 2$). Subsequently, only one resonance is non-zero and the orbit averaged mode amplitude is equal to unity (see figure 2.4(b)) under this condition. In this high energy range, one can find that $k_p z = p\theta$ in the linear theory limit. Canonical equations of motion assure $\theta = \Omega_{\alpha=\mathbf{P}}t$ so using equation (5.25), the resonance condition becomes $\omega = k_p v$, where v is the particle velocity. Consequently, solving equation (2.33) and differential equation (2.35) in the limit that $\zeta \gg 1$, reproduces

exactly the same results as in [53], which serves as the benchmark of the code and the numerical approach.

2.4 Results

For illustration, we have arbitrarily restricted attention to cases where $k_{\mathrm{p}} = k_{\mathrm{eq}}$. In the linear regime, the plasma mode will grow at different rates depending on the initial orbits of the electrons interacting with the mode. Figure 2.3 demonstrates that the linear growth rate decreases to zero in the limit of having resonance with the particles close to the separatrix of the equilibrium motion.

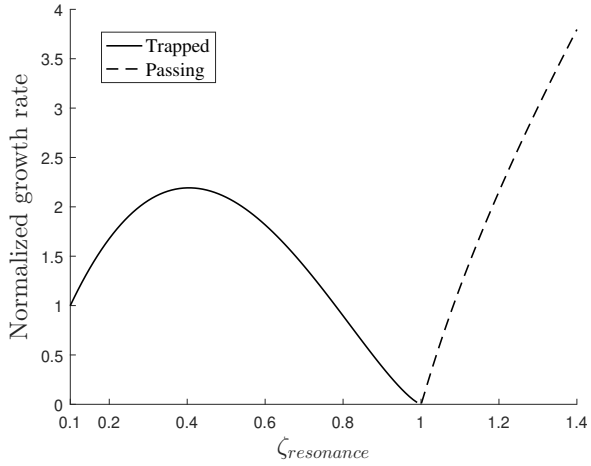

Figure 2.3: The linear growth rate behavior, corresponding to the first resonance, for different energy ranges of trapped and passing particles in the equilibrium magnetic field. All the values are normalized to the value at $\zeta = 0.1$.

As in subsection 2.2.3, the first resonance (l=1) is considered as the dominant resonance contributing to the interaction. The first four elements of the orbit averaged mode amplitude $\hat{V}_{\alpha,n,p}$, indicating the coupling strength, corresponding to the first ($\hat{V}_{\alpha,n,n}$) and the second ($\hat{V}_{\alpha,n,2n}$) resonance are plotted in figure 2.4 versus energy parameter by numerical integrating of equation (2.9) over θ. Investigation of figure 2.4 shows that there are regions (adjacent to $\zeta = 1$) where the values of the dominant element (n=1) belonging to the second resonance overtake the values of the dominant element of the first resonance. In itself, this may indicate that the corresponding second resonance is dominant. However, consideration of the linear growth rate for different resonances shows that the first resonant ($p = 1$) is dominant. This can be understood by inspection of equation (4.12): the term $\left|\frac{\mathrm{d}\Omega_\alpha}{\mathrm{d}\zeta_\alpha}\right|$ increases with increasing the resonance, so γ_l decreases with increasing resonance. In addition, evaluating the factors of equation (2.33) for higher resonances ($l \geq 2$) shows that its always the first resonance ($l = 1$) that has dominant contribution to the interaction in the hard nonlinear regime. Therefore, the submissive resonances are neglected. The other important point concerning the coupling strength is that all of its elements go asymptotically to zero as the energy parameter of the electrons approaches unity. Here, we explain this phenomenon in more detail: the equations (2.52) and (2.58) describe the equilibrium position (z) of the electrons in terms of the action–angle variables in the nonuniform magnetic field. Figure 2.5 illustrates this position at different times for different energy parameters. For the case of trapped (figure 2.5(a)) and passing (figure

2.5(b)) electrons, it is shown that for $\zeta \approx 1$, the electrons spend most of their period lingering at the two ends of the magnetic mirror system (the so-called magnetic bottle). This means that z is almost $-\pi/k_{\rm eq}$ during a half of the period and is almost $\pi/k_{\rm eq}$ in the other half. Therefore, $\exp(ink_p z)$ in the integrand of equation (2.9) is $\exp(ink_p\pi/k_{\rm eq})$ or $\exp(-ink_p\pi/k_{\rm eq})$ in each half period. For $k_p/k_{\rm eq} = m$ with m an integer, we have $\exp(ink_p\pi/k_{\rm eq}) = \exp(-ink_p\pi/k_{\rm eq}) = cte$ and consequently the value of the integral drops to zero as the energy parameter approaches one ($\zeta \approx 1$). These electrons barely move in z-direction, similar to the case where the electrons are deeply trapped ($\zeta \approx 0$).

Prior to solving the equations for the mode structure and the sweeping rate in the hard nonlinear regime, it is necessary to investigate the behavior of the adiabatic invariant (phase-space area) of the trapped electrons in the BGK mode that are trapped or passing in the equilibrium magnetic field. Figure 2.6 shows the values of the adiabatic invariant (equation (2.22)) at the separatrix determined by the BGK mode during frequency sweeping. For the case of downward frequency sweeping, the energy of the passing electrons in the equilibrium field decreases, so does the corresponding value of the adiabatic invariant (figure 2.6(b)). However, for trapped electrons, energy increases for downward frequency sweeping. Depending on the initial orbit, the adiabatic invariant can either initially increase ($\zeta < 0.4$ of figure 2.6(a)) or decrease ($\zeta \geq 0.4$ of figure 2.6(a)). Due to the assumption of a flat-top distribution function over the separatrix region, the model remains valid as long as the separatrix supported by the BGK mode shrinks and an expanding separatrix (an increasing adiabatic invariant) should be avoided. Therefore, the electrons in the following results have initial energy parameters $\zeta \geq 0.4$. In this energy range and for the electrons trapped in the magnetic field, the coherent phase-space structure is a hole whose separatrix area (and the correspoding amplitude of the mode)

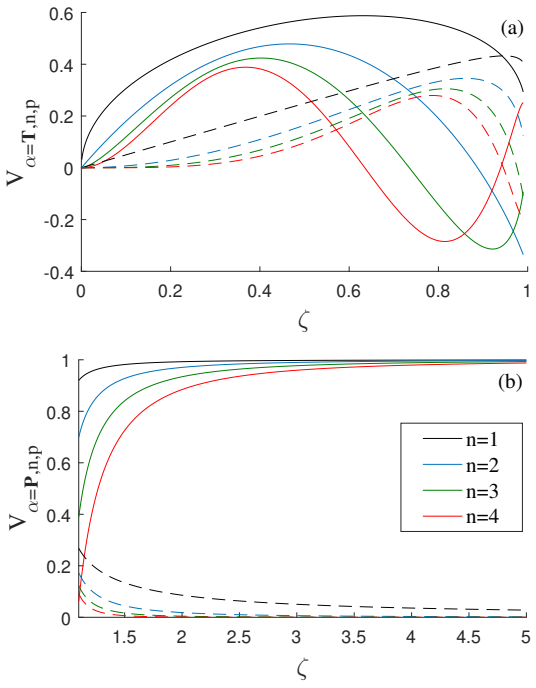

Figure 2.4: The orbit averaged mode amplitude versus energy parameter for (a) the trapped and (b) passing electrons in the equilibrium magnetic field. The solid and dashed lines correspond to first and second resonances, respectively.

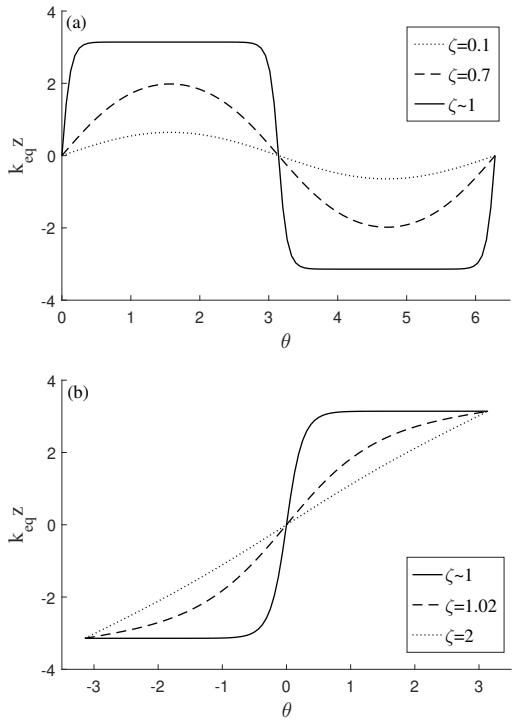

Figure 2.5: The position of energetic electrons (a) trapped and (b) passing in the equilibrium magnetic field in terms of the angle variable

is shrinking for a downsweeping frequency. For the case that new electrons are trapped into an expanding separatrix, it is required that the value of the distribution function of newly trapped particles is set to the value of the ambient distribution. The latter case is not the subject of this paper and the reader is referred to [55, 75, 77] where the subject of expanding separatrices is addressed.

2.4.1 The mode structure

Considering similar slopes for the initial distribution of both the trapped and passing electrons in the equilibrium magnetic field (simultaneously in resonance with the plasma mode), the structure of the BGK mode has been solved for different initial electron energy parameters, namely $\zeta_{\alpha=\mathbf{T}}(t=0) = 0.4$, 0.6 and 0.8. Figure 2.7 illustrates the mode structure for these initial energies in cases where $\hat{\omega}$= 0.8 and 0.6, constructed by solving equation (2.33) iteratively for the Fourier coefficients. The results reveal that for a nonzero change in $\hat{\omega}$, the nonlinear behavior of the BGK mode is determined by the initial electron orbits. For constant $\hat{\omega}$, e.g. figures 2.7(a), (c) and (e), the maximum amplitude of the normalized mode structure (maximum value of $\sum_n \hat{A}_n cos(nk_p z)$) changes with changing $\zeta_{\alpha=\mathbf{T},0}$, and the absolute values of the normalized mode amplitude decrease with increasing $\zeta_{\alpha=\mathbf{T},0}$. In other words, for higher values of initial energy parameter, the maximum amplitude drops to a lower fraction of its initial value. The shape of the nonlinear structure is not only affected by the amount of change in the frequency ($\hat{\omega}$) but also by the initial energy parameter ($\zeta_{\alpha=\mathbf{T},0}$). In order to explain the observed behavior, we first calculate the contribution of the trapped and passing particles to the mode structure seperately while they are simultaneously in resonance with the mode. Afterwards, the behavior of both the equilibrium frequency and the physical quantities appearing in equation (2.33)

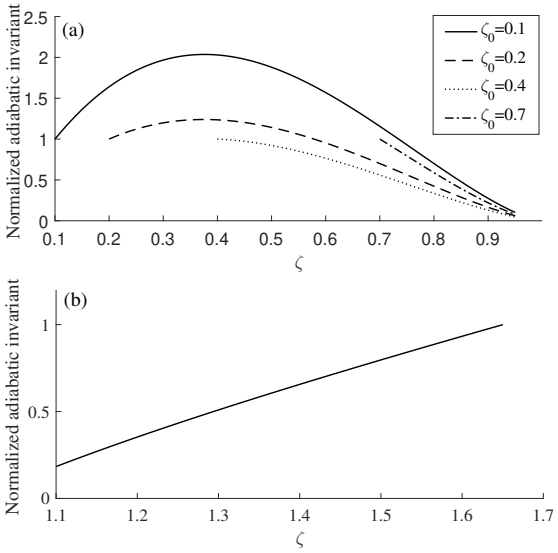

Figure 2.6: The values of the adiabatic invariant of (a) trapped and (b) passing particles in the equilibrium magnetic field for $k_p/k_{\rm eq} = 1$ at the separatrix determined by the BGK mode. The values are normalized with respect to the values at initial phase of chirping.

is investigated.

The Fourier coefficients are calculated by adding the two terms on the RHS of equation (2.33), corresponding to $\alpha = \mathbf{T}$ and $\mathbf{P}$. The seperate contributions of these two groups of particles to the mode structure are shown in figure 2.8 for similar values of distribution function and in case of simultaneous resonance between the plasma mode and these two types of energetic particles. It is clear that the contribution of the passing electrons to the nonlinear behavior of the mode is relatively much smaller than the trapped ones. The reason being that the resonance occurs in a region where the equilibrium frequency of passing particles has much steeper gradient in energy (see figure 2.1). Therefore, for the purpose of investigating the parameters of equation (2.33), we only consider the dominant contribution from the trapped electrons in the equilibrium magnetic field.

At a constant value of the normalized frequency $\hat{\omega}$, a simple evaluation of equation (2.33) gives

$$\hat{A}_n\left(t\right) \propto \frac{(\frac{\mathrm{d}\hat{\omega}}{\mathrm{d}\zeta})^2_{\alpha=\mathbf{T},0}[\zeta_{\alpha=\mathbf{T}}\left(t=0\right) - \zeta_{\alpha=\mathbf{T}}\left(t\right)]^2 \hat{V}^3_{\alpha=\mathbf{T},n,n}}{\hat{\Gamma}_{\alpha=\mathbf{T}}}. \tag{2.36}$$

Starting from different initial energies, the trapped electrons in the equilibrium magnetic field should be moved on different energy increments by the nonlinear mode in order to have the same amount of change in the frequency. This results from the nonlinear dependency of the equilibrium frequency on the energy parameter (see figure 2.1). As an example for $\hat{\omega} = 0.8$, the fast electrons having the initial energy parameters of $\zeta_{\alpha=\mathbf{T},0}$=0.4,0.6 and 0.8 should be moved in phase-space to the points where $\zeta(t)$=0.783, 0.863 and 0.94, respectively and the energy increments become shorter for higher values of initial energy parameter. For a linear equilibrium distribution, the difference in the energy increments will explicitly appear in the numerator of equation (2.33) through the perturbed density term, i.e. $[\zeta\left(t=0\right) - \zeta\left(t\right)]$. In general, the nonlinear dependency of the equilibiurm frequency on the energy parameter will affect the values of all the physical parameters appearing in equation (2.33) for a fixed amount of frequency shift. Figure 2.9 shows

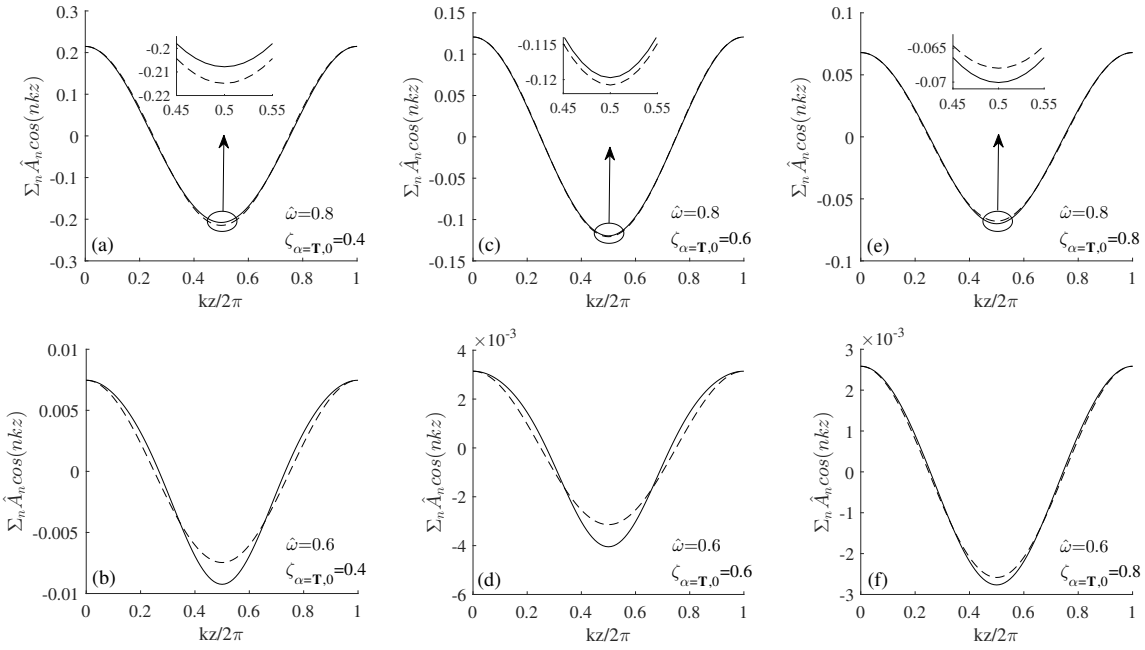

Figure 2.7: The normalized BGK mode structure affected by electrons having different initial energies. The dashed line, included here for comparison, represents the sinusoidal structure of the mode at early stage of frequency sweeping.

the dependency of the factors $\left(\frac{\mathrm{d}\hat{\omega}}{\mathrm{d}\zeta}\right)^2_{\alpha=\mathbf{T},0}[\zeta(t=0)-\zeta(t)]^2$, $\hat{V}^3_{\alpha=\mathbf{T},n=1,n=1}$ and $\hat{\Gamma}^{-1}_{\alpha=\mathbf{T}}$ in expression (2.36) for different $\zeta_{\alpha=\mathbf{T},0}$ and as a function of $\hat{\omega}$. The dependency of $\hat{A}_n$ with $\zeta_{\alpha=\mathbf{T},0}$ can be understood by inspection of these factors. At each $\hat{\omega}$ the factors decrease with increasing $\zeta_{\alpha=\mathbf{T},0}$ and so $\hat{A}_n$ decreases. It is noteworthy that $\left(\frac{\mathrm{d}\hat{\omega}}{\mathrm{d}\zeta}\right)_{\alpha=\mathbf{T},0}$ can be calculated by differentiating the normalized form of equation (2.8a) with respect to ζ, which together with the differentiation of equation (2.5a) can be used to derive $\hat{\Gamma}_{\alpha=\mathbf{T}}$.

2.4.2 The sweeping rate and adiabaticity validation

In this subsection, we first investigate the rate at which the frequency of the nonlinear mode evolves in time. Prior to solving the differential equation (2.35), we evaluate the dependency of the sweeping rate $\left(\frac{\mathrm{d}\hat{\omega}}{\mathrm{d}\tau}\right)$ on the initial energy parameter of the electrons (initial orbits) using the behavior of the factors illustrated in figure 2.9. Looking at the expression (2.35) for the sweeping rate at a constant value of $\hat{\omega}$, it can be inferred that

$$\frac{\mathrm{d}\hat{\omega}}{\mathrm{d}\tau} \propto \frac{\hat{A}_n(t)^{\frac{3}{2}}\hat{\Gamma}^{\frac{3}{2}}_{\alpha=\mathbf{T}}}{\left|\left(\frac{\mathrm{d}\hat{\omega}}{\mathrm{d}\tau}\right)_{\alpha=\mathbf{T},0}\right|[\zeta_{\alpha=\mathbf{T}}(t=0)-\zeta_{\alpha=\mathbf{T}}(t)]\hat{V}^{\frac{1}{2}}_{\alpha=\mathbf{T},n,n}}. \tag{2.37}$$

Using expression (2.36) one finds

$$\frac{\mathrm{d}\hat{\omega}}{\mathrm{d}\tau} \propto \left(\frac{\mathrm{d}\hat{\omega}}{\mathrm{d}\zeta}\right)^2_{\alpha=\mathbf{T},0}[\zeta_{\alpha=\mathbf{T}}(t=0)-\zeta_{\alpha=\mathbf{T}}(t)]^2\,\hat{V}^4_{\alpha=\mathbf{T},n,n}. \tag{2.38}$$

Similar to subsection 2.4.1, one can consider figures 2.9(a) and (c) at a constant $\hat{\omega}$ to investigate the value of the RHS of expression (2.38) for different electron orbits. It is clear that the RHS value becomes lower when the resonance occurs with the electrons (trapped in the fixed equilibrium magnetic field) having higher initial energy parameter ($\zeta_{\alpha=\mathbf{T},0}$). Therefore, we expect the mode frequency to chirp more slowly when the initial energy parameter of the electrons is higher. This can be verified by solving differential equation (2.35) using the numerical method stated in section 2.3 for different initial orbits. Figure 2.10 illustrates the time evolution of $\hat{\omega}$ for different values of $\zeta_{\alpha=\mathbf{T},0}$. The results reproduce the square root dependency for initial stages of chirping as in [35, 53]. However, it is shown that in this model, the holes and clumps can move with much lower rates compared with the sweeping rates observed in [53]. On the other hand, as predicted above, for higher initial energy parameter of the trapped electrons in the equilibrium magnetic field, the frequency tends to decrease more slowly.

As mentioned earlier in subsection 2.2.3, the adiabaticity condition invoked for the analysis, should be checked if it remains satisfied when the frequency deviates from the initial eigenfrequency. Using the total Hamiltonian of the resonant electrons (Equation (4.15)), the canonical equations of the perturbed motion of these electrons, read

$$\dot{\tilde{J}}_\alpha = \sum_n A_n V_{\alpha,n,n} n \sin\left(n\tilde{\theta}\right), \tag{2.39a}$$

$$\dot{\tilde{\theta}} = \left.\frac{\partial^2 H_{0,\alpha}}{\partial \tilde{J}_\alpha^2}\right|_{\tilde{J}_\alpha = J_{\mathrm{res},\alpha}} \left(\tilde{J}_\alpha - J_{\mathrm{res},\alpha}\right). \tag{2.39b}$$

In the absence of collisions, the motion of resonant electrons which are trapped in the equilibrium field and are deeply trapped in the BGK mode satisfies the pendulum equation

$$\ddot{\tilde{\theta}} = \Delta_{\alpha=\mathbf{T}} \sum_n A_n V_{\alpha=\mathbf{T},n,n} n^2 \tilde{\theta}, \tag{2.40}$$

with $\left|\Delta_{\alpha=\mathbf{T}} \sum_n A_n V_{\alpha=\mathbf{T},n,n} n^2\right| = \omega_{b,\alpha=\mathbf{T}}^2$, where we have used $\sin\left(n\tilde{\theta}\right) \approx n\tilde{\theta}$ at the center of the separatrix, the so-called O-point which is at $\tilde{\theta} = 0$ for trapped electrons in the

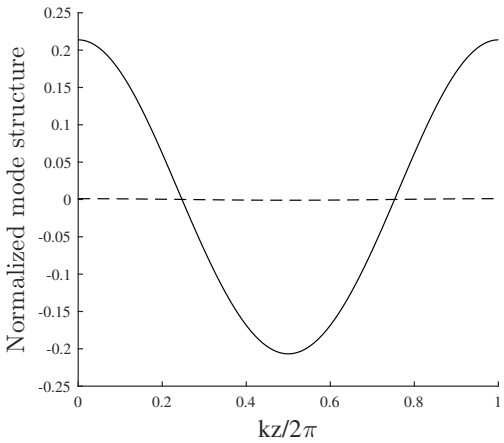

Figure 2.8: The contribution of trapped (solid line) and passing (dashed curve) electrons to the mode structure, where $\hat{\omega} = 0.8$ and $\zeta_{\alpha=\mathbf{T},0} = 0.4$. plotting on the same chart results in the small contribution of passing electrons to appear as a horizontal line

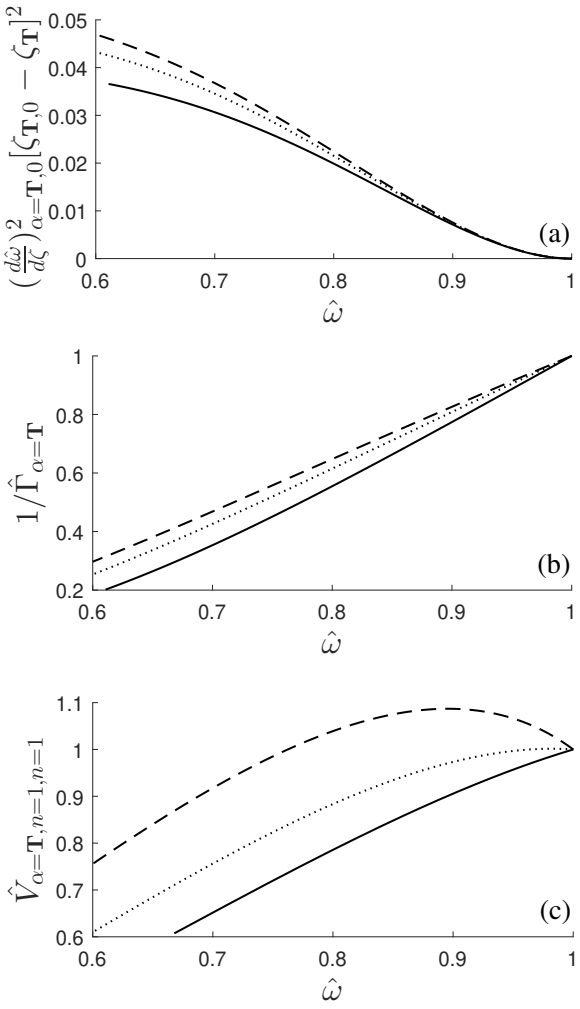

Figure 2.9: The factors in (2.36) versus normalized frequency ($\hat{\omega}$). The dashed, dotted and solid lines correspond to the initial energy parameter ($\zeta_{\alpha=\mathbf{T},0}$) values of 0.4, 0.6 and 0.8, respectively.

magnetic field (see figure 2.2(b)). Similarly, for passing electrons in the magnetic field that are deeply trapped in the BGK mode, we have

$$\frac{\mathrm{d}^2}{\mathrm{d}t^2} = \Delta_{\alpha=\mathbf{P}} \sum_n A_n V_{\alpha=\mathbf{P},n,n} n^2 \cos(n\pi) \times \left(\tilde{\theta} - \pi\right), \tag{2.41}$$

with $\left|\Delta_{\alpha=\mathbf{P}} \sum_n A_n V_{\alpha=\mathbf{P},n,n} n^2 \cos(n\pi)\right| = \omega^2_{b,\alpha=\mathbf{P}}$, where we have expanded $\sin\left(n\tilde{\theta}\right)$ about the O-point at $\tilde{\theta} = \pi$ for passing electrons in the magnetic field (see figure 2.2(a)).

We introduce the dimensionless variable $\tilde{\omega}_{b,\alpha} = \frac{\omega_{b,\alpha}}{\omega_{b,\alpha=\mathbf{T},t=0}}$, with

$$\omega_{b,\alpha=\mathbf{T},t=0} = \sqrt{|A_{1,t=0} V_{\alpha=\mathbf{T},n=1,n=1} \Delta_{\alpha=\mathbf{T}}|}, \tag{2.42}$$

the bounce frequency of resonant electrons (trapped in the magnetic field) in their corresponding separatrix in the BGK mode at early stage of chirping denoted by $t = 0$. We

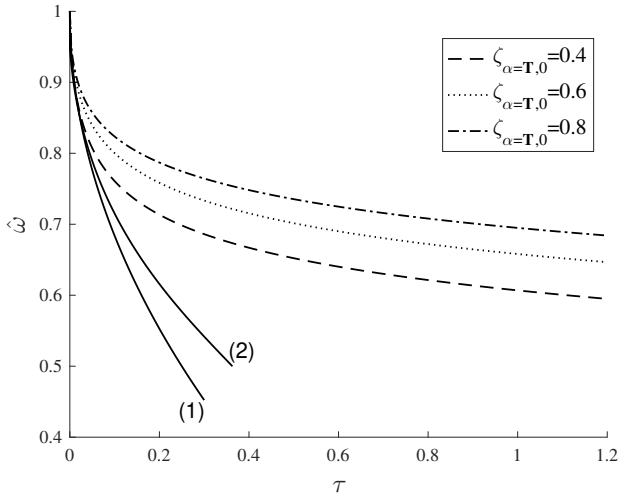

Figure 2.10: The evolution of normalized frequency versus normalized time. The solid lines labeled (1) and (2) correspond to the square root dependency, plotted for comparison, and the result reported in [53], respectively.

can write the adiabatic limit, introduced in subsection 2.2.3, in the form

$$\frac{\frac{\mathrm{d}\tau}{\mathrm{d}t}}{\omega_{b,\alpha=\mathbf{T},t=0}} \ll \frac{\tilde{\omega}_{b,\alpha}^2}{\left|\frac{\mathrm{d}\tilde{\omega}_{b,\alpha}}{\mathrm{d}\tau}\right|}. \tag{2.43}$$

Using equation (2.32) and the expression for the dimensionless time introduced in section 2.3, one finds

$$\frac{\nu\gamma_{l,\alpha=\mathbf{T}}}{w_{\mathrm{pe}}^2} \ll \frac{9\pi^2\tilde{\omega}_{b,\alpha}^2}{16\left|\frac{\mathrm{d}\tilde{\omega}_{b,\alpha}}{\mathrm{d}\tau}\right|}. \tag{2.44}$$

The time evolution of $\tilde{\omega}_b$ can be investigated in the same numerical code implemented to solve differential equation (2.35) for constructing figure 2.10. At each time step in the fourth-order Runge-Kutta method, the corresponding parameters can be used to derive $\tilde{\omega}_{b,\alpha}(\tau)$. Afterwards, one can readily use numerical differentiation methods to find $\frac{\mathrm{d}\tilde{\omega}_{b,\alpha}}{\mathrm{d}\tau}$.

Figures 2.11(a) and (b) show the normalized bounce frequency of the trapped electrons about the O-point of the separatrix inside the BGK mode corresponding to the trapped and passing electrons in the magnetic field, respectively, for the initial energy parameters considered in the previous subsections. The corresponding values of $\frac{\mathrm{d}\tilde{\omega}_{b,\alpha}}{\mathrm{d}\tau}$ are demonstrated in figures 2.11(c) and (d), where the values decrease to $-\infty$ as we approach $\tau = 0$. Therefore, the value of the RHS of (2.44), illustrated in figures 2.11(e) and (f), drops to zero at the early stage of frequency chirping. This means that the adiabatic limit is never formally satisfield at initial stage of phase-space structures evolution. Nevertheless, we have $\gamma_l, \nu \ll \omega_{\mathrm{pe}}$ and as a result the period during which the adiabatic condition is not satisfied is extremely short. The results reveal that as the system evolves while the adiabaticity limit is initially violated, for later evolution of phase–space structures the RHS value of (2.44) monotonically increases. Therefore, once the adiabatic limit (2.44) is satisfied with regards to the value of LHS, it will remain valid for later evolution. It should be noted that the adiabaticity condition is better satisfied for the passing electrons in the magnetic field compared to the trapped ones.

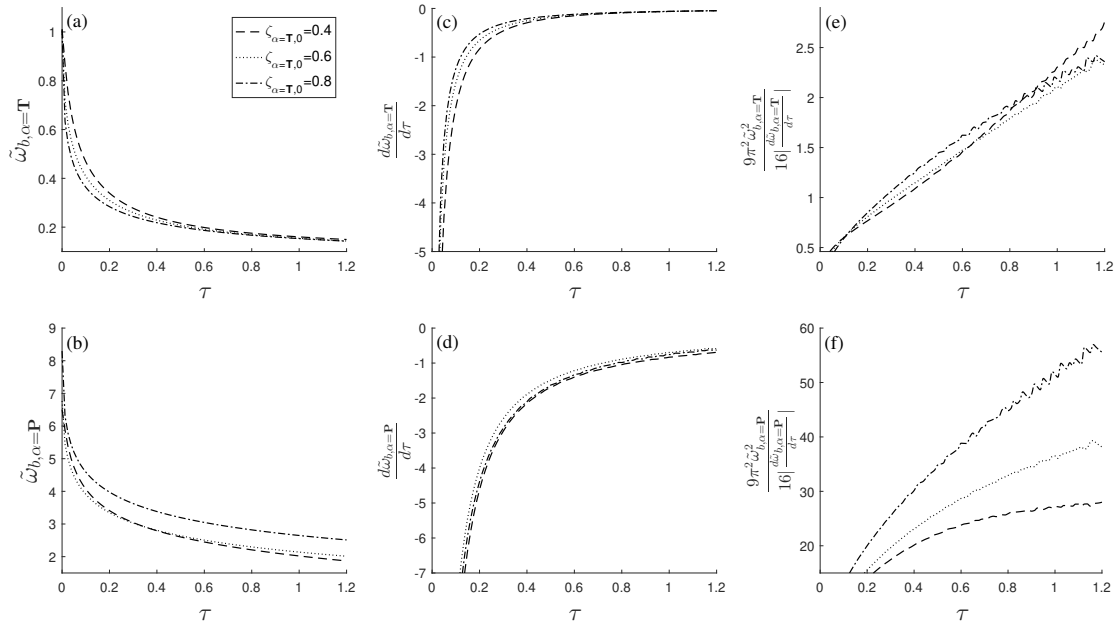

Figure 2.11: The evolution of the normalized bounce frequency (a and b), normalized time rate of change in the bounce frequency (c and d) and the value of the RHS of inequality (2.44) (e and f). Panels (a,c,e) and (b,d,f) correspond to trapped and passing electrons in the magnetic field, respectively. The dashed, dotted and dash-dotted curves represent an initial energy parameter value of 0.4, 0.6 and 0.8, respectively, for trapped electrons in the magnetic field. At $\tau = 0$, the values of the panels (c,d) go asymptotically to $-\infty$ and for the panels (e,f) the corresponding values are zero.

2.5 Concluding remarks

The more realistic 1D model shows that apart from the amount of deviation from the initial eigenfrequency during frequency sweeping, the initial orbit (initial energy parameter) of the particles in a nonuniform equilibrium magnetic field, determines both the linear and the hard nonlinear evolution behavior of a plasma mode. The model also resolves the simultaneous contributions from the two groups of particles having different orbit types as well as the contribution from higher resonances. We find however that the first resonance is dominant. We also identify different behavior of the adiabatic invariant in different energy regions. The model shows that for a constant trend in frequency sweeping, either upward or downward, the adiabatic invariant can have both positive and negative gradients in the energy parameter depending on the energy region considered. This behavior depends on factors such as the resonance number, the proportion of the plasma mode wave-number to the spatial frequency of the equilibrium field (k_p/k_{eq}) and whether the particles were initially trapped or passing in the equilibrium field. This indicates that for realistic geometries where particles interacting with the mode can follow different equilibrium orbits, an extended approach is required to calculate the perturbed density inside the holes and clumps. The required approach should take into account that the adiabatic invariant (phase-space area) at the separatrix can initially expand followed by a shrinking behavior and vice versa, depending on the initial orbit of the energetic particles. This extension can highly benefit from the method presented in [55].

The presented model in this manuscript provides a more effective understanding of

hard nonlinear wave-particle-plasma interactions in realistic geometries provided that the mode is subject to weak continuum damping (a global mode) i.e. its structure in the linear regime is not mainly determined by the energetic particles. Two different orbit topologies of energetic particles created by adding a nonuniform magnetic field to the 1D bump-on-tail instability problem, bring it into anology with tokamaks where trapped and passing topologies exist which can both resonate with modes with different coupling strength factors. In a high aspect ratio tokamak, the total magnetic field follows

$$B \propto \frac{1}{R_0 + r\cos\theta} \propto \frac{1}{R_0}\left(1 - \epsilon\cos\theta\right), \tag{2.45}$$

where B is the magnetic field, ϵ is the inverse aspect ratio, θ is the poloidal angle and R_0 and r are the major and minor radius, respectively.

Using the orbit-averaged Littlejohn's Hamiltonian, we have

$$H_0 - \mu B_0 = \frac{1}{2} m_i v_\parallel^2 - \mu B_0 \epsilon \cos\left(\theta\right), \tag{2.46}$$

where H_0 is the equilibrium Hamiltonian and $v_\parallel$ is the velocity in the direction of the magnetic field. Taking into account the symmetry of the magnetic field in toroidal direction in realistic geometries and assuming that the deviation of the fast particles from the flux surface is infinitesimal, the above Hamiltonian is comparable to the equilibrium Hamiltonian presented in equation (2.3). Further restrictions on the perturbation such as symmetry in toroidal direction, being localized on one flux surface and the assumption that the perturbation on different flux surfaces are unlinked, might let the presented model to describe some features of electrostatic axisymmetric modes ($n = 0$, where n is the poloidal mode number), namely global geodesic acoustic modes (GGAMs) in more realistic geometries [78]. Nevertheless, an exact description of excited Global-Alfven-Eigenmodes (GAEs) with an evolving mode structure during long range frequency deviations requires the extension of the presented model, which is a part of our ongoing research. Another avenue for further research is to relax the assumption that the fast electron distribution function is linear.

Acknowledgments

The authors wish to gratefully thank Prof. Boris Breizman from Institute for Fusion Studies, The University of Texas at Austin, USA for stimulating discussions that helped inspire this paper. The authors are grateful to Prof. Robert L. Dewar from Research School of Physics and Engineering, The Australian National University, Canberra, Australia and Dr. Michael Fitzgerald from CCFE, Culham Science Centre, UK for useful comments and discussions. This work was funded by the Australian Research Council through Grant No. DP140100790.

2.6 Appendix

2.6.1 Calculation of $z(J,\theta)$

Using the equilibrium Hamiltonian (2.3) and $p_z = m_e \frac{\mathrm{d}z}{\mathrm{d}t}$, we find

$$\frac{2}{k_{\mathrm{eq}}}\frac{\mathrm{d}\sigma}{\mathrm{d}t} = \sqrt{\frac{2}{m_e}\left[E + \mu\left(B_c + B_0\cos\left(2\sigma\right)\right)\right]} \tag{2.47}$$

where $\sigma = \frac{k_{\mathrm{eq}} z}{2}$. We take $\sigma\left(t=0\right)=0$, to have

$$\frac{\sqrt{2}k_{\mathrm{eq}}^{-1}}{\sqrt{\frac{E+\mu(B_0-B_c)}{m_e}}}\int_0^{\sigma}\frac{d\sigma}{\sqrt{1-\frac{2\mu B_0}{E+\mu(B_0-B_c)}\sin^2\left(\sigma\right)}} = \int_0^t dt, \tag{2.48}$$

where we have used $\cos(2\sigma) = 1 - 2\sin^2\sigma$.

I) For passing electrons in the nonuniform magnetic field, the coefficient of $\sin^2\left(\sigma\right)$ in integral equation (2.48) is less than unity. After changing the coordinates to action-angle variables in subsection 2.2.1, we can use the canonical equations of motion to find

$$t = \frac{\theta}{\Omega_{\mathrm{eq},\alpha}}, \tag{2.49}$$

where $\Omega_{\mathrm{eq},\alpha=\mathbf{P}}$ is presented by equation (2.8b). Substituing (2.49) into the RHS of (2.48), we find

$$\int_0^{\sigma}\frac{d\sigma}{\sqrt{1-\frac{2\mu B_0}{E+\mu(B_0-B_c)}\sin^2\left(\sigma\right)}} = \frac{\theta\mathbb{K}\left(\zeta^{-1}\right)}{\pi}. \tag{2.50}$$

According to the definition of Jacobi elliptic functions, we find

$$\mathrm{Sn}\left(\frac{\theta\mathbb{K}\left(\zeta^{-1}\right)}{\pi},\zeta^{-1}\right) = \sin\sigma, \tag{2.51}$$

which gives

$$z_{\alpha=\mathbf{P}} = \frac{2}{k_{\mathrm{eq}}}\sin^{-1}\left[\mathrm{Sn}\left(\frac{\theta\mathbb{K}\left(\zeta^{-1}\right)}{\pi},\zeta^{-1}\right)\right]. \tag{2.52}$$

II) For trapped electrons in the nonuniform magnetic field, the coefficient of $\sin^2\left(\sigma\right)$ in integral equation (2.48) is higher than unity. we implement a change of variables as follows,

$$\sin\left(\eta\right) = \frac{\sin\left(\sigma\right)}{\sin\left(\sigma_{\max}\right)}, \tag{2.53a}$$

$$d\sigma = \frac{\sin\left(\sigma_{\max}\right)\cos\left(\eta\right)}{\sqrt{1-\sin^2\left(\sigma_{\max}\right)\sin^2\left(\eta\right)}}d\eta. \tag{2.53b}$$

The maximum value of z is $\frac{1}{k_{\mathrm{eq}}}\cos^{-1}\left(\frac{\mu B_c - E}{\mu B_0}\right)$, derived from $p_z = 0$. Hence, $\cos\left(2\sigma_{\max}\right) = \frac{\mu B_c - E}{\mu B_0}$ and

$$\sin^2\left(\sigma_{\max}\right) = \frac{E+\mu\left(B_0-B_c\right)}{2\mu B_0}. \tag{2.54}$$

Now we substitute equations (2.53a) and (2.53b) into (2.48) and use (2.54) to have

$$\frac{\sqrt{2}\sin\left(\sigma_{\max}\right)}{k_{\text{eq}}\sqrt{\frac{E+\mu(B_0-B_c)}{m_e}}}\int_0^{\eta}\frac{d\eta}{\sqrt{1-\sin^2\left(\sigma_{\max}\right)\sin^2\left(\eta\right)}}=t, \tag{2.55}$$

where we have used $\frac{\cos\eta}{\sqrt{1-\frac{2\mu B_0}{E+\mu(B_0-B_c)}\sin^2(\sigma)}}=1$. Using equation (2.49) for trapped electrons in the magnetic field and equation (2.8b), we find

$$\int_0^{\eta}\frac{d\eta}{\sqrt{1-\sin^2\left(\sigma_{\max}\right)\sin^2\left(\eta\right)}}=\frac{2\theta\mathbb{K}\left(\zeta\right)}{\pi}, \tag{2.56}$$

which gives

$$\text{Sn}\left(\frac{2\theta\mathbb{K}\left(\zeta\right)}{\pi},\zeta\right)=\sin\eta=\frac{\sin\sigma}{\sin\sigma_{\max}}. \tag{2.57}$$

We find

$$z_{\alpha=\mathbf{T}}=\frac{2}{k_{\text{eq}}}\sin^{-1}\left[\sqrt{\zeta}\text{Sn}\left(\frac{2\theta\mathbb{K}\left(\zeta\right)}{\pi},\zeta\right)\right]. \tag{2.58}$$

It should be mentioned that equations (2.52) and (2.58) can be inverted for the corresponding angle $\theta(z,\zeta)$ variables.

2.6.2 Adiabatic invariant and bounce averaging method

The adiabatic invariant for a Hamiltonian $K(\hat{\theta},\hat{J},\lambda\equiv\beta t)$ with slow time dependency ($\beta\ll$ typical orbit frequencies) is

$$I^{\infty}=I\left(q,p,\lambda\right)+\beta I_1\left(q,p,\lambda\right)+\beta^2 I_2\left(q,p,\lambda\right)+..., \tag{2.59}$$

which the lowest term is commonly taken to be the action, $I\left(E,\lambda\right)=\oint\hat{J}\left(\hat{\theta},E,\lambda\right)d\hat{\theta}$ with $K\left(\hat{\theta},\hat{J},\lambda\right)=E$. We transform to action-angle variables using the generating function $\Phi_2\left(\hat{\theta},I,\lambda\right)=\int_{\hat{\theta}_0(I,\lambda)}^{\hat{\theta}}d\hat{\theta}'\hat{J}\left(\hat{\theta}',K\left(I,\lambda\right),\lambda\right)$. So the Hamiltonian transforms into $K_{new}\left(\Theta,I,\lambda\right)=K\left(I,\lambda\right)+\beta\frac{\partial\Phi_2}{\partial\lambda}$. Now we consider the trapped electron Vlasov equation

$$\frac{\partial f}{\partial t}+\frac{\partial f}{\partial\Theta}\frac{\partial K_{new}}{\partial I}-\frac{\partial f}{\partial I}\frac{\partial K_{new}}{\partial\Theta}=0. \tag{2.60}$$

Using the equations of motion we have

$$\dot{\Theta}=\frac{\partial K_{new}}{\partial I}=\omega_{Bounce}+\frac{\partial}{\partial I}\frac{\partial\Phi_2}{\partial t}, \tag{2.61a}$$

$$\dot{I}=-\frac{\partial K_{new}}{\partial\Theta}=-\frac{\partial}{\partial\Theta}\frac{\partial\Phi_2}{\partial t}. \tag{2.61b}$$

Substituting the above expressions in equation (2.60) gives

$$\frac{\partial f}{\partial t}+\frac{\partial f}{\partial\Theta}\omega_{Bounce}+\frac{\partial f}{\partial\Theta}\frac{\partial}{\partial I}\frac{\partial\Phi_2}{\partial t}-\frac{\partial f}{\partial I}\frac{\partial}{\partial\Theta}\frac{\partial\Phi_2}{\partial t}=0. \tag{2.62}$$

Following the same approach in [54], f can be expanded in terms of the small parameter $\beta=\frac{\tau_B}{\tau_s}$ to have

$$f=f_0+\beta f_1+\beta^2 f_2+..., \tag{2.63}$$

where f_0 is the bounce average of f over Θ. Using expression (2.63), we substitute for f in equation (2.62). To lowest order ($\mathcal{O}(1)$) in β, one finds

$$\frac{\partial f_0}{\partial \Theta} = 0. \tag{2.64}$$

To next order ($\mathcal{O}(\beta)$),

$$\frac{\partial f_0}{\partial t} + \beta\frac{\partial f_1}{\partial t} + \frac{\partial f_0}{\partial \Theta}\omega_{Bounce} + \beta\frac{\partial f_1}{\partial \Theta}\omega_{Bounce} + \frac{\partial f_0}{\partial \Theta}\frac{\partial}{\partial I}\frac{\partial \Phi_2}{\partial t} + \beta\frac{\partial f_1}{\partial \Theta}\frac{\partial}{\partial I}\frac{\partial \Phi_2}{\partial t} - \frac{\partial f_0}{\partial I}\frac{\partial}{\partial \Theta}\frac{\partial \Phi_2}{\partial t} - \beta\frac{\partial f_1}{\partial I}\frac{\partial}{\partial \Theta}\frac{\partial \Phi_2}{\partial t} = 0. \tag{2.65}$$

The second, sixth and eighth terms are on the order of β^2 $\left(\mathcal{O}\left(\beta^2\right)\right)$ and can be neglected at this stage. Equation (2.64) shows that f_0 is independent of Θ, which allows us to set the fifth term to zero. Therefore, we reach

$$\frac{\partial f_0}{\partial t} + \beta\frac{\partial f_1}{\partial \Theta}\omega_{Bounce} - \frac{\partial f_0}{\partial I}\frac{\partial}{\partial \Theta}\frac{\partial \Phi_2}{\partial t} = 0. \tag{2.66}$$

After averaging (2.66) over Θ, the second and third terms vanish and we find

$$\frac{\partial f_0}{\partial t} = 0. \tag{2.67}$$

We define $f_0 = \delta f + \langle F_{\text{eq}}(J_{\text{res}}(t))\rangle$, where $<>$ denotes averaging over Θ and $f_0(t=0) = F_{\text{eq}}(J_{\text{res}}(t=0))$. The uniformity assumption of the distribution function over the separatrix region assures $\langle F_{\text{eq}}(J_{\text{res}}(t))\rangle = F_{\text{eq}}(J_{\text{res}}(t))$. Hence, $f_0(t) = \delta f + F_{\text{eq}}(J_{\text{res}}(t))$. According to (2.67), f_0 should remain constant during frequency sweeping which gives

$$\delta f = F_{\text{eq}}(J_{\text{res}}(t=0)) - F_{\text{eq}}(J_{\text{res}}(t)). \tag{2.68}$$

2.6.3 Validation of the smallness of the perturbed potential energy change

As illustrated in figure 2.12, we consider the case of a long range frequency chirping where the separatrix has approximately vanished. Therefore, we have $J_{\alpha,+}(t) \approx 0$. The change in the equilibrium energy ($E_{\text{eq},\alpha}$) of the trapped electrons in the BGK mode is

$$\Delta E_{\text{eq},\alpha} = \frac{\partial H_{0,\alpha}}{\partial J_\alpha}\Delta J_{\text{res},\alpha} = \omega_{\text{pe}}\Delta J_{\text{res},\alpha}, \tag{2.69}$$

where $\Delta J_{\text{res},\alpha} = J_{\text{res},\alpha}(t=t_0) - J_{\text{res},\alpha}(t)$. Using equation (2.20) , we find

$$\Delta J_\alpha = J_{\alpha,+}(t=t_0) - J_{\alpha,+}(t) \approx \sqrt{\frac{A_{1,0}V_{\alpha,1,1,0}}{|\Delta_{\alpha,0}|}}, \tag{2.70}$$

where, $t = t_0$ is denoted by the subscript 0. The change in the perturbed energy ($E_{\text{perturbed},\alpha}$) of the electrons, which is the change in the perturbed potential energy, equals

$$\Delta E_{\text{perturbed},\alpha} = A_{1,0}V_{\alpha,1,1,0}. \tag{2.71}$$

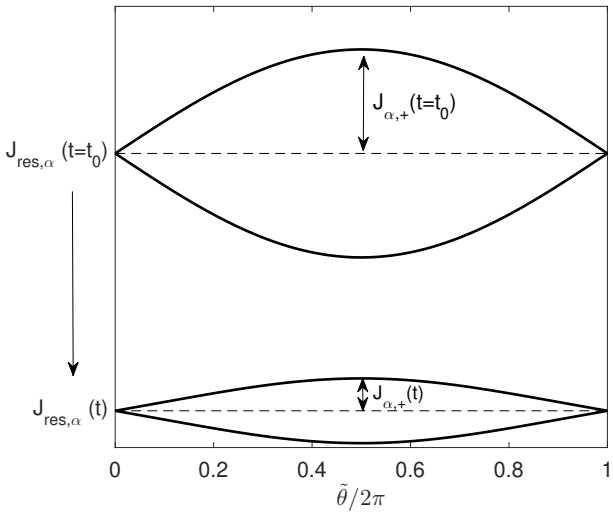

Figure 2.12: Schematic of a separatrix shrinkage with $J_{\alpha,+}(t) \approx 0$ during long range frequency chirping.

We have claimed that if the change in $J_{\mathrm{res},\alpha}$ is greater than the change in the separatrix width, then $\Delta E_{\mathrm{perturbed},\alpha} \ll \Delta E_{\mathrm{eq},\alpha}$. Therefore, we have

$$A_{1,0} V_{\alpha,1,1,0} \ll \omega_{\mathrm{pe}} \Delta J_{\mathrm{res},\alpha}. \tag{2.72}$$

The above inequality can be written into

$$\sqrt{\frac{A_{1,0} V_{\alpha,1,1,0}}{|\Delta_{\alpha,0}|}} \cdot \omega_B \ll \omega_{\mathrm{pe}} \Delta J_{\mathrm{res},\alpha}, \tag{2.73}$$

where $\omega_B = \sqrt{A_{1,0} V_{\alpha,1,1,0} |\Delta_{\alpha,0}|}$ is the bounce frequency of trapped particles inside the separatrix in the BGK mode. Using equation (2.70) we find

$$\frac{\Delta J_{\mathrm{res},\alpha}}{\Delta J_\alpha} \gg \frac{\omega_B}{\omega_{\mathrm{pe}}} \approx \frac{\gamma_l}{\omega_{\mathrm{pe}}}. \tag{2.74}$$

The RHS value is much less than unity ($\gamma_l \ll \omega_{\mathrm{pe}}$). Therefore, if the change in $J_{\mathrm{res},\alpha}$ is greater than the change in the width of the separatrix, the condition (2.74) is sufficiently satisfied.

Chapter 3

Long range frequency chirping of Alfvén eigenmodes

Abstract

A theoretical framework has been developed for an NBI scenario to model the hard nonlinear evolution of Global Alfvén Eigenmodes (GAEs) where the adiabatic motion of phase-space structures (holes and clumps), associated with frequency chirping, occurs in generalized phase-space of slowing down energetic particles. The radial profile of the GAE is expanded using finite elements which allows update of the mode structure as the mode frequency chirps. Constants of motion are introduced to track the dynamics of energetic particles during frequency chirping by implementing proper action-angle variables and canonical transformations which reduce the dynamics essentially to 1D. Consequently, we specify whether the particles are drifting inward/outward as the frequency deviates from the initial MHD eigenfrequency. Using the principle of least action, we have derived the nonlinear equation describing the evolution of the radial profile by varying the total Lagrangian of the system with respect to the weights of finite elements. For the choice of parameters in this work, it is shown that the peak of the radial profile is shifted and also broadens due to frequency chirping. The time rate of frequency change is also calculated using the energy balance and we show that the adiabatic condition remains valid once it is satisfied. This model clearly illustrates the theoretical treatment to study the long range adiabatic frequency sweeping events observed for Alfvén gap modes in real experiments.

3.1 Introduction

Alfvén waves can be unstable as a result of their interaction with energetic particles (EPs) which satisfy the resonance condition during the slowing down process [79]. In magnetic fusion devices e.g. tokamaks, Alfvén eigenmodes (AEs) [9, 11], located outside the shear Alfvén continuum, are subject to weak continuum damping and therefore can be destabilized by supra-thermal particles and fusion products. These modes are potentially dangerous for particle transport. The feedback between unstable waves and enhanced particle diffusion would degrade EP confinement (see the review article [80] and the references therein and also [61, 81, 82]), influence the fuel burnup [83–86] and subject the material of the containment vessel to increased erosion. On the other hand, destabilization of Alfvén waves may have some beneficial effects e.g. diagnostic purposes of the plasma core [87, 88],

achieving higher confinement regime due to redistribution of injected ions in DIII-D [89] and energy channeling of fusion born alpha particles [90]. Therefore, an ability to model and control these kinetically driven instabilities is crucial to the design and operation of a fusion power plant.

The wave-particle interaction, which is essentially one dimensional, may result in frequency sweeping behaviors [63–67, 91]. Refs. [34, 92], which successfully explain the chirping observed in experiments [69, 93], describe the possible formation of phase–space structures, namely holes and clumps, whose motions are associated with frequency sweeping events. In these models, the radial structure of the MHD mode is fixed, a logical assumption as long as the frequency remains close to the initial eigenfrequency. Subsequently, a nonperturbative model [53] was presented to investigate the long range sweeping events [48, 71, 72] in the hard nonlinear regime where the structure of the mode is considerably affected by the nonthermal fast particles population. Inclusion of collision operators into this model was accomplished in Refs. [54, 55]. More recently, a 1D theoretical framework was developed in Ref. [56], which investigates the impact of different EPs orbit topologies (magnetically trapped/passing) on long range frequency chirping of BGK modes. It should be noted that these models consider the adiabatic evolution of phase–space structures and therefore the Vlasov equation can be bounce averaged to find the perturbed phase–space density of resonant particles. In a very recent work [94], a new kinetic code, CHIRP, has been developed to study the nonlinear behavior of an energetic particle mode (EPM) which is established and evolved inside the shear Alfvén continuum.

In this paper, we develop a model to describe the hard nonlinear evolution of a Global Alfvén Eigenmode (GAE), which is destabilized outside the Alfvén continuum, using a Lagrangian formalism. We make two main assumptions in this work

- For a GAE, where poloidal components are weakly coupled, the toroidal effects are neglected in the description of the bulk plasma. However, we retain toroidal effects on EP dynamics, which determine the nonlinear behavior of an energetic particle driven mode, in the cylinderical tokamak limit. In other words, the bulk plasma is described in a periodic cylinder while EP dynamics are described in a high-aspect ratio tokamak.

- In a tokamak, all the components of the mode structure namely tororidal, poloidal and radial, needs to be updated during frequency chirping due to the non-linearity of the EPs current. The general formalism of the problem presented in section 3.2 explains the roadmap to update all the components of the mode structure during chirping. As mentioned in [53], when the frequency deviates from the initial eigenfrequency significantly, the mode preserves its periodic behavior but does not remain sinusoidal. Hence, the poloidal and toroidal components of the mode structure, which represent periodic behavior, can be treated using the Fourier expansion method implemented in [56]. The main challenge left is to treat the radial profile, which does not have a periodic behavior. Accordingly, we focus on the evolution of the radial profile and the nonlinear contribution of EPs current updates only the radial profile of the mode.

Therefore, the eigenfunction is presented by a single poloidal (m) and toroidal (n) mode number except for section 3.2. The initial eigenfrequency lies just below the shear Alfvén continuum and we study the dynamics associated with a downward branch of frequency chirping. There is no continuum crossing in this case, which is a requirement for the model

to remain valid as the frequency chirps. We consider the total Lagrangian of the system and use finite element method to expand the radial structure of the eigenmode. Varying the total Lagrangian with respect to finite element weights gives nonlinear equations describing evolution of the mode radial profile, which is analyzed by invoking the adiabatic condition.

Section 3.2 describes the general picture of the problem in tokamaks. In section 3.3, the equation of the mode driven by EPs is presented. The linear growth rate is calculated by finding an explicit expression for perturbed EPs phase–space density. Afterwards, we introduce an adiabatic Hamiltonian describing the dynamics of EPs during frequency chirping, which together with bounce averaging the Vlasov equation, allows us to solve the nonlinear equation for the evolving radial profile of the mode and the rate of frequency chirping. Section 3.4 describes a numerical procedure implemented to solve the nonlinear equations. Section 3.5 presents the results for a specific polodial and toroidal mode number. This includes equilibrium profiles, dynamics of EPs during frequency chirping, the evolution of the radial profile, the rate of frequency chirping and validation of the adiabatic condition. Section 3.6 is a summary.

3.2 General formalism for nonlinear GAEs

We consider a saturated MHD eigenmode with an already established structure in the case of a near-threshold instability. In the presence of weak damping, the coherent group of EPs locked in the mode results in signals with adiabatic frequency chirping in the EPs phase-space associated with the slow evolution of the saturated structure. These signals represent the nonlinear BGK modes with a chirping frequency. In tokamak geometry the general form of a nonlinear chirping mode whose radial profile is evolving slowly/adiabatically can be presented by

$$\Phi\left(\boldsymbol{r};t_s;t_f\right)=\sum_h \phi_h\left(\boldsymbol{r};t_s\right)\exp\{-ih\alpha\left(t_f\right)\}+c.c \tag{3.1}$$

with

$$\begin{aligned}\phi_h&=\sum_m \phi_{m;n;h}\left(r;t_s\right)\exp\{ih\left(m\theta+n\varphi\right)\}\\&=\sum_{m,l}\lambda\left(t_s\right)Y_l\left(r\right)\exp\{ih\left(m\theta+n\varphi\right)\},\end{aligned} \tag{3.2}$$

where m and n are the poloidal and toroidal mode numbers, respectively, $Y_l\left(r\right)$ are base functions and the corresponding weights λ_l used to describe the finite-element expansion of the radial mode structure, t_f represents fast time scale on the order of the inverse eigenfrequency, t_s represents the slow time scale on which the BGK mode evolves i.e. much longer than the bounce period of the particles trapped in the mode and $\alpha\left(t_f\right)=\int_0^{t_f}\omega\left(t'\right)dt'$. For simplicity, the indices are dropped from t in the following.

The total Lagrangian describing the system reads

$$L=L_{\text{wave}}+\sum_{\text{fast particles}}L_{\text{particles}}+\sum_{\text{fast particles}}L_{\text{int}}, \tag{3.3}$$

where L_{wave} is the MHD wave Lagrangian, $L_{\text{particles}}$ is the EP Lagrangian describing the equilibrium motion and the interaction Lagrangian is denoted by L_{int}. The total

Lagrangian contains all the dynamical variables of the system i.e. particle variables and field variables. In principle, one should vary the Lagrangian with respect to each dynamical variable and follow each variable individually. But instead, we use a kinetic description. Nevertheless, each particle trajectory is still a characteristic of the kinetic equation which needs to be solved. However, we do not need to follow each particle trajectory because of the rapid phase mixing in the field of the wave. Therefore, we can characterise the EPs by adiabatic invariants assuming that the mode frequency is evolving adiabatically on much slower time scales compared to the bounce period time of the EPs trapped in the mode. Within the adiabatic chirping approximation, we describe such an adiabatic response of the particles analytically by bounce-averaging the kinetic equation to find the perturbed phase-space density [53, 54, 56]. Hence, we do not vary the total Lagrangian with respect to fast particle variables but only with respect to the field variables. Starting from the Littlejohns Lagrangian [73] for the guiding center motion of the fast particles, we have

$$L_{\text{Littlejohn}} = e\left(\boldsymbol{A} + \rho_{\parallel}\boldsymbol{B}\right)\cdot\dot{\boldsymbol{X}} + \frac{m_i}{e}\mu\dot{\Omega} - H, \tag{3.4}$$

where $\boldsymbol{B} = \nabla\times\boldsymbol{A}$ is the total magnetic field with A the vector potential, $\rho_{\parallel}$ is the gyroradius, m_i is the ion mass, e is the electron charge, μ is the magnetic moment, $\dot{\Omega}$ is the time rate of change of gyrophase and $H = \frac{1}{2}mv_{\parallel}^2 + \mu B$ is the particle Hamiltonian with $v_{\parallel}$ being the particle velocity parallel to the equilibrium magnetic field. It should be noted that we have considered a gauge where the perturbed electrostatic potential is zero. Using Eq. (3.4), the particle and interaction Lagrangian can be found as

$$L_{\text{particles}} = P_\theta\dot{\theta} + P_\varphi\dot{\varphi} + P_\Omega\dot{\Omega} - H_0\left(P_\theta, P_\varphi, P_\Omega, \theta\right) \tag{3.5}$$

and

$$L_{\text{int}} = e\tilde{\boldsymbol{A}}\cdot\dot{\boldsymbol{X}} = -e\left[\frac{\partial\Phi}{\partial t} + v_{\parallel}\boldsymbol{b}\cdot\nabla\Phi\right], \tag{3.6}$$

respectively, where H_0 is the equilibrium Hamiltonian written in terms of the canonical variables: canonical momenta P_θ, P_φ and P_Ω conjugated to θ, φ and Ω, respectively, $\boldsymbol{b}$ is the unit vector in the direction of the equilibrium magnetic field $\boldsymbol{B}_0$ and $\tilde{\boldsymbol{A}}_\perp = \tilde{\boldsymbol{A}} - \frac{\boldsymbol{B}_0}{B_0^2}\left(\tilde{\boldsymbol{A}}\cdot\boldsymbol{B}_0\right)$ is the perturbed vector potential that can be represented by two independent scalar functions Φ and Ψ as

$$\tilde{\boldsymbol{A}}_\perp = \nabla\Phi - \boldsymbol{B}_0\left(\boldsymbol{B}_0\cdot\nabla\Phi\right)/\boldsymbol{B}_0^2 + \boldsymbol{B}_0\times\nabla\Psi/\boldsymbol{B}_0. \tag{3.7}$$

As mentioned in [30], the compressional perturbation Ψ is almost decoupled from the shear Alfvén perturbation Φ. We, therefore only consider the Φ term for a GAE.

The periodicity of the unperturbed motion allows us to implement action-angle (AA) variables $(\tilde{\theta}, \tilde{\varphi}, \tilde{\Omega}, P_{\tilde{\theta}}, P_{\tilde{\varphi}}, P_{\tilde{\Omega}})$ for EPs dynamics. The transformation to the AA variables is governed by the following type-2 generating function

$$G_2 = \varphi P_{\tilde{\varphi}} + \Omega P_{\tilde{\Omega}} + \int_0^\theta P_\theta d\theta. \tag{3.8}$$

The interaction Lagrangian can be written in a more explicit form by substituting Eqs. (3.1) and (3.2) in Eq. (3.6). The perturbed/interaction Hamiltonian reads

$$H_{\text{int}} = -L_{\text{int}}. \tag{3.9}$$

By neglecting the toroidal coupling between poloidal components of the mode and expanding in AA variables of the unperturbed motion, we find

$$H_{\text{int}} = -\sum_{l,h,p} \lambda_{l,h}(t)\, V_{p,n,l,h}\left(P_{\tilde{\theta}}, P_{\tilde{\varphi}}, P_{\tilde{\Omega}}\right) \exp\Big\{ip\tilde{\theta} + ih\left[n\tilde{\varphi} - \alpha(t)\right]\Big\} + c.c, \tag{3.10}$$

where $\tilde{\theta}$ and $\tilde{\varphi}$ are poloidal and toroidal angles, respectively, corresponding to the AA variables of the unperturbed motion, V is the coefficient of the Fourier expansion in $\tilde{\theta}$ and p is the indice of resonances in the linear stage, whereas in the nonlinear problem $\frac{p}{h}$ lables different resonances.

The equations governing the evolution of the mode structure and the frequency can be derived by varying the total lagrangian of the system with respect to the two dynamical field variables, namely λ and α. We write the system of equations for the evolution of the mode structure by varying the total Lagrangian with respect to λ, however, in the limit of adiabatic frequency chirping and the slow evolution of the radial profile $\frac{\mathrm{d}\ln\lambda_l}{\mathrm{d}t} \ll \dot{\alpha}$, the energy balance principle is used to track the evolution of the frequency ($\dot{\alpha}$) during chirping. Therefore, we find the equation corresponding to each harmonic (h) of the evolving mode structure by varying Eq. (3.3) with respect to λ, which gives

$$\begin{aligned}\left(h^2\dot{\alpha}^2\mathsf{M}_h - \mathsf{N}_h\right)\cdot\boldsymbol{\lambda}_h = -\frac{1}{4}\int d^3p d^3q \delta f\left(\boldsymbol{q},\boldsymbol{p},t\right)\\ \times\sum_p \begin{bmatrix} V_{p,n,l=1,h} \\ \vdots \\ V_{p,n,l=\mathbf{s},h}\end{bmatrix} \exp\Big\{ip\tilde{\theta} + ih\left[n\tilde{\varphi} - \alpha(t)\right]\Big\} + c.c,\end{aligned} \tag{3.11}$$

where matrices M_h and N_h, corresponding to each harmonic (h), are constructed by discretising the field and integrating over the plasma volume and the integration on the RHS is over the phase-space of the EPs. It is noteworthy that the derivation of Eq. (3.11) and the matrices are detailed in section 3.3. During the adiabatic evolution, the BGK mode acts like a bucket and the trapped EPs inside this mode will be moved slowly in phase-space, associated with adiabatic frequency chirping. Hence, the perturbed phase-space density (δf) is mainly due to the EPs trapped in the mode and can be found by solving the kinetic equation in the adiabatic regime.

In what follows, the theoretical picture is developed for a single harmonic ($h = 1$). In other words, this model focuses on the evolution of the radial component of the mode during adiabatic frequency chirping.

3.3 The model

We consider a GAE in the following calculations and therefore retain only one poloidal harmonic in the linear response of the cold particles. We, however, take into account poloidal variation of the confining magnetic field in our calculations of the EP trajectories and use a high aspect ratio approximation for that.

3.3.1 MHD wave Lagrangian

The kinetic (K) and potential energy (W) of MHD waves are given by

$$K = \frac{1}{2}\int \rho \dot{\boldsymbol{\xi}}^2 dV \tag{3.12a}$$

$$W = -\frac{1}{2}\int \boldsymbol{\xi}\cdot\boldsymbol{F}\left(\boldsymbol{\xi}\right)dV, \tag{3.12b}$$

where ρ is the mass density, $\boldsymbol{\xi}$ is the displacement vector, $\boldsymbol{F}$ is the force operator, dV denotes the differential volume element and the integration is performed over the whole plasma volume. For a low-β system and the linearized force operator and in the aforementioned gauge where the perturbed scalar electrostatic potential is zero, the wave Lagrangian reads

$$L_{\mathrm{w}} = \frac{1}{2}\int \rho\left(\frac{\dot{\tilde{A}}_{\perp}}{B_0}\right)^2 - \frac{\left|\nabla\times\tilde{A}_{\perp}\right|^2}{\mu_0} + \frac{J_{\parallel}}{B_0}\tilde{A}_{\perp}\cdot\nabla\times\tilde{A}_{\perp}dV \tag{3.13}$$

where $\tilde{A}$ is the perturbed vector potential, B_0 is the equilibrium magnetic field, μ_0 is the magnetic permeability, $J_{\parallel}$ is the unperturbed plasma current parallel to the equilibrium field and we have neglected the nonlinear bulk plasma response. Considering only the Φ term in Eq. (3.7) for a GAE, Eq. (3.13) reduces to

$$L_{\mathrm{w}} = \frac{1}{2\mu_0}\int \frac{\mu_0\rho}{B_0^2}\left(\nabla_{\perp}\dot{\Phi}\right)^2 - \left(B_0\nabla_{\perp}\frac{\boldsymbol{B}_0\cdot\nabla\Phi}{B_0^2}\right)^2 - \left[\frac{\left(\nabla\times\boldsymbol{B}_0\right)\left(\boldsymbol{B}_0\cdot\nabla\Phi\right)}{B_0^2}\right]^2 - \frac{\left(\boldsymbol{B}_0\cdot\nabla\Phi\right)\left(\nabla\Phi\cdot\Delta\boldsymbol{B}_0\right)}{B_0^2}dV, \tag{3.14}$$

which can be varied with respect to Φ to obtain the linear dispersion relation. For a single GAE, Φ can be written as

$$\Phi\left(\boldsymbol{r};t\right) = \sum_{l=1}^{\mathbf{s}}\lambda_l\left(t\right)Y_l\left(r\right)\exp\{im\theta + in\varphi - i\alpha\left(t\right)\} + c.c, \tag{3.15}$$

where (r,θ,φ) are cylinderical coordinates, $\alpha\left(t\right)$ represents rapid oscillations, $\mathbf{s}$ is the total number of finite elements and λ_l and α are real quantities with λ_l being assumed to change slowly compared to the mode frequency, $\frac{\mathrm{d}\ln\lambda_l}{\mathrm{d}t} \ll \dot{\alpha}$. This implies a proper set of the base functions that can represent a smooth radial profile of the global eigenmode. Substituting Eq. (3.15) into Eq. (3.14) gives

$$L_{\mathrm{wave}} = 2\dot{\alpha}^2\left[\boldsymbol{\lambda}^{\mathsf{T}}\cdot\mathsf{M}\cdot\boldsymbol{\lambda}\right] - 2\left[\boldsymbol{\lambda}^{\mathsf{T}}\cdot\mathsf{N}\cdot\boldsymbol{\lambda}\right], \tag{3.16}$$

where the fast time varying part is integrated out and the superscript $\intercal$ denotes the transpose operation, $\{\boldsymbol{\lambda}\}\in \mathbb{R}^{\mathsf{s}\times 1}$, $\{\mathsf{M},\mathsf{N}\} \in \mathbb{R}^{\mathsf{s}\times\mathsf{s}}$ whose elements are given by

$$M_{j,k} = \frac{1}{2\mu_0}\int \frac{rR_0}{V_A^2}\left[\frac{\mathrm{d}Y_j}{\mathrm{d}r}\frac{\mathrm{d}Y_k}{\mathrm{d}r} + \frac{m^2}{r^2}Y_jY_k\right] drd\theta d\varphi \tag{3.17a}$$

$$N_{j,k} = \frac{1}{2\mu_0}\int \left[B_0^2\left(\frac{\mathrm{d}}{\mathrm{d}r}\frac{k_\parallel Y_j}{B_0}\right)\left(\frac{\mathrm{d}}{\mathrm{d}r}\frac{k_\parallel Y_k}{B_0}\right) + \left(\frac{m^2k_\parallel^2}{r^2} + \frac{\mu_0^2J_\parallel^2k_\parallel^2}{B_0^2} + \mu_0 mk_\parallel\frac{\mathrm{d}}{\mathrm{d}r}\left(\frac{J_\parallel}{B_0}\right)\right)Y_jY_k\right] rR_0drd\theta d\varphi, \tag{3.17b}$$

where R_0 is the major radius, V_A is the Alfvén velocity and $k_\parallel$ is the wavenumber parallel to the equilibrium magnetic field.

3.3.2 Energetic particle and interaction Lagrangian

We write the unperturbed particle Lagrangian part of Eq. (3.4) using the high aspect ratio tokamak limit where the flux surfaces are approximated by the contours of constant r [95]. In these coordinates, one can write

$$\boldsymbol{A}_0 = \psi\nabla\theta - \chi\nabla\varphi + \nabla\eta, \tag{3.18}$$

and

$$\boldsymbol{B}_0 = \nabla\psi\times\nabla\theta - \nabla\chi\times\nabla\varphi = B_\theta\nabla\theta + B_\varphi\nabla\varphi. \tag{3.19}$$

where $\boldsymbol{A}_0$ is the equilibrium part of the vector potential and χ is the poloidal flux. We have $\nabla\varphi = R^{-1}\boldsymbol{e}_\varphi$ and according to Amperes law $B_0 \propto R^{-1}$. Hence, $B_\varphi \approx B_0R_0$ is a constant with B_0 being the equilibrium magnetic field at the center of the plasma. Using Eqs. (3.18) and (3.19), we have

$$\frac{\partial\psi}{\partial r} \approx rB_0\left(1-\epsilon\cos\theta\right), \tag{3.20}$$

where ϵ is the inverse aspect ratio.

Using a proper gauge to cancel $\nabla\eta$ in $\boldsymbol{A}_0$, $L_{\text{particles}}$ can be written in the canonical form given by Eq. (3.5) and the canonical variables are given by

$$P_\theta = e\psi(r,\theta) + m_iv_\parallel b_\theta(r,\theta), \tag{3.21}$$

$$P_\varphi = -e\chi(r) + m_iv_\parallel b_\varphi(r,\theta), \tag{3.22}$$

$$P_\Omega = \frac{m_i}{e}\mu, \tag{3.23}$$

where b_θ and b_φ are covariant components of $\boldsymbol{b}$, with $b_\theta \approx r^2/qR$ and $b_\varphi \approx R$, and $\chi(r)$ can be found using Eq. (3.20) and the safety factor $q(r,\theta) = \frac{\boldsymbol{B}_0\cdot\nabla\varphi}{\boldsymbol{B}_0\cdot\nabla\theta} = \frac{\partial\psi/\partial r}{\partial\chi/\partial r} \approx q(r)$. The conversion from r and $v_\parallel$ to the canonical variables are now implicitly given by Eq. (5.18) and Eq. (3.22).

The large aspect ratio assumption allows us to drop the θ dependency in Eq. (3.20). Taking into account that the toroidal equilibrium field is dominant, b_θ can also be ne-

glected. Hence, we have

$$P_\theta = \frac{1}{2} e X_r^2 B_0, \tag{3.24}$$

$$P_\varphi = -e\chi\left(X_r\left(P_\theta\right)\right) + m_i v_\parallel R, \tag{3.25}$$

and

$$H_0 = \frac{1}{2} m_i v_\parallel^2\left(P_\theta, P_\varphi, P_\Omega, \theta\right) + \mu B_0\left[1 - \frac{X_r\left(P_\theta\right)}{R_0}\cos\theta\right], \tag{3.26}$$

where X_r is the radial position of the EPs. By implementing the canonical equations of motion, we find

$$\frac{\partial H_0}{\partial P_\theta} = m_i v_\parallel \frac{\partial H_0}{\partial P_\theta} - \mu B_0 \frac{1}{R_0}\cos\theta \frac{\mathrm{d}X_r}{\mathrm{d}P_\theta} = \dot{\theta}, \tag{3.27}$$

$$\frac{\partial H_0}{\partial P_\varphi} = m_i v_\parallel \frac{\partial v_\parallel}{\partial P_\varphi} = \dot{\varphi}, \tag{3.28}$$

$$\frac{\partial H_0}{\partial \theta} = m_i v_\parallel \frac{\partial v_\parallel}{\partial \theta} + \mu B_0 \frac{X_r}{R_0}\sin\theta = -\dot{P}_\theta. \tag{3.29}$$

Using Eq. (3.25), we get

$$\dot{P}_\theta = -\left[\frac{m_i v_\parallel^2}{R} + \frac{\mu B_0}{R_0}\right] X_r \sin\theta, \tag{3.30}$$

$$\dot{\varphi} = \frac{v_\parallel}{R}, \tag{3.31}$$

$$\dot{\theta} = \frac{v_\parallel}{R q(X_r)} - \left[\frac{m_i v_\parallel^2}{R} + \frac{\mu B_0}{R_0}\right]\cos\theta \frac{1}{e B_0 X_r}. \tag{3.32}$$

It should be mentioned that in the high aspect ratio tokamak limit, the safety factor can be considered only as a function of the radius. The conjugate momenta corresponding to φ and Ω are constants of motion. Therefore, in terms of the AA variables introduced by (3.8), one can set $P_{\tilde{\varphi}} = P_\varphi$, $P_{\tilde{\Omega}} = P_\Omega$ and considering the definition of the angle variables from 0 to 2π, it is found that $\tilde{\varphi} = \varphi + \Delta\varphi$ for motion in the direction of the field line. In this work, we consider the case of a neutral beam injection (NBI) where the majority of the EPs are deeply passing ($\mu \approx 0$) inside the equilibrium field. Consequently, $v_\parallel$ becomes a constant of motion. We also assume the maximum orbit width (Δr) to be much smaller than the width of the radial mode structure and let $r_0\left(P_\theta, P_\varphi, P_\Omega\right)$ be the average position of a drift orbit. These conditions together with the large aspect ratio assumption make φ and θ approximately linear in time. Therefore, we find

$$\dot{\tilde{\theta}} = \omega_{\tilde{\theta}} \approx \frac{V_\parallel\left(\tilde{P}_\theta, \tilde{P}_\varphi, \tilde{P}_\Omega\right)}{q\left(r_0\right) R_0} \tag{3.33a}$$

$$\dot{\tilde{\varphi}} = \omega_{\tilde{\varphi}} \approx \frac{V_\parallel\left(\tilde{P}_\theta, \tilde{P}_\varphi, \tilde{P}_\Omega\right)}{R_0}, \tag{3.33b}$$

where $\omega_{\tilde{\theta}}$ and $\omega_{\tilde{\varphi}}$ represent the poloidal and toroidal guiding center frequency of deeply passing EPs.

Substituting Eq. (3.15) into Eq. (3.6) results in

$$L_{\text{int}} = ie\left[\dot{\alpha} - v_{\parallel}\frac{\left(\frac{m}{q(X_r)}+n\right)}{R_0}\right]\sum_l \lambda_l(t)\,Y_l(X_r)\exp\{im\theta + in\varphi - i\alpha(t)\} + c.c. \quad (3.34)$$

Now, we express the above Lagrangian in terms of the AA variables of the unperturbed motion to find

$$L_{\text{int}} = \sum_l\sum_p \lambda_l(t)\,V_{p,n,l}\exp\Big\{ip\tilde{\theta} + in\tilde{\varphi} - i\alpha(t)\Big\} + c.c, \quad (3.35)$$

where the coupling strength, $V_{p,n,l}$, is determined by

$$V_{p,n,l} = \frac{1}{2\pi}\int ie\left[\dot{\alpha}(t) - v_{\parallel}\frac{\left(\frac{m}{q(X_r)}+n\right)}{R_0}\right]Y_l(X_r)\exp\{im\theta + in\varphi\}\exp\Big\{-ip\tilde{\theta} - in\tilde{\varphi}\Big\}d\tilde{\theta} \quad (3.36)$$

whose detailed calculation for deeply co-passing orbit types of the EPs is presented in 3.7.1.

3.3.3 Mode equation

The total Lagrangian for one eigenmode can be presented by

$$L = 2\dot{\alpha}^2\left[\boldsymbol{\lambda}^{\mathsf{T}}\mathsf{M}\boldsymbol{\lambda}\right] - 2\left[\boldsymbol{\lambda}^{\mathsf{T}}\mathsf{N}\boldsymbol{\lambda}\right] + \sum_{\text{fast particles}} P_{\tilde{\theta}}\dot{\tilde{\theta}} + P_{\tilde{\varphi}}\dot{\tilde{\varphi}} + P_{\tilde{\Omega}}\dot{\tilde{\Omega}} - H_0\left(P_{\tilde{\theta}}, P_{\tilde{\varphi}}, P_{\tilde{\Omega}}\right) + \sum_{\text{fast particles}} \boldsymbol{\lambda}^{\mathsf{T}}(t)\,\boldsymbol{D} + c.c, \quad (3.37)$$

where the elements of $\{\boldsymbol{D}\} \in \mathbb{R}^{S\times 1}$ are $D_{l,1} = \sum_p V_{p,n,l}\exp\Big\{ip\tilde{\theta} + in\tilde{\varphi} - i\alpha(t)\Big\}$. Varying the above Lagrangian with respect to $\boldsymbol{\lambda}$ gives the following expression for the nonlinear mode structure

$$\left(4\dot{\alpha}^2\mathsf{M} - 4\mathsf{N}\right)\boldsymbol{\lambda} + \sum_{\text{fast particles}} \boldsymbol{D} + c.c = 0 \quad (3.38)$$

The sum over fast particles can be replaced by integration over initial phase–space. The canonicity of the transformation from the initial phase–space coordinates to the instant coordinates $[(\boldsymbol{q}_0, \boldsymbol{p}_0) \to (\boldsymbol{q}, \boldsymbol{p})]$ allows us to write the phase-space integration in terms of the instant coordinates. In addition, as mentioned in section 3.2, we take $h = 1$ and therefore we find the nonlinear mode equation in the form given by Eq. (3.11) with $h = 1$, where $\delta f = \sum_p \delta f_p$ is the perturbed part of the total distribution function ($f = \delta f + F_0$) of the EPs with F_0 being the equilibrium part. In this model, krook type collisions inside the bulk plasma provide the damping mechanism to the wave amplitude at a rate γ_d, which is implicitly included in Eq. (3.11) (see [29] and [30]).

3.3.4 Mode evolution

The total Hamiltonian of the EPs during the hard-nonlinear evolution reads,

$$H = H_0\left(P_{\tilde{\theta}}, P_{\tilde{\varphi}}, P_{\tilde{\Omega}}\right) + H_{\text{int}} \tag{3.39}$$

where $H_{\text{int}} = -L_{\text{int}} = \sum_p H_{\text{int},p}$ written in terms of the AA variables of the unperturbed motion. In order to simplify the dynamics, we consider the canonical transformation using the type-2 generating function

$$F_2\left(\boldsymbol{q}, \boldsymbol{p}_{\text{new}}, t\right) = P_1\left[p\tilde{\theta} + n\tilde{\varphi} - \alpha\left(t\right)\right] + P_2\tilde{\varphi} + P_3\tilde{\Omega}, \tag{3.40}$$

for the p-th resonance. The new variables are defined as follows

$$\begin{aligned} P_1 &= \frac{1}{p}P_{\tilde{\theta}} & Q_1 &= \zeta = p\tilde{\theta} + n\tilde{\varphi} - \alpha\left(t\right) \\ P_2 &= P_{\tilde{\varphi}} - \frac{n}{p}P_{\tilde{\theta}} & Q_2 &= \tilde{\varphi} \\ P_3 &= P_{\tilde{\Omega}} & Q_3 &= \tilde{\Omega} \end{aligned} \tag{3.41}$$

which shows that the wave-particle interaction is effectively one-dimensional in an isolated resonance, i.e. P_2 and P_3 corresponding to ignorable coordinates, are constants of the motion. The above canonical transformation is defined for a specific value of p corresponding to the p-th resonance. This can be emphasized by considering a subscript p on the new variables. However, such subscripts are neglected for simplicity.

In what follows, we first calculate an analytic expression for the perturbed phase–space density of EPs in the linear limit. Afterwards, the dynamics of the resonant particles during the adiabatic chirping of the GAE are identified, followed by the perturbed distribution function during the evolution of holes/clumps.

3.3.4.1 Linear regime

The linearized Vlasov equation for the p-th resonance

$$\frac{\partial \delta f_p}{\partial t} + \frac{\partial \delta f_p}{\partial \zeta}\frac{\partial H_0}{\partial P_1} = \frac{\partial F_0}{\partial P_1}\frac{\partial H_{\text{int},p}}{\partial \zeta}\bigg|_{P_2,P_3}, \tag{3.42}$$

where $\delta f_p = \hat{f}_p\left(P_1\right)\exp(i\zeta) + c.c$ and $H_{\text{int},p} = -\sum_l \lambda_l V_{p,n,l}\exp(i\zeta) + c.c$, can be used to derive an analytic expression for δf_p. During the linear evolution, we set $\alpha(t) = \omega t$, with ω being the complex frequency having the real part ω_r and imaginary part γ_l. By substituting the relevant expressions in Eq. (3.42), we find

$$\hat{f}_p = \frac{\sum_l \lambda_l V_{p,n,l}(\frac{\partial F_0}{\partial P_{\tilde{\varphi}}}n + \frac{\partial F_0}{\partial P_{\tilde{\theta}}}p)}{\omega - p\omega_{\tilde{\theta}} - n\omega_{\tilde{\varphi}}}, \tag{3.43}$$

which gives the resonance condition

$$\omega_r = p\omega_{\tilde{\theta}} + n\omega_{\tilde{\varphi}}. \tag{3.44}$$

In the limit of deeply passing particles, Eqs. (3.11) (with $h = 1$) and (3.43) are used

to find the linear dispersion relation of the mode given by

$$\left(\omega^2\mathsf{M}-\mathsf{N}\right)\boldsymbol{\lambda}=4\pi^3\sum_p\int dP_1dP_2\frac{\frac{\partial F_0}{\partial P_1}\Big|_{P_2,P_3}}{G\left(P_1\right)-\omega}\boldsymbol{T}\boldsymbol{\lambda}, \tag{3.45}$$

where $G\left(P_1\right)=\frac{\partial H_0}{\partial P_1}\Big|_{P_2,P_3}$, $\{\mathsf{T}\}\in\mathbb{C}^{S\times S}$ whose elements are given by $T_{j,k}=V_{p,n,l=j}V^*_{p,n,l=k}$ and $\boldsymbol{\lambda}$ represents the initial MHD eigenvector. Neglecting the infinitesimal contribution from the principal value allows us to set $\omega_r=\omega_{\mathrm{GAE}}$, where ω_{GAE} is the initial MHD frequency of the eigenmode. Therefore, the linear growth rate of the mode is found to be

$$\gamma_l=\left[\sum_p\int dP_2\,\frac{\partial F_0}{\partial P_1}\Big|_{P_2,P_3}\left(\frac{\partial G}{\partial P_1}\right)^{-1}\boldsymbol{T}\,\boldsymbol{\lambda}|_{P_1=P_{1,\mathrm{res}}}\right]\frac{2\pi^4\boldsymbol{\lambda}^\intercal}{\omega_{\mathrm{GAE}}\boldsymbol{\lambda}^\intercal\mathsf{M}\boldsymbol{\lambda}}, \tag{3.46}$$

where $P_{1,\mathrm{res}}$ is the value of P_1 at resonance denoted by Π throughout this manuscript and we have assumed $\gamma_l\ll\omega_{\mathrm{GAE}}$.

3.3.4.2 Nonlinear chirping GAE

The existence of the damping mechanism introduced in subsection 3.3.3 leads to an unstable plateau in the phase–space density of EPs which supports sideband oscillations that evolve into chirping modes [92, 96]. For the purpose of investigating the mode during frequency sweeping, we consider a marginal instability case where mode overlap is neglected and we take the limit where phase–space structures (holes and clumps) move adiabatically. Hence, we have

$$\left[\frac{\mathrm{d}\omega_b}{\mathrm{d}t},\frac{\mathrm{d}\dot{\alpha}}{\mathrm{d}t}\right]\ll\omega_b^2\sim\gamma_l^2\sim\gamma_d^2, \tag{3.47}$$

where ω_b is the bounce frequency of EPs trapped inside the separatrix. Therefore, the finite element amplitudes, $\lambda_l(t)$, evolve on a slow time scale; however, $\alpha(t)$ includes a fast time scale on the order of $\omega_{\mathrm{GAE}}^{-1}$, which corresponds to the periodic behavior of the field. The canonical transformation presented by Eq. (3.41) can be implemented to cancel this fast time scale dependency from the Hamiltonian given by Eq. (3.39). Therefore, for the p-th resonance, the total Hamiltonian converts to

$$K=H_0\left(P_1,P_2,P_3\right)-\dot{\alpha}P_1-\left[\sum_{p'=p,l}\lambda_lV_{p',n,l}\left(P_1,P_2,P_3\right)\exp\{i\zeta\}+c.c\right], \tag{3.48}$$

where highly oscillating terms corresponding to other resonances ($p'\neq p$) have been neglected. Assuming the separatrix width to be small compared with the characteristic width of the distribution function, we can Taylor expand the quantities around the middle of the separatrix ($\Pi(t)$), so we have

$$\begin{aligned}K\approx{}&H_0\left(\Pi,P_2,P_3\right)+\frac{\partial H_0}{\partial P_1}\left(\Pi,P_2,P_3\right)\left[P_1-\Pi\right]-\dot{\alpha}P_1\\&+\frac{1}{2}\frac{\partial^2H_0}{\partial P_1^2}\left[P_1-\Pi\right]^2-\sum_l\lambda_lV_{p,n,l}\left(\Pi,P_2,P_3\right)\exp\{i\zeta_p\}+c.c.\end{aligned} \tag{3.49}$$

The higher order terms in the expansion of the equilibrium Hamiltonian have been neglected due to the smallness of the separatrix width. Π satisfies: $\frac{\partial H_0}{\partial P_1}(\Pi, P_2, P_3) = \dot{\alpha}(t)$, consequently $\Pi = \Pi(P_2, P_3, t)$. Therefore, the new Hamiltonian is

$$K \approx \frac{1}{2}\frac{\partial^2 H_0}{\partial P_1^2}(\Pi, P_2, P_3)[P_1 - \Pi]^2 - \sum_l \lambda_l V_{p,n,l}(\Pi, P_2, P_3)\exp\{i\zeta_p\} + c.c. \tag{3.50}$$

which evolves adiabatically during frequency sweeping. It is noteworthy to mention that for $\frac{\partial^2 H_0}{\partial P_1^2}(\Pi, P_2, P_3) > 0$, substituting K in Eq. (3.50) with the maximum value of $\sum_l \lambda_l V_{p,n,l}(\Pi, P_2, P_3)\exp\{i\zeta_p\} + c.c$ gives the dynamics on the separatrix. The preserved adiabatic invariant corresponding to the above slowly evolving Hamiltonian is

$$I = \frac{1}{2\pi}\int P_1 d\zeta \tag{3.51}$$

and we denote the corresponding angle by η. The above equation can be solved for each P_2, corresponding to a separatrix, by substituting for P_1 and integrating from 0 to 2π over the angle variable ζ.

The perturbed distribution of the passing particles traveling around the separatrix remains approximately close to the equilibrium distribution [53,54]. Hence, the perturbed density is assumed to be dominantly from the trapped particles inside the separatrix. Considering the small separatrix width assumption mentioned above and bounce-averaging the Vlasov equation (see section 3 in [54] and appendix B in [56]), we find

$$\delta f = \begin{cases} f_0 - F_0(t) = F_0(t=0) - F_0(t), & \text{trapped} \\ 0, & \text{passing} \end{cases} \tag{3.52}$$

where δf is the perturbed distribution function of the particles inside holes/clumps, f_0 is the lowest order term in the expansion of f around the small parameter $\eta = \frac{\tau_b}{\tau_s}$ with τ_b and τ_s being the bounce period and the slow time scale of mode evolution, respectively. It should be noted that $t = 0$ denotes the initial stage of chirping in this paper. However, for the case of an expanding separatrix and for newly trapped particles during chirping, $t = 0$ in the above expression implies the time when EPs are trapped inside the separatrix.

3.3.4.3 Chirping rate

According to [31], the dissipated power (Q) via weak collisions due to the work of friction force is $2\gamma_d E_{\text{wave}}$, with E_{wave} being the MHD energy of the mode, which consists the perturbed energy of the cold plasma and the perturbed electromagnetic field. This absorbed power (Q) should be equal to the power (P) released by the phase–space structures energy. Therefore, we have

$$2\gamma_d E_{\text{wave}} = -\sum_{P_2} N_{P_2}\frac{\mathrm{d}E}{\mathrm{d}t}, \tag{3.53}$$

where N_{P_2} is the perturbed number of EPs inside each coherent phase–space structure (hole/clump) in the interval ΔP_2, given by

$$N_{P_2} = \iint \delta f dP_1 d\zeta \Delta P_2 \tag{3.54}$$

and E is the energy of each fast particle inside the hole/clump. This energy consists the kinetic energy and the potential energy of the EPs. Compared to the change in their kinetic energy, we neglect the contribution from the small change in their potential energy which is proportional to the change in the width of the separatrix (See Appendix C in [56]). Hence, E can be replaced by H_0. So we find

$$\frac{\mathrm{d}E}{\mathrm{d}t} = \frac{\mathrm{d}H_0}{\mathrm{d}t} = \left.\frac{\partial H_0}{\partial P_1}\right|_{P_2,P_3} G'(\Pi)^{-1}\ddot{\alpha}, \tag{3.55}$$

where $G = \left.\frac{\partial H_0}{\partial P_1}\right|_{P_2,P_3} = p\omega_{\tilde{\theta}} + n\omega_{\tilde{\varphi}} = \dot{\alpha}$ previously defined in subsection 3.3.4.1 and the last factor on RHS is the rate of chirping of the mode which is the same for all the separatrices corresponding to different P_2s in this model. We also have

$$\left.\frac{\partial^2 H_0}{\partial P_1^2}\right|_{P_2,P_3} = \frac{1}{mR_0^2}\left[\frac{p}{q} + n\right]^2 - \frac{pv_\parallel \frac{\mathrm{d}q}{\mathrm{d}r}p}{R_0 q^2\sqrt{2eB_0 P_{\tilde{\theta}}}}. \tag{3.56}$$

The MHD energy of the mode (E_{wave}) is the sum of Eqs. (3.12a) and (3.12b), which gives

$$E_{\mathrm{wave}} = W + K = \frac{1}{2\mu_0}\int \frac{\dot{\tilde{\boldsymbol{A}}}_\perp^2}{v_A^2} + \left|\nabla\times\tilde{\boldsymbol{A}}_\perp\right|^2 - \left(\tilde{\boldsymbol{A}}_\perp\cdot\nabla\times\tilde{\boldsymbol{A}}_\perp\right)\frac{\nabla\times\boldsymbol{B}\cdot\boldsymbol{B}}{B^2}dV, \tag{3.57}$$

which gives

$$E_{\mathrm{wave}} = 2\dot{\alpha}^2\left[\boldsymbol{\lambda}^\intercal\cdot\mathsf{M}\cdot\boldsymbol{\lambda}\right] + 2\left[\boldsymbol{\lambda}^\intercal\cdot\mathsf{N}\cdot\boldsymbol{\lambda}\right]. \tag{3.58}$$

Substituting the relevant terms into Eq. (3.53) yields

$$\frac{\partial\left(\dot{\alpha}-\dot{\alpha}_{t=0}\right)^2}{\partial t} = \frac{-8\gamma_d\left[\dot{\alpha}^2\boldsymbol{\lambda}^\intercal\cdot\mathsf{M}\cdot\boldsymbol{\lambda} + \boldsymbol{\lambda}^\intercal\cdot\mathsf{N}\cdot\boldsymbol{\lambda}\right]\left(\dot{\alpha}-\dot{\alpha}_{t=0}\right)}{\sum_{P_2}\left[\iint \delta f dP_1 d\zeta \frac{\dot{\alpha}}{\left.\frac{\partial^2 H_0}{\partial P_1^2}\right|_{P_2,P_3}}\Delta P_2\right]}, \tag{3.59}$$

where $\dot{\alpha}_{t=0} = \omega_{GAE}$.

3.4 Numerical approach

In this section, the numerical approach implemented to solve for the rate of chirping along with the nonlinear mode structure is presented. We have used cubic Hermite elements as the base functions. It is noteworthy that sufficient number of elements should be implemented in order to ensure that the weight/coefficient of each element (λ_l) varies slowly ($\frac{\mathrm{d}\ln\lambda_l}{\mathrm{d}t} \ll \dot{\alpha}$) during frequency chirping and the radial structure is smooth. The MHD eigenfrequency (ω_{GAE}) and eigenvector ($\boldsymbol{\lambda}_{\mathrm{GAE}}$) of the mode are derived separately by solving the MHD eigenvalue problem by setting the fast particle contribution in Eq. (3.11) to zero. The equilibrium profiles used to solve the MHD problem and the resonance condition are given in section 3.5 (see figure 3.3).

The general roadmap is as follows

- A 5th order Runge-Kutta method is used to solve the differential equation for the chirping rate

- The resonance condition is solved for each new frequency (see section 3.5)
- At each time step of the Runge-Kutta method, the nonlinear mode structure is calculated by solving Eq. (3.11) with h=1 for $\boldsymbol{\lambda}$ iteratively. This stage is visualised in figure 3.1 where we choose a fixed number of iterations. In our numerical experiment, we found that after 14 iterations, the maximum relative error in the convergence of the elements of $\boldsymbol{\lambda}$ vector is on the order of 10^{-4}.

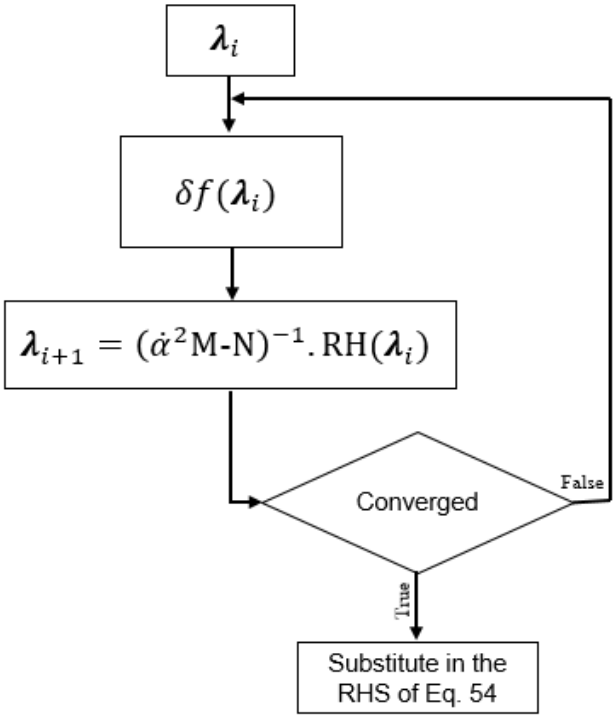

Figure 3.1: The iterative scheme of solving for the mode structure. The index i denotes the number of iteration and RH represents the RHS of Eq. (3.11).

The explanation of this diagram including the integration over phase-space in RHS of Eq. (3.11) or Eq. (3.59), how to treat a/an shrinking/expanding separatrix and the special treatment for the initial stage are detailed below.

3.4.1 Integration over phase-space

Investigation of the hard nonlinear evolution of the mode structure requires one to consider the contribution of different groups of particles that are simultaneously in resonance with the mode and provide Eq. (3.11) with the coressponding perturbed densities during frequency sweeping. It should be noted that in this model ($P_3 = 0$), each P_2 corresponds to a slice of resonance line (a specific group of particles in resonance with the mode) associated with a separatrix. For a specific value of P_2, there exists a corresponding separatrix in (P_1, ζ) space whose dynamics affects the mode behavior during chirping.

3.4.1.1 Integration over P_2

The integration over P_2 is performed by the Trapezoidal rule. As the frequency of the mode begins to deviate from the initial value, there may be some groups of EPs that

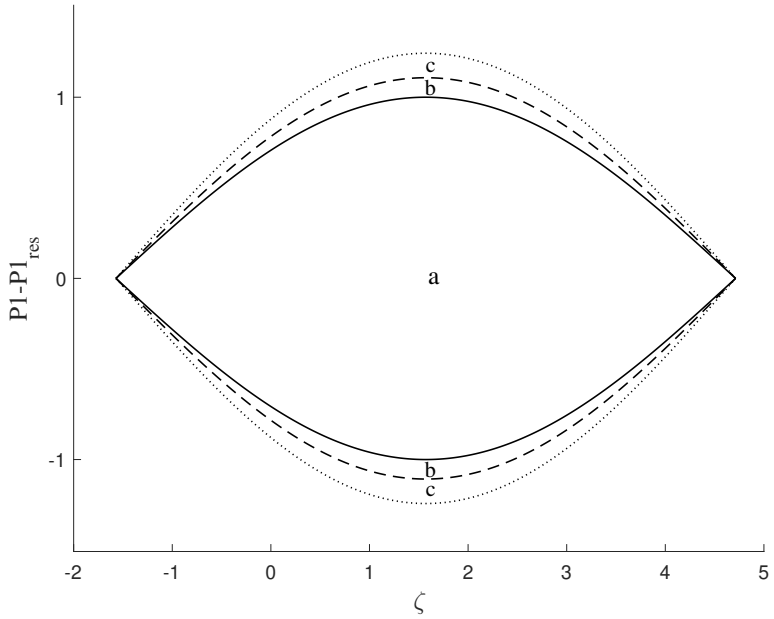

Figure 3.2: Schematic of a separatrix at initial stage (solid line) and expansion of the separatrix after two time steps (dashed and dotted lines). The phase–space area of the initial separatrix is denoted by (a) and the two areas added are specified by (b) and (c).

lose resonance with the mode. On the other hand, there are other groups of EPs whose dynamics satisfy the new resonance condition associated with the updated frequency and will contribute to the interaction. Consequently, after each time step where the frequency is updated, new values of P_2 are added to the domain over which the trapezoidal rule is performed.

3.4.1.2 Integration over (P_1,ζ)

Provided that all the separatrices shrink during the evolution, one can integrate over P_1 analytically. Nevertheless, it is shown in [56] that even for a constant trend in frequency sweeping i.e. upward or downward, the value of the adiabatic invariant can have different behaviors depending on the initial equilibrium orbits. Therefore, even for deeply passing energies and for a constant trend in frequency sweeping, the adiabatic invariant corresponding to different groups of the resonant particles may exhibit different behaviors in terms of the expansion/shrinkage. This needs to be considered in developing a numerical treatment for the evolution of each separatrix [55, 97, 98]. Accordingly, the procedure designed to calculate the integral over each separatrix includes the following main steps:

- Calculating the energy related to the EPs dynamics on the separatrix for the given $\boldsymbol{\lambda}$ and the corresponding value of the adiabatic invariant ($I_{\max}$).
- Calculating the ambient phase-space density using the slowing-down distribution given by Eq. (3.62).
- Calculating δf using Eq. (3.62) and
  - the special treatment presented in 3.4.2 at early stage.
  - the stored phase-space data together with Eq. (3.52) during later evolution.

- Storing/updating the phase-space data,

  -At initial stage: Discretising the separatrix using different adiabatic invariants and assigning an ambient phase-space density value to each region and storing the corresponding data.

  -At later evolution: Updating the stored information: Identifying the shrinkage/expansion by comparing each new $I_{\max}$ to the saved data and updating the data accordingly.

The first two steps can be accomplished by using Eq. (3.51) and the notes thereafter for a constant value of P_2. As mentioned above, the numerical scheme should be able to resolve a shrinking separatrix as well as an expanding one. In the first instance, this may imply that a fully numerical method should be implemented to perform the integration over the phase–space (P_1, ζ) since the perturbed phase–space density term can not be taken out of the integral to allow further analytic calculations/simplifications. However, we implement the following justification to further simplify the integral over each region inside the separatrix with a constant value of the distribution function and speedup the calculations: For the case of an expanding separatrix, it is necessary to chirp continuously between the initial and final frequency in order to derive an exact nonlinear structure at a specific frequency after chirping. This means that the corresponding frequency/time step of the numerical approach is chosen to be sufficiently small so that each group of newly trapped particles will carry the value of their distribution function prior to becoming trapped inside the separatrix. Subsequently, sufficiently small time steps result in a sufficiently small phase–space area added around the previous separatrix. Hence, this enables us to consider a flat-top phase-space density over each newly added region/ring around the previous separatrix and simplify the integral for each region having a constant density. Figure 3.2 shows the phase–space area of an expanding separatrix after two time steps during chirping. Regions b and c represent the small areas added to the initial phase-space area (a) and the value of the distribution function is taken to be the same over each region.

At the initial stage, we discretise the phase-space area surrounded by the separatrix using different values of the adiabatic invariant inside the range $I = [0, I_{\max}]$. This is achieved by substituting different energy values for K in Eq. (3.50). Each adiabatic invariant is assigned a corresponding value of the phase-space density, which represents the value of the distribution function inside the separatrix between two neighbouring discretised adiabatic invariants. Therefore, we define one adiabatic invariant and one phase-space density vector for each separatrix to track its evolution in the numerical scheme. At each time step, depending on whether the value of the new adiabatic invariant at the separatrix ($I_{\max}$) is greater or smaller than its value at the previous time step, both vectors are being updated.

During the evolution of each phase-space structure, the value of the ambient phase-space density is the same as the equilibrium distribution function. The difference between this value and the phase-space density inside the separatrix, stored from the previous steps, gives the perturbed distribution function across the separatrix, which can be associated to the height of the coherent structure (hole/clump) in a 3D picture.

3.4.2 Early stage of chirping

In order to investigate the sweeping rate and the mode structure at early stage of chirping, we rewrite the differential Eq. (3.59) and Eq. (3.11) (with $h = 1$) at $t = 0$. If the separatrix does not trap new particles (a shrinking separatrix) during chirping, f_0 remains the same as $F_{0,t=0}$ [54,56]. For an expanding separatrix the phase–space density of newly trapped particles should be set to the value of the ambient distribution function at the point where the particles are trapped. However, for the very initial stage, one can still set $\delta f = F_0\left(P_{1,\mathrm{res},t=0}, P_2\right) - F_0\left(P_{1,\mathrm{res}}\left(t\right), P_2\right)$. Using the expansion of $F_0\left(P_{1,\mathrm{res}}\left(t\right), P_2\right)$ around $t = 0$ and $\frac{\Pi-\Pi(t=0)}{\dot{\alpha}-\dot{\alpha}_{t=0}} \approx \left(\frac{\partial^2 H_0}{\partial P_1^2}\right)^{-1}\Big|_{P_1=\Pi(t=0)}$, we find

$$\frac{\partial\left(\dot{\alpha}-\dot{\alpha}_{t=0}\right)^2}{\partial t} = \frac{8\gamma_d\left[\dot{\alpha}^2\boldsymbol{\lambda}^\intercal\cdot\mathsf{M}\cdot\boldsymbol{\lambda}+\boldsymbol{\lambda}^\intercal\cdot\mathsf{N}\cdot\boldsymbol{\lambda}\right]}{\sum_{P_2}\left[\iint dP_1 d\zeta\frac{\partial F_0}{\partial P_1}\,|_{P_1=\Pi(t=0)}\,\frac{\dot{\alpha}}{\left(\frac{\partial^2 H_0}{\partial P_1^2}\right)^2\,|_{P_1=\Pi(t=0)}}\Delta P_2\right]} \tag{3.60}$$

at the initial stage of frequency chirping. For analysing the saturated mode structure at the early stage of chirping, we write $\dot{\alpha} = \dot{\alpha}_{t=0} + \Delta\dot{\alpha}$ and substitute in Eq. (3.11) (with $h = 1$) for $\dot{\alpha}$, to have

$$a = \frac{\boldsymbol{\lambda}^\intercal_{\mathrm{GAE}}}{8\dot{\alpha}\boldsymbol{\lambda}^\intercal_{\mathrm{GAE}}\cdot\mathsf{M}\cdot\boldsymbol{\lambda}_{\mathrm{GAE}}}\int d^3p d^3q\frac{\partial F_0}{\partial P_1}\left(\frac{\partial^2 H_0}{\partial P_1^2}\right)^{-1}\,|_{P_1=\Pi(t=0)}\sum_p\begin{bmatrix}V_{p,n,l=1}\\ \vdots\\ V_{p,n,l=\mathbf{s}}\end{bmatrix}\exp\{i\zeta_p\} + c.c. \tag{3.61}$$

where we have considered the saturated mode structure to be a linear factor of the MHD eigenvector ($\boldsymbol{\lambda}_{\mathrm{GAE}}$), $\boldsymbol{\lambda} = a\boldsymbol{\lambda}_{\mathrm{GAE}}$. For an eigenmode growing outside the shear Alfvén continuum, the structure of the radial profile remains almost the same as the initial eigenvector [30].

3.5 Results

We set the values of physical parameters as follows: the axial magnetic field at the center $B_\varphi(r = 0) = 2\,\mathrm{T}$, $R_0 = 3.5\mathrm{m}$, the minor radius $r_m = 1\mathrm{m}$, the ion mass $m_i \approx 3.3\times10^{-27}\mathrm{kg}$, the number density of bulk plasma ions $n_{\mathrm{Bulk}} = 5\times10^{20}\mathrm{m}^{-3}$. The fast particles density n_f is taken to be $(1-10)\%$ of n_{Bulk}.

3.5.1 Equilibrium profiles and resonance condition

For the purpose of this work, we consider the density and current profiles mentioned in [7] to solve the equilibrium condition and the MHD eigenmode problem (Eq. (3.11) without the contribution of fast particles) in the low-β limit. Figure 3.3 shows the equilibrium parameters as a function of the radial position. We have benchmarked the eigenvectors of the MHD eigenvalue problem code with the radial component of displacement vectors reported in [7]. In this model, the GAE exists just below the shear Alfvén continuum since the singularity in the eigenfunction no longer occurs at $r \approx r|_{\omega=\omega_{\min}}$ due to the inclusion of the current dependent terms. The choice of the mode numbers is based on two factors: An MHD eigenmode should exist for the corresponding mode numbers and also there should

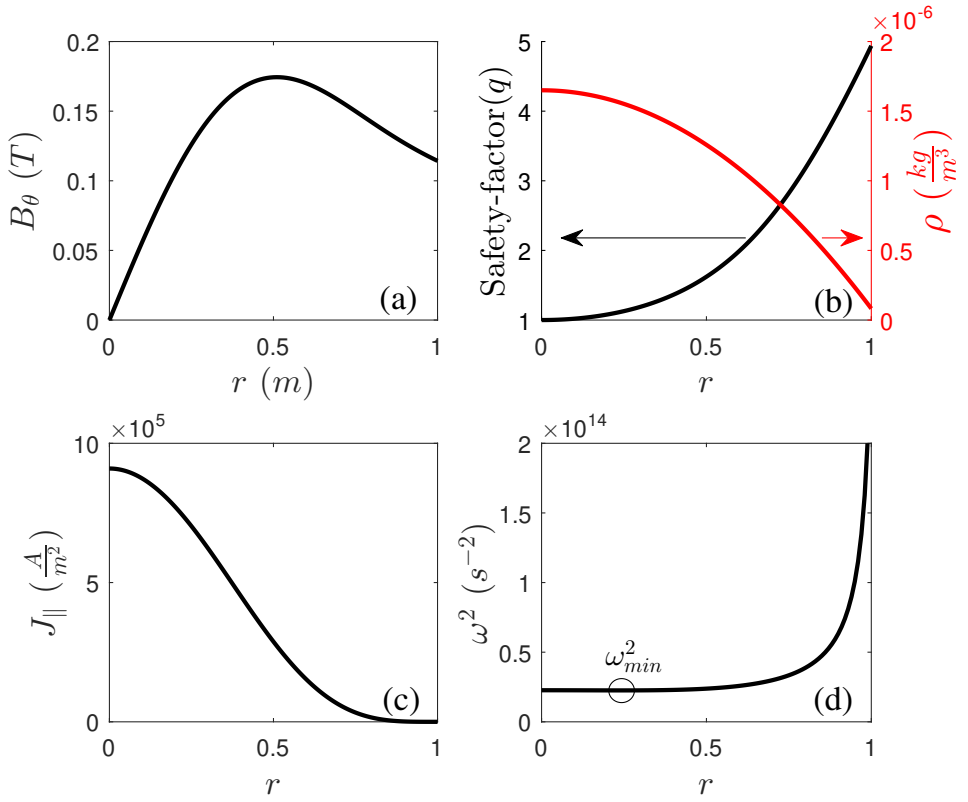

Figure 3.3: MHD equilibrium profiles: (a) the poloidal component of the magnetic field (b) the black and red lines represent the q and the density profiles, respectively (c) the parallel current density and (d) Alfvén continuum for $m = 3$ and $n = 9$.

be sufficient drive for the corresponding mode with respect to a realistic description of EPs distribution. Consequently, we have considered the mode numbers $m = 3$, $n = 9$ for the case of a slowing down distribution of energetic ions presented by

$$F_0 = \frac{n_0 A}{v_\parallel^3 + v_c^3} \exp\left\{\frac{P_\varphi}{\Delta P_\varphi}\right\} \delta\left(P_3 - 0^+\right) \tag{3.62}$$

where n_0 is the density of the fast particles at the center, $A = \frac{3\sqrt{3}v_c^2}{4\pi^2 eBm_i}$ is the normalization constant with v_c being the critical velocity and ΔP_φ the width of F_0 on P_φ. The aforementioned mode numbers correspond to an eigenfrequency of $\omega_{\mathrm{GAE}} = 4.73 \times 10^6 \mathrm{rad\,s^{-1}}$ where the radial wavenumber is 1. The fast ions parameters are chosen to satisfy $\gamma_l \ll \omega_{\mathrm{GAE}}$. By setting $v_c = 2.6 \times 10^6$, $\Delta P_\varphi = 0.47 \times 10^{-20}$ and $n_f = 10\% n_{\mathrm{Bulk}}$, we find the linear growth rate $\gamma_l = 1.13 \times 10^4 \mathrm{s^{-1}}$ for $p = 2$. It is noteworthy that for highly co-passing energetic ions studied in this model, the coupling strength is nonzero for $p = m \pm 1$ (see 3.7.1). Prior to investigating the evolution of the nonlinear structure, the resonance condition Eq. (3.44) should be solved to find the values of action variables, Eq. (3.41), at the resonance and also to track the dynamics of the resonant particles. For a downward trend in frequency chirping, figure 3.4a, b and c illustrate the resonance line for $v_\parallel$, P_1 and P_2 respectively, versus radial position for different frequencies. The conservation of conjugate momenta P_2 and P_3, with the latter being ≈ 0 for deeply passing EPs, allows us to track the dynamics

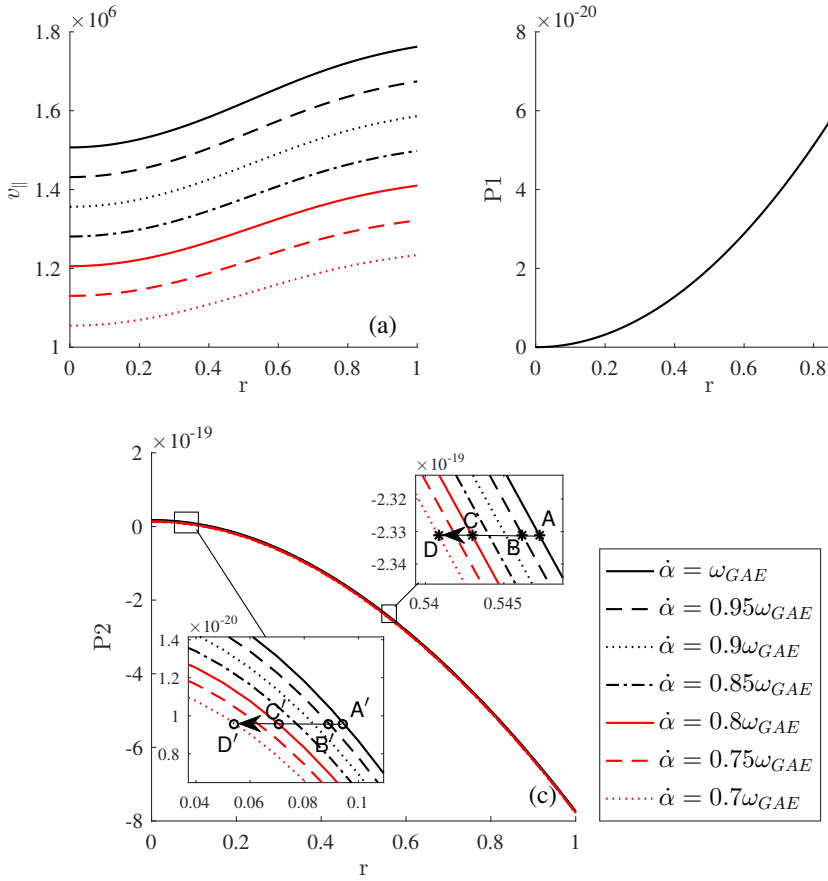

Figure 3.4: Resonance line of $v_{\parallel}$ (a), P_1 (b) and P_2 (c) for different wave frequencies. Points A and A' on (c) represent the initial position of a separatrix that moves to points $\{B, C, D\}$ and $\{B', C', D'\}$, respectively, during frequency chirping while the value of P_2 is preserved.

of EPs and identify whether the motion of nonlinear structures (holes/clumps) in phase–space results in an inward or outward flux of the fast ions in resonance with the chirping GAE. Since P_2 corresponds to an ignorable coordinate, its value must be preserved during the motion of holes/clumps. Therefore, the motion of the corresponding separatrix in the radial direction occurs in a way that the value of P_2 remains the same during chirping. As an example, the group of particles that satisfy the resonance condition at point A on figure 3.4c should move to point D in order to conserve the value of P_2 while satisfying the resonance condition. Therefore, this results in an inward flux of fast ions towards the plasma core during frequency sweeping of the eigenmode.

Figure 3.5 shows the equilibrium phase–space density of EPs as well as the resonance line for four different frequencies. Initially, the value of the total phase-space density inside each separatrix is the same as the equilibrium distribution function. This is illustrated by using circles on the initial resonance line (1) in figure 3.5. As the frequency chirps, the separatrices (phase–space structures) preserve the initial value of the phase-space density during their motion and carry the initially-in-resonance EPs with the mode to new regions in phase-space. Therefore, depending on whether the value of F_0 at these new regions is lower or higher than the value of F_0 at initial resonance i.e. $\delta f > 0$ or $\delta f < 0$ (see

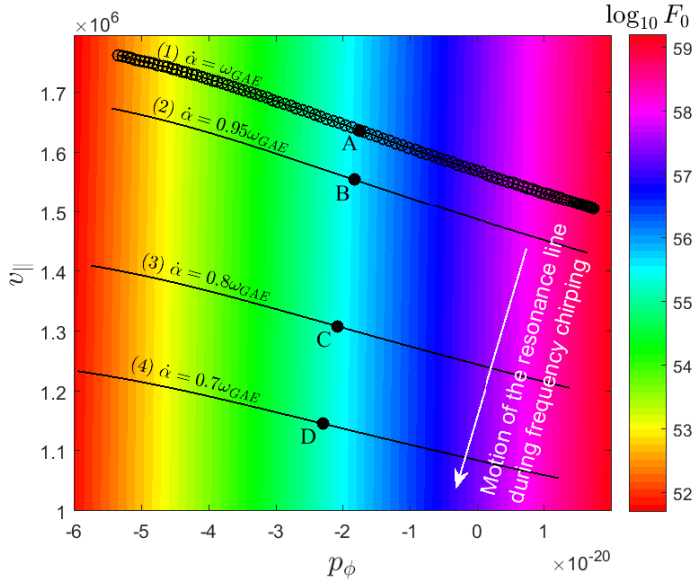

Figure 3.5: The equilibrium phase-space density and the resonance line at different frequencies. The initial resonance line is denoted by unfilled circles implying that the phase–space density of each separatrix is the same as the equilibrium distribution function shown at the background. Points A,B,C and D correspond to the position of the same separatrix on both figure 3.4c and figure 3.5 at each corresponding frequency, e.g. Point B denotes the radial and the phase-space position of the same separatrix on figure 3.4c and figure 3.5, respectively at $\dot{\alpha} = 0.95\omega_{\mathrm{GAE}}$.

Eq. (3.52)), a clump or hole will be developed inside the separatrix. If the separatrices trap new EPs on their way due to the expansion (see figure 3.2) and carry them, the preservation of the phase–space density of the newly trapped EPs should also be taken into account. The separatrix, which is initially located at point A on figure 3.5, will move to points B, C and D at each corresponding frequency. It can be observed that the separatrices move to regions where the value of the ambient equilibrium phase-space density is lower. Therefore, a clump will be developed inside the phase-space structure to preserve the distribution function value inside the separatrix. Figure 3.6 illustrates the total distribution function inside the separatrix at point A which moves down in P_1 to point B as a result of frequency chirping in this model.

Further explanations can be given to identify the phase-space structures as clumps: In this case, the value of $\frac{\partial F_0}{\partial P_1}|_{P_1=P_{1,\mathrm{res}}}$, namely the drive, remains positive for all the separatrices during frequency chirping of the mode. For deeply passing particles, we have

$$X_r = r_0 + \Delta r \cos\theta, \tag{3.63}$$

and using Eqs. (3.24) and (3.41), we find

$$P_{\tilde{\theta}} = \frac{1}{2} e B_0 r_0^2. \tag{3.64}$$

In this case, the separatrices move inward in the radial direction, hence the value of $P_{1,res}$ for each separatrix decreases as the mode chirps down as does the value of the ambient distribution function. This means that in this case, the phase-space structures are clumps.

An upward trend of frequency sweeping in this case will result in an outward flux of

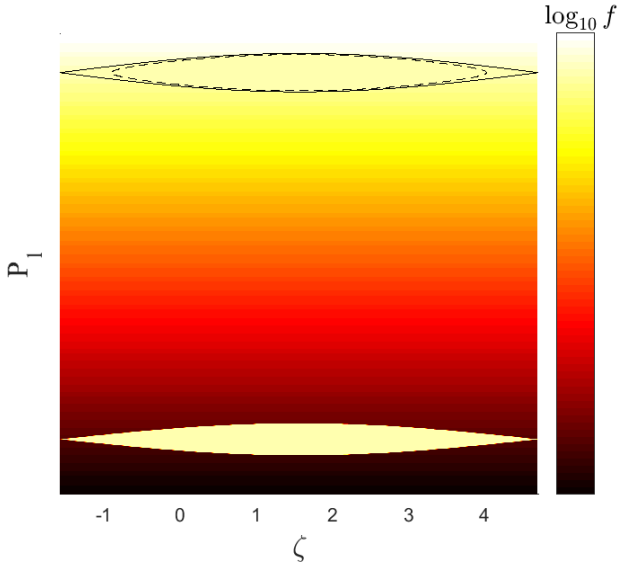

Figure 3.6: Evolution of the phase–space clump. The dashed line represents the adiabatic invariant corresponding to the separatrix at the bottom.

the fast ions towards the first wall and the phase–space coherent structures will be holes. However, it should be taken into consideration that the model remains valid only for eigenmodes subject to weak continuum damping where the linear structure is not mainly identified by the fast particles as opposed to energetic particle modes (EPMs). Therefore, crossing the continuum edge should be avoided during chirping.

3.5.2 chirping rate, structure evolution and adiabaticity validation

For the case of a near threshold instability $|\gamma_l - \gamma_d| \ll \gamma_d \leq \gamma_l$, we choose $\gamma_d = 1.1 \times 10^4 \mathrm{s}^{-1}$ and solve the differential Eq. (3.59) coupled with the integral Eq. (3.11) with the approach mentioned in section 3.4 to determine the nonlinear behavior during long range frequency chirping.

The radial current created by the population of the energetic ions modifies the structure of the MHD eigenmode in the hard nonlinear regime. Figure 3.7 demonstrates the evolution of the radial profile of $\phi(\boldsymbol{r}, t)$ while the frequency of the mode deviates from the initial eigenfrequency. The peak of the initial eigenmode structure, located at the point where the extremum of the Alfvén continuum occurs, will be shifted inward towards the center of the plasma and the mode becomes more localized close to the plasma center. This inward displacement is in compliance with the inward drift of EPs explained above. In addition, it can be observed that the radial profile is broadened as the frequency moves away from the shear Alfvén continuum. As the frequency decreases, the amplitude of the radial profile initially grows and then starts to decrease. It is noteworthy that the amplitude value at $\tilde{\omega} = 1$ represents the saturated amplitude corresponding to the aforementioned linear growth rate. In this model, the axial current resolves a pole in the MHD equations and allows weakly damped GAEs with smooth radial profiles as opposed to highly damped continuum modes with spiky radial structures. However, the eigenfrequency of this GAE lies just below the shear Alfvén continuum and the initial frequency is very close to the value corresponding to the pole in the MHD equations. Therefore, for a fixed frequency change, the mode structure changes more when the frequency change occurs closer to the

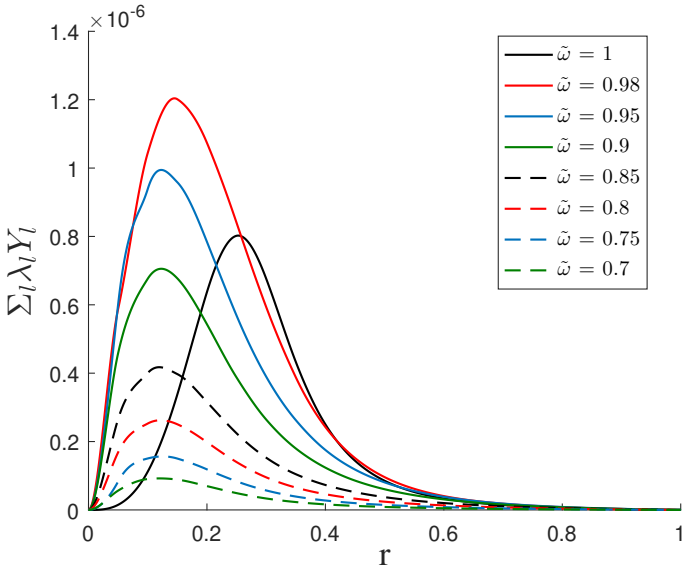

Figure 3.7: Evolution of the radial profile of the GAE during frequency chirping. $\tilde{\omega} = 1$ represents no change in the mode frequency

initial eigenfrequency. This can be investigated using figure 3.7. It has been shown that the radial profile changes more when the frequency changes from $\tilde{\omega} = 1$ to $\tilde{\omega} = 0.98$ as opposed to the case where it changes from $\tilde{\omega} = 0.98$ to $\tilde{\omega} = 0.95$.

The change in the radial component of various plasma quantities during chirping can also be analyzed using $\Phi(\boldsymbol{r}, t)$. The displacement vector reads,

$$\boldsymbol{\xi} = -\frac{1}{B_0^2}\left(\tilde{\boldsymbol{A}}_\perp \times \boldsymbol{B}_0\right). \tag{3.65}$$

Using Eq. (3.7), we have

$$\boldsymbol{\xi} B_0 = \frac{\partial \Phi(\boldsymbol{r}, t)}{\partial r}\hat{\boldsymbol{e}}_\perp - i\frac{m}{r}\left(\Phi(r, t)\exp\{i\left(m\theta + n\varphi - \alpha(t)\right)\} - c.c\right)\hat{\boldsymbol{e}}_r, \tag{3.66}$$

where the poloidal component of the equilibrium magnetic field has been neglected compared to the toroidal component. Eq. (3.66) clearly demonstrates the relation between radial component of the displacement vector and the radial mode structure plotted in figure 3.7. Figure 3.8 illustrates the rate at which the frequency chirps. It is shown that the square root dependency holds for the very early stages of frequency chirping.

The adiabatic condition represented in subsection 3.3.4.2, which is implemented for the formalism, needs to be validated if it remains satisfied [34, 97, 99]. Eq. (3.50) can be written as

$$K = \frac{1}{2}\frac{\partial^2 H_0}{\partial P_1^2}(\Pi, P_2, P_3)\left[P_1 - \Pi\right]^2 - \sum_l 2|\lambda_l V_{p,n,l}|\cos(\zeta + \sigma), \tag{3.67}$$

where $\sigma = \tan^{-1}\frac{\Im(\lambda_l V_{p,n,l})}{\Re(\lambda_l V_{p,n,l})}$ and for the case of EPs with highly passing orbit types, we have $\sigma = \pm\frac{\pi}{2}$. It is worth noting that in this case we have $\Re(\lambda_l V_{p,n,l}) = 0$. Using canonical

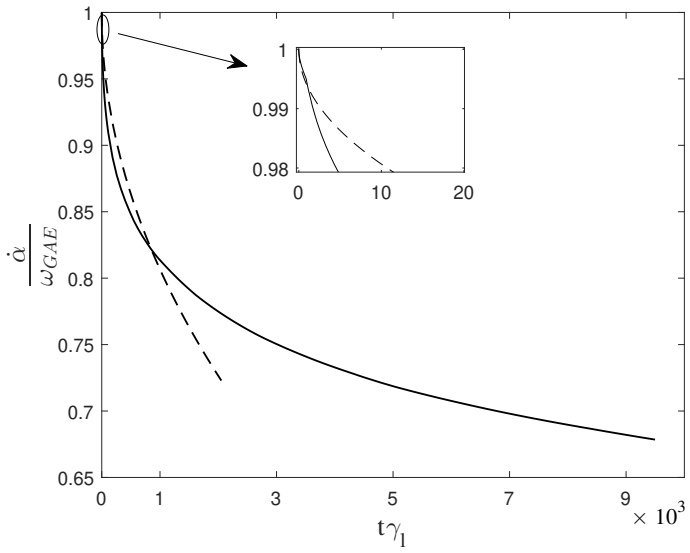

Figure 3.8: The solid line represents the time evolution of the mode frequency in the hard nonlinear regime and the dashed line, plotted for comparison, corresponds to the square root dependency.

equations of motion, one finds

$$\dot{P}_1 = -\sum_l 2|\lambda_l V_{p,n,l}| \cos(\zeta + \sigma), \tag{3.68a}$$

$$\dot{\zeta} = \frac{\partial^2 H_0}{\partial P_1^2} [P_1 - \Pi]^2 . \tag{3.68b}$$

The motion of the deeply trapped EPs inside the separatrix satisfies the pendulum equation

$$\frac{\mathrm{d}^2}{\mathrm{d}t^2}(\zeta + \sigma) = -\frac{\partial^2 H_0}{\partial P_1^2} \sum_l 2|\lambda_l V_{p,n,l}| \sin(\zeta + \sigma), \tag{3.69}$$

where we have used $\sin(\zeta + \sigma) \approx (\zeta + \sigma)$ at the center of the separatrix, the so-called O-point. As shown in figure 3.2, we have $\sigma = -\frac{\pi}{2}$ for the results reported in this paper and the O-point is located at $\zeta = \frac{\pi}{2}$. Subsequently, the bounce frequency of the deeply trapped EPs inside the separatrix is

$$\omega_b = \sqrt{2\frac{\partial^2 H_0}{\partial P_1^2} \sum_l |\lambda_l V_{p,n,l}|}. \tag{3.70}$$

The RHS of the adiabatic condition $1 \gg \frac{\left|\frac{\mathrm{d}\omega_b}{\mathrm{d}t}\right|}{\omega_b^2}$ is plotted in figure 3.9 for separatrices with different initial radial positions. Consistent with the previousely reported results [56, 99], we also observe that the adiabatic condition is never formally satisfied at the very early stage of chirping. However, it is shown that once the adiabatic condition is satisfied, it remains valid for later evolution of the mode. In addition, it was discussed in [56] that the assumption of $\gamma_l \ll \omega_{\mathrm{GAE}}$ implies that the period during which the adiabatic limit is not satisfied is very short.

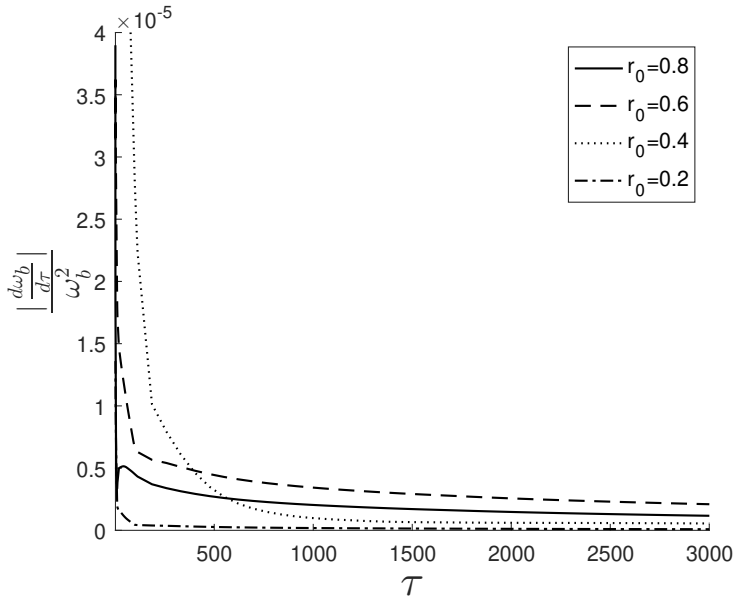

Figure 3.9: The evolution of time rate of change in the bounce frequency divided by squared value of the bounce frequency for different initial radial positions (r_0) of the separatrices i.e. different values of $P_{1,res}$ before chirping.

3.6 Concluding remarks

A theoretical description has been developed to study the hard nonlinear evolution of a Global Alfvén Eigenmode (GAE) in resonance with co-passing energetic particles (EPs) in an NBI scenario during the adiabatic frequency chirping behavior of the mode. Constructing appropriate constants of motion allows us to track the dynamics of EPs as the frequency of the mode changes. In addition, a finite element method using cubic Hermite base functions, has been implemented to represent the radial profile of the GAE. This enables the derivation of an analytic expression for the nonlinear radial structure of the mode by varying the total Lagrangian of the system with respect to the weight of the finite elements. Hence, the radial structure can be updated as the frequency deviates from the initial MHD eigenfrequency. During chirping, the possibility of both the shrinkage and the expansion of a phase-space structure (a hole/clump) has been taken into account. The phase-space structures, identified to be clumps, move in order to extract energy from the EPs distribution function and deposit it into the bulk plasma. This energy balance is used to derive an expression for the time rate of the change in the frequency. The adiabatic condition is also evaluated which remains valid once it is satisfied.

Energetic-ion parameters, such as orbit width or pressure, can cause a shift and a broadening in the radial profile of the mode [100]. In addition, for the case of a near threshold instability, we have shown how the deviation of the frequency from the initial eigenfrequency can also result in shifting the peak location of the radial profile and also radial broadening during the hard nonlinear stage. For the case presented in this manuscript, the slowing down EPs move radially inward as clumps when the frequency chirps downward. The orbit width of the EPs follows

$$\Delta r = \frac{q m_i v_\parallel}{eB}, \tag{3.71}$$

where q is the safety factor, m_i is the ion mass, $v_\parallel$ is the velocity of the EPs parallel to the equilibrium magnetic field, e is the electron charge and B is the magnetic field. The range of orbit widths from the plasma center to the boundary is 0.01-0.08m. This corresponds to an energy range of 23-32 kev for the EPs initially in resonance with the mode.

With respect to applications to actual geometries, the presented formalism can be applied to shear Alfvén eigenmodes without or with very weak effect of mode coupling e.g. GAEs, in an NBI scenario. The calculation of the EPs dynamics is done for the deeply passing particles where the coupling strength is nonzero for only two values of m, i.e. $m \pm 1$. A comprehensive description of the problem is aimed in our research plan. This includes

- calculation of action-angle variables for more general EP orbits and
- Adding the effect of toroidal coupling for the mode which does not require any fundamental difficulties as all the main ingredients are already introduced in this work. It should be noted that the effect of toroidicity on the EPs dynamics is already included in the formalism, and
- allowing the EPs nonlinearity to update all the components of the mode structure simultaneously, namely poloidal, toroidal and radial using the general formalism presented in section 3.2.

In this manuscript, we have taken a short-cut, associated with some assumptions, to the above roadmap to build the presented model along the way and produce the core of the full problem which requires more effort but is feasible. To our knowledge, this is the first attemp to present a technique for the evolution of the radial structure in the nonlinear regime and this technique can be generalised which requires heavier computations. A further study is to allow the frequency to cross the continuum edge and behave as realistically as possible inside the continuum.

Acknowledgments

This work was funded by the Australian Research Council through Grant No. DP140100790. The first author is very grateful to the Australian Nuclear Science and Technology Organisation (ANSTO), NSW, Australia and the National Institute for Fusion Sciences (NIFS), Japan and Festival de Théorie, France for travel supports to present this work.

3.7 Appendix

3.7.1 Calculation of the coupling strength

Using Eq. (3.31) and the resonance condition ($p\dot{\tilde{\theta}} = \dot{\alpha}(t) + n\dot{\tilde{\varphi}}$), Eq. (3.36) can be written as

$$V_{p,n,l} = \frac{1}{2\pi}\int_0^{2\pi} ie\left[p\dot{\tilde{\theta}} - \frac{m\dot{\varphi}}{q(X_r)} + n\dot{\tilde{\theta}}\frac{\partial\Delta\varphi}{\partial\tilde{\theta}}\right] Y_l(X_r)\exp\left\{im\theta - in\Delta\varphi - ip\tilde{\theta}\right\}d\tilde{\theta}. \quad (3.72)$$

The integral over the first term of the integrant can be performed using integration by parts. Therefore,

$$V_{p,n,l} = \frac{1}{2\pi}\int_0^{2\pi} e\left[\dot{\tilde{\theta}}\frac{\partial X_r}{\partial\tilde{\theta}}\frac{\mathrm{d}Y_l(X_r)}{\mathrm{d}r} + im\left(\dot{\theta} - \frac{\dot{\varphi}}{q(X_r)}\right)Y_l(X_r)\right]\exp\left\{im\theta - in\Delta\varphi - ip\tilde{\theta}\right\}d\tilde{\theta} \quad (3.73)$$

Eqs. (3.24) and (3.30) can be used to find

$$\dot{X}_r = \dot{\tilde{\theta}}\frac{\partial X_r}{\partial\tilde{\theta}} = -\left[\frac{m_i v_\parallel^2}{R} + \frac{\mu B_0}{R_0}\right]\sin\theta\frac{1}{eB_0}. \quad (3.74)$$

Simple implementation of Eqs. (3.31) and (3.32) gives

$$\dot{\theta} - \frac{\dot{\varphi}}{q(X_r)} = -\left[\frac{m_i v_\parallel^2}{R} + \frac{\mu B_0}{R_0}\right]\cos\theta\frac{1}{eB_0 r_0}. \quad (3.75)$$

Under the small orbit width assumption, $V_{p,n,l}$ reads

$$V_{p,n,l} = -\frac{1}{2\pi}\int_0^{2\pi}\left[\frac{m_i v_\parallel^2}{RB_0} + \frac{\mu}{R_0}\right]\left[\frac{\mathrm{d}Y_l(r_0)}{\mathrm{d}r}\sin\theta + \frac{imY_l(r_0)}{r_0}\cos\theta\right]\exp\left\{im\theta - in\Delta\varphi - ip\tilde{\theta}\right\}d\tilde{\theta} \quad (3.76)$$

For deeply passing EPs inside the equilibrium field, one can neglect the infinitesimal perpendicular velocity of the particles to the magnetic field and set $\mu \approx 0$. In this limit, $v_\parallel$ becomes a constant of motion and we can set $\theta \approx \tilde{\theta}$ and $\Delta\varphi = cte$. Using Euler's formula and the orthogonality of trigonometric functions, one finds

$$V_{p,n,l} = \frac{-im_i v_\parallel^2}{2B_0R_0}\left[\pm Y_l' + \frac{m}{r_0}Y_l\right], p = (m \mp 1), \quad (3.77)$$

where we have set $\Delta\varphi = 0$. Non-zero values of $\Delta\varphi$ results in a shift of the separatrix in phase–space compared to the existing model.

Chapter 4

Theoretical description of chirping waves using phase-space waterbags

Abstract

The guiding centre dynamics of fast particles can alter the behaviour of energetic particle driven modes with chirping frequencies. In this paper, the applicability of an earlier trapped/passing locus model [H. Hezaveh et al 2017 Nucl. Fusion 57 126010] has been extended to regimes where the wave trapping region can expand and trap ambient particles. This extension allows the study of waves with up-ward and down-ward frequency chirping across the full range of energetic particle orbits. Under the adiabatic approximation, the phase-space of energetic particles is analysed by a Lagrangian contour approach where the islands are discretised using phase-space waterbags. In order to resolve the dynamics during the fast formation of phase-space islands and find an appropriate initialisation for the system, full-scale modelling is implemented using the bump-on-tail (BOT) code. In addition to investigating the evolution of chirping waves with deepening potentials in a single resonance, we choose specific pitch-angle ranges in which higher resonances can have a relatively considerable contribution to the wave-particle interaction. Hence, the model is also solved in a double-resonance scenario where we report on the significant modifications to the behaviour of the chirping waves due to the 2^{nd} resonance. The model presented in this paper gives a comprehensive 1D paradigm of long range frequency chirping signals observed in experiments with both up-ward and down-ward chirping and multiple resonances.

4.1 Introduction

The confinement of energetic particles (EPs), which affects the operation of a fusion device, can be markedly modified by their interaction with weakly damped plasma waves [12, 14, 101]. In case of inverse Landau damping in a bump-on-tail model (BOT), the nonlinear saturation of the eigenmode [102–104] due to particle trapping aligns with flattening of the distribution function of energetic particles [16]. During this process, side-band oscillations emerge and if the system provides these oscillations with weak damping, they may develop into signals with chirping frequencies [44]. This phenomenon is governed by the fast formation of phase-space islands i.e. the holes and clumps, in the generalised phase-space of energetic particles [35]. Once formed, these structures evolve slowly in time hence the adiabatic invariant of the EPs trapped in the chirping mode is conserved.

In realistic geometries and for long deviations of the frequency from the initial eigenfrequency [46, 105, 106], the EPs can be carried by the wave potential on slices of the phase-space which results in a change in particles toroidal angular momentum [47, 94]. This is in conjunction with a change in the number of the flux surface on which the particles lie. Consequently, an inward or outward convective transport of the EPs occur leading to unwanted confinement losses. Therefore, it is essential to perform a detailed study of holes and clumps shape as well as EPs dynamics to identify and control the hard nonlinear evolution of an EP driven mode. It is worth mentioning that formation of holes/clumps structures has also been recently demonstrated in Ref. [107] for energetic particle-induced geodesic acoustic modes (EGAMs).

For highly passing EPs, the theoretical picture of long range adiabatic frequency chirping, using a Langmuir wave as an example, was first developed by Breizman [53]. At each frequency, the nonlinear wave equation is represented as the long-term solution of a Vlasov-Poisson system, hence called a BGK-type mode [68]. Subsequently, the impact of EPs collisions, namely Krook, drag and diffusion was studied by Nyqvist *et al* in Refs. [54] and [55]. The latter allows the separatrix to expand and trap new EPs. Hezaveh *et al* [56] studied the impact of energetic particle orbit topologies on the long range frequency sweeping of a BGK-type mode. This model shows how the inclusion of trapped particle orbits as well as barely passing types can considerably alter the behaviour of a nonlinear chirping wave. For the range of magnetically trapped EPs and a constant trend i.e. up-ward or down-ward in frequency chirping, it has been shown that the trapping region of the BGK mode may initially grow and then shrink (see fig.6 in [56]). In the topic of long range adiabatic frequency chirping, this model is comprehensive from the perspective of capturing a range of typical guiding centre orbits. However, the assumption of a flat-top phase-space density across the trapping region (separatrix) restricts the applicability of this model only to the regions where the trapping region of the perturbed mode shrinks and particle trapping due to the expansion in phase-space is avoided. In this work, we aim to relax the flat-top assumption of Ref. [56] and extend the trapped-passing locus model to cases where the wave potential can deepen and trap new ambient particles as well as shrink leading to a loss of trapped particles. Consequently, this allows us to explore the adiabatic evolution of the chirping wave over the full range of EPs orbits for both up-chirping and down-chirping BGK modes.

In Ref. [55], the adiabatic evolution of phase-space holes has been studied in a system where these structures are initialised somewhat off the linear resonance using a given initial profile and a grid-based numerical method. The claim that holes and clumps form off the initial resonance consists with theory [44] and numerical simulations [43]. Nevertheless, the initial profile of the holes is chosen such that the amplitude of the chirping wave is a smooth function of time. This may not necessarily correspond to a proper initial shape for the just-formed phase-space structures. In this regard, a more comprehensive approach is to apply full-scale modelling to the fast formation stage of these structures to find their phase-space profile prior to the adiabatic evolution. Accordingly, we also perform simulations using the BOT code, developed by Lilley [43], and initialise the phase-space using the simulation data. Subsequently, we resolve the EPs response to the chirping mode using a non-perturbative approach under the adiabatic ordering. For a growing separatrix in phase-space, we implement a Lagrangian mesh approach i.e. a waterbag model [108] where each contour of constant phase-space density is a waterbag associated with the EPs adiabatic invariants. This enables capturing the particle trapping effect in phase-space and implies that as the separatrix expands and moves due to frequency chirping, the

phase-space density of the trapped EPs is set to the ambient distribution at the trapping point.

In section 4.2, the model is introduced and the main equations governing the shape of the BGK-type chirping mode and the frequency chirping rate are derived. Simulation data of the BOT code is analysed in section 4.3 from which the initial shape of the coherent phase-space islands is established. The numerical scheme implemented to solve the model equations is briefly given in section 4.4. In section 4.5, a single-resonance chirping wave with deepening potentials is studied. Therein, specific ranges of fast particles pitch-angles are introduced in which higher particle resonances, in this case 2^{nd}, can have a non-negligible contribution to the linear growth rate (γ_l) of the wave-particle interaction. Hence, we also report on the impact of higher resonances on the evolution of chirping waves for both up-chirping and down-chirping cases. This is achieved by comparing the evolution of the plane wave potential and the frequency chirping rate for a single and double resonance interaction. We also evaluate the validity of the adiabatic limit for each reported case. Finally, section 4.6 is a summary. It is noteworthy that the formalism and the notation presented throughout the manuscript are based on the previously reported model of Ref. [56] to which the reader is referred for a more detailed derivation.

4.2 Theoretical framework

We consider the bump-on-tail instability problem of a plasma wave in which the energetic electrons drive the mode marginally unstable until it saturates due to the nonlinear coarse-graining of the electron distribution function in phase-space. Then, if the mode is subject to weak damping into the bulk plasma with a rate denoted by γ_d, the sideband oscillations are excited and evolve into chirping modes. It is remarkable to mention that fast particles collisions can change the nonlinear evolution of the mode which are neglected here. Hence, the physical picture is a BGK mode with a chirping frequency in a time scale (t_{slow}) much smaller than the bouncing time scale (t_{fast}) of electrons trapped in the mode. Therefore, we have

$$\left[\left|\frac{\mathrm{d}\omega_b}{\mathrm{d}t}\right|, \left|\frac{\mathrm{d}\omega}{\mathrm{d}t}\right|\right] \ll \omega_b^2, \tag{4.1}$$

where ω_b is the bounce frequency of the electrons trapped in the wave and ω is the wave frequency. We consider $\gamma_l \ll \omega_{\text{pe}}$ which implies the separatrix width is much smaller than the characteristic width of the phase-space density and the near-threshold unstable resonance is isolated i.e. overlap of resonances leading to diffusive transport and wave-wave coupling are ignored.

The equilibrium picture of fast electrons dynamics is built by applying a nonuniform static magnetic field. Fast electrons bounce or transit along the field lines. This resembles trapped and passing particles along the field lines in 3D geometries, with the effect of drift orbit width and toroidal precession ignored. The Hamiltonian governing the equilibrium guiding-centre motion of electrons, denoted by H_{eq}, can be derived by applying the Legendre transformation to the gyro-averaged Littlejohn Lagrangian [73]. This gives

$$H_{\text{eq},\alpha} = \frac{p_z^2}{2m_e} - \mu B_0 \cos(k_{\text{eq}} z) + \mu B_c, \tag{4.2}$$

where α is a label that denotes the orbit type of the fast electrons motion in the magnetic field based on their pitch angle: throughout the paper, $\alpha = \mathbf{T}$ and $\alpha = \mathbf{P}$ represent the

trapped and passing electrons in the equilibrium field, respectively, p_z is the momentum of energetic electrons aligned with the field, m_e is the electron mass, μ is the magnetic moment and $k_{\rm eq}$ denotes the spatial periodicity of the field. The constants B_0 and B_c are chosen such that the wave frequency $\omega_{\rm pe}$ is low compared to the ion cyclotron oscillations and its wavelength is large compared to the electron Larmor radius. Also, it is assumed that all the particles have a single value of the magnetic moment μ. The 1D equilibrium Hamiltonian given by (4.2) resembles that of a large aspect ratio tokamak i.e. $\epsilon = \frac{r}{R_0} \ll 1$, where $\epsilon = \frac{B_0}{B_c}$ is the inverse aspect ratio with r and R_0 being the minor and major radius, respectively, and higher order terms in the expansion of the magnetic field in $\epsilon \cos(kz)$ are neglected. A canonical transformation to action-angle variables $(J_\alpha, \theta_\alpha)$ enables a description of the unperturbed motion using $H_{{\rm eq},\alpha}(J_\alpha)$ independent of the corresponding coordinate (θ) which scales linearly with time. Using $\dot{\theta} = \frac{\partial H_{{\rm eq},\alpha}}{\partial J_\alpha}$, one can investigate the equilibrium bounce or transit frequency of the fast electrons motion depicted in figure 4.1. The energy parameter,

$$\zeta = \frac{E + \mu(B_0 - B_c)}{2\mu B_0} \tag{4.3}$$

with E being the equilibrium energy, specifies the orbit type of each fast electron.

In this model, it is assumed that the bulk plasma responds linearly to the field (U) and therefore the corresponding response is found by implementing a perturbative approach to the fluid description. In the presence of the perturbations, the total Hamiltonian of the fast electrons reads

$$H_{{\rm total},\alpha} = H_{{\rm eq},\alpha} + U. \tag{4.4}$$

In principle, one should implement the Liouville's theorem or the Vlasov equation $\{f, H\} = 0$ and either follow the fast electrons trajectories corresponding to the above Hamiltonian i.e. a Lagrangian point approach, or apply a fixed grid discretisation to the phase-space i.e. an Eulerian approach, in order to find the perturbed phase-space density of energetic electrons. Nevertheless, we focus on two separate stages of the wave evolution, namely the linear stage and the nonlinear long range chirping stage. In the former, we resolve the perturbed phase-space density of fast electrons using a linear perturbative analysis while the latter benefits from the Liouville theorem and the adiabatic ordering which enables a Lagrangian contour approach in fast electrons phase-space and construct a non-

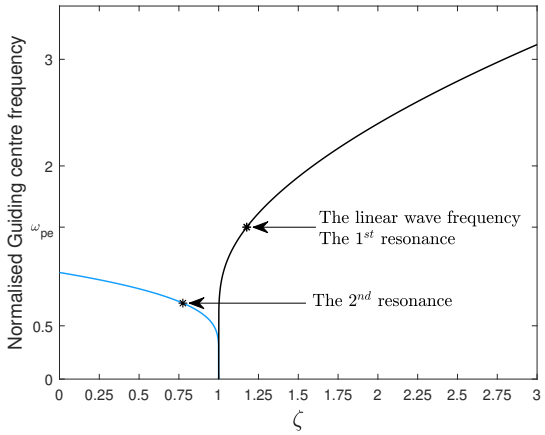

Figure 4.1: Guiding centre frequency vs. the energy parameter for the fast electrons equilibrium motion.

perturbative approach to find the perturbed density of fast electrons. Here, f is the total distribution function of fast electrons given by $f_\alpha = F_{\mathrm{eq},\alpha} + \tilde{f}_\alpha$, with $F_{\mathrm{eq},\alpha}$ and $\tilde{f}_\alpha$ being the initial and the perturbed parts, respectively. For simplicity, we consider $F_{\mathrm{eq},\alpha}$ to be linear in the energy parameter i.e. $F_{\mathrm{eq},\alpha} = c\zeta_\alpha$, where c is a constant.

We firstly analyse the linear evolution of the plasma wave. This is achieved by finding analytic expressions for the linear response of the bulk plasma in a single-fluid model and of the fast electrons using the linearised Vlasov equation in a kinetic description. Then, the total Hamiltonian governing the fast electrons dynamics during the adiabatic chirping is described. Hence, we implement a kinetic description for the energetic electrons in the framework of the adiabatic theory and find the corresponding nonlinear contribution. Subsequently, the Poisson equation is fed with the perturbed density of both the fluid and the fast electrons to solve for the nonlinear field of a sideband of the plasma wave during the frequency chirping. At each frequency, the wave potential is a long-term nonlinear solution of the Vlasov-Poisson system, hence a BGK-type wave.

4.2.1 Linear evolution of the plasma wave

For a linear analysis, a perturbative approach is used to find the perturbed density of the bulk and the energetic electrons. Therefore, we represent the wave potential energy (U) and the perturbed distribution function ($\tilde{f}_\alpha$) as

$$\begin{aligned} U &= \sum_{n=1}^{\infty} \frac{e\phi_n}{2} \exp\left[in\left(k_p z - \omega t\right)\right] + c.c \\ &= \sum_{n=1}^{\infty}\sum_{p=-\infty}^{\infty} \frac{e\phi_n}{2} V_{\alpha,n,p}\left(J_\alpha\right) \exp\left[i\left(p\theta - n\omega t\right)\right] + c.c \end{aligned} \tag{4.5}$$

and

$$\tilde{f}_\alpha = \sum_{n=1}^{\infty}\sum_{p=-\infty}^{\infty} \hat{f}_{\alpha,n,p}\left(J_\alpha\right) \exp\left[i\left(p\theta - n\omega t\right)\right] + c.c, \tag{4.6}$$

where we have expanded $\exp\{in\left(k_p z - \omega t\right)\}$ in action-angle variables of the unperturbed motion i.e.

$$\exp\left[in\left(k_p z - \omega t\right)\right] = \sum_{p=-\infty}^{\infty} V_{n,p}(J) \exp\left[i\left(p\theta - n\omega t\right)\right], \tag{4.7}$$

$\omega = \omega_r + i\gamma_l$ is the complex frequency, k_p the wave-number of the plasma mode, $V_{\alpha,n,p}\left(J_\alpha\right)$ is the orbit averaged mode amplitude which specifies the coupling strength and plays the same role as the matrix elements introduced in Ref. [30, 32].

4.2.1.1 The bulk plasma response - MHD

For an isotropic distribution and a uniform density of the bulk plasma along the equilibrium field, we focus on the perturbations along the field lines in which case the equilibrium field does not interact with the bulk plasma. The equation of motion and the linearised

continuity equation read

$$\frac{\partial V_c}{\partial t} = -\frac{1}{m_e}\frac{\partial U}{\partial z} - \nu V_c, \tag{4.8a}$$

$$\frac{\partial \delta n_c}{\partial t} = -n_c \frac{\partial V_c}{\partial z}, \tag{4.8b}$$

where U is the energy of the electrostatic mode, ϵ_0 is the permittivity of free space, $\nu = 2\gamma_d$ is the Krook collision frequency of the cold electrons, V_c is the flow velocity of the cold electrons and n_c and δn_c are the unperturbed and perturbed density of the cold electrons, respectively. For a linear response, we consider n=1 and substitute Eq. (4.5) into Eq. (4.8a) to find V_c. Next, Eq. (4.8b) can be implemented to find

$$V_c = \frac{k_p U}{\omega m_e}, \tag{4.9a}$$

$$\delta n_c = \frac{k_p^2 n_c U}{m_e \omega^2}. \tag{4.9b}$$

4.2.1.2 Energetic electrons response - Kinetic description

To first order in perturbations ($n = 1$), the fast electron population responds linearly and one can find an analytic perturbative solution,

$$\hat{f}_{\alpha,n=1,p} = \frac{pe\phi_{n=1} V_{\alpha,n=1,p}\left(J_\alpha\right) \frac{\partial F_{\mathrm{eq}}(J_\alpha)}{\partial J_\alpha}}{2\left(p\Omega_\alpha - \omega\right)}, \tag{4.10}$$

to the linearised Vlasov equation, from which one can find the resonance condition $\omega_r = p\Omega_\alpha$, which if satisfied, fast electrons can resonate with the mode. Provided that the mode has a non-zero component of the electric field aligned with the particles guiding centre trajectories, electrons will exchange energy with the mode. Here, $\omega_r \approx \omega_{\mathrm{pe}}$ and p is an integer denoting the resonance number. More precisely, p is the number of the Fourier coefficient as a result of expanding the wave equation (4.13) in AA variable (θ_α) of the equilibrium motion.

The linear perturbative responses of both the bulk plasma and the energetic electrons, represented in Eqs. (4.9b) and (4.10), can be substituted in the Poisson equation, given by

$$\frac{\epsilon_0}{e}\frac{\partial^2 U}{\partial z^2} = -e\left[\sum_\alpha \int \tilde{f}_\alpha dv + \delta n_c\right], \tag{4.11}$$

to find the linear dispersion relation and subsequently the linear growth rate of the initial plasma mode as

$$\gamma_l = \frac{\omega_{\mathrm{pe}} \pi e^2}{2\epsilon_0 k_p m_e} \sum_\alpha \sum_p \left[\frac{\partial F_{\mathrm{eq},\alpha}}{\partial \zeta_\alpha} V_{\alpha,n=1,p}^2 \left|\frac{\mathrm{d}\Omega_\alpha}{\mathrm{d}\zeta_\alpha}\right|^{-1}_{\Omega_\alpha(J_\alpha)=\frac{\omega_{\mathrm{pe}}}{p}}\right]. \tag{4.12}$$

In the next part, we find the perturbed density of fast electrons during the evolution of the chirping wave and construct the nonlinear equation of the wave potential amplitude.

4.2.2 Chirping waves

For a dispersion relation of the form $\omega = \omega_{\mathrm{pe}}$ and in a non-perturbative approach subject to the adiabatic limit where the mode evolves slowly, we represent the BGK-type mode with a chirping frequency by

$$U[z,t] = \sum_n A_n(t) \cos\left[n\left(k_p z - \phi\left(t\right)\right)\right], \tag{4.13}$$

where $\phi(t) = \int_0^t \omega(t')dt'$. The wave oscillates on a fast time scale on the order of $\omega_{\mathrm{pe}}^{-1}$ whereas its envelope A_n, as the Fourier coefficient of the n-th harmonic, evolves on a slow time scale i.e.

$$\frac{\mathrm{d}\ln A_n}{\mathrm{d}t} \ll \dot{\phi}\left(t\right). \tag{4.14}$$

It is noteworthy that for dispersion relations of the form $\omega = ck_p$, where c is a constant, Eq. (4.13) represents a sum over linear modes and subsequently alternative discretisation methods should be used.

The nonlinear dynamics of the fast electrons can be described in a frame that moves with the fast time scale of the wave but remains stationary with regards to the frequency chirping time scale. This leaves us with a time-dependent Hamiltonian that evolves adiabatically in time. Using (4.4) and (4.13), this time-dependent Hamiltonian is written as

$$\begin{aligned} H_{\mathrm{total},\alpha} = \frac{1}{2}\left.\frac{\partial^2 H_{0,\alpha}}{\partial \tilde{J}_\alpha^2}\right|_{\tilde{J}_\alpha = \tilde{J}_{\mathrm{res},\alpha}(t)} \left(\tilde{J}_\alpha - \tilde{J}_{\mathrm{res},\alpha}\left(t\right)\right)^2 \\ + \frac{1}{2}\sum_n A_n\left(t\right) V_{\alpha,n,n} \exp\left(in\tilde{\theta}\right) + c.c, \end{aligned} \tag{4.15}$$

where a canonical transformation as

$$\tilde{\theta}_l = l\theta - \phi\left(t\right), \tag{4.16a}$$

$$\tilde{J}_\alpha = \frac{J_\alpha}{l}, \tag{4.16b}$$

is implemented to cancel the fast time scale dependency from the Hamiltonian, the wave potential energy (U) of Eq. (4.13) has been Fourier decomposed in AA variables of the unperturbed motion with $V_{\alpha,n,p}$ denoting the Fourier coefficients, p is a label that denotes the resonance number for the linear perturbations (n=1) whereas in the nonlinear case, $l = \frac{p}{n}$ identifies the resonance number. Eqs. (4.16a) and (4.16b) are evaluated at a particular $\phi(t)$ in time and thus is a transformation to an inertial frame. The above Hamiltonian is expanded around the middle of the chirping wave trapping region (separatrix) specified by $\tilde{J}_{\mathrm{res},\alpha}$ and assumes infinitesimal detuning for the energetic electrons bouncing in the trapping region of the wave, $V \approx V(\tilde{J}_{\mathrm{res}})$.

For such a system, the lowest order term corresponding to the expansion of the adiabatic invariant in the small parameter β, as the proportion of the bounce period of the electrons trapped in the chirping wave to the slow time scale of the mode evolution), is commonly taken to be the action [109, 110], which reads

$$I = \frac{1}{2\pi}\int \tilde{J} d\tilde{\theta}, \tag{4.17}$$

where the integration is performed from 0 to 2π over the angle variable. The above Hamiltonian (4.15), contains the fictitious force acting on the trapped electrons in the wave potential during the frequency chirping. This force is proportional to the rate at which the frequency chirps. In this model, we have invoked the adiabatic ordering (4.1) to neglect this term when calculating I for a slowly chirping wave. The same assumption has been implemented in the models of Refs. [53, 54, 56]. An alternative way to look at this assumption is to use a different canonical transformation to a non-inertial frame that is exactly moving with the chirping wave, as the one implemented in Ref. [94]. In this case, the term corresponding to the fictitious force, proportional to $\frac{\mathrm{d}\omega}{\mathrm{d}t}$, will explicitly appear in the Hamiltonian. One can readily observe that under the adiabatic ordering given by (4.1), this term can be neglected since it is much smaller than the other terms (proportional to ω_b^2) in the Hamiltonian.

Conservation of the adiabatic invariant implies that the corresponding phase-space area occupied by each adiabatic invariant is conserved. This means that in a discretised picture, the phase-space area between adiabatic invariants, denoted by A_i is preserved as the wave chirps. Figure 4.2 shows the phase-space of an expanded separatrix. The unshaded area surrounded by the dashed curve in the middle of the separatrix corresponds to the initial separatrix i.e. the shape of phase-space structures just after formation and prior to the adiabatic evolution. Each shaded region (A_i) is the area between two adjacent adiabatic invariants (I_i, I_{i+1}). In addition, in the absence of collisions, the number of electrons (N_i) in the area A_i remains fixed during the frequency chirping. The integral form of the Liouville theorem reads

$$\int_{I_i}^{I_{i+1}} f_i dA_i = N_i = \int_{I_i}^{I_{i+1}} f_i' dA_i' \tag{4.18}$$

where f_i is the distribution function of electrons in A_i and the primes denote the values after the motion of an island in phase-space during frequency chirping. Under the adiabatic ordering and taking an infinitesimal width for A_i by choosing small time steps, the fast bounce frequency of the trapped electrons in the BGK mode allows one to assume f_i to

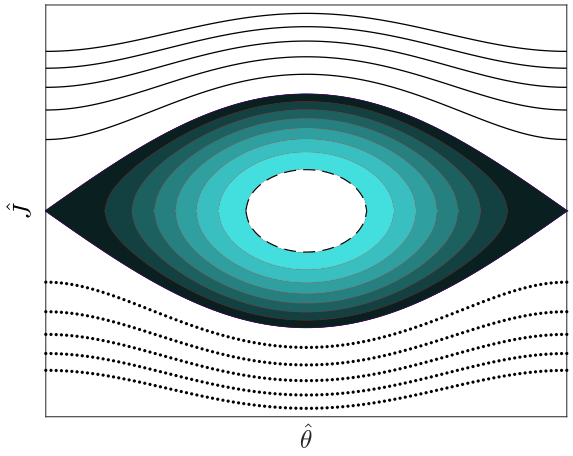

Figure 4.2: An expanded phase-space island. The unshaded area inside the separatrix represents the initial island just after the explosive formation stage. The dashed area illustrates the phase-space waterbags as contours of the distribution function.

be the same across A_i, which gives

$$f_i \times A_i = N_i = f_i' \times A_i'. \tag{4.19}$$

The preservation of the adiabatic invariants explained above ensures $A_i = A_i'$ which guarantees that the distribution function remains constant in between adjacent adiabatic invariants i.e a phase-space waterbag. This implies that instead of taking an Eulerian grid approach of solving the Vlasov equation or a Lagrangian approach to solve the equations of motion for each particle to resolve the perturbed phase-space density, we can define a set of Lagrangian contours along which the density remains fixed.

The trapped electrons in the BGK mode move with the wave in phase-space as the frequency chirps and hence have the dominant contribution to the perturbed density ($\tilde{f}$) which equals the difference between the value of distribution function at that point and the ambient distribution. Therefore, we can find $\tilde{f} = f_0 - F_{\text{eq}}(t) = F_{\text{eq}}(t=0) - F_{\text{eq}}(t)$ for each point inside the separatrix and $\tilde{f} = 0$ otherwise. Here, f_0 is the lowest order term of the expansion of f around β. Similarly, one can bounce-average the Vlasov equation under the adiabatic ordering to derive the above expression (see [55,56]). Consequently, we discretise the phase-space area inside the wave trapping region using the adiabatic invariants of the fast electrons and hence create level sets of the distribution function in phase-space i.e. a stepped distribution profile. Now, the problem of resolving the perturbations in fast electrons population during frequency chirping is framed as tracking the dynamics of the phase-space curves corresponding to the adiabatic invariants.

At this stage, the expressions (4.9b) and (4.13) can be substituted into the Poisson

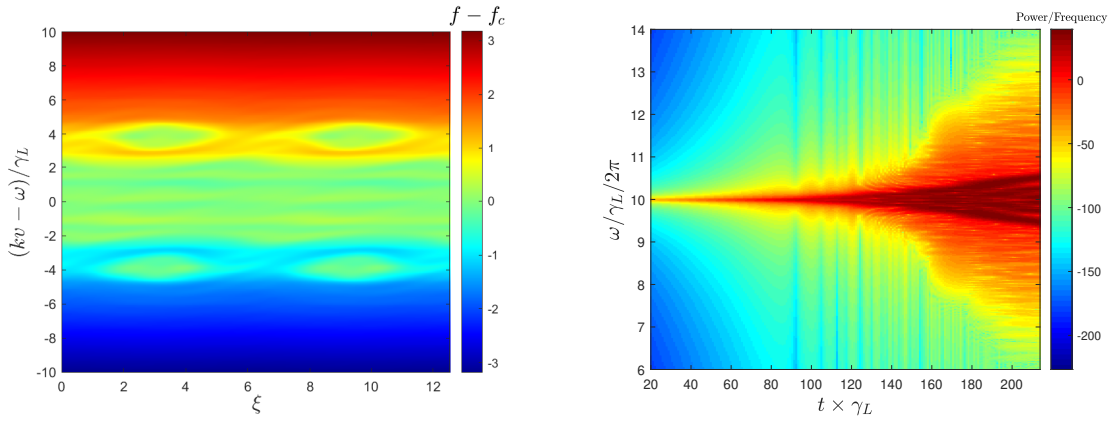

(a) (b)

Figure 4.3: Formation of islands in the phase-space of energetic particles (a) where the color bar represents the total distribution function f. In BOT code, for a linear distribution function in phase velocity, the initial resonance is located at the origin and therefore the distribution function is shifted by f_c. Consequently, negative values appear on the color bar of panel a. The short-time Fourier transform of the wave signal (b) with the color bar in logarithmic scale. Panel a corresponds to the last time slice of panel b where the frequency has chirped to $\approx 5.5\%$ of its initial value.

equation to solve for the field

$$A_n \quad (t) = \frac{1}{2\pi k_p n_c}\left[\frac{\omega^2}{n^2\hat{\omega}^2-1}\right]\sum_\alpha \sum_l \int_0^{2\pi}\int_0^{\infty}\Big[\tilde{f}_{\alpha,l}(\tilde{\theta}_l,\tilde{J}_l) \times V_{\alpha,n,p\times l}\exp\Big(in\tilde{\theta}_l\Big)+c.c\Big]\,d\tilde{J}_l d\tilde{\theta}_l. \tag{4.20}$$

The above expression sets the nonlinear integral equation for each Fourier coefficient, $A_n(t)$, which takes into account the contribution of fast electrons with different orbit types as well as the higher resonances, denoted by the sum over l. It is noteworthy that the summation over different resonances is removed in Ref. [56].

The chirping mechanism is based on extracting energy from the fast particles distribution and deposit it into the bulk plasma. Equating the energy released by the phase-space structure(s) with the energy deposited into the bulk gives

$$\frac{\mathrm{d}\omega\,(t)}{\mathrm{d}t} = -\left[\frac{\nu n_c \pi k_p}{\omega^3 m_e}\sum_n A_n^2\,(t)\right]\frac{1}{\sum_{\alpha,l} N_{\alpha,l}\left(\frac{\mathrm{d}\Omega_{\alpha,l}}{\mathrm{d}J_{\alpha,l}}\right)^{-1}}. \tag{4.21}$$

The total number of the particles inside each coherent structure reads

$$N_{\alpha,l} = \frac{1}{m_e}\int_0^{2\pi}\int_{\tilde{J}_{\alpha,max-}}^{\tilde{J}_{\alpha,max+}} \tilde{f}_{\alpha,l}\left(\tilde{J}_{\alpha,l},\tilde{\theta}_l\right)d\tilde{J}_\alpha d\theta. \tag{4.22}$$

In general, $\tilde{f}$ depends on the phase-space coordinates $(\tilde{J},\tilde{\theta})$ and a numerical treatment of the phase-space integral is required. For a growing separatrix, the newly trapped electrons inside the separatrix, specified by their adiabatic invariants, will carry the ambient phase-space density at the time of trapping. Therefore, in a time-discretised scheme, such a phase-space structure consists of an initial shape, which corresponds to the time when holes/clumps are just formed, surrounded by Lagrangian contours (waterbags) having different phase-space densities (see figure 4.2). As the separatrix expands, phase-space waterbags with uniform distribution functions are added around the initial separatrix.

So far, we have set the necessary tools to investigate the evolution of the chirping wave and a numerical approach is required to solve (4.21) along with (4.20). However, as shown in Refs. [53,56] and discussed in Ref. [55], evaluation of (4.21) at early stages of frequency chirping in this model reveals a square root dependency of the frequency on time. This dependency implies that the adiabatic condition is never formally satisfied for very early stages of chirping. In addition, for an expanding phase-space island, this may result in numerical errors due to large particle trapping at the early stages. In order to tackle this issue, we use the following facts:

- The holes and clumps form off the initial resonance [44],
- The violation of the adiabatic condition occurs over a very short period and this is implied by the condition $\gamma_l \ll \omega_{\mathrm{pe}}$,
- The adiabatic condition will remain valid once its satisfied [56].

These enable solving the system somewhat off resonance by considering an initial shift to the eigenfrequency. This frames the question of what shape the phase-space island will take after the initial shift. In other words, subsequent to an imposed frequency shift to the linear resonance, an appropriate description of the phase-space density is required for the

unshaded phase-space area encircled by the dashed curve depicted in figure 4.2. At this point, the challenge concerns the fact that holes/clumps are formed on a characteristic time scale in the order of the bounce period. Thereby, full-scale modelling is required and one can not invoke the adiabatic ordering and Liouville theorem to avoid following the particle dynamics on the fast time scale i.e. ω_b^{-1}. As a result, we perform simulations using the BOT code to resolve the dynamics during the fast formation stage. This part is covered in the next section where we prescribe an appropriate initialisation for the system.

4.3 Implementation of the BOT code for phase-space initialisation

In this section, the procedure taken to find a realistic shape for holes/clumps (phase-space structures) using the simulation data is detailed. The BOT code is an open source Vlasov solver which resolves the evolution of an unstable plasma wave in a bump-on-tail model. It also captures EPs collisions of Krook, drag and diffusion type which has been used to study the effect of dynamical friction force [33] and the formation process of holes and clumps [44]. In BOT code, the angular dependency ($\cos(kz)$) of the linear plasma wave and its subsequent sidebands oscillations are fixed to be sinusoidal and do not evolve. On the other hand, as a result of the excitation of the sidebands and damping into the bulk plasma, the frequency of the BGK-type chirping modes deviates from the initial eigenfrequency. As this occurs, the nonlinear contribution of the EPs current modifies the sinusoidal mode and adds non-linearity to the angular shape of the mode. This phenomenon is not captured in the BOT code. A consequence of this is the phase-space structures being perfectly eye-shaped. However, for short deviations of the frequency from the initial eigenfrequency the change of the mode shape is negligible and the simulation data remains valid. It was shown in Ref. [56] that frequency shifts of around 5% cause tiny modifications to the plane wave. On the other hand, as mentioned in the previous section, holes/clumps form on a time scale comparable to the bounce period and hence the

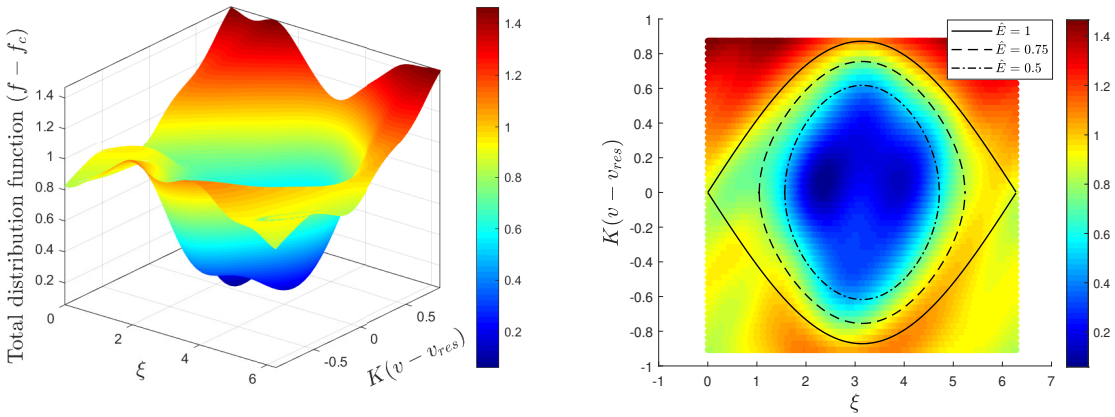

(a) (b)

Figure 4.4: (a) A Phase-space island (hole) in the BGK wave-frame formed at the top of the flattened region in figure 4.3. (b) The contour plot of the phase-space density inside the hole shown in panel a. The curves represents contours of constant normalised energy given by (4.23).

formation process occurs in a short range of frequency sweeping. Consequently, the phase-space analysis of the BOT code at the very early stages of chirping can be used to identify the structure of holes/clumps in phase-space just after their formation and prior to the adiabatic evolution. This information can be implemented to initialise the phase-space of our adiabatic model which can handle long range frequency deviations. In the following, we base our calculations around the time where holes/clumps (phase-space structures) are just formed and the phase-space of the adiabatic model is initialised accordingly.

The simulation results of the BOT code are illustrated in figure 4.3, where the phase-space of energetic electrons is demonstrated (figure 4.3a) after the saturation and nonlinear phase-mixing of the electrons when the sideband oscillations has just been excited. The corresponding frequency evolution of the plasma wave is shown in figure 4.3b where it can be observed that the frequency starts sweeping at $t\gamma_l \approx 120$ after the mode saturation. At the last time slice, the frequency experiences a shift of $\approx 5.5\%$ of the initial eigenfrequency ($\delta\omega_0 = \frac{\Delta\omega_0}{\omega_{\rm pe}} \approx 5.5\%$). The phase-space density inside the structures can be used to find an approximated shape for the holes/clumps just after their explosive formation process in order to initialise the adiabatic model for the evolution of these structures. To perform this simulation using the BOT code, the value of γ_d/γ_l is set to be 0.9 as a near-threshold instability case and the collisional coefficients are set to zero.

In figure 4.4, the structure of an up-chirping hole is depicted together with the contour plot of the phase-space density. As the frequency evolves, snapshots of phase-space reveal that for a fixed wave amplitude, the phase-space density remains the same along the contours of constant energy in the wave frame. However, it is noteworthy that as the frequency evolves, there is a subsequent change in the amplitude of the BGK-type wave and $\tilde{J}_{\rm res}$. Therefore, the functional dependency between the adiabatic invariant and energy of the trapped electrons in the wave does not remain the same during frequency chirping. However, since the structures are evolving adiabatically, conservation of the adiabatic invariants of the system ensures that the phase-space density remains constant in between the adiabatic invariants. Consequently, we discretise the phase-space using the adiabatic invariants with each region having a constant distribution; a stepped distribution profile (a waterbag model) as a function of the adiabatic invariants for the numerical analysis.

For each 2D phase-space element of figure 4.4, the Hamiltonian (4.15) can be utilised to find the corresponding energy in the wave denoted by $E_{\rm total}$. Subsequently, a polynomial fitting to the data gives the shape of the distribution function inside the phase-space structure which is illustrated in figure 4.5. The normalised energy $\hat{E}$ is defined as

$$\hat{E} = \frac{E_{\rm total} - U_{\rm min}}{U_{\rm max} - U_{\rm min}}, \tag{4.23}$$

where $U_{\rm max}$ and $U_{\rm min}$ denote the maximum and minimum potential energy of the chirping wave, respectively. This prescribed shape is implemented in section 4.5 as the initial shape of holes and clumps which start evolving from $\approx 5.5\%$ off the initial resonance. In what follows, the phase-space structures are initialised according to the shape of figure 4.5.

4.4 Numerical Algorithm/procedure

In this part, The numerical algorithm implemented to solve the system equations is explained and we introduce the normalisation used on the system equations. For the purpose of normalisation, we firstly need to evaluate (4.20) and (4.21) at the early stages

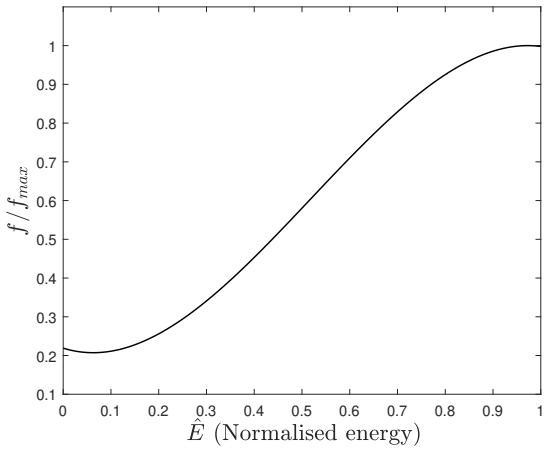

Figure 4.5: The shape of the phase-space structure found using the BOT code simulations

of frequency chirping. In the limit ($t \approx 0$), the plane wave is still almost sinusoidal/linear ($A_{n\geq 2} \approx 0$). Regardless of whether the separatrix is expanding or shrinking and for the case where only magnetically passing electrons ($\alpha = \mathbf{P}$) contribute to the EPs current through the first resonance ($l = 1$), one can analyse the integral Eq. (4.20) at $t \approx 0$ to find

$$A_{1,0} = \frac{4\omega_{\text{pe}}^2 \frac{\partial F_{\text{eq},\mathbf{P}}}{\partial \zeta_{\mathbf{P}}} \frac{\partial \zeta_{\mathbf{P}}}{\partial \hat{\omega}}\Big|_{\hat{\omega}=1}}{3\pi k_p n_c} V_{\mathbf{P},1,1,0} \tilde{J}_{\text{max},\mathbf{P},\mathbf{0}} \tag{4.24}$$

with $\tilde{J}_{\text{max},\mathbf{P},\mathbf{0}}$ being the maximum half width of the saturated/initial trapping region (separatrix at $\tilde{\theta} = \pi$) of the BGK mode corresponding to the first resonance with magnetically passing electrons, given by

$$\tilde{J}_{l,\text{max},\alpha=\mathbf{P},\mathbf{0}}\left(\tilde{\theta} = \pi\right) = 2\sqrt{\frac{A_{n=1,0} V_{\mathbf{P},1,1,0}}{|\Delta_{\alpha=\mathbf{P}}|_{t=0}}}. \tag{4.25}$$

It is worth mentioning that the trapping region of the BGK mode carrying the magnetically trapped electrons has a phase shift of π with respect to the one corresponding to the magnetically passing ones (see fig.2 in Ref. [56]). Now, we use $A_{1,0}$ to normalise Eq. (4.20). This gives

$$\hat{A}_n(t) = \frac{3\hat{\omega}^2}{8(n^2\hat{\omega}^2-1)\frac{\partial F_{\text{eq},\mathbf{P}}}{\partial \zeta_{\mathbf{P}}} \frac{\partial \zeta_{\mathbf{P}}}{\partial \hat{\omega}}\Big|_{\hat{\omega}=1}} \sum_\alpha \sum_l \int_0^{2\pi} \int_0^{\infty} \Big[\tilde{f}_{\alpha,l}(\tilde{\theta}_l, \tilde{J}_l) \hat{V}_{\alpha,n,p\times l} \exp\Big(in\tilde{\theta}_l\Big) + c.c\Big] d\hat{\tilde{J}}_l d\tilde{\theta}_l, \tag{4.26}$$

where $\hat{A}_n = \frac{A_n}{A_{1,0}}$, $\hat{\omega} = \frac{\omega}{\omega_{\text{pe}}}$, $\hat{V}_{\alpha,n,p\times l} = \frac{V_{\alpha,n,p\times l}}{V_{\mathbf{P},1,1,0}}$ and $\hat{\tilde{J}}_l = \frac{\tilde{J}_l}{\tilde{J}_{l,\text{max},\alpha=\mathbf{P},\mathbf{0}}}$.

Using (4.12), (4.24) and the normalised time $\tau = \frac{\nu}{3}(\frac{16\gamma_l}{3\pi^2\omega_{\text{pe}}})t$, one can normalise the

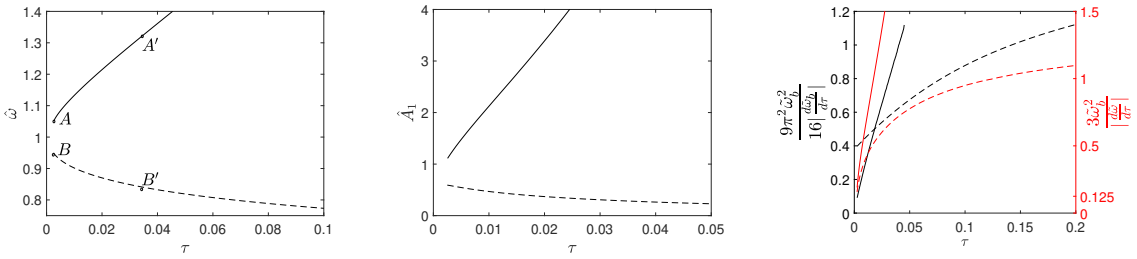

(a) (b) (c)

Figure 4.6: Evolution of (a) the frequency, (b) the first Fourier coefficient as a measure of the chirping wave amplitude and (c) the RHS of the adiabatic orderings given by (4.29) and (4.30) in black and red, respectively, for a single resonance. An initial frequency shift of $\delta\omega_0 = 0.055\omega_{\rm pe}$ is considered which corresponds to $\tau_0 = 0.0025$ following the square root dependency. Solid and dashed curves correspond to up-chirping and down-chirping waves, respectively.

differential equation (4.21) and find

$$\frac{\mathrm{d}\left(\hat{\omega}-1\right)^2}{\mathrm{d}\tau} = \left[\frac{8\left(\hat{\omega}-1\right)\frac{\partial F_{\mathrm{eq},\mathbf{T}}}{\partial \zeta_{\mathbf{T}}}\left.\frac{\partial \zeta_{\mathbf{T}}}{\partial \hat{\omega}}\right|_{\hat{\omega}=1}}{\hat{\omega}^3}\sum_n \hat{A}_n^2\left(t\right)\right] \times \frac{1}{\sum_\alpha \sum_l \int_0^{2\pi}\int_{\hat{\hat{J}}_{\alpha,max-}}^{\hat{\hat{J}}_{\alpha,max+}} \tilde{f}_{\alpha,l} d\hat{\hat{J}}_\alpha d\theta \hat{\Gamma}_\alpha^{-1}}. \tag{4.27}$$

The frequency of the chirping waves is evolved using the above ODE by a 4^{th} order Runge-kutta method. At each time step, the nonlinear field is solved by performing iterations on the Fourier coefficients using (4.26). In each iteration the phase-space integral is resolved numerically by a 2D trapezoidal rule. Energetic electrons are labeled using their adiabatic invariants. Hence each separatrix is identified/discretised using an array of adiabatic invariants and a corresponding array of distribution function values which are initialised using the BOT code data. At the end of each time step, these arrays are updated depending on whether the separatrix is shrunk or expanded.

4.5 Results and discussions

At this stage, we solve the model equations, introduced in section 4.2, starting off the initial resonance where the system is initialised by manipulating the simulation data discussed in section 4.3. As the main goal of this work, we report the results for cases which include the deepening of the wave trapping region(s) hence both particle orbit topology and particle trapping in phase-space affect the behaviour of the chirping mode simultaneously, i.e. not tractable using the flat-top model of Ref. [56]. This is accompanied by our observations on the behaviour of the chirping mode under the impact of multiple resonances. Accordingly, chirping waves with both downward or upward trend whose initial frequency lies in the range of magnetically passing particles are studied.

The initial plasma mode is in resonance with electrons having $1.1 \leq \zeta_{\mathbf{P}} \leq 1.3$ (see

figure 4.1). This corresponds to pitch-angle,

$$\Lambda = \frac{1}{(2\zeta_{\mathbf{P}}\epsilon - \epsilon + 1)}, \tag{4.28}$$

values of $0.65 \leq \Lambda \leq 0.71$ for an inverse aspect ratio of $\epsilon = 1/3$. It is noteworthy that $\Lambda = 0.75$ corresponds to the trapped-passing boundary ($\zeta = 1$) in the background field. Firstly, we start the analysis by assuming that the 1^{st} resonance is dominant and thereby neglect higher order resonances. Subsequently, it is discussed that neglecting higher order resonances for the range of orbits under consideration is a naive assumption and there exist ranges in which a single resonance number (l) can not be regarded as the dominant one. This necessitates taking into account multiple resonances in the wave-particle interaction model. In order to demonstrate the impact of higher resonances on the nonlinear behaviour of the mode, we analyse the evolution of BGK-type chirping waves under the simultaneous influence of multiple resonances, in this case 1^{st} and 2^{nd}. For each case, the validity of the adiabatic condition is analysed.

4.5.1 A single resonance

We set $k_p/k_{\text{eq}} = 1$ and $\zeta_{\mathbf{P},\mathbf{0}} = 1.176$ (see ω_{pe} on figure 4.1), the self-consistent system of Eqs. (4.27) and (4.26) is solved for both up-chirping and down-chirping modes under the impact of only the 1^{st} resonance and for the linear equilibrium distribution function introduced in section 4.2. The corresponding evolution of the amplitude and the frequency is depicted in figure 4.6. The up-chirping mode with a growing amplitude is controlled by the dynamics of a phase-space hole ($\tilde{f} < 0$) with an expanding trapping region and therefore the effect of particle trapping in a deepening potential well is included in the behaviour of the mode. On the other hand, the downward trend is supported with a shrinking clump from which the particles are being detrapped as the mode chirps. Figure 4.6 shows the time-dependency of the wave parameters. The evolution of the frequency demonstrates an asymmetry in upward and downward branches. It can be observed that the upward branch is chirping faster. Both branches are initialised with the same absolute initial shift ($|\delta\hat{\omega}_0| = 0.055$) in the frequency, denoted by points A and B on each curve of figure 4.6a. The non-linear shape of the plane wave at $\tau = 0.0346$ where the up-chirping and down-chirping waves experience $\approx 32\%$ and 16% frequency chirping, denoted by A' and B', respectively, is shown in figure 4.7. This shows that the shape of the down-chirping wave is more deviated from the linear wave at this point. The phase-space density of holes and clumps is illustrated in figure 4.8. Panels A' and B' illustrate the full phase-space density contours of an up-chirping hole and a down-chirping clump at $\hat{\omega} = 1.32$ and $\hat{\omega} = 0.84$ with their corresponding initial separatrices shown in panels A and B, respectively. Initial separatrices are initialised with the shape of figure 4.5 and $\delta\omega_0 = 0.055\omega_{\text{pe}}$. The particle trapping into the separatrix can be observed for the up-chirping hole, the top row, where the wave sweeps the ambient particles on its motion, as opposed to the down-chirping clump whose trapping region shrinks.

In order to check the validity of the adiabatic condition ($\left|\frac{\mathrm{d}\omega_b}{\mathrm{d}t}\right| \ll \omega_b^2$) [34,75,98], given by (4.1), we write it as [56]

$$\frac{\nu\gamma_{l,1^{\text{st}}}}{\omega_{\text{pe}}^2} \ll \frac{9\pi^2\tilde{\omega}_b^2}{16\left|\frac{\mathrm{d}\tilde{\omega}_b}{\mathrm{d}\tau}\right|}, \tag{4.29}$$

where $\tilde{\omega}_b = \frac{\omega_b}{\omega_{b,0}}$, with $\omega_{b,0}$ being the initial bounce frequency corresponding to the 1^{st}

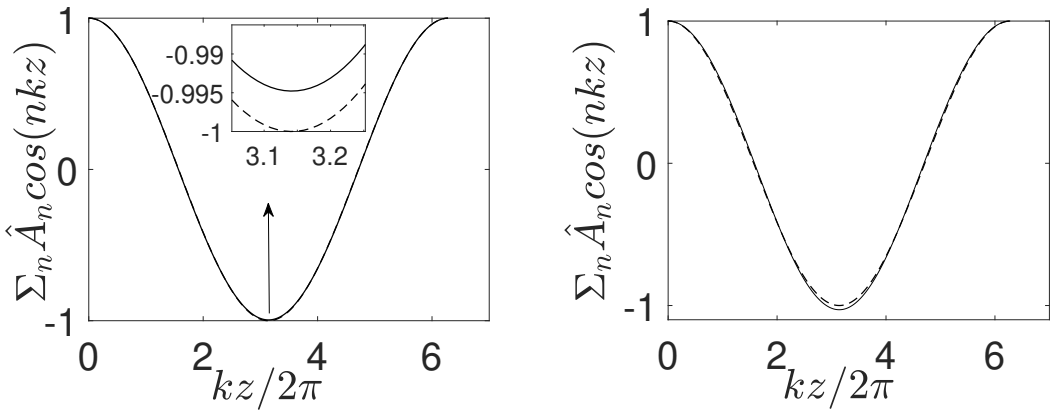

Figure 4.7: Nonlinear chirping wave potential at $\tau = 0.0346$ for (a) the up-chirping wave with $\hat{\omega} = 1.32$ and (b) the down-chirping wave with $\hat{\omega} = 0.84$. The dashed curve represents the linear sinusoidal potential.

resonance. For a near-threshold instability with typical value of the linear growth rate to be 1 per cent of the linear mode frequency and with $\gamma_d = 0.9\gamma_l$, the LHS value is ≈ 0.00018. The RHS of (4.29) is shown in figure 4.6c as a function of time for both of the waves. This validates the adiabatic ordering as the wave evolves where the RHS value increases in time. Similarly, one can write the ordering $\left|\frac{\mathrm{d}\omega}{\mathrm{d}t}\right| \ll \omega_b^2$ as

$$\frac{\nu}{\omega_{\mathrm{pe}}} \ll \frac{3\tilde{\omega}_b^2}{\left|\frac{\mathrm{d}\tilde{\omega}}{\mathrm{d}\tau}\right|}, \tag{4.30}$$

where the LHS takes the value of ≈ 0.018 for the range of parameters considered above. The RHS of the ordering (4.30) is depicted in figure 4.6c which confirms its validity as the wave chirps.

4.5.2 Impact of higher resonances

For the range of linear plasma wave frequencies studied in Ref. [56], the first resonance ($l = 1$) is the dominant contributor to the interaction. In this part, we illustrate that if the 1^{st} resonance ($l = 1$) is formed with magnetically passing electrons having specific pitch angles, then the 2^{nd} resonance ($l = 2$) of the interaction can have relatively significant contribution to the wave excitation. The wave frequency studied in the previous part is an example of such cases for which the 2^{nd} resonance lies in the range of magnetically trapped electrons (see figure 4.1). The 1^{st} resonance does not include any contribution from the magnetically trapped electrons since the resonance condition with $p = 1$ can not be satisfied for these electrons. However, technically speaking, the 2^{nd} resonance is interacting with a group of magnetically trapped electrons as well as a group of magnetically passing ones; the contribution of the latter is relatively negligible though (see section 4 and figure 8 in Ref. [56]). We firstly show the contribution of higher resonances by investigating their impact on the linear growth rate of the mode. For this purpose, we focus on the contribution of the 2^{nd} resonance and other resonances can be treated likewise. The proportion of the eigenmode wave-number (k_p) to the spatial periodicity of the equilibrium field (k_{eq}) is a 1D proxy for the poloidal mode numbers in realistic geometries. We denote

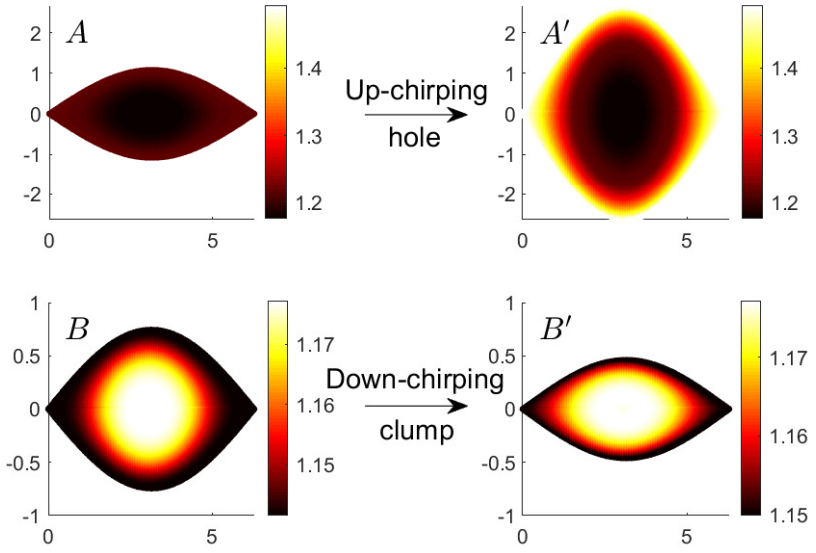

Figure 4.8: The phase-space islands for the single resonance case with the vertical and horizontal axis being $\tilde{J} - J_{\text{res}}$ and $\tilde{\theta}$, respectively. The color denotes the total distribution function.

the total growth rate, associated with the 1st and 2nd resonance, by ($\gamma_{l,\text{total}}$) and normalise it to the growth rate of the first resonance ($\gamma_{l,1^{\text{st}}}$). Figure 4.9 demonstrates $\gamma_{l,\text{total}}/\gamma_{l,1^{\text{st}}}$, where

$$\frac{\gamma_{l,\text{total}}}{\gamma_{l,1^{\text{st}}}} = 1 + \frac{\gamma_{l,2^{\text{nd}}}}{\gamma_{l,1^{\text{st}}}}, \tag{4.31}$$

versus the energy parameter for different values of k_p/k_{eq}. It can be observed that there are regions in figure 4.9 where the contribution of the 2nd resonance can be significantly higher than the 1st one. Although these cases elaborate the significance of the higher order resonances, however, the strong dominancy of the 2nd resonance allows neglecting the 1st resonance and treat the interaction as having a single resonance. Accordingly, our attention is mainly focused on the more interesting regions in which one finds $1.2 < \gamma_{l,\text{total}}/\gamma_{l,1^{\text{st}}} < 3$, which indicates that the contribution of the 2nd resonance is not negligible and can even be comparable to that of the 1st resonance. Investigation of figure 4.9a at $\zeta_{\mathbf{P},\mathbf{0}} = 1.176$ shows that the contribution of the 2nd resonance to the interaction is more than 47% of the 1st resonance and it is not negligible. Therefore, the impact of the dynamics governed by the 2nd resonance should be included in the analysis of the chirping waves under study. We will show the results for this choice hereafter.

The non-linear behaviour of the chirping waves are depicted in figure 4.10. As predicted by the linear growth analysis, the inclusion of the 2nd resonance into the interaction results in considerable change in the nonlinear behaviour of the up-chirping energetic particle driven mode. In this case, the rate of frequency chirping is smaller than the single resonance case during the evolution of the mode. The evolution of the RHS of the adiabatic ordering, introduced in (4.29) and (4.30), is investigated at the o-point of the phase-space structures for each resonance in figure 4.10c and figure 4.10d for the up-chirping and down-chirping waves, respectively. It is demonstrated that as the system evolves after initialisation using the BOT code data for both resonances, the value of the

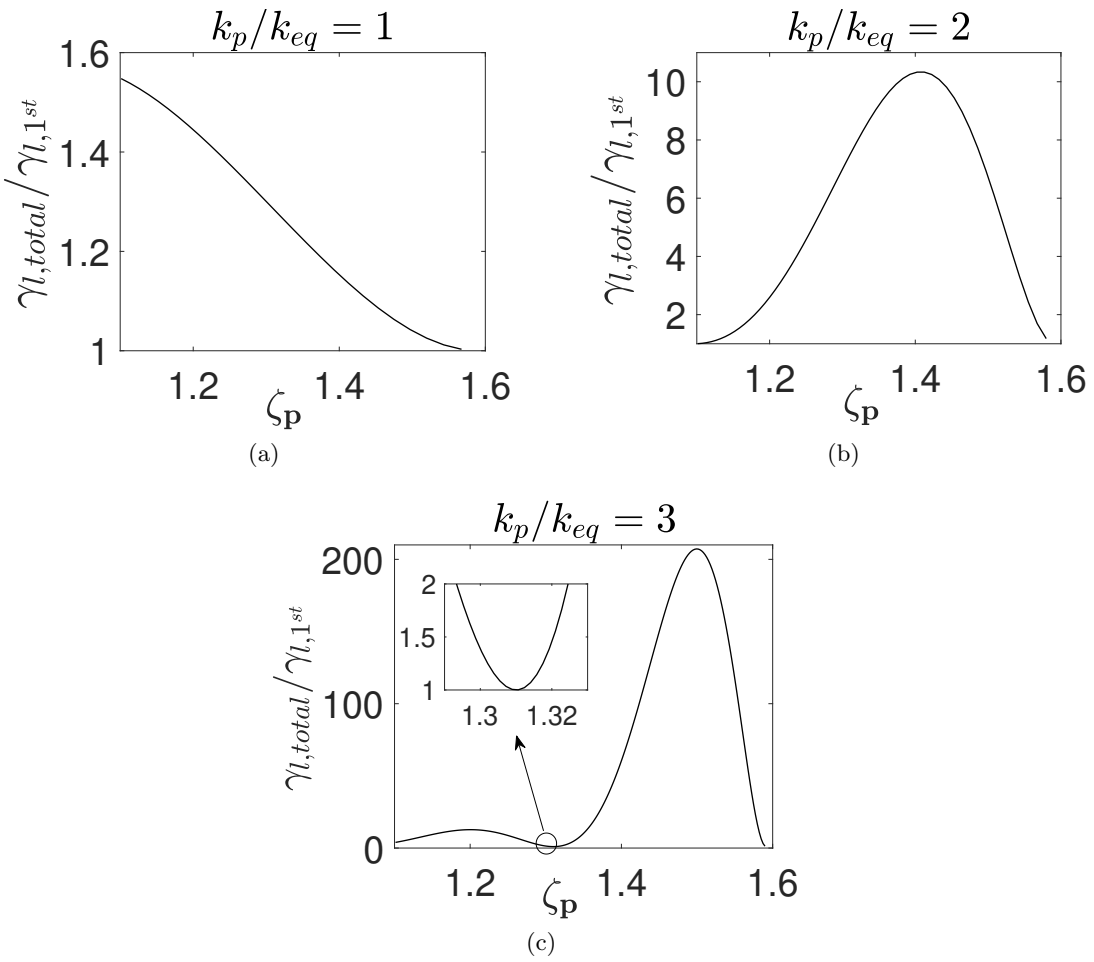

Figure 4.9: The linear growth rate normalised to the growth rate of the 1st resonance vs. the energy parameter as a function of $\frac{k_p}{k_{\text{eq}}}$.

RHS of (4.29) and (4.30) remain above the initial value throughout the simulation. With regards to the evolution of the first Fourier harmonic, figure 4.10b, the up-chirping wave initially grows faster than the single resonance case until $\tau \approx 0.009$, thereafter the rate of the amplitude change becomes smaller. Interestingly, the amplitude of the up-chirping wave saturates at $\tau \approx 0.113$ followed by a decrease. Here, we elaborate this behaviour by investigating the evolution of the phase-space structures of the up-chirping wave.

In the single resonance case, the phase-space structure of the up-chirping wave is a hole that constantly grows and traps ambient particles whereas for the double-resonance case, the phase-space islands supporting the up-chirping branch are a hole and a clump corresponding to the 1st and the 2nd resonance, respectively. The time evolution of the adiabatic invariants at the separatrix are illustrated in figure 4.11 for the up-chirping wave of the double-resonance case. The values are normalised to the corresponding initial value of the 1st resonance hole. Unlike the single-resonance case, it can be observed that neither of the structures constantly grow in phase-space. The separatrix of the 2nd resonance clump initially grows until $\tau \approx 0.051$ and then starts to shrink. This has an impact on the behaviour of the 1st hole where it deepens until $\tau \approx 0.141$. The asymptotic behaviour observed in figure 4.10c corresponds to the times when each phase-space structure reaches the maximum expansion and does not grow further as shown in figure 4.11. At this point,

the change in the bounce frequency of the trapped electrons around the O-point drops to zero (see Eq. (4.29)).

Furthermore, snapshots of the phase-space for the up-chirping wave, illustrated in figure 4.12, reveal that the particle trapping will not constantly occur as these structures evolve. As mentioned above, it can be observed that at $\tau = 0.044 < 0.051$ the clump has expanded and trapped the ambient particles. It is worth mentioning that the 2$^{\text{nd}}$ resonance clump moves towards magnetically trapped electrons having smaller values of the energy parameter $\zeta_{\mathbf{T}}$ and for the choice of a linear equilibrium distribution function in ζ, the newly trapped electrons have smaller distribution function values. Later evolution of the clump shows a loss of the trapped particles at $\tau = 0.207$. Similarly, an illustration of the phase-space hole for the 1$^{\text{st}}$ resonance at $\tau = 0.1371 < 0.141$ shows the particle trapping inside the structure while it moves towards electrons having higher energy parameters values. At $\tau = 0.207$, the separatrix of the hole has slightly shrunk as expected from figure 4.11.

The shape of the chirping waves corresponding to the upward and downward branch is illustrated in figure 4.13a and figure 4.13b, respectively. The deviation of the frequency for both branches is the same as that of figure 4.7. Compared to the shape of the down-chirping wave, the up-chirping wave is more deviated from the linear sinusoidal wave. This

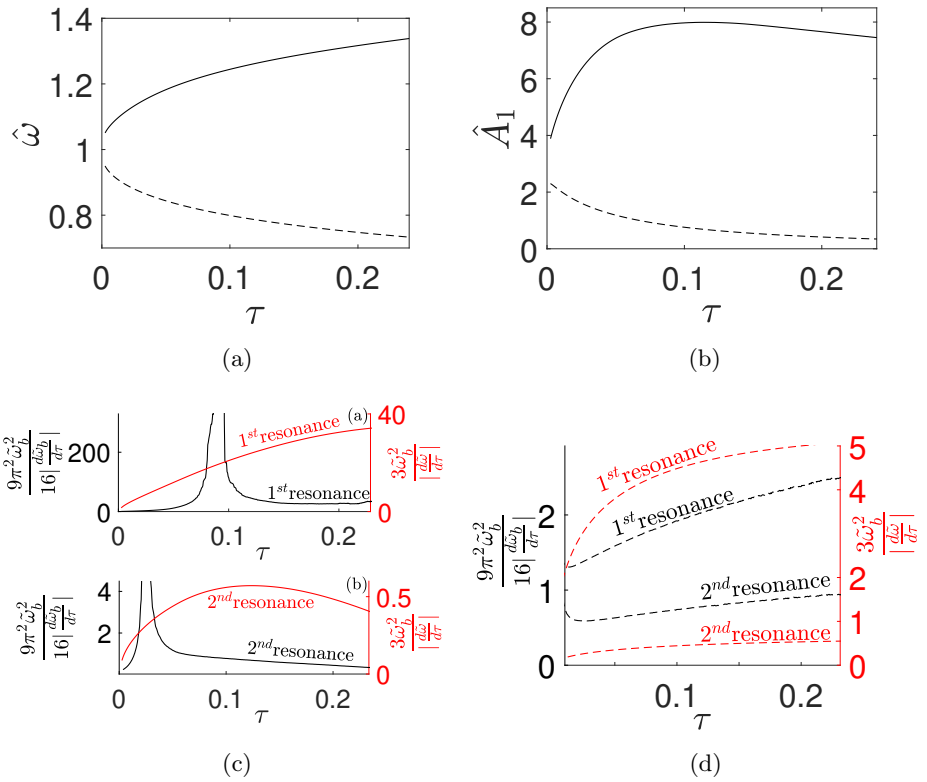

Figure 4.10: Nonlinear behaviour of the chirping wave under the simultaneous effect of 1$^{\text{st}}$ and 2$^{\text{nd}}$ resonances. Evolution of the frequency (a), the first Fourier harmonic (b) and the RHS of the adiabatic ordering at the O-point for (c) the up-chirping and (d) the down-chirping waves. In panels c and d, black and red curves correspond to the adiabatic ordering of (4.29) and (4.30), respectively. In all the figures, the solid and dashed curves correspond to the up-chirping and down-chirping waves, respectively.

is contrast with the single resonance case where the down-chirping wave experiences more change in the wave potential (see figure 4.6).

4.6 Summary

The study of adiabatically chirping waves with deepening potentials is enabled in the trapped-passing locus model of Ref. [56]. This is associated with inclusion of the particle trapping effect in phase-space as the trapping region of the wave expands. This work allows the study of chirping waves with up-ward and downward frequency chirping in full range of fast particles orbit topologies which is a 1D paradigm of guiding centre motions in realistic geometries. The BOT code simulations are performed to find an appropriate shape for the phase-space structures namely holes and clumps, after their fast scale formation process. Under the adiabatic ordering, fast particles are labeled using their adiabatic invariants in a slowly evolving system. In a discretised scheme, this ordering and the Liouville theorem imply that the phase-space density remains constant in between waterbags/rings of adiabatic invariants. Hence, we resolve the perturbation of the phase-space density of fast particles using a Lagrangian mesh approach. In fact, each contour of the distribution function is considered as a waterbag.

The evolution of the system is analysed for up-chirping and down-chirping modes in a single resonance interaction. Subsequently, we introduce regions in the fast particles orbit space where the 2$^{\text{nd}}$ resonance can have remarkable contribution to the linear growth rate of the mode. This stimulates a nonlinear study of the chirping waves by including the contribution of the 2$^{\text{nd}}$ resonance to the density of the fast particles. The analysis reveals that the nonlinear behaviour of the mode can be considerably altered by the 2$^{\text{nd}}$ resonance. Therefore, depending on the linear frequency of the wave, it is essential to include the contribution of higher resonances when studying the evolution of chirping waves in real experiments.

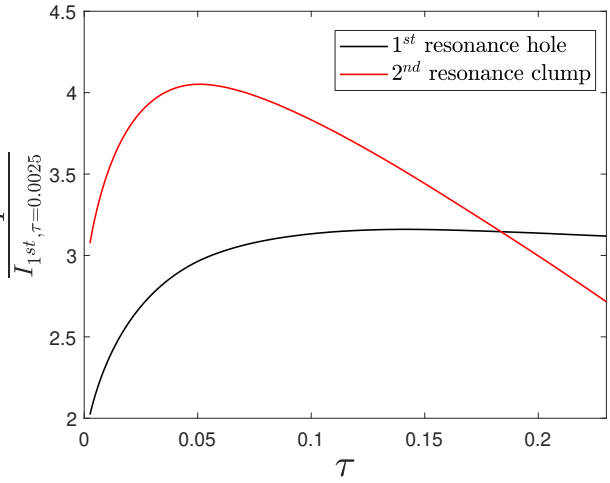

Figure 4.11: Evolution of the adiabatic invariants at the separatrix for the up-chirping wave in the double-resonance case. The black and red curves correspond to the 1$^{\text{st}}$ resonance hole and the 2$^{\text{nd}}$ resonance clump, respectively. The y-axis values are normalised to the adiabatic invariant of the separatrix corresponding to the 1$^{\text{st}}$ resonance hole at $\tau = 0.0025$ denoted by $I_{1^{\text{st}},\tau=0.0025}$.

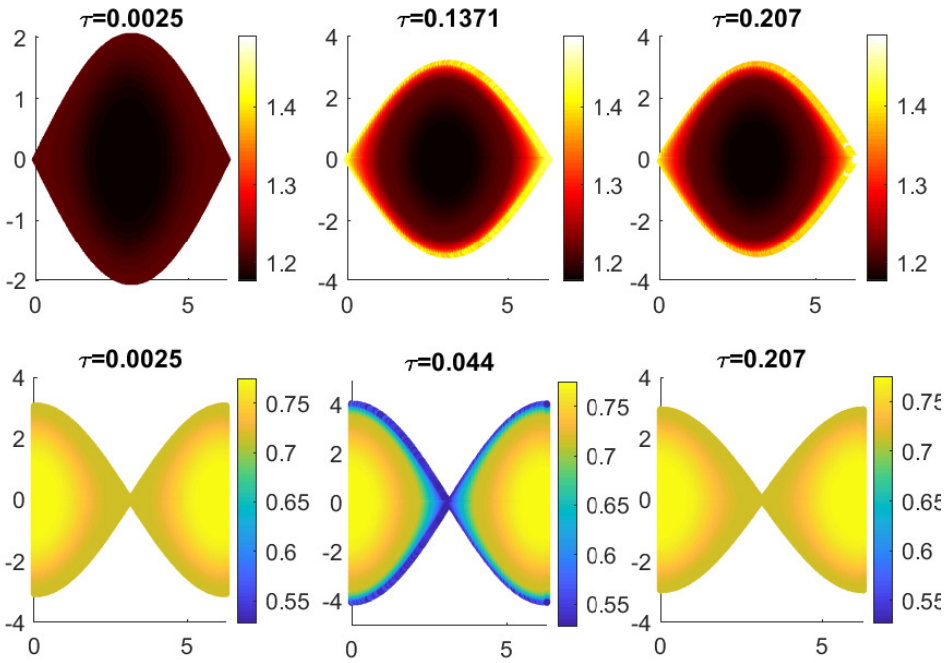

Figure 4.12: Snapshots of the phase-space corresponding to the up-chirping wave with the vertical and horizontal axis being $\tilde{J} - J_{\text{res}}$ and $\tilde{\theta}$, respectively. The color denotes the total distribution function. The first and the second row correspond to the 1$^{\text{st}}$ resonance hole and the 2$^{\text{nd}}$ resonance clump, respectively.

So far, in this work and the previous models on the adiabatic frequency chirping, the amplitude of the chirping wave experienced by the particles i.e. the orbit averaged mode amplitude denoted by V in this work, is not a function of the phase-space action at each corresponding wave frequency. Instead, it is approximated around the centre of the separatrix by truncating the Taylor expansion of the mode amplitude around $\tilde{J}_{\text{res}}$ after

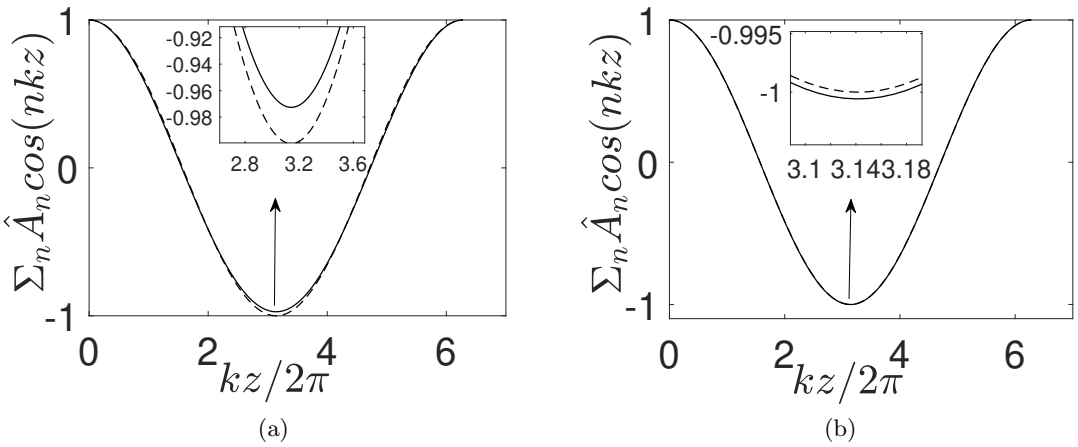

Figure 4.13: Nonlinear potential of (a) the up-chirping wave at $\tau = 0.21$ with $\hat{\omega} = 1.32$ and (b) the down-chirping wave at $\tau = 0.053$ with $\hat{\omega} = 0.84$. The dashed curve represents the linear sinusoidal potential.

the first term and is justified under the assumption of $\gamma_l \ll \omega_{\mathrm{pe}}$, where γ_l is the linear growth rate and ω_{pe} is the linear frequency. This implies that particle detuning from the initial linear resonance is small. However, for cases where the mode amplitude has deep gradients in the action of the fast particles equilibrium motion [111], taking into account the higher order terms of the aforementioned Taylor expansion is a next step extension to this work which is included in our research plan.

Acknowledgments

This work was funded by the Australian Research Council through Grant No. DP140100790. The first author is indebted to in depth discussions with Prof. Boris Breizman about frequency chirping in tokamaks and very grateful to Dr. Robert Nyqvist for fruitful correspondence that helped inspire this work.

Chapter 5

Simulation of convective transport for TAE frequency chirping using the MEGA code

Abstract

We present a procedure to examine energetic particle phase-space during long range frequency chirping phenomena in tokamak plasmas. To apply the proposed method, we have performed self-consistent simulations using the MEGA code and analyzed the simulation data. We demonstrate a travelling wave in phase-space and that there exist specific slices of phase-space on which the resonant particles lie throughout the wave evolution. For non-linear evolution of an $n = 6$ toroidicity-induced Alfvén eigenmode (TAE), our results reveal the formation of coherent phase-space structures (holes/clumps) after coarse-graining of the distribution function. These structures cause a convective transport in phase-space which implies a radial drift of the resonant particles. We also demonstrate that the rate of frequency chirping increases with the TAE damping rate. Our observations of the TAE behaviour and the corresponding phase-space dynamics are consistent with the Berk-Breizman (BB) theory.

5.1 Introduction

The physics of energetic particles (EPs) plays an essential role in fusion plasmas. It has very attractive diagnostic applications but, on the other hand, it involves the possibility of unacceptably fast particle losses. A famous example is the destabilization of weakly damped plasma waves inside the gaps of the shear Alfvén continuum, which entails redistribution or ejection of EPs either through diffusive transport or a convective transport where an isolated resonance moves radially like a bucket that carries resonant particles. The latter is associated with long range frequency chirping and has been observed for a variety of modes in experiments [46, 52, 105, 106, 112]. Refs. [113–118] show a correlation between wave-particle resonant interactions and fast ion loss and redistribution.

The formation of coherent structures in fast electrons phase-space was observed in non-linear simulations of a 1D electrostatic wave in Ref. [35]. These structures (holes and clumps) are BGK-type modes [68] with a chirping frequency. They evolve adiabatically and carry the trapped particles. Non-perturbative adiabatic models [53–57] suggest the slow evolution of a Langmuir wave as a 1D paradigm of the more general wave-particle

interactions in realistic geometries. In Refs. [47, 94], the theory has been extended to tokamak applications where the frequency chirping of Alfvénic perturbations are studied. Ref. [107] demonstrates the formation of holes and clumps during frequency chirping of the $n = 0$ EGAM modes, where the toroidal momentum (P_φ) of the EPs is conserved in the presence of the electrostatic perturbations. The impact of EP beta value (β_{EP}) on chirping of a TAE mode was studied in Ref. [119] and it has been shown that as the frequency of the wave changes, the dominant perturbation occurs at different slices of phase-space (P_φ vs E with μ = const). In Ref. [120], the phase-space dynamics of EPs are studied during the long range frequency chirping of a TAE with a fixed eigenfunction, where phase-space slices are determined using two constants of motion, namely μ and $C = \omega_{\mathrm{TAE}} P_\varphi - nE$ (see Refs. [121, 122]) with μ, ω_{TAE}, n and E being the magnetic moment, linear eigenfrequency, toroidal mode number and the EP energy, respectively. Still the question of how the chirping wave transports particles in phase-space deserves more detailed analysis. Technically speaking, best suited constants of motion for EPs dynamics need to be defined as the frequency evolves.

In this work, we describe an appropriate procedure to observe the EPs dynamics on sub-slices of the phase-space during frequency chirping of a TAE mode. Subsequently, we validate this method by applying the corresponding analysis to the results of EP simulations with the MEGA code [58, 123]. We also show that the rate of frequency chirping is directly related to the damping rate of the mode in the bulk plasma. We demonstrate the latter by altering the dissipation coefficients when the mode has already evolved into chirping regime. In order to increase the resolution in phase-space, we have added test particles to the code. These test particles are pushed by the fields but do not contribute to the total EP current.

The rest of the paper is structured as follows: In section 5.2, we introduce a set of equations implemented in the hybrid MEGA code. Section 5.3 describes the appropriate coordinates and constants of motion needed to analyse the guiding centre dynamics of EPs in phase-space during the non-linear frequency chirping. This involves canonical action-angle variables. Subsequently, we apply our phase-space analysis to the simulation data of the MEGA code in section 5.4 and report on the evolution of the TAE parameters. We identify resonant particles and exhibit their convective transport in phase-space. Section 5.5 contains concluding remarks.

5.2 The simulation model in MEGA

We simulate the evolution of the energetic particle driven mode within a hybrid model implemented in the MEGA code, where the bulk plasma particles are described as a fluid by the non-linear MHD equations and the fast particles are treated in a drift-kinetic approach. The MEGA code solves the following set of equations:
The momentum balance equation given by

$$\rho \frac{\partial \boldsymbol{v}}{\partial t} = -\rho \boldsymbol{v} \cdot \boldsymbol{\nabla} \boldsymbol{v} - \boldsymbol{\nabla} p + \left(\frac{1}{\mu_0} \boldsymbol{\nabla} \times \boldsymbol{B} - \boldsymbol{j}_\alpha \right) \times \boldsymbol{B} + \frac{4}{3} \boldsymbol{\nabla} \left(\nu \rho \boldsymbol{\nabla} \cdot \boldsymbol{v} \right) - \boldsymbol{\nabla} \times \left(\nu \rho \boldsymbol{\nabla} \times \boldsymbol{v} \right), \tag{5.1}$$

where $\boldsymbol{j}_\alpha$ denotes the EP current, ν is the viscosity coefficient and ρ and p are the density and scalar pressure of the bulk plasma, respectively. In hybrid models, the contribution

of fast particles is coupled to the MHD equations either through the current term or the pressure term. Here, a current coupling approach has been implemented. It is noteworthy that the perpendicular component of the EP current arises from curvature drift, grad-B drift and magnetization current. This component of the EP current can be expressed in terms of the parallel and perpendicular EP pressure.
The continuity equation for the bulk plasma

$$\frac{\partial \rho}{\partial t} = -\boldsymbol{\nabla} \cdot (\rho \boldsymbol{v}) + \nu_n \Delta (\rho - \rho_0), \tag{5.2}$$

where ν_n is the mass diffusivity. The energy balance equation for the evolution of the bulk plasma pressure

$$\begin{aligned} \frac{\partial p}{\partial t} \quad &= -\boldsymbol{\nabla} \cdot (p\boldsymbol{v}) - (\gamma - 1)\, p \boldsymbol{\nabla} \cdot \boldsymbol{v} + (\gamma - 1) \\ &\times \left[\nu\rho (\boldsymbol{\nabla} \times \boldsymbol{v})^2 + \tfrac{4}{3} \nu\rho (\boldsymbol{\nabla} \cdot \boldsymbol{v})^2 + \eta \boldsymbol{j} \cdot (\boldsymbol{j} - \boldsymbol{j}_0) \right] \\ &+ \lambda \Delta (p - p_0), \end{aligned} \tag{5.3}$$

where γ is the adiabatic constant and λ represents the heat conductivity.
The set of Maxwell's equations and the Ohm's law given by

$$\frac{\partial \boldsymbol{B}}{\partial t} = -\boldsymbol{\nabla} \times \boldsymbol{E}, \tag{5.4a}$$

$$\boldsymbol{j} = \frac{1}{\mu_0} \boldsymbol{\nabla} \times \boldsymbol{B}, \tag{5.4b}$$

$$\boldsymbol{E} = -\boldsymbol{v} \times \boldsymbol{B} + \eta (\boldsymbol{j} - \boldsymbol{j}_0), \tag{5.4c}$$

where η represents resistivity.

In the above equations, all the other quantities are conventional. The subscript 0 represents the equilibrium values of the parameters and the corresponding terms, as the source terms, have been used to enforce MHD equilibrium and compensate the diffusion and dissipation of the equilibrium fields. This set of equations is discretized using the method of finite difference and the fields are solved in an Eulerian scheme where the computational domain is gridded.

The EPs are treated kinetically in a Lagrangian picture. A particle-in-cell method is applied to project the impact of EPs (EPs charge) on the grid points and update the fields in a self-consistent manner at each time step. The perturbation of the EPs, due to the wave, is calculated using the δf approach as the time evolution of the weight of each particle. This gives the following expression for the EPs current

$$\begin{aligned} \boldsymbol{j}_\alpha = \quad & \textstyle\sum_{i=1}^{N} e Z_\alpha w_i \left(\boldsymbol{v}^*_{\parallel,i} + \boldsymbol{v}_{B,i} \right) S(x - x_i) \\ & -\boldsymbol{\nabla} \times \left[\boldsymbol{b} \textstyle\sum_{i=1}^{N} \mu_i w_i S (x - x_i) \right], \end{aligned} \tag{5.5}$$

where the second term on the right-hand side is the magnetization current, the subscript i represents the ith EP, eZ_α is the charge of the EPs, w_i is the weight, $\boldsymbol{v}_{B,i}$ is the drift due to the gradient of the magnetic field, S is the shape factor and $\mu = E_k \left(1 - \lambda^2\right) / B$ is the magnetic moment with E_k, λ and B being the kinetic energy, pitch angle and 0the magnetic field at the guiding centre, respectively, $\boldsymbol{v}^*_\parallel$ contains the parallel velocity $v_\parallel$ to

the magnetic field and magnetic curvature drift, and is given by

$$\boldsymbol{v}_{\parallel}^{*} = \frac{v_{\parallel}}{B^{*}}[\boldsymbol{B} + \rho_{\parallel} B \boldsymbol{\nabla} \times \boldsymbol{b}], \tag{5.6}$$

where $\rho_{\parallel} = \frac{m_i v_{\parallel}}{eZ_{\alpha}B}$ is the parallel gyro-radius, $B^{*} = B(1+\rho_{\parallel}\boldsymbol{b}\cdot\nabla\times\boldsymbol{b})$ [73] and m_i is the ion mass. It is noteworthy that $\boldsymbol{j}_{\alpha}$ does not contain $\boldsymbol{E}\times\boldsymbol{B}$ drift due to quasi-neutrality [58]. The EPs current is coupled to the MHD equations through Eq. (5.1).

5.3 Phase-space study

In (E, p_{φ}, μ) coordinate, the conservation of the conventional constant of motion $C = \omega_{\mathrm{TAE}} P_{\varphi} - nE$ will break down as the frequency of the wave chirps. Therefore, in order to study the phase-space during chirping, we need to identify generalised canonical momenta that remain constant not only in the perturbative linear phase of the TAE evolution but also during the long range frequency chirping. This is done in this section, where we introduce a set of coordinates using which the dynamics of EPs interacting with a chirping wave is reduced to essentially 1D. We start from the Littlejohn's Lagrangian [73] for singly-charged ions given by

$$L_{\mathrm{littlejohn}} = e(\boldsymbol{A} + \rho_{\parallel}\boldsymbol{B})\cdot\dot{\boldsymbol{X}} + \frac{m_i}{e}\mu\dot{\Omega} - H, \tag{5.7}$$

where e is the electron charge, $\boldsymbol{X}$ is the guiding centre position, Ω is the gyro angle, $\boldsymbol{A}$ is the total vector potential and $\boldsymbol{B} = \boldsymbol{\nabla}\times\boldsymbol{A}$ and $H = \frac{1}{2}mv_{\parallel}^{2} + \mu B$ is the Hamiltonian. It should be noted that a gauge is considered where the perturbed electrostatic potential is zero. The expression of (5.7) contains both the particle/unperturbed and the interaction Lagrangian.

For common choices of magnetic field line coordinates e.g. Boozer [124], PEST [125], Hamada [126] and etc, the guiding centre Lagrangian does not immediately reveal three canonical pairs of the Hamiltonian structure. This is due to the fact that the Lagrangian contains the time derivative of four variables as opposed to three. There have been several attempts to tackle this issue [124,127,128] but each has its own disadvantages. In Ref. [129], the problem is resolved by introducing canonical angles, namely (θ_c, ξ_c), which give a new type of global coordinates called canonical straight field line coordinates.

Using the new coordinates, a Legendre transformation can be implemented to find the unperturbed Hamiltonian

$$H_0(P_{\theta_c}, P_{\xi_c}, P_{\Omega}, \theta_c) = P_{\theta_c}\dot{\theta}_c + P_{\xi_c}\dot{\xi}_c + P_{\Omega}\dot{\Omega} - L_{\mathrm{eq}}, \tag{5.8}$$

where L_{eq} is the unperturbed part of the Little John's Lagrangian. This Hamiltonian describes the unperturbed guiding centre dynamics of EPs with

$$P_{\theta_c} = e\psi + mv_{\parallel}b_{\theta_c}, \tag{5.9a}$$
$$P_{\xi_c} = -e\chi + mv_{\parallel}b_{\xi_c}, \tag{5.9b}$$
$$P_{\Omega} = \frac{m}{e}\mu. \tag{5.9c}$$

where χ and ψ denote the poloidal and toroidal flux, respectively. The set $(P_{\theta_c}, P_{\xi_c}, P_{\Omega})$ are the canonical momenta conjugated to $(\theta_c, \xi_c, \Omega)$. For this completely integrable system, the θ_c-dependence of the Hamiltonian can be eliminated by using a canonical transformation

to action-angle variables. In these variables, we have

$$H_0 = H_0(P_{\tilde{\theta}_c}, P_{\tilde{\xi}_c}, P_{\tilde{\Omega}}), \tag{5.10}$$

where the action variables $(P_{\tilde{\theta}_c}, P_{\tilde{\xi}_c}, P_{\tilde{\Omega}})$ correspond to the angles $(\tilde{\theta}_c, \tilde{\xi}_c, \tilde{\Omega})$ that are linear functions of time in the unperturbed motion, i.e.,

$$\dot{\tilde{\theta}}_c = \frac{\partial H_0}{\partial P_{\tilde{\theta}_c}} = \omega_{\tilde{\theta}_c}, \tag{5.11a}$$

$$\dot{\tilde{\xi}}_c = \frac{\partial H_0}{\partial P_{\tilde{\xi}_c}} = \omega_{\tilde{\xi}_c}. \tag{5.11b}$$

To describe the perturbed motion of the particles, we write their total Hamiltonian H_{total} as a sum of the unperturbed Hamiltonian H_0 and a perturbation U associated with the wave. This gives

$$H_{\text{total}} = H_0 + U. \tag{5.12}$$

We use the following representation for the perturbation U

$$U = \Sigma_{h,m}\phi_{m;n;h}\left(r_c; t\right)^{ih(m\theta_c + n\xi_c - \alpha(t))}. \tag{5.13}$$

where h denotes the h^{th} harmonic of the non-linear wave and r_c is the generalised radial coordinate corresponding to $\tilde{\theta}_c$ and $\tilde{\xi}_c$. This representation corresponds to a single chirping wave formed and evolved as a BGK-type wave through excitation of sideband/secondary oscillations of a single eigenmode in an isolated resonance. BGK modes are long-term non-linear solutions to the Vlasov–Poisson system which propagate steadily and in Ref. [35] chirping waves are described as BGK nonlinear waves that last much longer than the inverse linear damping rate while they are upshifting and downshifting in frequency. We rewrite U in terms of the action-angle variables of the unperturbed motion to have

$$H_{\text{total}} = H_0 + U(P_{\tilde{\theta}_c}; P_{\tilde{\xi}_c}; P_{\tilde{\Omega}}; p\tilde{\theta}_c + h\left[n\tilde{\xi}_c - \alpha\left(t\right)\right]). \tag{5.14}$$

Here, U is associated with an individual particle resonance, denoted by $l = \frac{p}{h}$, which includes several terms from expression (5.13) i.e. U is a periodic function but not necessarily sinusoidal. The coefficients of the aforementioned expansion are the orbit-averaged mode amplitudes which represent the coupling strength (see Refs. [30, 47]). For the dynamics governed by the total Hamiltonian given above, $P_{\tilde{\Omega}}$ is already a conserved quantity and since the Hamiltonian depends on a combination of $\tilde{\theta}_c$ and $\tilde{\xi}_c$, we have another immediate conservation law which makes the problem essentially one dimensional. This 1D description of wave-particle interaction can be represented by transferring the coordinates canonically to a frame co-moving with the chirping wave. A type-2 generating function for such a transformation is

$$G_2\left(\boldsymbol{q}, \boldsymbol{p}_{\text{new}}, t\right) = P_1\left[l\tilde{\theta}_c + n\tilde{\xi}_c - \alpha\left(t\right)\right] + P_2\tilde{\xi}_c + P_3\tilde{\Omega}. \tag{5.15}$$

It can be used to write the explicit expressions for the new variables and constants of

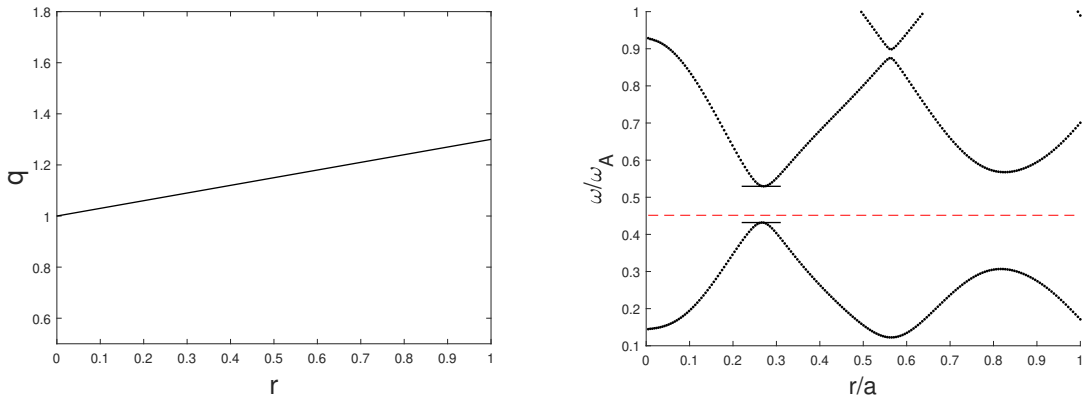

(a) (b)

Figure 5.1: (a) The safety factor and (b) the corresponding shear Alfvén continuum in a circular cross section configuration for $n = 6$. The red dashed line represents the linear frequency of the toroidal Alfvén eigenmode.

motion as

$$\begin{aligned} P_1 &= \frac{1}{l} P_{\tilde{\theta}_c} & Q_1 &= \zeta_l = l\tilde{\theta}_c + n\tilde{\xi}_c - \alpha\,(t) \\ P_2 &= P_{\tilde{\xi}_c} + \frac{n}{l} P_{\tilde{\theta}_c} & Q_2 &= \tilde{\xi}_c \\ P_3 &= P_{\tilde{\Omega}} & Q_3 &= \tilde{\Omega}, \end{aligned} \tag{5.16}$$

after which the new Hamiltonian takes the form

$$H_{\text{new}} = H_{\text{eq}}(P_1, P_2, P_3) + U(\zeta, P_1, P_2, P_3) + \frac{\partial G_2}{\partial t}, \tag{5.17}$$

where P_2 and P_3 are constants of motion and a generalized momentum (P_1) and its corresponding coordinate (ζ), to which the momentum is conjugated, constitute the dynamical variables. We thereby follow the EPs dynamics in $P_1 - \zeta$ on sub-slices of $P_2 = \text{const}$ and $P_3 = \text{const}$. The distinctive feature of the chosen variables is that P_2 remains conserved as the frequency chirps. In what follows, we focus on the first harmonic of the nonlinear wave $l = 1$ and we drop the subscript $l = 1$ from ζ for simplicity.

So far, we have introduced proper coordinates for our phase-space analysis, and the next step is to identify how the six-dimensional coordinate transformation of $(P_{\theta_c}, P_{\xi_c}, P_\Omega, \theta_c, \xi_c, \Omega) \rightarrow (P_{\tilde{\theta}_c}, P_{\tilde{\xi}_c}, P_{\tilde{\Omega}}, \tilde{\theta}_c, \tilde{\xi}_c, \tilde{\Omega})$ is carried out. We do that by relating the EPs frequencies to $P_{\tilde{\theta}_c}$ and $P_{\tilde{\xi}_c}$ using Eqs. (5.11a), (5.11b) and (5.10).

Given (5.10), H_0 is known as the particle energy (E), and $P_{\tilde{\xi}_c}$ and $P_{\tilde{\Omega}}$ are also known quantities and can be evaluated using (5.9b) and (5.9c), respectively, for ξ_c and Ω being ignorable coordinates in H_0 of (5.8). Hence, Eq. (5.10) can be inverted to write

$$P_{\tilde{\theta}_c} = P_{\tilde{\theta}_c}(H_0 = E, P_{\tilde{\xi}_c}, P_{\tilde{\Omega}}). \tag{5.18}$$

We use the following procedure to implement this inversion. For a slice of $\mu = \text{const}$, we write

$$P_{\tilde{\theta}_c} = G(E, P_{\tilde{\xi}_c}), \tag{5.19}$$

where G is a 2D polynomial of $\sqrt{E}$ and $P_{\tilde{\xi}_c}$. The reason we take G as a function of $\sqrt{E}$ is that in this work we focus on the highly passing particles ($\mu = 0$), as in a neutral beam injection (NBI) scenario, for which $\omega_{\tilde{\theta}_c} = \frac{v_\parallel}{qR_0} \propto \sqrt{E}$ and $\omega_{\tilde{\xi}_c} = \frac{v_\parallel}{R_0} \propto \sqrt{E}$. Therefore, we have $H_0(G(E, P_{\tilde{\xi}_c}), P_{\tilde{\xi}_c})$. Applying the derivative operator to both sides of (5.19) with respect to $P_{\tilde{\theta}_c}$ and $P_{\tilde{\xi}_c}$ gives

$$\frac{\partial G}{\partial E} = \frac{1}{\hat{\omega}_{\tilde{\theta}_c}} \text{and} \tag{5.20a}$$

$$\frac{\partial G}{\partial P_{\tilde{\xi}_c}} = -\frac{\partial G}{\partial E}\hat{\omega}_{\tilde{\xi}_c}, \tag{5.20b}$$

respectively, where Eqs. (5.11a) and (5.11b) are used and $\hat{}$ denotes the frequencies calculated using the fitting function G. To fit G, we use the method of least squares with the following minimization function

$$M = \frac{1}{N}[\sum_{i=1}^{N}(\frac{1}{\hat{\omega}_{\tilde{\theta}_c}} - \frac{1}{\omega_{\tilde{\theta}_c}})^2 + \sum_{i=1}^{N}(\frac{1}{\hat{\omega}_{\tilde{\xi}_c}} - \frac{1}{\omega_{\tilde{\xi}_c}})^2], \tag{5.21}$$

where N is the total number of EPs on a $\mu = \text{const}$ slice. In order to evaluate M, the equilibrium frequencies $(\omega_{\tilde{\theta}_c}, \omega_{\tilde{\xi}_c})$ must be determined from simulation. These are computed by tracing particle trajectories for different $P_{\tilde{\xi}_c}$ and E. Once known, the polynomial coefficients of G are varied until Eq. (5.21) is minimised. This determines G.

Considering the set (R, z, φ) as the cylinderical coordinate, we consider $\tilde{\theta}_c = 0$ and $\tilde{\xi}_c = \varphi$ on the $z = 0$ plane with largest R where we also record the particle data. On this plane, the canonical angles (θ_c, ξ_c) equal geometrical angles (see [129] and Eq.23 of Ref. [130]). As a convenient choice, this plane can also be used to show $P_{\tilde{\xi}_c} = P_\varphi$, where P_φ is the toroidal angular momenta conjugated to φ.

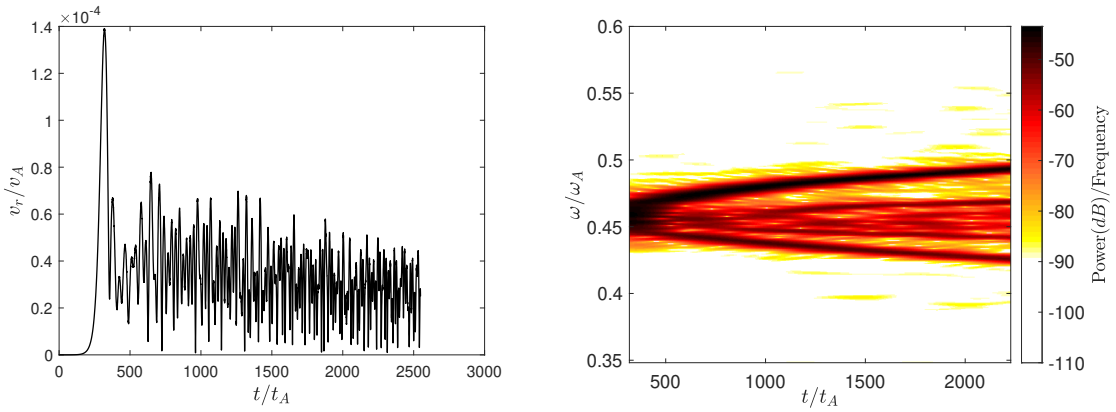

Figure 5.2: Time evolution of the TAE envelope (a) and the frequency spectrogram (b) for $n = 6$, $m = 6$ oscillations at $r/a = 0.27$. The y-axis of panel a shows the normalised radial component of the plasma velocity. The color bar of panel b represents an estimate of the short-term time-localized frequency content of cos component of v_r. The dissipative coefficients are kept the same as given in expression (5.23) throughout the mode evolution.

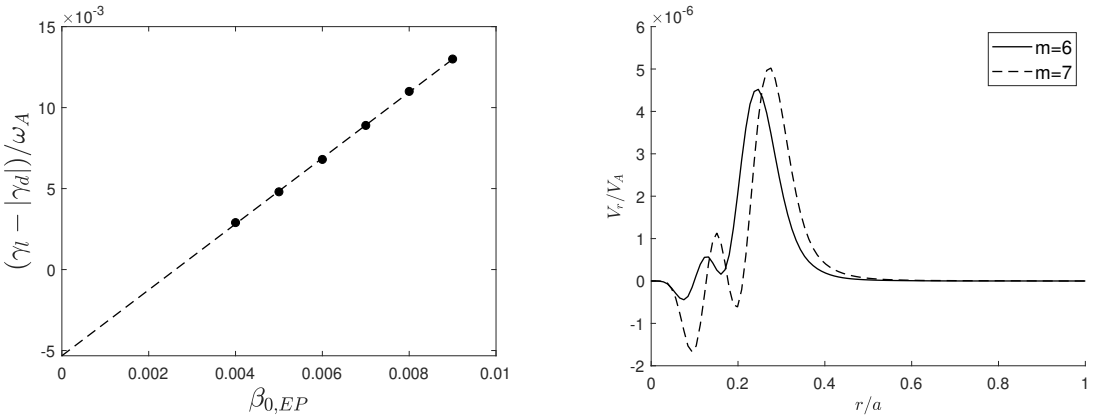

(a) (b)

Figure 5.3: (a) A scan of the net growth rate versus EP pressure on axis from simulation data (the black circles) and a linear fit to the data (dashed line) and (b) the structure of the radial component of the bulk plasma velocity (v_r), normalised to the Alfvén velocity on the axis (v_A), versus the normalised minor radius at $t/t_A = 217.6$. Here, t_A is the Alfvén time on the axis.

The above approach gives an essentially 1D representation of the wave-particle interaction using phase-space plots in P_1-ζ space. A notable advantage of this method is that P_2 is conserved even when the frequency experiences long deviation from the initial eigenfrequency. This has important implications when resolving the question of whether the EPs trapped inside the chirping wave are carried with the wave (consistent with the adiabatic theory of frequency chirping) or different particles are perturbed by the wave as the frequency chirps. The mapping technique of transferring to the canonical coordinates, introduced above, is not restricted to TAE-type perturbations and can be implemented to study the phase dynamics of particles interacting with other types of perturbations such as tearing modes, energetic particle modes and fishbone-type oscillations, amongst others.

5.4 Analysis of the simulations

The MEGA code uses an equilibrium configuration constructed by a Grad-Shafranov solver for a given q-profile. In this work, we use a linear q-profile depicted in figure 5.1a. The novel phase-space analysis tool described in section 5.3 is not restricted to the shape of the q-profile and the choice of the linear q-profile here is just for the purpose of illustration and simplicity. We choose the inverse aspect ratio $\epsilon = 3.2$. The density and pressure are uniform throughout the plasma. The corresponding shear Alfvén continuum for $n = 6$ is plotted in figure 5.1b. The accumulation points of the first gap are located at $r/a = 0.26$. For a TAE, the q-profile has a rational value at the cylindrical cross-over points, where $q = (2m + 1)/2n$. As shown in figure 5.1a, the first gap corresponds to $m = 6$ coupled to $m = 7$, and the second gap located at $r/a = 0.82$ corresponds to $m = 7$ that is coupled to $m = 8$. The equilibrium phase-space density of EPs is initialized using a slowing down distribution given by

$$F_{\mathrm{eq},\alpha} = \frac{\kappa}{E^3 + E_{\mathrm{crt}}^3}[1 + \mathrm{erf}(\frac{E_0 - E}{\Delta E})] \exp\left(-\frac{\langle\psi\rangle}{\Delta\psi}\right), \tag{5.22}$$

where $E_{\rm crt}$ and E_0 represent the critical and birth energies of the alpha particles, respectively, ψ is the poloidal magnetic flux, $\langle\rangle$ denotes averaging over the particle orbit, ΔE and $\Delta\psi$ specify the characteristic width of the equilibrium phase-space density in energy and ψ, respectively. For the purpose of this work, the values are set as $E_0 = 1.44E_A$, $E_{\rm crt} = 0.25E_A$, $\Delta E = 0.0144E_A$ and $\Delta\psi = 0.148\psi_{\rm max}$, where $\psi_{\rm max}$ is the maximum value of ψ and $E_A = \frac{1}{2}mv_A^2$ with v_A being the Alfvén velocity at the centre of the plasma. The EPs pressure is set to give an EP beta value of $\beta_{0,EP} = 0.6\%$ on the magnetic axis. The damping coefficients are

$$\nu = \eta = 0.3 \times 10^{-7} v_A R_0, \qquad \nu_n = \lambda = 0. \tag{5.23}$$

5.4.1 Evolution of the driven eigenmode

By solving the initial value problem with the MEGA code we find that the dominant perturbation is a TAE excited above the lower tip of the first gap with a linear frequency $\omega_{\rm TAE}/\omega_A = 0.4553$, where ω_A is the Alfvén frequency on the axis. Figure 5.2 shows the evolution of the amplitude and the frequency of the mode. The absolute value of the plasma radial velocity v_r is depicted in figure 5.2a as a function of time. Using an exponential fit to the early/linear stage data of figure 5.2a, we find that the net growth rate of the mode is $(\gamma_l - |\gamma_d|)/\omega_A = 0.0067$. Similarly, we perform a scan of the net growth rate over $\beta_{0,EP}$ to find the damping rate (γ_d) of the mode. This is depicted in figure 5.3a where a linear polynomial, fitted to the simulation data, identifies the intercept with the vertical axis. This gives a damping rate of $\gamma_d/\omega_A = 0.0053$ which corresponds to the energy being dissipated due to viscosity and resistivity in the coupled set of Eqs. (5.1) to (5.5). It does not account for any damping mechanism related with kinetic effects by the thermal ions. Subsequently, the linear growth rate of the TAE is $\gamma_l/\omega_A = 0.012$. Hence,

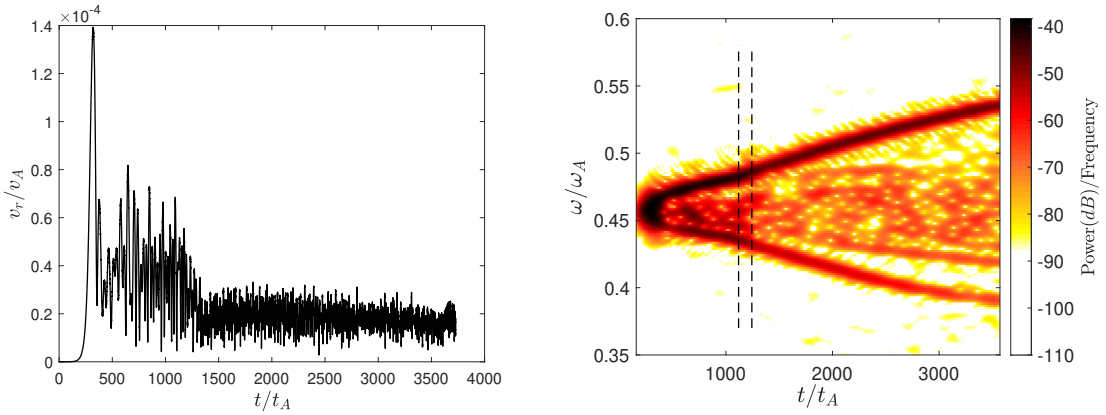

(a) (b)

Figure 5.4: Time evolution of the TAE envelope (a) and the frequency spectrogram (b) for $n = 6$, $m = 6$ oscillations at $r/a = 0.27$. The two vertical dashed lines on panel b denote the times, namely $t/t_A = 1119.1$ and 1243.4, at which the damping coefficients has been increased. The color bar represents an estimate of the short-term time-localized frequency content of cos component of v_r.

in this simulation we have

$$\gamma_d/\gamma_l = 0.44, \qquad \gamma_l/\omega_{\mathrm{TAE}} = 2.64\%.$$

The two dominant radial profiles of the TAE corresponding to the poloidal mode numbers $m = 6$ and 7 are shown in figure 5.3b. We observe that the peak lies around the location of the first gap of the shear Alfvén continuum.

Figure 5.2b shows an evolving spectrum of the cosine part of v_r. It reveals the primary up-ward and down-ward branches of frequency chirping. There are also secondary branches in the spectrogram. For a 1D electrostatic wave, Ref. [35] explains the frequency sweeping at early stages of sweeping as

$$\frac{\delta\omega}{\gamma_l} = \frac{16\sqrt{2}(\gamma_d t)^{1/2}}{3\sqrt{(3)}\pi^2}, \tag{5.24}$$

where $\delta\omega$ represents the frequency shift. Accordingly, Refs. [47, 53–57], provide a theory for long range frequency chirping for unstable eigenmodes in a dissipative background plasma. In these works, the frequency chirping is explained as a self-sustained nonlinear balance between the power extracted from the energetic particles and the power dissipated in the background plasma. To examine that in our self-consistent simulations, we have modified the dissipation coefficients during the frequency chirping.

We change the dissipation coefficients at $t/t_A = 1119.1$ and 1243.4, from their initial

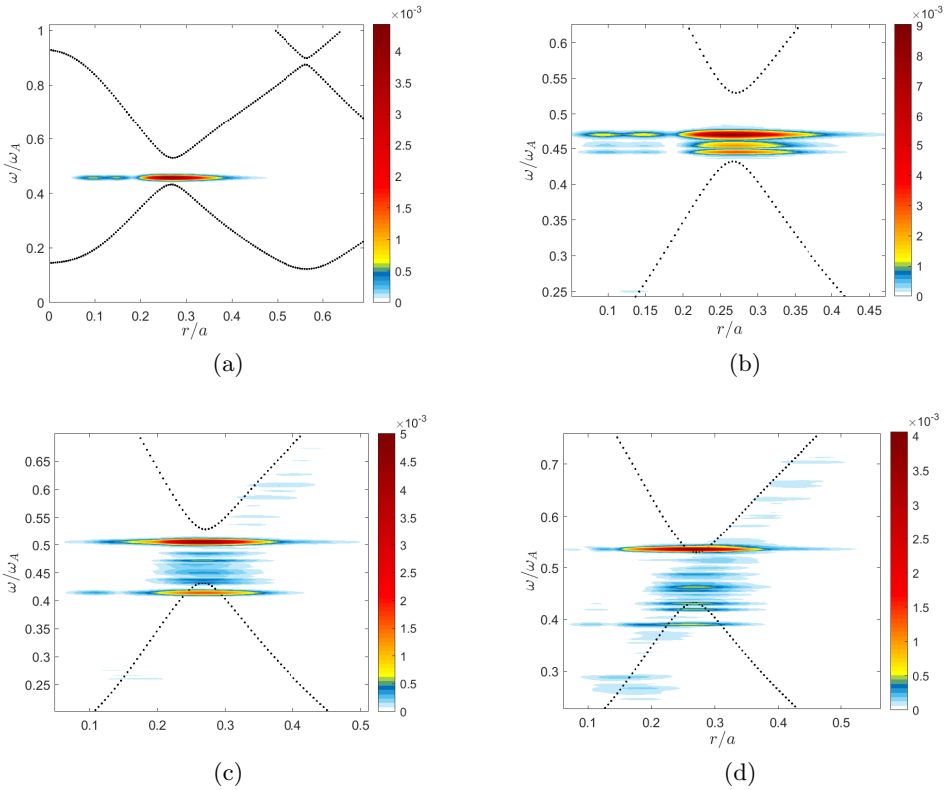

Figure 5.5: Frequency spectrum across the radial coordinate at different time slices. The color bar represents the absolute value of power(dB) per frequency. Panels (a), (b), (c) and (d) correspond to $t/t_A = 196.1$, $t/t_A = 469.7$, $t/t_A = 1713.1$ and $t/t_A = 3570.4$ respectively. The dotted line shows the Shear Alfvén continuum.

values of (5.23) to $\nu = \eta = 6 \times 10^{-7} v_A R_0$ and $\nu = \eta = 1.2 \times 10^{-6} v_A R_0$, respectively. We note that this change will not affect the linear evolution of the TAE. Figure 5.4 shows the resulting amplitude and frequency of the TAE as functions of time that we analyze subsequently. The times at which the damping rate has increased are denoted by vertical dashes in figure 5.4b. A comparison of figs. 5.2 and 5.4 shows that besides an expected drop in the amplitude of the signals, the rate of frequency chirping has increased in figure 5.4b after increasing the dissipation coefficients. Figure 5.4 confirms the essential role of dissipation in the chirping mechanism. The above technique of increasing the damping coefficients during the non-linear process of chirping provides a useful probing tool for nonlinear simulations. It can also save computational resources in large-scale simulations.

Figure 5.5 shows the frequency content at each radial location at four different stages of the wave evolution. The linear mode structure of figure 5.5a is comparable to the one shown in figure 5.3b. Figure 5.5b corresponds to the early stages of frequency chirping where the sideband/secondary waves have just formed inside the toroidicity gap. In figs. 5.5c and 5.5d, the frequencies of the chirping waves deviate further from the initial eigenfrequency towards the tips of the gap which leads to the excitation of continuum waves. Finally, the frequencies of the chirping waves enter the shear Alfvén continuum and exhibit different frequencies at different radial locations as they follow the continuum.

5.4.2 Resonance condition

In tokamak plasmas, the resonance condition between the particle guiding center motion and a wave with a toroidal mode number n reads [11]

$$\omega = n\omega_{\tilde{\xi}_c} + p\omega_{\tilde{\theta}_c}. \tag{5.25}$$

where p is an integer. In the case of TAE, the mode has two dominant poloidal components of the field (m and $m+1$). These two components have opposite phase velocities along the magnetic field. Consequently, the strongly co-passing particles resonate at $p = -m$, whereas the strongly counter-passing particles resonate at $p = -(m+1)$ [58]. For our

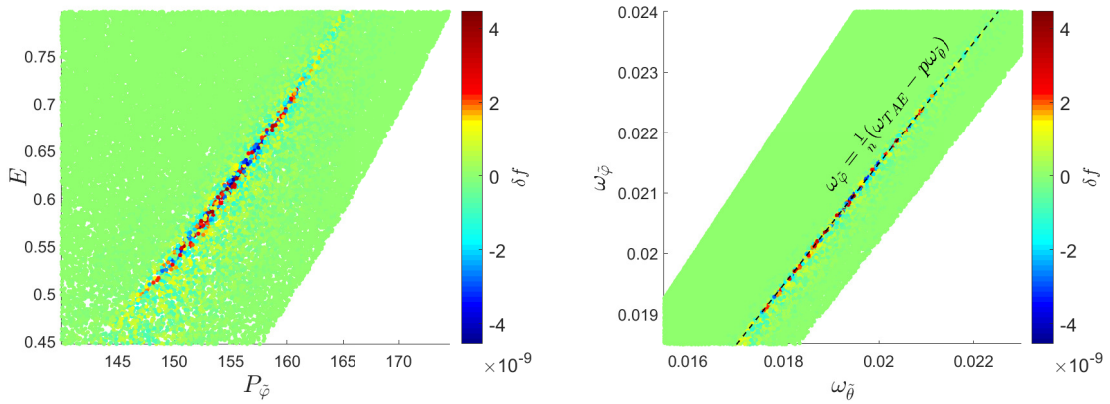

(a) (b)

Figure 5.6: The resonance curve (a) and the resonance line (b) in E vs. P_φ and $\omega_{\tilde{\xi}_c}$ vs. $\omega_{\tilde{\theta}_c}$ plane, respectively. Each panel shows a $\mu = 0$ slice of the phase-space for co-passing EPs. The color bar represents the particle weights (perturbed distributions). The dashed line is a fit using the resonance condition of (5.25).

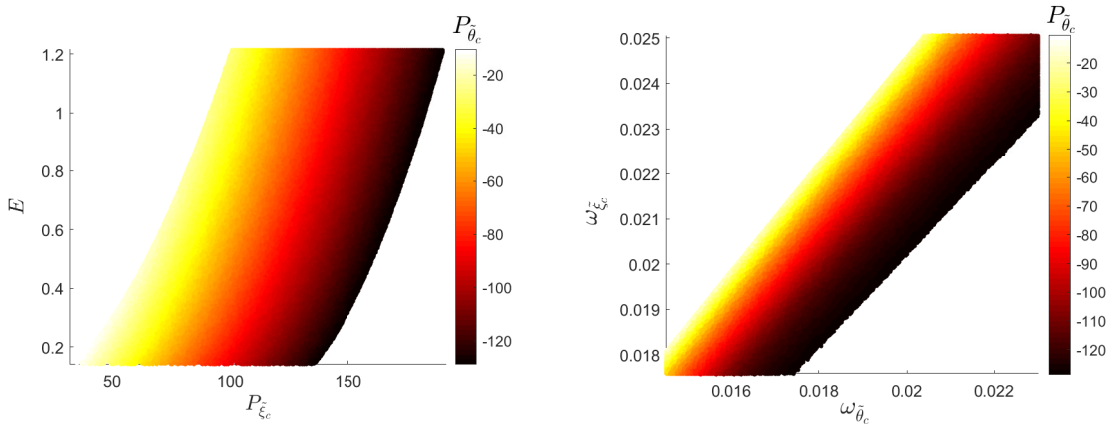

Figure 5.7: The action corresponding to the poloidal angular momenta for $\mu = 0$ in (a) E vs. P_φ plane and (b) $\omega_{\tilde{\xi}_c}$ VS. $\omega_{\tilde{\theta}_c}$

.

modes of interest, we expect the co-passing particle resonance to be at $n = 6$ and $p = -6$ in the simulations.

Figure 5.6 shows two images of the perturbed particle distribution function: the color-coded particle weights on the $E - P_\varphi$ plane and on the $\omega_{\tilde{\xi}_c} - \omega_{\tilde{\theta}_c}$ plane at the same time. As expected, the perturbed distribution is strongly localized around the resonance line with $n = 6$ and $p = -6$.

5.4.3 Numerical calculation of $P_{\tilde{\theta}}$

The known frequencies of the unperturbed motion for $\mu = 0$ enable calculation of $P_{\tilde{\theta}_c}$ and, thereby, the generating function of the canonical transformation to action-angle variables. To solve this problem, we have used the CVX package [131] which supports disciplined convex programming to convex optimization. Figure 5.7a shows $P_{\tilde{\theta}_c}$ as a function of E and P_φ. Similarly, the dependence of $P_{\tilde{\theta}_c}$ on the precession frequency $\omega_{\tilde{\xi}_c}$ and the bounce frequency $\omega_{\tilde{\theta}_c}$ is depicted in figure 5.7b. We observe that for fixed values of E, the absolute value of $P_{\tilde{\theta}_c}$ is directly proportional to P_φ. However, a slice of $P_\varphi = \text{const}$ demonstrates an inverse relation between the absolute values of P_φ and E. It should be mentioned that for each $\mu = cnst$ layer of the phase-space, $P_{\tilde{\theta}_c}$ can be calculated similarly using the fitting method described above.

At this point, we have introduced all the ingredients to observe/analyse the phase-space dynamics using (P_1, P_2, P_3). Figure 5.8 demonstrates the data of figure 5.6 in the $P_{\tilde{\theta}_c} - P_\varphi$ plane. The black lines represent $P_2 = \text{const}$ trajectories. Each $P_2 = \text{const}$ line corresponds to a sub-layer of the phase-space on which the EPs lie during the evolution of the instability; from the linear phase towards the long range frequency chirping stage. In what follows, we study the detailed dynamics of the resonance in the $P_1 - \zeta$ plane.

5.4.4 Convective transport of EPs in phase-space

In what follows, we analyze a set of particle data recorded at the moments when the particle trajectory crosses the $z = 0$ plane with $R > R_0$. The corresponding plots of $P_1 - \zeta$ are essentially Poincaré plots generated for $P_2 = \text{const}$ lines in figure 5.8. We focus on the

particles with $P_2 = 39$. This value is chosen to present EPs with the most perturbed phase-space density (see figure 5.8). To improve numerical resolution, we record the particle data in the narrow interval $|P_2 - 39| \leq 0.2$. The aforementioned Poincaré plots are shown in figure 5.9 at different stages of the TAE evolution. The colors in figs. 5.9a, 5.9c, 5.9e, 5.9g and 5.9i represent the perturbed weight/phase-space density of each particle. In the unperturbed state, each EP is assigned a color label according to its corresponding value of P_1 (see figure 5.9b). This label/color is kept the same throughout the simulations. Using this label, we produce a set of snapshots of the phase-space i.e. figs. 5.9b, 5.9d, 5.9f, 5.9h and 5.9j where the color bar denotes the particle label. The importance of these color labelled plots i.e. right panels of figure 5.9, in identifying whether the convective transport occurs can be explained as follows: In the left panels of figure 5.9, the color denotes the weight of the EPs related to the perturbed phase-space density. After the saturation of the wave, the plots demonstrate a group of detached perturbed particles at either side of the flattened area. One might imagine that the chirping waves cause local perturbations in phase-space and leave the particles behind and perturb another new set of particles. However, to reject this idea, we use the color labelled panels to show that the particles inside the chirping wave are the ones initially located around the linear resonance and are being carried by the BGK-type chirping waves in a moving phase-space bucket in a convective way.

Figures 5.9a and 5.9b correspond to the linear stages of the TAE excitation i.e. $t/t_A = 205.4$. Figures 5.9c and 5.9d demonstrate the coarse graining of the distribution function around $P_1 \approx 19.5$ in phase-space just before the non-linear saturation of the TAE. Figures 5.9e and 5.9f demonstrate the phase-space dynamics during the frequency chirping of the wave at $t/t_A = 2477.8$. At this point, the up-chirping and down-chirping waves have experienced a frequency sweep of 13.55% and 11.33%, respectively. We observe the holes (blue) and clumps (red) centered around $P_1 \approx 19.91$ and $P_1 \approx 18.95$, corresponding to the down-chirping and up-chirping waves, respectively. They form at either side of the flattened region and move in the phase-space of EPs as the frequencies chirp. The rest of the panels correspond to further evolution of the frequencies. It is worth mentioning that the dashed ovals in figure 5.9g mark the detachment of a second set of

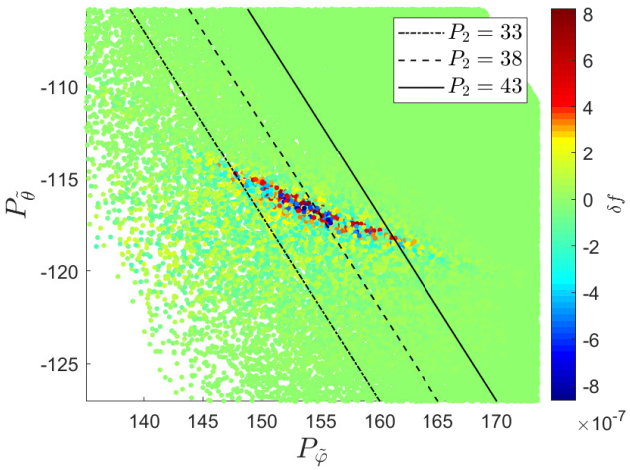

Figure 5.8: Phase-space dynamics of co-passing EPs on the $P_{\tilde{\theta}}$ vs. $P_{\tilde{\varphi}}$ plane with $\mu = 0$ prior to wave saturation. The black lines denote exact constants of motion during the wave evolution.

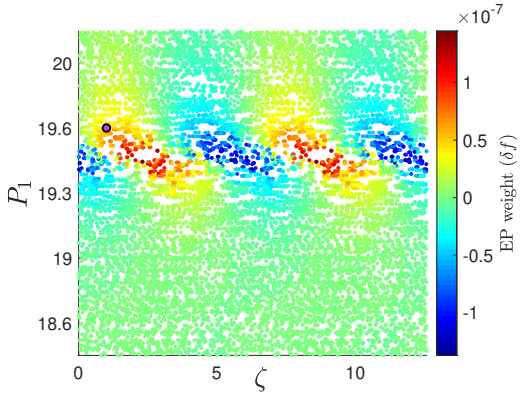

(a) $t/t_A = 205.4$

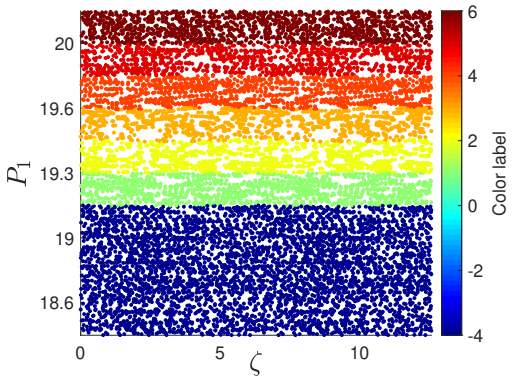

(b) $t/t_A = 205.4$

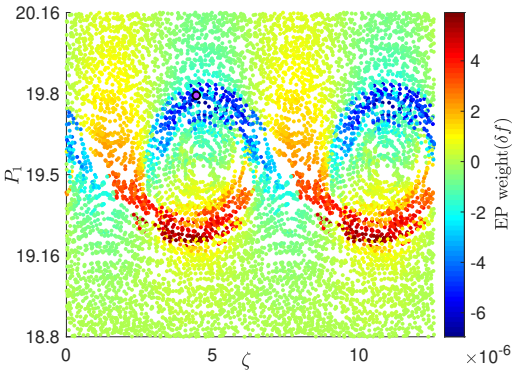

(c) $t/t_A = 314.5$

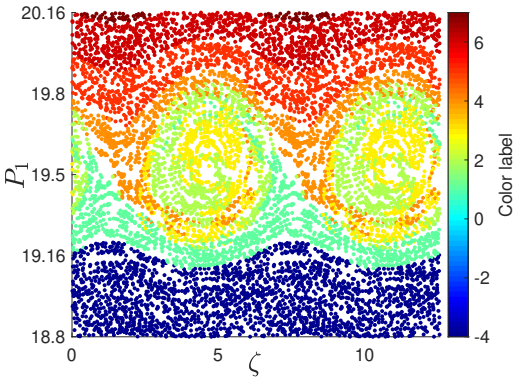

(d) $t/t_A = 314.5$

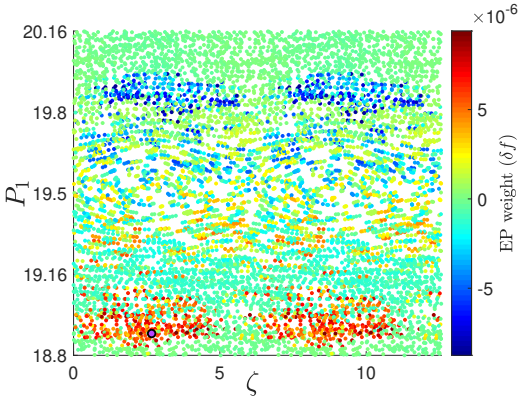

(e) $t/t_A = 2477.8$

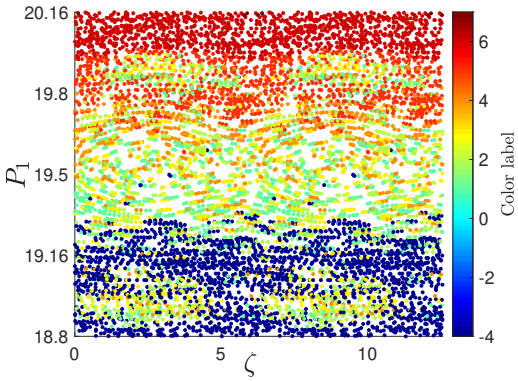

(f) $t/t_A = 2477.8$

Figure 5.9: A $\mu = 0$ and $P_2 \approx 39$ slice of the EPs phase-space as a function of EP weights (panels a,c and e) and EPs color label (panels b,d and f) at different stages of the wave evolution. The purple circle denotes a particle that is convected by the phase-space clump, continued ...

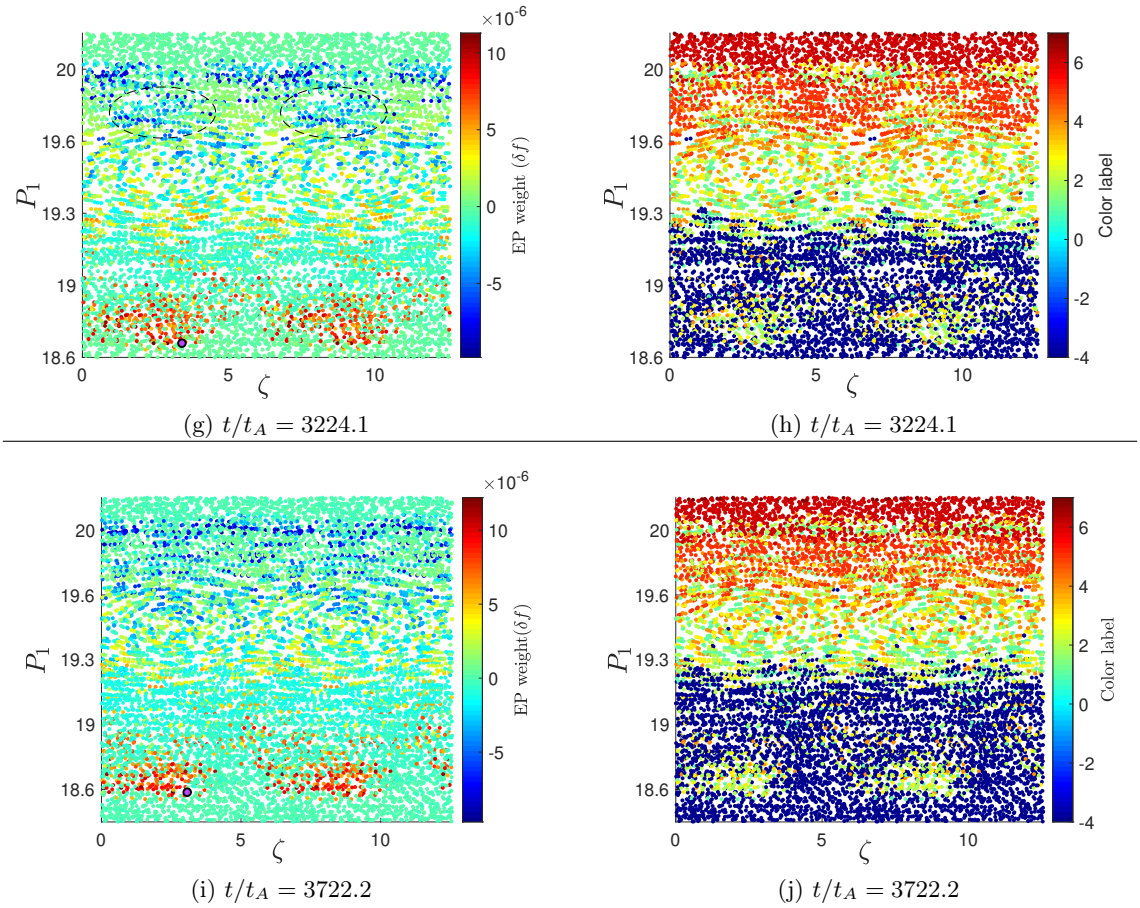

(g) $t/t_A = 3224.1$ (h) $t/t_A = 3224.1$

(i) $t/t_A = 3722.2$ (j) $t/t_A = 3722.2$

Figure 5.9: A $\mu = 0$ and $P_2 \approx 39$ slice of the EPs phase-space as a function of EP weights (panels g and i) and EPs color label (panels h and j) at different stages of the wave evolution. The purple circle denotes a particle that is convected by the phase-space clump.

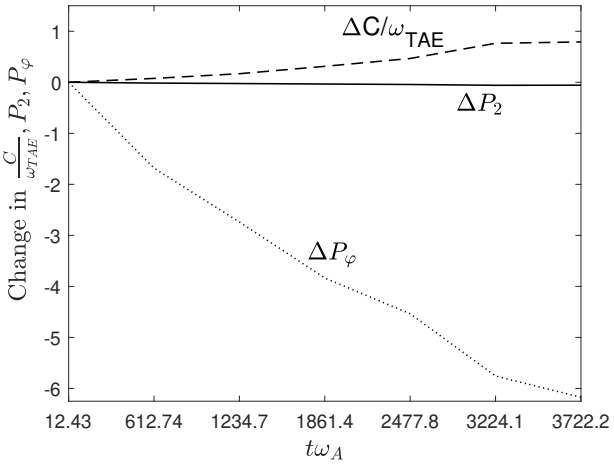

Figure 5.10: Variation of $\frac{C}{\omega_{\text{TAE}}}$, P_2 and P_φ at various stages of the TAE evolution.

phase-space holes. We attribute these structures to the second branch of down-chirping waves illustrated in figure 5.4b.

Since EPs remain on the same sub-layer of the phase-space, on which P_2 is a constant of motion, the constructed phase-space plots ascertain the mechanism under which the phase-space density is being perturbed. As figs. 5.9f, 5.9h and 5.9j clearly demonstrate, the phase-space islands act like buckets that carry particles in phase-space and lead to radial convection of the EPs.

Conservation of the generalised momentum P_2, given by (5.16), is the key part of this understanding. Although the constancy of P_2 is evident in phase-space plots of figure 5.9, we investigate the value of P_2 as a function of time for an EP which is transported by the up-chirping wave. This particle is denoted in figs. 5.9a, 5.9c, 5.9e, 5.9g and 5.9i by a purple circle. Simultaneously, we calculate the value of C, introduced in section 5.1, for the same EP. This comparison is depicted in figure 5.10 where the value of C, unlike P_2, changes as the mode frequency begins to chirp. It is worth noting that P_2 is comparable to $\frac{C}{\omega_{\mathrm{TAE}}}$ in terms of units. Hence, slices of $C = \text{const}$ do not represent the most appropriate sub-layers of the phase-space to study/observe the dynamics during the long range frequency chirping. Here, we explain why C can not be an appropriate constant during frequency chirping. In (E, p_φ, μ) coordinate, the φ and t dependency of the perturbation (δH) can be represented by $\delta H(n\varphi - \omega t)$. Then, Hamilton's equations give

$$\dot{p}_\varphi = -\frac{\partial \delta H}{\partial \varphi} = -n\delta H' \tag{5.26a}$$

$$\dot{E} = \frac{\partial \delta H}{\partial t} = -\omega \delta H', \tag{5.26b}$$

A simple arrangement gives

$$\frac{\dot{p}_\varphi}{n} = -\delta H' \tag{5.27a}$$

$$-\frac{\dot{E}}{\omega} = \delta H'. \tag{5.28}$$

This gives $\frac{\dot{p}_\varphi}{n} - \frac{\dot{E}}{\omega} = 0$. Therefore, $\frac{\mathrm{d}(\omega p_\varphi - nE)}{\mathrm{d}t} = 0$. Hence, $C = \omega p_\varphi - nE$ is a constant of motion. Nevertheless, all the above calculations are based on a fixed frequency (ω) and when $\omega(t)$, $\frac{\mathrm{d}C}{\mathrm{d}t}$ will not be zero anymore and hence the conventional constant of motion (C) for electromagnetic perturbations will not be an appropriate choice to analyse the phase-space of chirping waves.

5.5 Summary

We have refined the formalism for the phase-space analysis of the chirping modes driven by resonant energetic particles in a tokamak. As an application of this refinement, we analyze the results of self-consistent simulations performed with the MEGA code (an initial value problem solver in a hybrid MHD-kinetic model). The initial perturbation under study is a shear Alfvén eigenmode in the toroidicity-induced gap of the Alfvén continuum (TAE). The initial population of the energetic particles has an isotropic slowing down distribution. The EPs current provides a linear growth drive of $\gamma_l/\omega_{\mathrm{TAE}} = 2.64\%$ to the mode in the presence of background dissipation at a rate of $\gamma_d/\gamma_l = 0.44$.

Subsequent to the non-linear saturation of the eigenmode, the sideband (secondary)

oscillations appear inside the toroidicity gap. These modes evolve into chirping waves. In this case, we observe both up-ward and down-ward trends as the frequency chirps. We demonstrate that the rate of frequency sweeping increases with the damping rate of the eigenmode. As the chirping waves enter the shear Alfvén continuum, the radial structure of the perturbation experiences different frequencies at different radii. This is consistent with the theoretical model of Ref. [94].

A new conservation law is introduced which remains valid as the frequency of the wave chirps. This allows defining sub-layers of the EPs distribution function on which the particles are expected to remain even during the frequency chirping stage. Investigation of the energetic particle dynamics reveals that these particles lie on the same sub-layer of the phase-space throughout the simulations. Contingent on the formation and evolution of the chirping waves, phase-space islands form and evolve adiabatically. This means that the same particles are carried inside the coherent phase-space islands providing a convective or bucket transport in phase-space. Once formed in the gap, the phase-space holes and clumps survive even in the shear Alfvén continuum.

In fusion plasmas, Alfvénic chirping waves are commonly observed in the non-linear phase of wave-particle interaction. This work clearly demonstrates that apart from diffusive transport of particles due to overlap of multiple resonances, a single isolated resonance of TAEs can also lead to the transport of particles in phase-space through convection. Such convective transports demonstrated in this work will result in a change in the particles flux surface label i.e. an inward or outward drift of the particles. This can lead to the ejection of the particles from the hot core of the plasma and negatively influence the machine performance by degrading particle confinement.

Acknowledgments

This work was funded by the Australian Research Council through Grant No. DP140100790 and supported by the U.S. Department of Energy Contract No. DEFG02–04ER54742. This research was undertaken with the assistance of resources and services from the National Computational Infrastructure (NCI), which is supported by the Australian Government. The National Institutes of Natural Sciences (NINS) and National Institute for Fusion Sciences (NIFS) have supported two internships of the first author at NIFS, Japan in 2018 and 2019. The first author is very thankful to Prof. Yasushi Todo, Prof. Masayuki Yokoyama, Prof. Hao Wang, Dr. Malik Idouakass and Dr. Jialei Wang for their kind hospitality and fruitful discussions during his stay at NIFS, Japan.

Chapter 6

Conclusion

In this PhD research, progress has been made in fields of Alfvénic chirping waves in tokamak plasmas. This research extends the theory of chirping waves in tokamaks by developing more realistic theoretical models accompanied by self-consistent simulations. By developing a novel phase space analysis tool and self-consistent hybrid simulations using the MEGA code, the mechanism of long range frequency chirping for toroidicity-induced Alfvén eignemodes (TAEs) has been clarified. The particle data of the simulations has been analysed using the proposed method. A distinctive conservation law is presented for particle dynamics which remains valid even if the frequency of the perturbation changes. This is achieved by constructing constants of motion for energetic particle dynamics in resonance with Alfvénic chirping modes in tokamak plasmas. The results show that chirping waves, which emerge after saturation of the linear TAE, are accompanied by the formation and evolution of coherent phase space structures, holes and clumps, which carry the energetic particles in the generalised phase space and lead to a convective transport. These observations are in agreement with the Berk-Breizman theory for chirping waves.

In terms of fast particle dynamics, the 1D adiabatic model of Boris [53] for long range electrostatic chirping waves does not capture particle orbits i.e. the highly passing limit where particles move freely. The guiding centre dynamics of the energetic particles, affected by the parallel field gradients, can impact the evolution of chirping waves in resonance with the particles. For the same amount of frequency shift, the rate of frequency chirping and the amount of change to the spatial profile of a chirping wave is a function of particles guiding centre orbits e.g. trapped or passing. In this thesis, a model has been developed that investigates the impact of particle orbits on BGK-type waves with long range frequency chirping. As an example, it has been shown that in the energy range for which the particle is trapped, the wave chirps faster when it is in resonance with more deeply trapped particles. An interesting behaviour is observed in the range of trapped particles. For monotonic chirping, the amplitude of the mode grows then decays. Hence, the above model needs to be extended to include particle trapping in phase space for cases where the amplitude of the chirping wave grows i.e. the separatrix of the corresponding phase space island expands.

A phase space waterbag model is developed to enable particle trapping for chirping waves with growing potentials. Since numerical simulations reveal the formation of holes/clumps off the initial resonance, this new model uses the BOT code data to initialise the shape of phase space islands at the point where they have just been formed. This model allows a study over the full range of particle orbits. In addition, it has been demonstrated that there are energy regions in which the contribution of higher particle resonances to the linear growth rate can be higher than the 1^{st} resonance. In these regions, investigation of the model shows a considerable change in the hard-nonlinear evolution of chirping

waves under the impact of higher particle resonances. The implication to frequency chirping models for experimental observations is that depending on the wave frequency under study, the contribution of higher resonances must be taken into account.

The nonperturbative theoretical framework for describing chirping waves has been extended to Alfvénic waves in tokamaks [47]. The model investigates the excitation of a Global Alfvén eigenmode that evolves into chirping modes in a neutral beam injection scenario in the limit of a high aspect ratio configuration. The radial profile of the Alfvén wave is described using the method of finite elements and the nonlinear wave equation is derived by varying the total Lagrangian of the system with regards to the weights of the elements. It is inferred that the frequency chirping changes the radial structure of the corresponding chirping wave. The model shows how the energetic particles can be drifted radially in a tokamak plasma due to long range Alfvénic chirping observed in fusion experiments.

Last but not least, further avenues of research that stem from this PhD can be outlined as follows

- All the reduced frequency chirping theoretical models discussed in this thesis assume a uniform effective electric field V_{eff} (the orbit averaged mode amplitude or the coupling strength), inside the wave trapping region; a zeroth order approximation around the middle of the separatrix in phase space. The cases where this assumption holds include: the limit of very highly passing particles for $k_{\text{pert}}/k_{\text{eq}} = 1$ or the small separatrix width limit $\gamma_l \ll \omega_{\text{pe}}$ where γ_l is the linear growth rate of the plasma wave with linear oscillations in a time scale on the order of ω_{pe}^{-1}. In the chirping problem of chapter 2, the orbit averaged mode amplitude depends on factors such as the spatial periodicity of the equilibrium field ($\lambda_{\text{eq}} = 2\pi/k_{\text{eq}}$), the wavenumber of the perturbation (k_{pert}) and the action (J) corresponding to the equilibrium motion of particles in the absence of the perturbations. In cases where V_{eff} is a steep function of the particle action, approximating V_{eff} inside the island by the first term of its Taylor expansion around J implies the island separatrix width is small. For typical values of mode growth rates observed in experiments, this might not be always true. Therefore, a further study can be done by firstly introduce regions of steep gradient for V_{eff} in the particle action. Then, for the physical parameters which result in experimentally relevant values of the growth rate, a new model can be developed to investigate the phase-space dynamics and identify the island shape. In this model, V_{eff} should be updated along the perturbed phase-space dynamics of the particles. This implies that the self-consistent electric field of the wave is a function of the velocity of the particles bouncing inside the wave separatrix.

- A future direction is to generalize the Lagrangian model given in chapter 3 such that all the spatial components of the global Alfvén wave are simultaneously updated. This can be achieved by considering a Fourier decomposition for the periodic component of the wave structure in addition to the finite element representation of the radial profile.

- For higher values of the linear growth rate than the one reported in chapter 5, the frequency of the lower sideband oscillation, which emerges after saturation of the toroidicity-induced Alfvén eigenmode, lies inside the shear Alfvén continuum. In this case, numerical analysis reveals that the downward chirping wave almost vanishes i.e. the corresponding signal significantly weakens and holes and clumps

do not form in phase space. Further investigation of this phenomenon using the MEGA code, together with a theoretical framework to study the influence of shear continuum on the formation of sideband waves, would shed light on the impact of continuum damping as the mode chirps into the continuum.

Bibliography

[1] F. Chen, *Introduction to Plasma Physics and Controlled Fusion.* Springer International Publishing, 2015.

[2] *Nonlinear Properties of Electrostatic Vlasov Plasmas*, ch. 5, pp. 215–296. John Wiley Sons, Ltd, 2019.

[3] J. P. H. Goedbloed and S. Poedts, *Principles of Magnetohydrodynamics: With Applications to Laboratory and Astrophysical Plasmas.* Cambridge University Press, 2004.

[4] A. A. Vlasov, "The oscillation properties of an electron gas," *Zhur. Eksp. Teor. Fiz.*, vol. 8, p. 291–318, 1938.

[5] A. A. Vlasov, "Vibrational properties, crystal structure, non-dissipated counterdirected currents and spontaneous origin of these properties in a "gas"," *J. Phys. USSR*, vol. 9, pp. 25–40, 1945.

[6] L. D. Landau, "On the vibrations of the electronic plasma," *J. Phys. USSR*, vol. 10, p. 574, 1946.

[7] K. Appert, R. Gruber, F. Troyuon, and J. Vaclavik, "Excitation of global eigenmodes of the Alfven wave in Tokamaks," *Plasma Physics*, vol. 24, no. 9, p. 1147, 1982.

[8] T. A. A. Fukuyama, "Kinetic global analysis of alfven eigenmodes in toroidal plasmas," *In Proceedings of the 19th International Conference on Fusion Energy*, vol. 238, pp. TH/P3–14, IAEA 2002.

[9] C. Cheng, L. Chen, and M. Chance, "High-n ideal and resistive shear Alfvén waves in tokamaks," *Annals of Physics*, vol. 161, no. 1, pp. 21–47, 1985.

[10] W. W. Heidbrink, E. J. Strait, M. S. Chu, and A. D. Turnbull, "Observation of beta-induced alfvén eigenmodes in the diii-d tokamak," *Phys. Rev. Lett.*, vol. 71, pp. 855–858, Aug 1993.

[11] W. W. Heidbrink, "Basic physics of Alfvén instabilities driven by energetic particles in toroidally confined plasmasa)," *Physics of Plasmas*, vol. 15, no. 5, 2008.

[12] A. Fasoli, C. Gormenzano, H. Berk, B. Breizman, S. Briguglio, D. Darrow, N. Gorelenkov, W. Heidbrink, A. Jaun, S. Konovalov, R. Nazikian, J.-M. Noterdaeme, S. Sharapov, K. Shinohara, D. Testa, K. Tobita, Y. Todo, G. Vlad, and F. Zonca, "Chapter 5: Physics of energetic ions," *Nuclear Fusion*, vol. 47, pp. S264–S284, jun 2007.

[13] S. Sharapov, B. Alper, H. Berk, D. Borba, B. Breizman, C. Challis, I. Classen, E. Edlund, J. Eriksson, A. Fasoli, E. Fredrickson, G. Fu, M. Garcia-Munoz, T. Gassner,

K. Ghantous, V. Goloborodko, N. Gorelenkov, M. Gryaznevich, S. Hacquin, W. Heidbrink, C. Hellesen, V. Kiptily, G. Kramer, P. Lauber, M. Lilley, M. Lisak, F. Nabais, R. Nazikian, R. Nyqvist, M. Osakabe, C. P. von Thun, S. Pinches, M. Podesta, M. Porkolab, K. Shinohara, K. Schoepf, Y. Todo, K. Toi, M. V. Zeeland, I. Voitsekhovich, R. White, V. Yavorskij, and and, "Energetic particle instabilities in fusion plasmas," *Nuclear Fusion*, vol. 53, p. 104022, sep 2013.

[14] N. Gorelenkov, S. Pinches, and K. Toi, "Energetic particle physics in fusion research in preparation for burning plasma experiments," *Nuclear Fusion*, vol. 54, p. 125001, nov 2014.

[15] L. Chen, "Theory of magnetohydrodynamic instabilities excited by energetic particles in tokamaks*," *Physics of Plasmas*, vol. 1, no. 5, pp. 1519–1522, 1994.

[16] T. O'Neil, "Collisionless Damping of Nonlinear Plasma Oscillations," *Physics of Fluids*, vol. 8, pp. 2255–2262, Dec. 1965.

[17] Y. A. Mazitov, "K. 1. rozental and vi veselovskii," *Elektrokhimiya*, vol. 1, p. 36, 1965.

[18] R. L. DEWAR and J. C. C. YAP, "Adiabatic wave-particle interaction revisited," *Plasma and Fusion Research*, vol. 4, pp. 001–001, 2009.

[19] A. A. Vedenov, E. P. Velichov, and R. Z. Sagdeev *Usp. Fiz. Nauk*, vol. 73, p. 701, 1961.

[20] W. E. Drummond and D. pines *Nucl. Fusion Suppl.*, vol. 3, p. 1049, 1962.

[21] B. D. Fried, C. S. Liu, R. W. Means, and R. Z. Sagdeev *See National Technical Information Service Document No. AD730123, University of California, Los Angeles*, pp. Report No. PPG–93, 1971.

[22] M. B. Levin, M. G. Lyubarsky, I. N. Onishchenko, V. D.Shapiro, and V. I. Shevchenko *Sov. Phys. JETP35*, vol. 35, p. 898, 1972.

[23] V. E. Zakharov and V. I. Karpman *Zh. Eksp. Teor. Fiz.*, vol. 43, p. 490, 1962.

[24] X. Garbet, P. Donnel, C. Ehrlacher, E. Caschera, R. Dumont, M. Faganello, V. Grandgirard, P. Ghendrih, M. Idouakass, M. Lesur, Y. Sarazin, and D. Zarzoso, "On the relationship between residual zonal flows and bump-on tail saturated instabilities.," *Journal of Physics: Conference Series*, vol. 775, p. 012004, nov 2016.

[25] H. L. Berk and B. N. Breizman, "Saturation of a single mode driven by an energetic injected beam. i. plasma wave problem," *Physics of Fluids B: Plasma Physics*, vol. 2, no. 9, pp. 2226–2234, 1990.

[26] H. L. Berk and B. N. Breizman, "Saturation of a single mode driven by an energetic injected beam. ii. electrostatic "universal" destabilization mechanism," *Physics of Fluids B: Plasma Physics*, vol. 2, no. 9, pp. 2235–2245, 1990.

[27] H. L. Berk and B. N. Breizman, "Saturation of a single mode driven by an energetic injected beam. iii. alfvén wave problem," *Physics of Fluids B: Plasma Physics*, vol. 2, no. 9, pp. 2246–2252, 1990.

[28] H. L. Berk, B. N. Breizman, and H. Ye, "Scenarios for the nonlinear evolution of alpha-particle-induced alfvén wave instability," *Phys. Rev. Lett.*, vol. 68, pp. 3563–3566, Jun 1992.

[29] H. L. Berk, B. N. Breizman, and M. Pekker, "Numerical simulation of bump-on-tail instability with source and sink," *Physics of Plasmas*, vol. 2, no. 8, pp. 3007–3016, 1995.

[30] H. Berk, B. Breizman, and M. Pekker, "Simulation of alfven-wave-resonant-particle interaction," *Nuclear Fusion*, vol. 35, pp. 1713–1720, dec 1995.

[31] H. L. Berk, B. N. Breizman, and M. Pekker, "Nonlinear Dynamics of a Driven Mode near Marginal Stability," *Phys. Rev. Lett.*, vol. 76, pp. 1256–1259, Feb 1996.

[32] B. N. Breizman, H. L. Berk, M. S. Pekker, F. Porcelli, G. V. Stupakov, and K. L. Wong, "Critical nonlinear phenomena for kinetic instabilities near threshold," *Physics of Plasmas*, vol. 4, no. 5, pp. 1559–1568, 1997.

[33] M. K. Lilley, B. N. Breizman, and S. E. Sharapov, "Destabilizing Effect of Dynamical Friction on Fast-Particle-Driven Waves in a Near-Threshold Nonlinear Regime," *Phys. Rev. Lett.*, vol. 102, p. 195003, May 2009.

[34] H. L. Berk, B. N. Breizman, J. Candy, M. Pekker, and N. V. Petviashvili, "Spontaneous hole–clump pair creation," *Physics of Plasmas*, vol. 6, no. 8, pp. 3102–3113, 1999.

[35] H. Berk, B. Breizman, and N. Petviashvili, "Spontaneous hole-clump pair creation in weakly unstable plasmas," *Physics Letters A*, vol. 234, no. 3, pp. 213–218, 1997.

[36] N. P. H.L. Berk, B.N. Breizman, "pontaneous hole-clump pair creation in weakly unstable plasmas," *Phys. Lett. A*, vol. 238, no. 3, p. 408(E), 1998.

[37] S. Pinches, L. Appel, J. Candy, S. Sharapov, H. Berk, D. Borba, B. Breizman, T. Hender, K. Hopcraft, G. Huysmans, and W. Kerner, "The hagis self-consistent nonlinear wave-particle interaction model," *Computer Physics Communications*, vol. 111, no. 1, pp. 133–149, 1998.

[38] M. Lesur, Y. Idomura, and X. Garbet, "Fully nonlinear features of the energetic beam-driven instability," *Physics of Plasmas*, vol. 16, no. 9, p. 092305, 2009.

[39] M. Lesur and Y. Idomura, "Nonlinear categorization of the energetic-beam-driven instability with drag and diffusion," *Nuclear Fusion*, vol. 52, p. 094004, sep 2012.

[40] R. G. L. Vann, R. O. Dendy, and M. P. Gryaznevich, "Theoretical interpretation of frequency sweeping observations in the mega-amp spherical tokamak," *Physics of Plasmas*, vol. 12, no. 3, p. 032501, 2005.

[41] M. Lesur, *The Berk-Breizman Model as a Paradigm for Energetic Particle-driven Alfven Eigenmodes*. PhD thesis, PhD Thesis, diss., Ecole Polytechnique X, 2010. (FRCEA-TH–3018). France.

[42] A. Dudkovskaia, X. Garbet, M. Lesur, and H. Wilson, "Stability analysis of secondary modes, driven by the phase space island," *Nuclear Fusion*, vol. 59, p. 086010, jun 2019.

[43] M. K. Lilley, B. N. Breizman, and S. E. Sharapov, "Effect of dynamical friction on nonlinear energetic particle modes," *Physics of Plasmas*, vol. 17, no. 9, 2010.

[44] M. K. Lilley and R. M. Nyqvist, "Formation of phase space holes and clumps," *Phys. Rev. Lett.*, vol. 112, p. 155002, Apr 2014.

[45] M. Lilley and B. Breizman, "Convective transport of fast particles in dissipative plasmas near an instability threshold," *Nuclear Fusion*, vol. 52, p. 094002, sep 2012.

[46] M. Gryaznevich and S. Sharapov, "Frequency sweeping alfvén instabilities driven by super-alfvénic beams in the spherical tokamak START," *Nuclear Fusion*, vol. 40, pp. 907–912, may 2000.

[47] H. Hezaveh, Z. S. Qu, B. N. Breizman, and M. J. Hole, "Long range frequency chirping of alfvén eigenmodes," *Nuclear Fusion*, vol. 60, p. 056014, apr 2020.

[48] E. D. Fredrickson, R. E. Bell, D. S. Darrow, G. Y. Fu, N. N. Gorelenkov, B. P. LeBlanc, S. S. Medley, J. E. Menard, H. Park, A. L. Roquemore, W. W. Heidbrink, S. A. Sabbagh, D. Stutman, K. Tritz, N. A. Crocker, S. Kubota, W. Peebles, K. C. Lee, and F. M. Levinton, "Collective fast ion instability-induced losses in National Spherical Tokamak Experimenta)," *Physics of Plasmas*, vol. 13, no. 5, 2006.

[49] Y. Kusama, G. Kramer, H. Kimura, M. Saigusa, T. Ozeki, K. Tobita, T. Oikawa, K. Shinohara, T. Kondoh, M. Moriyama, F. Tchernychev, M. Nemoto, A. Morioka, M. Iwase, N. Isei, T. Fujita, S. Takeji, M. Kuriyama, R. Nazikian, G. Fu, K. Hill, and C. Cheng, "Characteristics of alfvén eigenmodes, burst modes and chirping modes in the alfvén frequency range driven by negative ion based neutral beam injection in JT-60u," *Nuclear Fusion*, vol. 39, pp. 1837–1843, nov 1999.

[50] S. D. Pinches, H. L. Berk, M. P. Gryaznevich, S. E. Sharapov, and J.-E. Contributors, "Spectroscopic determination of the internal amplitude of frequency sweeping TAE," *Plasma Physics and Controlled Fusion*, vol. 46, pp. S47–S57, may 2004.

[51] P. W. Shi, W. Chen, Z. B. Shi, X. R. Duan, L. M. Yu, W. L. Zhong, M. Jiang, Z. C. Yang, J. X. Li, J. Wen, X. T. Ding, Y. Liu, and Q. W. Yang, "Destabilization of toroidal alfvén eigenmode during neutral beam injection heating on hl-2a," *Physics of Plasmas*, vol. 24, no. 4, p. 042509, 2017.

[52] M. J. Hole, Z. S. Qu, B. Layden, C. A. Michael, M. H. Woo, J. G. Bak, J. Kim, H. Hezaveh, and the KSTAR team, "Bursting toroidal alfvén eigenmodes in KSTAR plasmas," *Plasma Physics and Controlled Fusion*, vol. 61, p. 025016, jan 2019.

[53] B. N. Breizman, "Nonlinear travelling waves in energetic particle phase space," *Nuclear Fusion*, vol. 50, no. 8, p. 084014, 2010.

[54] R. Nyqvist, M. Lilley, and B. Breizman, "Adiabatic description of long range frequency sweeping," *Nuclear Fusion*, vol. 52, no. 9, p. 094020, 2012.

[55] R. M. Nyqvist and B. N. Breizman, "Modeling of long range frequency sweeping for energetic particle modes," *Physics of Plasmas*, vol. 20, no. 4, 2013.

[56] H. Hezaveh, Z. Qu, B. Layden, and M. Hole, "Impact of energetic particle orbits on long range frequency chirping of BGK modes," *Nuclear Fusion*, vol. 57, no. 12, p. 126010, 2017.

[57] H. Hezaveh, Z. Qu, M. J. Hole, and R. L. Dewar, "Theoretical description of chirping waves using phase-space waterbags," *Plasma Physics and Controlled Fusion*, 2021.

[58] Y. Todo and T. Sato, "Linear and nonlinear particle-magnetohydrodynamic simulations of the toroidal alfvén eigenmode," *Physics of Plasmas*, vol. 5, no. 5, pp. 1321–1327, 1998.

[59] H. Hezaveh, Y. Todo, Z. S. Qu, B. N. Breizman, and M. Hole, "Simulation of convective transport in phase-space during the frequency chirping of a TAE using the mega code," *to be submitted*, 2021.

[60] L. Chen, "Theory of magnetohydrodynamic instabilities excited by energetic particles in tokamaks*," *Physics of Plasmas*, vol. 1, no. 5, pp. 1519–1522, 1994.

[61] H. ITER Physics Expert Group on Energetic Particles, C. Drive, and I. P. B. Editors, "Chapter 5: Physics of energetic ions," *Nuclear Fusion*, vol. 39, no. 12, p. 2471, 1999.

[62] W. Heidbrink and G. Sadler, "The behaviour of fast ions in tokamak experiments," *Nuclear Fusion*, vol. 34, no. 4, p. 535, 1994.

[63] W. Heidbrink, E. Strait, E. Doyle, G. Sager, and R. Snider, "An investigation of beam driven Alfvén instabilities in the DIII-D tokamak," *Nuclear Fusion*, vol. 31, no. 9, p. 1635, 1991.

[64] K. L. Wong, R. J. Fonck, S. F. Paul, D. R. Roberts, E. D. Fredrickson, R. Nazikian, H. K. Park, M. Bell, N. L. Bretz, R. Budny, S. Cohen, G. W. Hammett, F. C. Jobes, D. M. Meade, S. S. Medley, D. Mueller, Y. Nagayama, D. K. Owens, and E. J. Synakowski, "Excitation of toroidal Alfvén eigenmodes in TFTR," *Phys. Rev. Lett.*, vol. 66, pp. 1874–1877, Apr 1991.

[65] S. D. Pinches, H. L. Berk, M. P. Gryaznevich, S. E. Sharapov, and J.-E. Contributors, "Spectroscopic determination of the internal amplitude of frequency sweeping TAE," *Plasma Physics and Controlled Fusion*, vol. 46, no. 7, p. S47, 2004.

[66] E. Fredrickson, N. Gorelenkov, R. Bell, J. Menard, A. Roquemore, S. Kubota, N. Crocker, and W. Peebles, "Fast ion loss in a 'sea-of-TAE'," *Nuclear Fusion*, vol. 46, no. 10, p. S926, 2006.

[67] K. Shinohara, Y. Kusama, M. Takechi, A. Morioka, M. Ishikawa, N. Oyama, K. Tobita, T. Ozeki, S. Takeji, S. Moriyama, T. Fujita, T. Oikawa, T. Suzuki, T. Nishitani, T. Kondoh, S. Lee, M. Kuriyama, J.-. Team, G. Kramer, N. Gorelenkov, R. Nazikian, C. Cheng, G. Fu, and A. Fukuyama, "Alfvén eigenmodes driven by Alfvénic beam ions in JT-60U," *Nuclear Fusion*, vol. 41, no. 5, p. 603, 2001.

[68] I. B. Bernstein, J. M. Greene, and M. D. Kruskal, "Exact Nonlinear Plasma Oscillations," *Phys. Rev.*, vol. 108, pp. 546–550, Nov 1957.

[69] A. Fasoli, B. N. Breizman, D. Borba, R. F. Heeter, M. S. Pekker, and S. E. Sharapov, "Nonlinear Splitting of Fast Particle Driven Waves in a Plasma: Observation and Theory," *Phys. Rev. Lett.*, vol. 81, pp. 5564–5567, Dec 1998.

[70] R. F. Heeter, A. F. Fasoli, and S. E. Sharapov, "Chaotic Regime of Alfvén Eigenmode Wave-Particle Interaction," *Phys. Rev. Lett.*, vol. 85, pp. 3177–3180, Oct 2000.

[71] M. Gryaznevich and S. Sharapov, "Frequency sweeping Alfvén instabilities driven by super-Alfvénic beams in the spherical tokamak START," *Nuclear Fusion*, vol. 40, no. 5, p. 907, 2000.

[72] D. Maslovsky, B. Levitt, and M. E. Mauel, "Observation of Nonlinear Frequency-Sweeping Suppression with rf Diffusion," *Phys. Rev. Lett.*, vol. 90, p. 185001, May 2003.

[73] R. G. Littlejohn, "Variational principles of guiding centre motion," *Journal of Plasma Physics*, vol. 29, pp. 111–125, 002 1983.

[74] R. B. White, *The Theory of Toroidally Confined Plasmas*. London: Imperial College Press, 2nd ed. ed., 2006.

[75] D. Y. Eremin and H. L. Berk, "Frequency sweeping of phase space structures," *Physics of Plasmas*, vol. 9, no. 3, pp. 772–785, 2002.

[76] G. Wang and H. Berk, "Simulation and theory of spontaneous TAE frequency sweeping," *Nuclear Fusion*, vol. 52, no. 9, p. 094003, 2012.

[77] G. Wang and H. Berk, "Model for spontaneous frequency sweeping of an Alfvén wave in a toroidal plasma," *Communications in Nonlinear Science and Numerical Simulation*, vol. 17, no. 5, pp. 2179–2190, 2012. Special Issue: Mathematical Structure of Fluids and PlasmasDedicated to the 60th birthday of Phil Morrison.

[78] H. Berk, C. Boswell, D. Borba, A. Figueiredo, T. Johnson, M. Nave, S. Pinches, S. Sharapov, and J. E. contributors, "Explanation of the JET n = 0 chirping mode," *Nuclear Fusion*, vol. 46, no. 10, p. S888, 2006.

[79] L. Chen, "Theory of magnetohydrodynamic instabilities excited by energetic particles in tokamaks*," *Physics of Plasmas*, vol. 1, no. 5, pp. 1519–1522, 1994.

[80] N. Gorelenkov, S. Pinches, and K. Toi, "Energetic particle physics in fusion research in preparation for burning plasma experiments," *Nuclear Fusion*, vol. 54, no. 12, p. 125001.

[81] B. N. Breizman and S. E. Sharapov, "Major minority: energetic particles in fusion plasmas," *Plasma Physics and Controlled Fusion*, vol. 53, no. 5, p. 054001, 2011.

[82] D. S. Darrow, S. J. Zweben, S. Batha, R. V. Budny, C. E. Bush, Z. Chang, C. Z. Cheng, H. H. Duong, J. Fang, N. J. Fisch, R. Fischer, E. D. Fredrickson, G. Y. Fu, R. F. Heeter, W. W. Heidbrink, H. W. Herrmann, M. C. Herrmann, K. Hill, E. F. Jaeger, R. James, R. Majeski, S. S. Medley, M. Murakami, M. Petrov, C. K. Phillips, M. H. Redi, E. Ruskov, D. A. Spong, E. J. Strait, G. Taylor, R. B. White, J. R. Wilson, K. Wong, and M. C. Zarnstorff, "Alpha particle losses from Tokamak Fusion Test Reactor deuterium–tritium plasmas," *Physics of Plasmas*, vol. 3, no. 5, pp. 1875–1880, 1996.

[83] H. Duong and W. Heidbrink, "Confinement of fusion produced MeV ions in the DIII-D tokamak," *Nuclear Fusion*, vol. 33, no. 2, p. 211, 1993.

[84] D. Sigmar, R. Gormley, and G. Kamelander, "Effects of anomalous alpha particle diffusion on fusion power coupling into tokamak plasma," *Nuclear Fusion*, vol. 33, no. 5, p. 677, 1993.

[85] D. Anderson, P. Batistoni, and M. L. Anderson, "Influence of radial diffusion on triton burnup," *Nuclear Fusion*, vol. 31, no. 11, p. 2147, 1991.

[86] M. Yamagiwa, "Effects of spatial diffusion and direct loss on burnup fractions of fast ions," *Plasma Physics and Controlled Fusion*, vol. 34, no. 9, p. 1503, 1992.

[87] A. Fasoli, D. Testa, S. Sharapov, H. L. Berk, B. Breizman, A. Gondhalekar, R. F. Heeter, M. Mantsinen, and c. t. t. E.-J. Workprogramme, "MHD spectroscopy," *Plasma Physics and Controlled Fusion*, vol. 44, no. 12B, p. B159, 2002.

[88] M. J. Hole, C. M. Ryu, M. H. Woo, J. G. Bak, S. E. Sharapov, M. Fitzgerald, and t. K. Team, "First evidence of Alfvén wave activity in KSTAR plasmas," *Plasma Physics and Controlled Fusion*, vol. 55, no. 4, p. 045004, 2013.

[89] K. Wong, W. Heidbrink, E. Ruskov, C. Petty, C. Greenfield, R. Nazikian, and R. Budny, "Internal transport barrier driven by redistribution of energetic ions," *Nuclear Fusion*, vol. 45, no. 1, p. 30, 2005.

[90] M. C. Herrmann and N. J. Fisch, "Cooling Energetic $\alpha\alpha$ Particles in a Tokamak with Waves," *Phys. Rev. Lett.*, vol. 79, pp. 1495–1498, Aug 1997.

[91] N. Gorelenkov, S. Bernabei, C. Cheng, K. Hill, R. Nazikian, S. Kaye, Y. Kusama, G. Kramer, K. Shinohara, T. Ozeki, and M. Gorelenkova, "Stability properties of toroidal Alfvén modes driven by fast particles," *Nuclear Fusion*, vol. 40, no. 7, p. 1311, 2000.

[92] H. Berk, B. Breizman, and N. Petviashvili, "Spontaneous hole-clump pair creation in weakly unstable plasmas," *Physics Letters A*, vol. 234, no. 3, pp. 213–218, 1997.

[93] R. F. Heeter, A. F. Fasoli, and S. E. Sharapov, "Chaotic Regime of Alfvén Eigenmode Wave-Particle Interaction," *Phys. Rev. Lett.*, vol. 85, pp. 3177–3180, Oct 2000.

[94] G. Wang, H. Berk, B. Breizman, and L.-J. Zheng, "Frequency chirping in the alfvén continuum," *Nuclear Fusion*, vol. 58, p. 082014, jun 2018.

[95] I. G. Abel, B. N. Breizman, and S. E. Sharapov, "Resonant excitation of shear Alfvén perturbations by trapped energetic ions in a tokamak," *Physics of Plasmas*, vol. 16, no. 10, p. 102506, 2009.

[96] M. K. Lilley and R. M. Nyqvist, "Formation of Phase Space Holes and Clumps," *Phys. Rev. Lett.*, vol. 112, p. 155002, Apr 2014.

[97] D. Y. Eremin and H. L. Berk, "Frequency sweeping of phase space structures," *Physics of Plasmas*, vol. 9, no. 3, pp. 772–785, 2002.

[98] G. Wang and H. Berk, "Simulation and theory of spontaneous TAE frequency sweeping," *Nuclear Fusion*, vol. 52, p. 094003, sep 2012.

[99] G. Wang and H. Berk, "Simulation and theory of spontaneous TAE frequency sweeping," *Nuclear Fusion*, vol. 52, no. 9, p. 094003, 2012.

[100] Y. Todo, K. Shinohara, M. Takechi, and M. Ishikawa, "Nonlocal energetic particle mode in a JT-60U plasma," *Physics of Plasmas*, vol. 12, no. 1, p. 012503, 2005.

[101] N. Gorelenkov, H. Berk, R. Budny, C. Cheng, G.-Y. Fu, W. Heidbrink, G. Kramer, D. Meade, and R. Nazikian, "Study of thermonuclear instabilities in next step burning plasma proposals," *Nuclear Fusion*, vol. 43, pp. 594–605, jul 2003.

[102] H. L. Berk, B. N. Breizman, and H. Ye, "Scenarios for the nonlinear evolution of alpha-particle-induced alfvén wave instability," *Phys. Rev. Lett.*, vol. 68, pp. 3563–3566, Jun 1992.

[103] H. L. Berk, B. N. Breizman, and H. Ye, "Map model for nonlinear alpha particle interaction with toroidal alfvén waves," *Physics of Fluids B: Plasma Physics*, vol. 5, no. 5, pp. 1506–1515, 1993.

[104] B. N. Breizman, H. L. Berk, and H. Ye, "Collective transport of alpha particles due to Alfven wave instability." Unknown, Feb. 1993.

[105] D. Maslovsky, B. Levitt, and M. E. Mauel, "Observation of nonlinear frequency-sweeping suppression with rf diffusion," *Phys. Rev. Lett.*, vol. 90, p. 185001, May 2003.

[106] E. D. Fredrickson, R. E. Bell, D. S. Darrow, G. Y. Fu, N. N. Gorelenkov, B. P. LeBlanc, S. S. Medley, J. E. Menard, H. Park, A. L. Roquemore, W. W. Heidbrink, S. A. Sabbagh, D. Stutman, K. Tritz, N. A. Crocker, S. Kubota, W. Peebles, K. C. Lee, and F. M. Levinton, "Collective fast ion instability-induced losses in national spherical tokamak experiment," *Physics of Plasmas*, vol. 13, no. 5, p. 056109, 2006.

[107] H. Wang, Y. Todo, and C. C. Kim, "Hole-clump pair creation in the evolution of energetic-particle-driven geodesic acoustic modes," *Phys. Rev. Lett.*, vol. 110, p. 155006, Apr 2013.

[108] H. L. Berk and K. V. Roberts, "Nonlinear study of vlasov's equation for a special class of distribution functions," *The Physics of Fluids*, vol. 10, no. 7, pp. 1595–1597, 1967.

[109] J. R. Cary, D. F. Escande, and J. L. Tennyson, "Adiabatic-invariant change due to separatrix crossing," *Phys. Rev. A*, vol. 34, pp. 4256–4275, Nov 1986.

[110] J. R. Cary and R. T. Skodje, "Phase change between separatrix crossings," *Physica D: Nonlinear Phenomena*, vol. 36, no. 3, pp. 287 – 316, 1989.

[111] L. Chen and F. Zonca, "Physics of alfvén waves and energetic particles in burning plasmas," *Rev. Mod. Phys.*, vol. 88, p. 015008, Mar 2016.

[112] D. Maslovsky, B. Levitt, and M. E. Mauel, "Suppression of nonlinear frequency-sweeping of resonant interchange modes in a magnetic dipole with applied radio frequency fields," *Physics of Plasmas*, vol. 10, no. 5, pp. 1549–1555, 2003.

[113] H. Duong, W. Heidbrink, E. Strait, T. Petrie, R. Lee, R. Moyer, and J. Watkins, "Loss of energetic beam ions during TAE instabilities," *Nuclear Fusion*, vol. 33, pp. 749–765, may 1993.

[114] M. Garcia-Munoz, I. Classen, B. Geiger, W. Heidbrink, M. V. Zeeland, S. Äkäslompolo, R. Bilato, V. Bobkov, M. Brambilla, G. Conway, S. da Graça, V. Igochine, P. Lauber, N. Luhmann, M. Maraschek, F. Meo, H. Park, M. Schneller,

and G. T. and, "Fast-ion transport induced by alfvén eigenmodes in the ASDEX upgrade tokamak," *Nuclear Fusion*, vol. 51, p. 103013, aug 2011.

[115] F. Nabais, D. Borba, M. Garcia-Muñoz, T. Johnson, V. Kiptily, M. Reich, M. Nave, S. Pinches, and S. S. and, "Impact of strongly driven fishbones and alfvén eigenmodes on fast ion losses," *Nuclear Fusion*, vol. 50, p. 115006, sep 2010.

[116] W. W. Heidbrink, J. R. Ferron, C. T. Holcomb, M. A. V. Zeeland, X. Chen, C. M. Collins, A. Garofalo, X. Gong, B. A. Grierson, M. Podestà, L. Stagner, and Y. Zhu, "Confinement degradation by alfvén-eigenmode induced fast-ion transport in steady-state scenario discharges," *Plasma Physics and Controlled Fusion*, vol. 56, p. 095030, aug 2014.

[117] E. D. Fredrickson, N. A. Crocker, R. E. Bell, D. S. Darrow, N. N. Gorelenkov, G. J. Kramer, S. Kubota, F. M. Levinton, D. Liu, S. S. Medley, M. Podestá, K. Tritz, R. B. White, and H. Yuh, "Modeling fast-ion transport during toroidal alfvén eigenmode avalanches in national spherical torus experiment," *Physics of Plasmas*, vol. 16, no. 12, p. 122505, 2009.

[118] M. Podestà, W. W. Heidbrink, D. Liu, E. Ruskov, R. E. Bell, D. S. Darrow, E. D. Fredrickson, N. N. Gorelenkov, G. J. Kramer, B. P. LeBlanc, S. S. Medley, A. L. Roquemore, N. A. Crocker, S. Kubota, and H. Yuh, "Experimental studies on fast-ion transport by alfvén wave avalanches on the national spherical torus experiment," *Physics of Plasmas*, vol. 16, no. 5, p. 056104, 2009.

[119] X. Q. Wang, H. Wang, Y. Todo, Y. Xu, J. L. Wang, H. F. Liu, J. Huang, X. Zhang, H. Liu, J. Cheng, and C. J. Tang, "Nonlinear simulations of energetic particle-driven instabilities interacting with alfvén continuum during frequency chirping," *Plasma Physics and Controlled Fusion*, vol. 63, p. 015004, nov 2020.

[120] R. B. White, V. N. Duarte, N. N. Gorelenkov, E. D. Fredrickson, and M. Podesta, "Phase-space dynamics of alfvén mode chirping," *Physics of Plasmas*, vol. 27, no. 5, p. 052108, 2020.

[121] R. White, "Modification of particle distributions by mhd instabilities i," *Communications in Nonlinear Science and Numerical Simulation*, vol. 17, no. 5, pp. 2200–2214, 2012. Special Issue: Mathematical Structure of Fluids and Plasmas.

[122] S. Briguglio, M. Schneller, X. Wang, C. D. Troia, T. Hayward-Schneider, V. Fusco, G. Vlad, and G. Fogaccia, "Saturation of alfvén modes in tokamak plasmas investigated by hamiltonian mapping techniques," *Nuclear Fusion*, vol. 57, p. 072001, mar 2017.

[123] Y. Todo, "Properties of energetic-particle continuum modes destabilized by energetic ions with beam-like velocity distributions," *Physics of Plasmas*, vol. 13, no. 8, p. 082503, 2006.

[124] A. Boozer, "Plasma equilibrium with rational magnetic surfaces," *Physics of Fluids*, vol. 24, no. 11, pp. 1999–2003, 1981. cited By 256.

[125] R. C. GRIMM, J. M. GREENE, and J. L. JOHNSON, "Computation of the magnetohydrodynamic spectrum in axisymmetric toroidal confinement systems," in *Controlled Fusion* (J. KILLEEN, ed.), vol. 16 of *Methods in Computational Physics: Advances in Research and Applications*, pp. 253–280, Elsevier, 1976.

[126] S. Hamada, "Hydromagnetic equilibria and their proper coordinates," *Nuclear Fusion*, vol. 2, pp. 23–37, jan 1962.

[127] R. White, *The Theory of Toroidally Confined Plasmas*. Imperial College Press, 2014.

[128] J. D. Meiss and R. D. Hazeltine, "Canonical coordinates for guiding center particles," *Physics of Fluids B: Plasma Physics*, vol. 2, no. 11, pp. 2563–2567, 1990.

[129] M. Li, B. N. Breizman, and L. Zheng, "Canonical straight field line magnetic flux coordinates for tokamaks," *Journal of Computational Physics*, vol. 326, pp. 334–341, 2016.

[130] Z. S. Qu, M. Fitzgerald, and M. J. Hole, "Analysing the impact of anisotropy pressure on tokamak equilibria," *Plasma Physics and Controlled Fusion*, vol. 56, p. 075007, may 2014.

[131] M. Grant and S. Boyd, "CVX: Matlab software for disciplined convex programming, version 2.1," Mar. 2014.